Fall 2009

Structure-based mechanism of proton transport through the influenza A M2 protein

Alexei L. Polishchuk
University of Pennsylvania, alexeip@mail.med.upenn.edu

Structure-based mechanism of proton transport through the influenza A M2 protein

Abstract
Influenza A/M2 is a minimalistic integral membrane protein that mediates proton transport across the viral membrane and is of interest as an antiviral drug target. This protein has been extensively studied by electrophysiologists, biophysicists, structural biologists, and medicinal chemists, but a synthesis and unified extension of the knowledge bases from these fields has not been undertaken. The principal aim of this thesis is to develop a comprehensive, quantitative, structure-based mechanism that accounts for the key functional and biophysical properties of A/M2. To demonstrate the electrophysiological equivalence of the protein's transmembrane domain (M2TM) and full length A/M2, proteoliposome flux experiments are conducted as a first step. Next, high-resolution crystals of an M2TM variant are obtained; the resulting structure and computational simulations provide a structural basis for the unusually high degree of charge stabilization inside the M2TM helical bundle, suggest a previously unseen mechanism used by Nature to stabilize charge in a membrane, and shed light on the likely pH-dependent structural transitions that the protein undergoes. Fluorescence quenching and EPR spectroscopy experiments confirm that M2 reconstituted in bilayers undergoes pH-driven changes in its conformational equilibrium that are consistent with available structures and governed by previously reported pKa values. Mechanistic models of this process are constructed and successfully fit to functional data. The fitting results show that proton transport and rectification are mediated by conformational transitions between structural ensembles with different proton affinities. Finally, the functional implications of targeted changes to the geometric and electronic properties of the key His 37 sidechain are observed, indicating that the shape of the His 37 imidazole rings is exquisitely tuned to mediate proton transport.

Degree Type
Dissertation

Degree Name
Doctor of Philosophy (PhD)

Graduate Group
Biochemistry & Molecular Biophysics

First Advisor
William F. DeGrado

Keywords
H+ crystal structure transporter mechanism channel

Subject Categories
Biochemistry

STRUCTURE-BASED MECHANISM OF PROTON TRANSPORT THROUGH THE INFLUENZA A/M2 PROTEIN

Alexei Polishchuk

A DISSERTATION

in

Biochemistry and Molecular Biophysics

Presented to the Faculties of the University of Pennsylvania

in

Partial Fulfillment of the Requirements for the

Degree of Doctor of Philosophy

2009

Supervisor of Dissertation: _____
Dr. William F. DeGrado, George W. Raiziss Professor of Biochemistry and Biophysics

Graduate Group Chairperson: _____
Dr. Kathryn M. Ferguson, Associate Professor of Physiology

Dissertation Committee:
Dr. Gregory Van Duyne, Jacob Gershon-Cohen Professor of Medical Science

Dr. Lawrence Brass, Professor of Medicine, Pathology, and Pharmacology

Dr. Robert Doms, Chair, Department of Microbiology

Dr. Feng Gai, Associate Professor of Chemistry

Dr. Mark Lemmon, Professor of Biochemistry and Biophysics

Dr. Jane Vanderkooi, Professor of Biochemistry and Biophysics

Dedicated to my wife, parents and grandparents,

and to the memory of those who left us along the way.

ACKNOWLEDGMENT

This journey in science would not have reached its completion without the contributions of many individuals. My sincere gratitude goes out to everyone who has helped me grow and learn along the way.

I would like to thank my advisor, Dr. DeGrado, for his guidance, optimism, and boundless scientific creativity. Every time we talked, I learned something new in how to approach a scientific problem, skills that I know I will rely upon greatly in the years to come.

To my coworkers in the DeGrado lab, especially Dr. James Lear, Dr. Lidia Cristian, Dr. Rudresh Acharya, and Dr. Paul Billings, thank you for the patient hands-on teaching, many thoughtful discussions, and your day-to-day presence in the group. It has truly been a pleasure working with you, and I have learned much from our time together.

To the many collaborators with whom I worked on this project: Dr. Larry Pinto and Dr. Robert Lamb and your group members, especially Dr. Chunlong Ma and Dr. Joshua Rausch, and the groups of Dr. Kathleen Howard, Dr. Michael Klein, and Dr. Feng Gai, thank you for welcoming me into your cities and your labs, and teaching me much about your work. Our interactions have broadened my scientific horizons greatly. It's been an honor to work with you.

To my thesis committee, thank you for your many good suggestions and continued support over the years. Your time and input is always much appreciated.

To the MD-PhD program office, and especially Maggie Krall, thank you for your guidance and advice, and for having a never-empty candy jar on the front desk.

Finally, to my wife, my parents, my extended family, and my friends, much love and thanks for being there every day over the years. I could not have done it without you.

ABSTRACT

STRUCTURE-BASED MECHANISM OF PROTON TRANSPORT THROUGH THE INFLUENZA A/M2 PROTEIN

Alexei Polishchuk

Supervisor: Dr. William F. DeGrado

Influenza A/M2 is a minimalistic integral membrane protein that mediates proton transport across the viral membrane and is of interest as an antiviral drug target. This protein has been extensively studied by electrophysiologists, biophysicists, structural biologists, and medicinal chemists, but a synthesis and unified extension of the knowledge bases from these fields has not been undertaken. The principal aim of this thesis is to develop a comprehensive, quantitative, structure-based mechanism that accounts for the key functional and biophysical properties of A/M2. To demonstrate the electrophysiological equivalence of the protein's transmembrane domain (M2TM) and full length A/M2, proteoliposome flux experiments are conducted as a first step. Next, high-resolution crystals of an M2TM variant are obtained; the resulting structure and computational simulations provide a structural basis for the unusually high degree of charge stabilization inside the M2TM helical bundle, suggest a previously unseen mechanism used by Nature to stabilize charge in a membrane, and shed light on the likely pH-dependent structural transitions that the protein undergoes. Fluorescence quenching and EPR spectroscopy experiments confirm that M2 reconstituted in bilayers undergoes pH-driven changes in its conformational equilibrium that are consistent with available structures and governed by previously reported pK_a values. Mechanistic models of this process are constructed and successfully fit to functional data. The fitting results show that proton transport and rectification are mediated by conformational transitions between structural ensembles with different proton affinities. Finally, the functional implications of targeted changes to the geometric and electronic properties of the key His 37 sidechain are observed, indicating that the shape of the His 37 imidazole rings is exquisitely tuned to mediate proton transport.

TABLE OF CONTENTS

LIST OF TABLES

LIST OF ILLUSTRATIONS

PREFACE

Influenza A/M2 is a fascinating little protein from many perspectives. It's inhibited by one of the two classes of currently available anti-influenza drugs, and is thus of great interest to the virology, public health, and pharmacology communities, especially as new strains of the flu emerge and drug resistance among existing strains skyrockets.

A homotetramer of 97 amino acid subunits, each with only a single transmembrane domain, A/M2 is among the smallest integral membrane proteins known and is therefore an excellent model system to the chemical theoreticians, biophysicists, and structural biologists studying how membrane proteins fold and assemble in the membrane.

What's more, A/M2 is an ion transport protein (one of the most compact identified to date) that's exquisitely selective for protons, transports them preferentially in one direction versus the other, and is regulated by its cargo (i.e. pH). Its electrophysiological properties have therefore been extensively studied by the ion channel community.

The goal of this thesis is to develop a unified understanding of how the compact structural elements of M2 can underlie its rich and complex electrophysiological properties.

Chapter 1 summarizes the large body of A/M2 literature that has been generated by the aforementioned fields, and points out an obstacle to an integrated approach to

understanding this protein: different scientific fields have employed different model systems and protein fragments of different lengths. Therefore findings from one scientific community may not necessarily correlate with the findings of another. In Chapter 2, we demonstrate that a small core of the protein represented by its transmembrane domain, studied extensively by biophysicists and structural biologists, recapitulates the relevant functional properties of the full-length protein studied by the ion channel community. This finding paves the way for constructing a comprehensive, structure-based transport mechanism.

In Chapter 3, we describe a new, high-resolution crystal structure of the protein's transmembrane segment. The helical conformations observed in this structure are consistent with a mechanistic hypothesis where changes in pH cause the A/M2 transmembrane helices to bend and straighten in well-defined ways. Furthermore, the high resolution of the structure shows the sidechains and ordered water molecules that make up the proton transport pathway in exquisite detail, suggesting a mechanism by which M2 can stabilize an unexpectedly large number of bound protons in its core. High-level computational simulations on this structure confirm this stabilizing effect, and shed light on the functional importance of the water molecules that populate the interior of the protein's transmembrane segment.

In Chapter 4, we test our mechanistic hypothesis with full-length protein in bilayers at equilibrium. The detailed structures of the protein have been obtained in non-native

micelles, and most represent conformational snapshots that successfully crystallized. It is therefore important to find out whether the protein undergoes the proposed conformational changes in a native-like environment at equilibrium. Fluorescence quenching experiments and electron paramagnetic resonance spectroscopy show that indeed, A/M2 changes its conformational ensemble in bilayers, driven by protonation events that take place according to previously measured pK_a values of its His 37 sidechains.

In Chapter 5, we quantify our mechanistic hypothesis by constructing kinetic models of proton transport which correlate changes in conformational ensembles to proton binding and release. We find that such a mechanism can accurately describe the electrophysiological properties of this protein reported by two different groups, and can also account for the unusual behavior of certain M2 mutants. From this exercise, we learn that unidirectional, pH-regulated proton transport through M2 takes place because different conformational states of M2 have different affinities for protons, and varying accessibilities to proton-carrying water molecules on either side of the membrane. The transport cycle consists of M2 conformations with high proton affinities binding protons from water molecules at the viral exterior, and conformations with lower proton affinities releasing them to waters at the viral interior.

Finally, in Chapter 6, we focus in on the functionally critical tetrad of His 37 residues in the M2 transmembrane segment. Using mutagenesis with unnatural amino acids that

preserve either key electronic or geometric properties of histidine while varying the other, we find that the geometry of the imidazole ring is precisely tuned for function in the protein, while the ring's proton affinity can be changed with predictable functional effects.

In summary, this thesis develops an integrated, unified explanation for how protein structure and changes in pH underlie the highly complex electrophysiological behavior of this model membrane protein. The relatively simple functional mechanism derived here can be used to inform drug design efforts and further our understanding of the fascinating biology and electrophysiology of the transmembrane proteome.

Chapter 1: Introduction and literature Review - influenza A/M2, a minimalistic membrane protein.

1.1. The public health threat of influenza infection.

Influenza virus infection presents a significant public health threat, having resulted in epidemics and major pandemics recorded in history for hundreds (Hirsch 1883; Thomson and Thomson 1933; Crosby 1976), and perhaps thousands of years (Langmuir, Worthen et al. 1985). Even with recent medical advances, complications of annual epidemic influenza cause severe and sometimes fatal illness (Thompson, Shay et al. 2003) especially among the elderly and immunocompromised (Barker and Mullooly 1980; Glezen, Keitel et al. 1991), and can cause substantial debility even in otherwise healthy patients (Kavet 1977; Schonenbaum 1996), resulting in large direct and indirect economic costs (Szucs 1999). Major pandemics, which have occurred approximately every 30-40 years in the past century, have caused significantly higher mortality even among healthy young adults (Simonsen, Clarke et al. 1998); it is estimated that the especially severe 1918-1920 “Spanish Flu” pandemic resulted in more deaths than did World War 1 (Wilton 1993). Unfortunately, new potential pandemic threats are on the horizon, such as the recent worldwide outbreak of swine flu in the spring of 2009, and the persistence of highly virulent avian influenza strains in Asia that have caused greater than 60% mortality rates in documented human infection (de Jong 2008).

While an influenza vaccine and four antiviral drugs are now on the market, significant concerns remain about the availability of effective treatment and prophylaxis for influenza, particularly in a pandemic situation (Memoli, Morens et al. 2008). Vaccine production to target a new influenza strain presently takes several months (Tripp and Tompkins 2008), and levels of resistance to antivirals have recently increased, in some cases dramatically (Bright, Shay et al. 2006; Bright

RA, Shay et al. 2006; Hurt, Ho et al. 2006; Monto 2008). Furthermore, vaccine effectiveness has been shown to be lower in those most vulnerable to influenza infection (Powers and Belshe 1993; Govaert, Thijs et al. 1994), and currently available antivirals must be given within a very narrow time window for optimal results, which in and of themselves are generally modest (Galbraith, Oxford et al. 1971; Nicholson, Aoki et al. 2000; Treanor, Hayden et al. 2000). Thus, there is continuing interest and urgency in better understanding the detailed underpinnings of influenza infection and pathogenesis, so that better therapeutic tools can be obtained (Hayden 2009). This thesis focuses on developing a comprehensive molecular mechanism based on the structure and function of a key influenza protein that is targeted by two currently available antiviral drugs.

1.2. The influenza virus family.

The three types of influenza viruses (A, B and C) belong to the orthomyxoviridae family. First isolated in 1933 (Smith, Andrewes et al. 1933), influenza A viruses can infect multiple hosts, including humans, swine, ferrets, and birds, while influenza B (Francis Jr 1940) infects humans only, and influenza C (Taylor 1951) viruses infect humans and swine (Treanor 2005). The most serious human disease, manifest by high fevers, body aches, fatigue and dry cough, followed on occasion by bacterial superinfection, is caused by influenza A and, to a somewhat lesser extent, influenza B strains (Nigg, Ecklund et al. 1942; Blaine, Luby et al. 1980). Influenza C is believed to cause mild infection more similar to a common cold (Mogabgab 1963).

Influenza viral particles are enclosed in a lipid membrane envelope, and contain a genome made up of 7-8 single strand RNA segments, each segment encoding for particular proteins used by the virus. It is this segmented genome that makes influenza viruses highly problematic from the standpoint of vaccine development and human immune response, since two genetically different viruses infecting the same cell can swap segments to create a novel virus with a new set of antigenic and virulence properties. This phenomenon typically does *not* take place with the small, subtle changes in the genetic makeup of influenza, known as antigenic drift (Wilson and Cox

1990), that regularly results in the annual epidemic flu and occasionally in more severe outbreaks (Morens, Taubenberger et al. 2009). However, it has been hypothesized to underlie (Dowdle and Schild 1976) the rare but more substantial changes, often in non-human hosts, that are known as antigenic shifts. Antigenic shifts can lead to viruses with a novel immunological signature to which pre-existing immunity in the population is lacking, and can therefore cause deadly worldwide pandemic disease if the virus also has high replicative fitness and human-human transmissibility.

1.3. Influenza virus membrane proteins are targets of vaccines and antivirals.

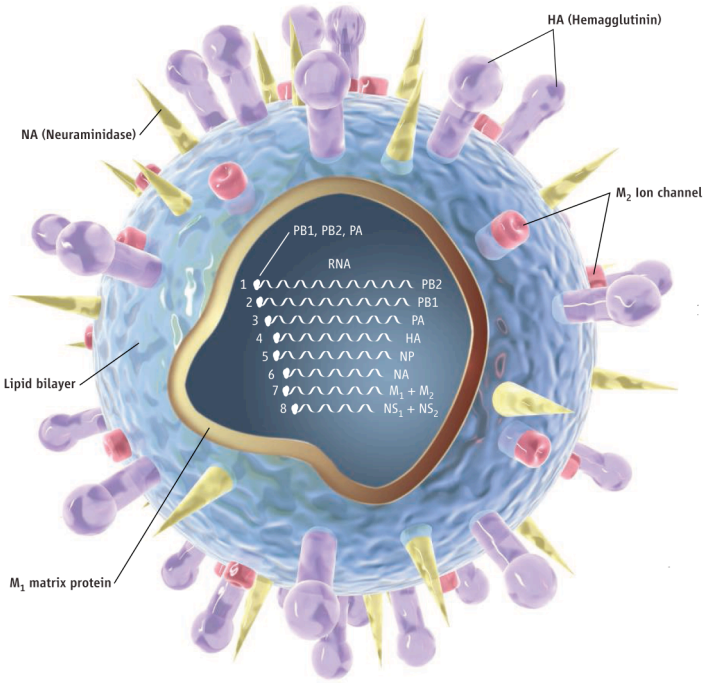

Figure 1.1 Schematic of influenza virus envelope and membrane proteins. Adapted from (Kaiser 2006).

The influenza virus lipid envelope (shown in schematic form in Fig. 1.1) contains three types of membrane proteins: hemagglutinin, neuraminidase, and relatively much less abundant M2 protein (Brooks, Butel et al. 2004). Hemagglutinin (HA or H) and neuraminidase (NA or N) are key

antigenic determinants of the virus, and their variants are reflected in the nomenclature of influenza virus subtypes, e.g. H1N1 or H3N2. These proteins play critical roles in the viral life cycle and are the only targets of existing immunologic and pharmacologic anti-influenza therapies, thus a detailed understanding of their function is key to improving treatments for influenza infection.

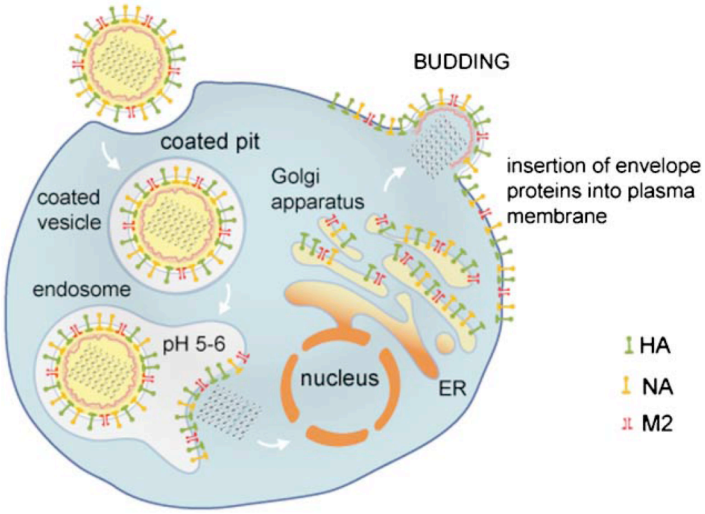

Figure 1.2. Influenza virus infection cycle. Illustration from (Pinto and Lamb 2007).

In a typical viral infection cycle, outlined in Fig. 1.2 and reviewed in reference (Lagoja and De Clercq 2008), hemagglutinin on the viral particle binds sialic acid residues on the target epithelial cell surface. The viral particle is endocytosed, trafficked inside an endocytic vesicle, and eventually ends up in the cell endosome, where extraviral pH is lowered. The M2 protein transports protons from the endosome lumen into the viral interior, dissociating the viral RNA genome from the matrix protein with which it is packaged. In a pH-dependent manner, the influenza hemagglutinin undergoes a dramatic conformational change to trigger fusion of the viral envelope and the target cell endosomal membrane. The viral RNA is then replicated in the target cell nucleus, and newly synthesized viral proteins are trafficked in the Golgi apparatus membrane for assembly and export. There, M2 plays its second role in the infection cycle, allowing proton

efflux from the slightly acidic Golgi lumen to prevent premature hemagglutinin pH-triggering in certain influenza strains (Sugrue, Bahadur et al. 1990; Sagakuchi, Leser et al. 1996). Finally, after new viral particles are assembled and bud off from the cell surface, neuraminidase cleaves sialic acid linkages to detach the virion from the cell membrane and allow for infection of other cells.

The influenza hemagglutinin, a large trimeric glycoprotein (Wilson, Skehel et al. 1981) used by the virus to bind sialic acid receptors on target cells and mediate pH-triggered membrane fusion, is the most abundant influenza envelope protein (Brooks, Butel et al. 2004) and a target of currently available influenza vaccines (Wood 1998). However, it is highly variable between strains (Knossow and Skehel 2006) and analyses of human clinical isolates show continuous genetic change with time even in non-pandemic years (Bragstad, Nielsen et al. 2008). This drift is likely caused by continuous selective pressure by pre-existing host antibodies (Webster, Laver et al. 1980), and therefore limits the antigenic precision of the annual influenza vaccine and its disease-preventing utility. There is thus a need for antiviral drugs that can be administered to treat existing influenza infection or as additional prophylaxis in areas of an ongoing outbreak. The other two influenza membrane proteins are targets of such agents.

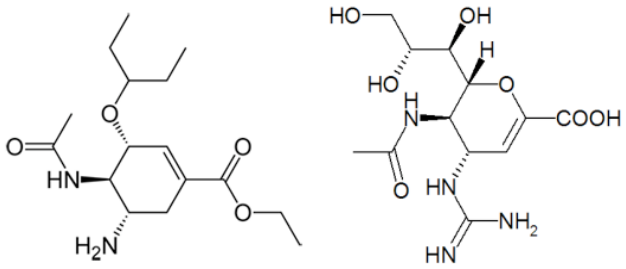

Figure 1.3. Influenza neuraminidase inhibitors oseltamivir (left) and zanamivir (right).

The influenza neuraminidase protein, an enzyme that cleaves sialic acid linkages to free newly synthesized virions (Compans, Dimmock et al. 1969; Colman, Varghese et al. 1983; Varghese, Laver et al. 1983), has been successfully targeted using structure-based drug design in the 1990s

(von Itzstein, Wu et al. 1993; von Itzstein and Thomson 2009). Efforts to date have resulted in two commercially available inhibitors shown in Fig 1.3, oseltamivir (Tamiflu) and zanamivir (Relenza), which are licensed to treat influenza A and B infection and are now recommended as first line therapy (Fiore, Shay et al. 2008). These compounds target a highly conserved site in the neuraminidase enzyme that is necessary for catalytic function, and thus were predicted to face little clinically meaningful resistance. However, in recent years, spontaneously emerging oseltamivir-resistant viruses have entered worldwide circulation (Lackenby, Thompson et al. 2008). More alarmingly, development of resistance during oseltamivir treatment has been reported in cases of human infection with the highly virulent avian H5N1 influenza strain (de Jong, Tran et al. 2005).

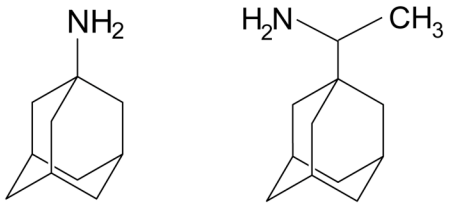

Figure 1.4. Influenza M2 protein inhibitors amantadine (left) and rimantadine (right).

The least abundant influenza membrane protein, M2, is the target of the oldest class of anti-influenza drugs, the aminoadamantanes amantadine and rimantadine, shown in Fig. 1.4. The activity of the parent compound amantadine was discovered empirically in the 1960s and predated the identification of its protein target by some two decades (Davies, Grunert et al. 1962). That amantadine acts on the M2 protein was inferred by sequence analysis of amantadine-resistant influenza A strains, where mutations mapped to the transmembrane domain of M2 (Hay, Wolstenholme et al. 1985). Interestingly, influenza B is naturally amantadine-insensitive (Davies, Grunert et al. 1962), presumably because of inherent differences in the transmembrane domain sequence of its M2 homolog BM2 (Ma, Soto et al. 2008). Amantadine (Symmetrel) and its second-generation analog rimantadine (Flumadine) have been a mainstay of anti-influenza A

therapy and prophylaxis for over thrity years, with low levels of naturally occurring resistance (Ziegler, Hemphill et al. 1999). However, in recent years, resistance levels shot up dramatically to over 90% in the United States (Bright, Shay et al. 2006), prompting the CDC to urge physicians to avoid the use of adamantane drugs for influenza treatment and prophylaxis until further notice (Fiore, Shay et al. 2008). While some progress has been made in generating novel M2 inhibitors (Kurtz, Luo et al. 1995; Kolocouris, Zoidis et al. 2007; Wang, Cady et al. 2009), no new compounds with significant activity against the most common amantadine-resistant M2 variants have been developed.

1.4. Influenza A/M2 is a minimalistic membrane transport protein.

In addition to being a validated target for influenza antivirals, influenza A M2 (A/M2) has become a system of interest in many other basic science fields. It has been studied as a model integral membrane protein given its relatively small size (each amino acid strand is only 97 residues long), self-association (the functional protein is a tetramer), and ion transport function (reviewed in (Pinto and Lamb 2006; Pinto and Lamb 2007)). In fact, A/M2 is among the smallest known proteins involved in ion translocation (Decoursey 2003), and is furthermore ligand-regulated. Thus, it has been an attractive model system for the investigation of membrane protein folding, assembly and structure, ion transport physiology, computational biology, and, of course, pharmacology and medicinal chemistry. While much progress has been made in many of these fronts, a definitive, unified mechanism of A/M2 transport that correlates findings from all of these fields has not been established. One of the key aims of this thesis is to develop such a mechanism, combining concepts and results from electrophysiology, biophysics, and structural biology. A sequence of a common naturally occurring A/M2 variant (A/Udorn/72 strain) and a domain diagram of A/M2 are shown in Figures 1.5 and 1.6 to assist the reader in following the more detailed experiments described in later sections of this chapter.

Figure 1.5. Sequence of A/M2 (A/Udorn/72).

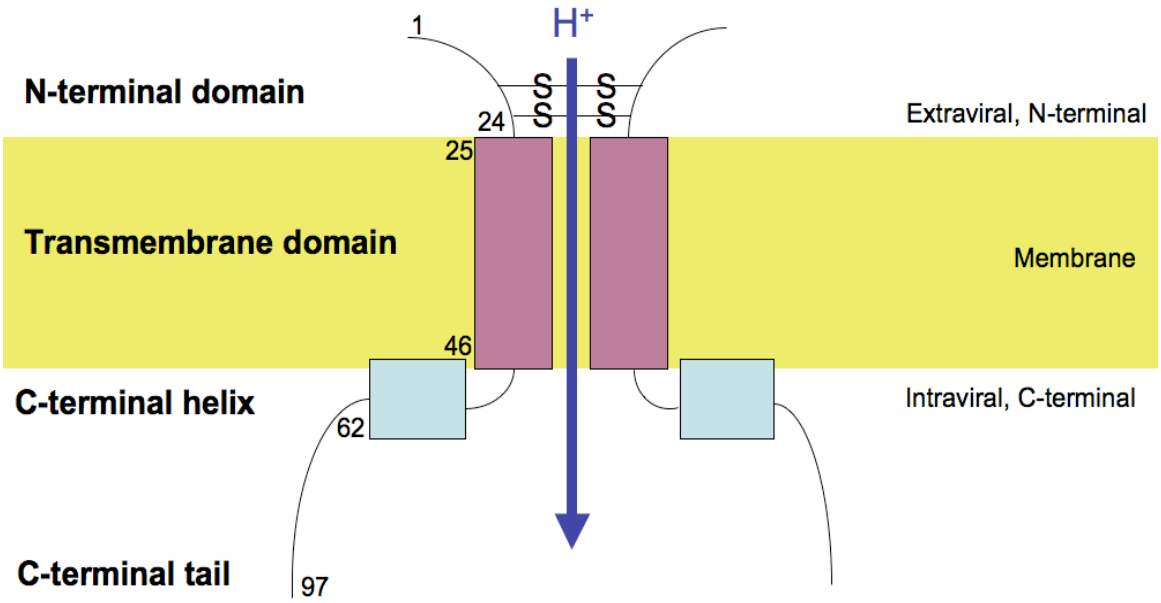

Figure 1.6. Domain diagram of A/M2. One half of the tetramer is shown for simplicity.

Soon after A/M2 was identified as a transmembrane protein and the target of amantadine (Hay, Wolstenholme et al. 1985; Lamb, Zebedee et al. 1985), it was shown to mediate the pH-dependent dissociation of the viral RNA from its packaging M1 or matrix protein (Zhirnov 1990; Helenius 1992; Zhirnov 1992). A/M2 inhibition was also shown to lead to premature triggering of hemagglutinin during its export from influenza-infected cells (Sugrue, Bahadur et al. 1990). Thus, it was surmised that A/M2 was involved in proton transport. The minimal active form of A/M2 was shown to be a homotetramer (Sakaguchi, Tu et al. 1997) stabilized by a pair of N-terminal disulfide bonds, and its transmembrane domain was demonstrated to form alpha helices in membranes (Duff, Kelly et al. 1992). Confirmation that A/M2 transported ions across the membrane came in 1992, when A/M2 expressed in *Xenopus laevis* oocytes, a model system for the study of ion channels, and found to mediate cation currents in a pH-regulated fashion (Pinto,

Holsinger et al. 1992). As shown in Figure 1.7, when the pH of buffer bathing the oocytes was lowered from ~7.5 to ~5.5, cation flux increased, although a single residue mutation in the heart of the protein's transmembrane domain (His37Ala) could abrogate the pH regulation. Baseline currents were seen from oocytes injected with antisense mRNA. Chizhmakov and Hay found a similar pH-regulating effect by expressing A/M2 in another electrophysiological model system, murine erythroleukemia cells (Brooks, Butel et al.), and established that A/M2 is stringently (over 10^6 fold) proton-selective.

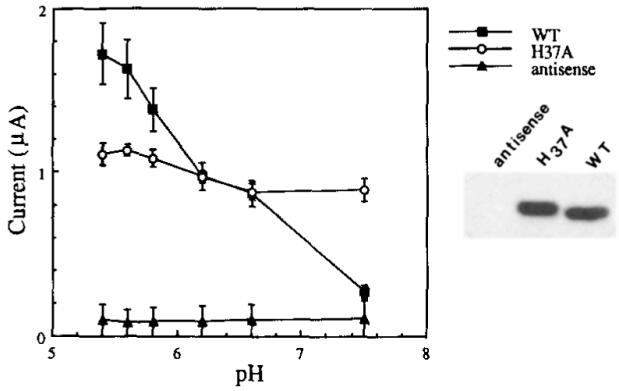

Figure 1.7. The first direct evidence that M2 functions as an ion transport protein. M2 expressed in oocytes mediates increasing inward cation currents as bathing pH is decreased. Figure from (Pinto, Holsinger et al. 1992).

1.5. Functional studies of influenza A/M2.

Before embarking on further discussion of detailed functional experiments on A/M2, the most commonly used model systems for studying membrane transport proteins will be reviewed, along with their advantages and limitations. The gold standard measurement for ion channels is of single-channel behavior, where parameters such as per-protein current amplitude, open time and probability, inactivation, and inhibition can be ascertained. Systems to obtain such measurements involve application of a constant electrical potential (voltage clamp) across an electrically isolated area (patch) of membrane containing the protein of interest (Neher and Sakmann 1976). As

shown in Figures 1.8 and 1.9 the membrane may come from a cell expressing the protein, or from an artificially formed planar bilayer. Unfortunately, single-channel measurements (typical results for small membrane-spanning peptides are shown in Fig. 1.9) remain a relatively untouched holy grail for A/M2, as its per-protein currents are extremely small and thus very difficult to measure individually. To this end, a comparison of M2 current magnitudes with those of some other known proton channels is shown in Figure 1.10. Therefore, the vast majority of functional studies of A/M2 transport have relied on whole-cell or otherwise averaged measurements of the simultaneous currents of many proteins; single channel properties have been estimated by quantifying the amount of protein present in the system.

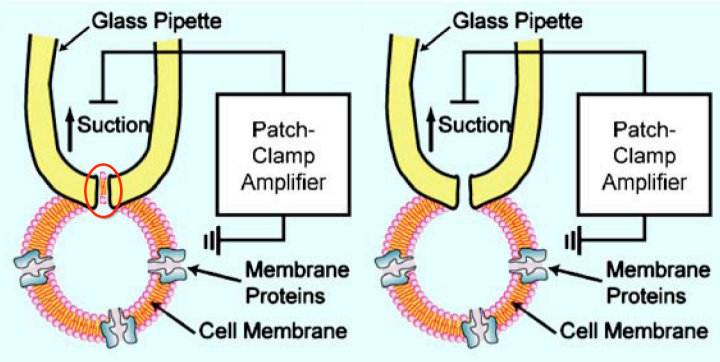

Figure 1.8. Diagram of a cellular patch clamp experiment. A gigaohm seal is formed between the glass pipette to isolate a small area (patch) of the cell membrane (circled in red). If membrane proteins are also present in the patch, their currents can be recorded (left panel). Alternatively, the pipette may pierce the cell membrane (right panel), in which case membrane currents from the whole cell are recorded. Illustration adapted from (Suzuki and Takeuchi 2008).

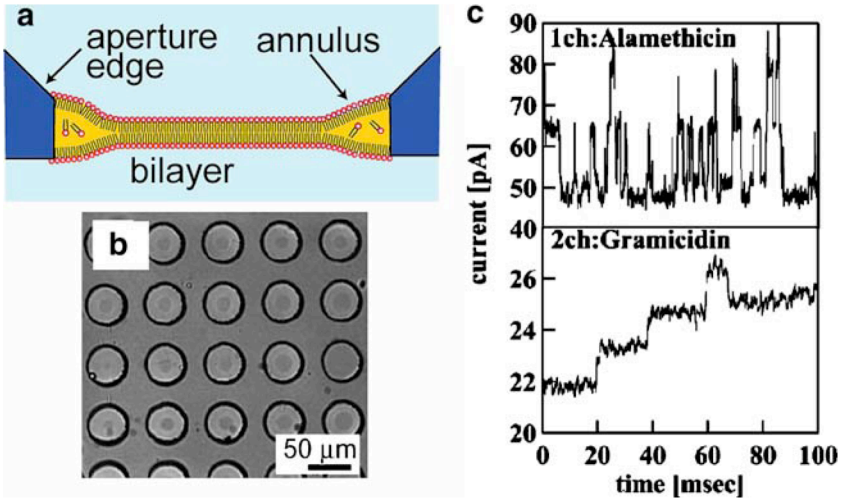

Figure 1.9. a) Planar bilayer electrophysiology experiment, cartoon depiction of side view. A voltage is applied between the upper and lower compartments. b) Top view of parallel planar bilayer systems. c) Example single-channel current recordings (seen as current spikes) of simple channel-forming peptides. Illustration from (Suzuki and Takeuchi 2008).

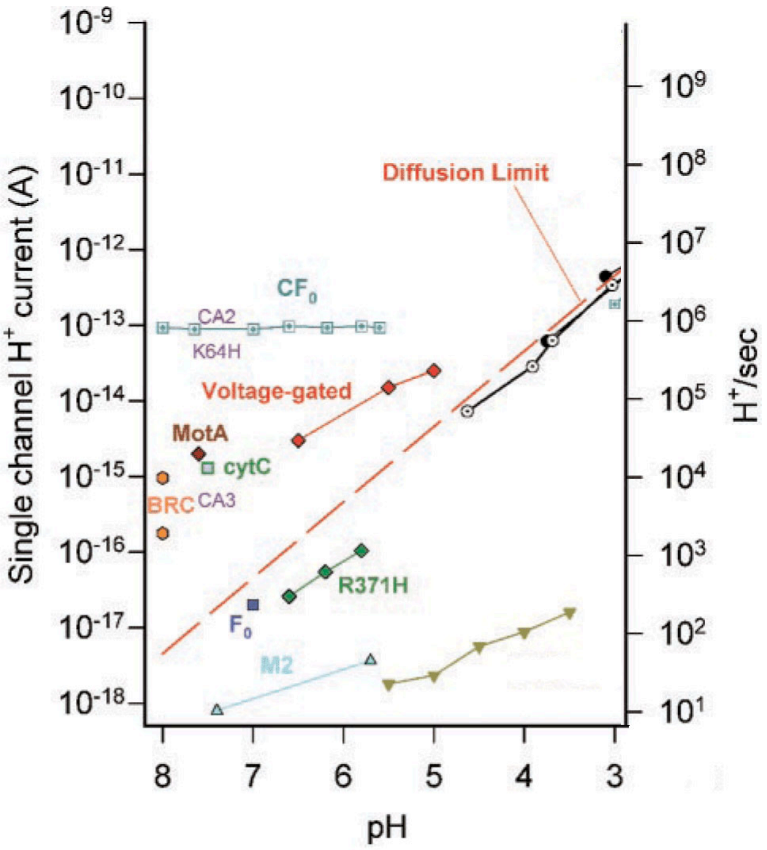

Figure 1.10. Measured or estimated single channel currents for a variety of proton channels. M2 (light blue, near bottom of figure) is one of the slowest known proton channels with transport rates estimated at ~10-100 protons/second (right axis). Figure from (Decoursey 2003).

Xenopus laevis (African clawed frog) oocytes are very convenient model systems for the study of ion channels (Tammaro, Shimomura et al. 2008): they are extremely large cells often exceeding 1 mm in diameter and are therefore easy to manipulate, and can be induced to express transport proteins of interest by intracytoplasmic injection of mRNA encoding the desired protein. However, transport measurements with the oocyte system require special care, since expression of heterologous proteins or voltage extremes can activate normally quiescent endogenous membrane currents (Kowdley, Ackerman et al. 1994; Shimbo, Brassard et al. 1995), leading to artifactual measurements. Furthermore, as living cells, the oocytes may not withstand extremes of pH and buffer ionic compositions. Therefore, great care must be taken to ensure that observed

currents are in fact through the protein of interest, and non-physiological conditions must be avoided.

Other eukaryotic cells, such as CV-1 (fibroblast) and MEL (murine erythroleukemia) have also served as model systems for expressing ion-transporting membrane proteins (Wang, Lamb et al. 1994). They have similar advantages and disadvantages as oocytes (Witchel, Milnes et al. 2002), and may be prone to artifacts from endogenous channels or extreme conditions. While in early studies of A/M2, these systems have been somewhat more robust in delivering M2-specific measurements, (Chizhmakov, Geraghty et al. 1996) more recently studies in both oocytes and CV-1/MEL cells have provided highly reliable and mutually consistent data.

Channel proteins have also been reconstituted in the membranes of unilamellar phospholipid vesicles (Miller 1984), and this method provides a way to completely isolate the construct of interest from other protein components that are present in cells. Ion fluxes can be determined by spectral measurements of ion-sensitive dyes (as shown in Figure 1.11), or by ion-sensitive electrodes. Liposome measurements are usually of bulk transport, as the properties of multiple liposomes and proteins are averaged. This system requires a membrane of very low intrinsic permeability, and relies on reconstitution of purified protein from a separate source. Thus, it becomes important to ensure that the reconstitution process is efficient without loss of material, since the protein machinery that performs membrane insertion in living cells is not present in the liposome system. Also, it is difficult to control protein orientation once reconstituted in the liposome bilayer (N-terminal inside or N-terminal outside) (Niu, Doctrow et al. 2009).

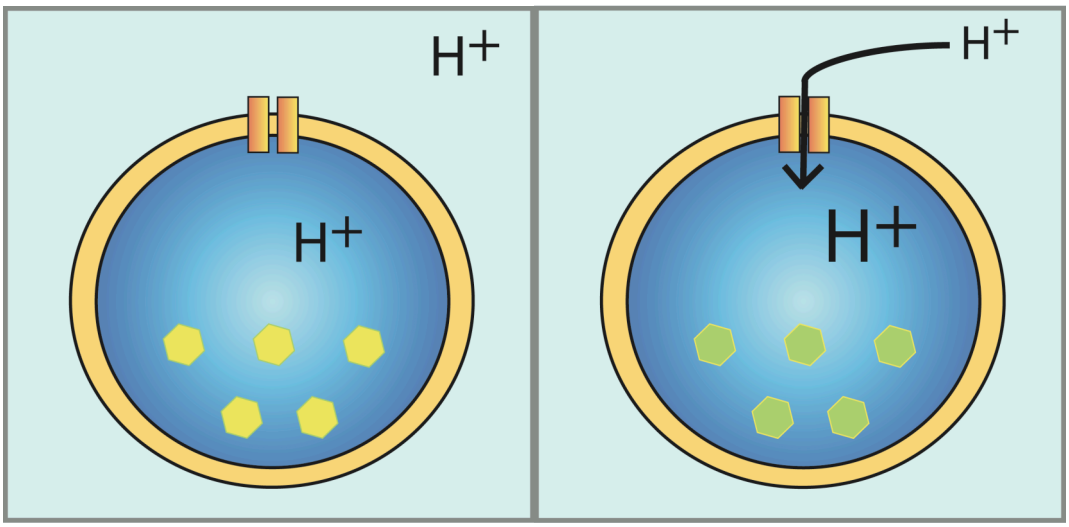

Figure 1.11. Left panel: a membrane protein is reconstituted in a liposome membrane (unilamellar membrane vesicle) that contains a pH-sensitive fluorescent dye (depicted as yellow hexagons). Right panel: the spectral properties of the dye change in response to proton influx or efflux from the liposome.

Finally, channel proteins can be studied in the planar lipid bilayer system, where a highly impermeable unilamellar membrane bilayer is created in a small opening between two bathing chambers, as reviewed in (Miller 1983) and shown diagrammatically in Figure 1.9. The protein fragment of interest can be added to the bilayer in a number of ways; for example by injection in detergent micelles, or by membrane fusion with liposomes or other cell membrane fragments containing the protein. Therefore, this system also relies on efficient protein insertion. An electrical potential can be applied across the bilayer much like in the cell-based studies, although this system allows the use of non-physiological buffer conditions, making such results potentially more difficult to correlate to biological processes. It should also be kept in mind that planar lipid bilayer recordings of small, single-channel currents are highly sensitive to inadvertent contamination.

Some of the first direct measurements of M2 activity came from *Xenopus laevis* oocytes, which when injected with A/M2 mRNA exhibited inward whole-cell cation currents that were inhibited by amantadine and increased by negative internal voltages and low external pH (Pinto, Holsinger et al. 1992). Loss of the His 37 sidechain led large pH-insensitive currents, whereas other mutations in the transmembrane domain abrogated amantadine sensitivity (Pinto, Holsinger et al. 1992), and deletions of 3-5 residues in the transmembrane domain led to marked changes or complete loss of activity (Holsinger, Nichani et al. 1994). In the initial oocyte channel experiments, it was incorrectly concluded that M2 is selective for Na^+, which was also the finding in a planar lipid bilayer study of M2 (Tosteson, Pinto et al. 1994). These erroneous findings were likely obtained because of unrecognized endogenous oocyte currents, and pH extremes in the planar lipid bilayer study.

Nevertheless, the stimulating effect of decreased pH_{out} on transport activity was interpreted to mean that A/M2 is regulated by pH, and possible sites that mediate this regulation phenomenon were examined. The only residue in the M2 transmembrane sequence that titrated in the pH range of A/M2 activation was His37, the mutation of which to Ala was shown in the initial oocyte study to render M2 currents pH-insensitive (Pinto, Holsinger et al. 1992). Building on this evidence, constructs with this residue mutated to Gly, Glu, Arg, or Lys were tested (Wang, Lamb et al. 1995). As shown in Figure 1.12, the His37Gly and His37Glu mutants had almost completely abrogated pH regulation and much greater estimated currents, while oocytes expressing His37Arg and His37Lys were non-viable. Thus, it was concluded that His 37 is the pH sensing residue of A/M2, and is the key regulator of its function via protonation from external buffer. That a variety of mutant amino acid sidechains in terms of size and pK_a led to significantly perturbed properties suggested that both the steric and electrostatic properties of the His side chain were important in the pH regulation of M2.

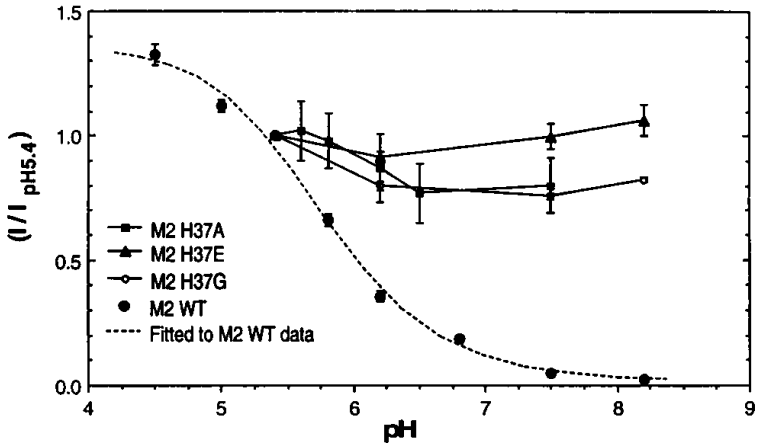

Figure 1.12. A variety of His 37 mutants lead to loss of pH regulation of M2 currents (plotted as current ratios above), suggesting that the properties of His 37 in the protein are highly tuned for pH sensing. Figure from (Wang, Lamb et al. 1995).

The unique, highly tuned nature of the His 37 side chain in the function of M2 was also demonstrated with chemical rescue experiments (Venkataraman, Lamb et al. 2005). A/M2 His37Gly and other His37 mutants expressed in oocytes were functionally "rescued" by addition of imidazole, the histidine sidechain, to the bathing buffer, suggesting that the imidazole noncovalently interacts with the M2 pore in a manner sufficient to restore function. Interestingly, much larger heterocyclic molecules of a similar pK_a or those of a similar size but with substantially different pK_a values were ineffective at restoring function, and some were even inhibitory.

With His 37 established as the pH sensor, focus renewed on nature of the ionic cargo transported by A/M2. Experiments with a pH-sensitive dye entrapped in A/M2 proteoliposomes determined that A/M2 translocated protons in an amantadine-sensitive manner (Schroeder, Ford et al. 1994); this was also seen in oocyte experiments performed under more stringent conditions. These findings were supported by results from A/M2 expressed in MEL cells, where it was determined that the degree of A/M2 proton selectivity over Na^+ was over 1,000,000 fold (Chizhmakov,

Geraghty et al. 1996). This high level of proton selectivity was also demonstrated in subsequent oocyte and proteoliposome experiments (Mould, Drury et al. 2000; Lin and Schroeder 2001).

A/M2 is inwardly rectifying: that is, proton flux from its outer, N-terminal side to the inner, C-terminal side is much faster than the reverse. It was hypothesized that a bulky residue located C-terminal to His 37 mediated this effect by sterically occluding water access to the His 37 side chain from the C-terminal side. The only such residue in the A/M2 transmembrane domain is Trp 41, which is highly conserved in A/M2 and in its influenza B homolog BM2. As shown in part in Figure 1.13, mutating Trp 41 to Phe in the oocyte system abrogated rectifying behavior; a similar result was seen for a Trp41Cys mutation, while Trp41Tyr only slightly weakened the rectification (Tang, Zaitseva et al. 2002). The steric effect of Trp 41 was also demonstrated using copper (II), which inhibits M2 by complexing His residues or water structures in the aqueous pore when added from the N-terminal side of A/M2, but which has no effect when injected from the C-terminal side unless the Trp 41 side chain is mutated away. Amantadine was also found to be ineffective when added from the C-terminal side to WT A/M2 (Tang, Venkataraman et al. 2005). Thus, the Trp 41 indole (with a requirement for large size and rich electron density, as shown by the mutant results) forms the gate of A/M2, blocking reverse proton flow.

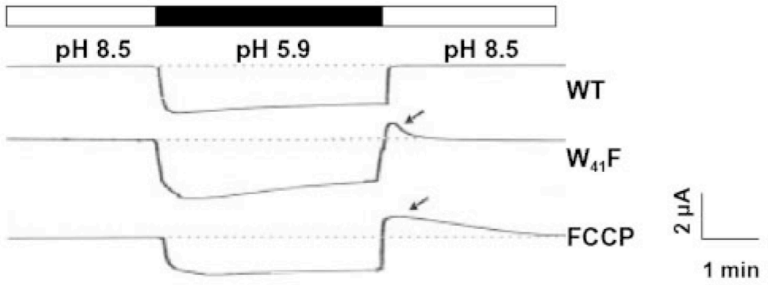

Figure 1.13. Currents through *Xenopus* oocytes expressing WT and Trp 41 mutant M2 plotted vs. time as the oocyte exterior is washed with buffers of different pH (top panel). Inward proton currents are negative on the y axis. The Trp41 residue of M2 prevents outward flow of protons. Mutation of the Trp to Phe allows outward proton flow (arrow), which is also observed when the

non-directional small molecule proton carrier FCCP is added. Figure from (Tang, Zaitseva et al. 2002).

1.6. Low resolution structural and spectroscopic studies of A/M2.

Not only did A/M2 prove to be a fruitful model system for the study of proton transport across membranes, it was also an attractive target for the fields of structural biology, biophysics, and bioinformatics, because of its small size, pharmacological relevance, and highly regulated transport function. Since many biophysical and computational techniques become difficult to apply on larger systems, interest immediately focused on a peptide representing the transmembrane domain of M2, as the location of conserved residues important for function. This peptide was demonstrated to form alpha helices in membranes (Duff, Kelly et al. 1992), and since the minimal functional oligomeric state of full length M2 was shown to be tetrameric (Sakaguchi, Tu et al. 1997), it was surmised that the transmembrane domain of the active protein is a four helix bundle. The transmembrane peptide sequence corresponding to the A/Udorn/72 strain of influenza is shown in Figure 1.14.

H_2N-**SSDPLVVAASIIGILHLILWILDRL**-*COOH*

Figure 1.14. Transmembrane peptide (M2 TM, residues 22-46) sequence of A/Udorn/72. The pH-sensing His 37 residue and the gating Trp 41 residue are highlighted in red.

The first detailed models of the transmembrane domain were published by Pinto et al. (Pinto, Dieckmann et al. 1997) and Sansom et al. (Sansom, Kerr et al. 1997) in 1997. In the former work, a functionally defined model was constructed using cysteine-scanning mutagenesis of the transmembrane domain of full length A/M2 expressed in *Xenopus* oocytes. Functional parameters of each mutant were assayed and scored in a perturbation index, which was then parameterized in a periodic function (to correspond to the amino acid periodicity in an alpha helix) as shown in the left panel of Figure 1.15. The most highly perturbing mutants were expected to

correspond to pore-lining residues, whereas those with minimal impact on function would face outside the helix bundle. The resulting energy-minimized model was a left-handed coiled coil with a 15 degree helical tilt from the membrane normal. A large N-terminal aqueous pore was observed (shown in right panel of Figure 1.15), lined by Val 27, Ala 30, Ser 31, and Gly 34, and blocked at the C-terminal end by the imidazole sidechains of His 37. The spaces between these groups were insufficiently large for water or hydronium ion penetration. At the next level of residues, Trp 41, the pore is once again accessible to water.

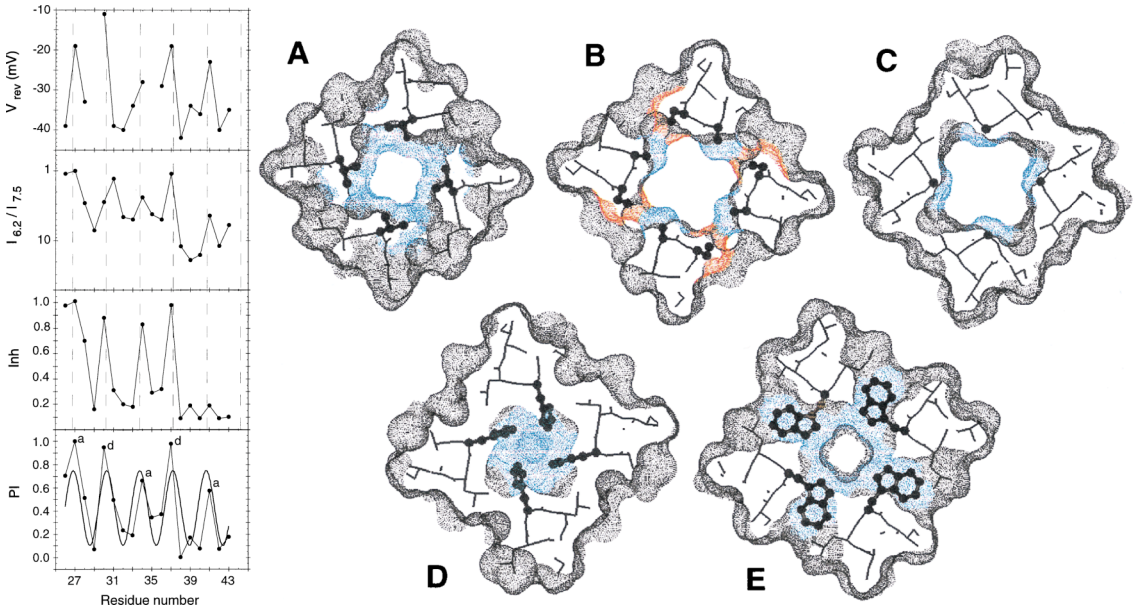

Figure 1.15. Perturbation index-based structural model of A/M2 transmembrane domain. In the left panel, functional parameters of single-residue Cys mutants (from top, reversal potential, pH_{out} activation, and inhibition) are combined into a perturbation index (bottom) that is parameterized as a periodic sine function corresponding to an alpha helix. The resulting structural model, when energy-minimized and viewed as N- to C-terminal slices along the membrane normal, shows a large N-terminal aqueous pore lined by Val 27 (A), Ala 30, Ser 31 (B), Gly 34 (C) and blocked at the C-terminal end by His 37 (D), before opening again at Trp 41. Figure from (Pinto, Dieckmann et al. 1997).

In the Sansom et al. model, simulated annealing *in vacuo* of template helical bundles was followed by water solvation of the pore and molecular dynamics (MD) simulations on the minimized, solvated, structure. (Sansom, Kerr et al. 1997) 1 ns MD runs were performed with all His 37 groups deprotonated (neutral) and with one of the groups protonated. Models derived from the MD simulation had average helix tilts of 21-25 degrees relative to the bilayer normal, and pore facing residues similar to the mutagenesis model. Again, a large N-terminal aqueous pore was seen with water wires (aligned water pathways) throughout. In the fully neutral protonation state, the His 37 sidechains occluded the pore from the C-terminal end, but in the 1+ state, these sidechains moved from the pore lumen to the interface, creating space for an uninterrupted water wire throughout the transmembrane segment.

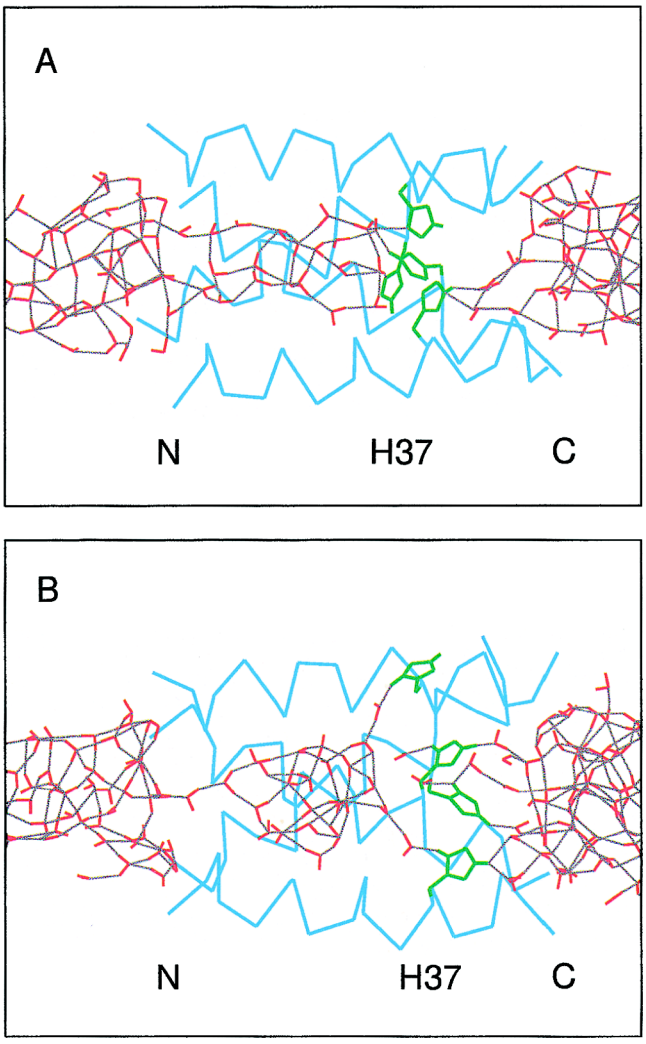

Figure 1.16. Model of A/M2 TM domain generated by molecular dynamics simulations by Sansom et al. Peptide helices are in blue, and water molecules (red) are linked in hydrogen bonded networks (gray). His 37 sidechains are shown in green. (A) Neutral state with all histidine residues deprotonated and occluding the aqueous pore. (B) Upon protonation of a single His 37, the sidechains shift apart to allow continuous water wires to permeate through the His 37 constriction. Figure from (Sansom, Kerr et al. 1997).

The secondary and low-resolution tertiary structure of M2 was also studied using purely biophysical methods, such as solid state NMR spectroscopy and infrared dichroism. Solid-state

NMR is advantageous as it provides a native-like phospholipid membrane environment, where the protein of interest is reconstituted. The sample consists of stacks of membrane bilayer "disks" aligned in a tube, which is oriented at a fixed angle relative to the magnetic field. Unfortunately, because of the isotropic alignment, solid state methods cannot provide high resolution structural information, but they can be used to obtain helix orientations with respect to the membrane normal, as well as to obtain data on dynamics via relaxation and hydrogen exchange, and to determine distance restraints in some cases (Hong 2007; McDermott 2009).

ssNMR experiments by Cross *et al*. on the transmembrane domain of M2 and on the full length protein showed that the construct is helical and takes on a variety of tilt angles with respect to the membrane normal, ranging from 25 to 38 degrees depending on the length of the protein fragment studied (Wang, Kim et al. 2001; Tian, Gao et al. 2003). Only one inter-helical distance restraint, at a maximum of 3.9 Å between the π nitrogen of His 37 and the γ carbon of Trp 41, could be reliably obtained (Nishimura, Kim et al. 2002). The resulting model (based on data obtained at pH 7.0) has a large N-terminal aqueous pore interrupted only by the Trp 41 indoles and is shown in Fig 1.17; however, later work by Hong *et al*. (Luo, Mani et al. 2007) using ^{19}F-labeled Trp 41 residues obtained an interhelical F-F distance restraint of nearly 12 Å at both neutral and low pH, and was most consistent with a different Trp 41 rotamer.

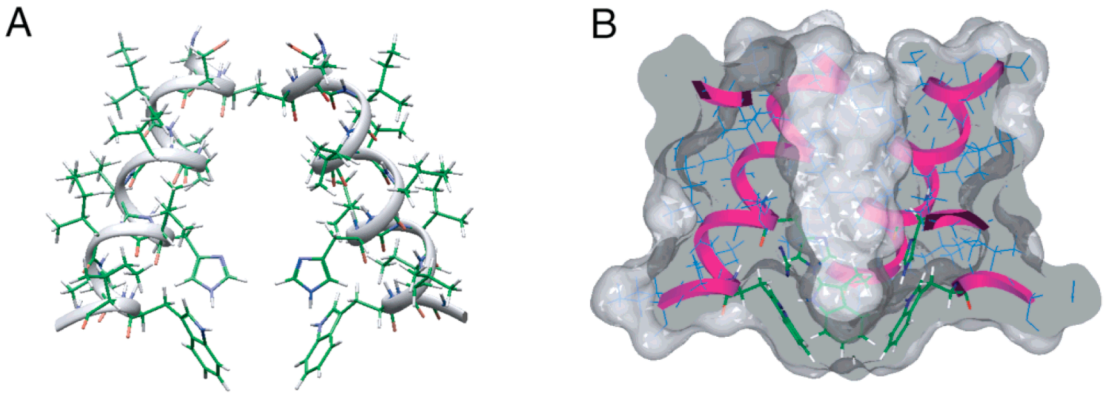

Figure 1.17. Model of the M2 transmembrane domain generated from ssNMR measurements and a single interhelical His37-Trp41 distance restraint. (A) Model with sidechains shown. (B) Space-filling model depicting aqueous pore, which is open near His 37 but constricted by Trp 41 indoles. Figure from (Nishimura, Kim et al. 2002).

Structural determination of the transmembrane domain of M2 was also attempted using IR dichroism, where samples of the transmembrane peptide were reconstituted into an aligned solid-state bilayer (Torres, Kukol et al. 2000; Torres and Arkin 2002). The differential absorption of parallel and perpendicular-polarized infrared light by the helical amide band as well as by isotopically labeled amino acids was used to calculate helix orientations, with resulting tilt angles relative to the membrane normal of 30 to 35 degrees.

While the majority of structural work in the late 1990s and early 2000s was devoted to building a secondary structure model of the M2 bundle, other investigators zeroed in on the functionally critical dyad of M2 residues, His 37 and Trp 41, which were found to be in close geometric proximity in earlier ssNMR experiments (Nishimura, Kim et al. 2002). Since indole and deuterated imidazole are weakly active in UV resonance Raman (UVRR) experiments, the pH-dependent UVRR spectra of the transmembrane peptide of M2 in bilayers were measured, which showed concomitant, pH-driven changes in the spectra of both sidechains (Okada, Miura et al. 2001). The spectra were most consistent with a cation-π interaction between a deuterated (positively charged) imidazole and the indole; and it was proposed that upon deuteration, the His 37 imidazole undergoes a rotamer shift and interacts closely (<5 Å) with a Trp 41 indole on an adjacent helix. A pH-dependent cation- π interaction of the two sidechains was also observed using fluorescence spectroscopy in micelles (Czabotar, Martin et al. 2004), where the intrinsic fluorescence of Trp 41 was increasingly quenched with decreasing pH, presumably by protonated His 37.

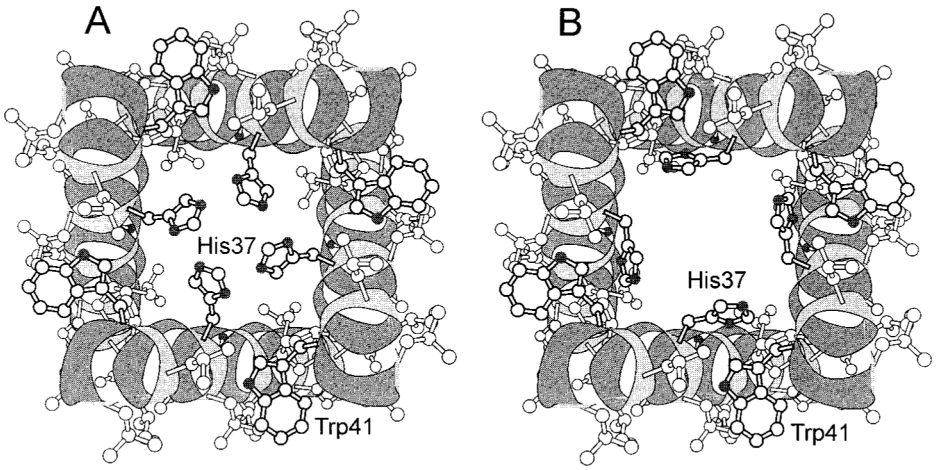

Figure 1.18. Model of the high-pH closed (A) and low-pH open (B) states of M2 TM based on UV resonance Raman data, viewed C-terminal to N-terminal along the membrane normal. As pH is lowered, His 37 changes rotamer states and interacts closely with Trp 41, resulting in opening of the pore lumen. Figure from (Okada, Miura et al. 2001).

In summary, over the span of approximately 10 years, multiple low-resolution models of the transmembrane domain of M2, and of the more detailed structure of the His 37 and Trp 41 sidechains, have been generated using a variety of computational and biophysical techniques. While it is comforting to observe that all the models agreed on the basics (a parallel, left-handed four helix bundle tilted ~15-40 degrees from the membrane normal), there remained substantial disagreement on the fine details of the structure. For one, the findings disagreed on whether water can fully penetrate the pore under certain conditions or is stopped by His 37, Trp 41, or a combination of the two. There was also controversy on how the His 37 and Trp 41 side chains are arranged relative to each other, although some form of close, pH-dependent interaction was seen in multiple systems. Therefore, while the outlines of the M2 transmembrane domain structure were coming into view, the resolution was too low to definitively correlate structural phenomena to the regulation of pH-dependent currents observed in functional experiments.

Nevertheless, multiple mechanistic hypotheses were generated, as will be discussed in the next section.

1.7. Early mechanistic theories and experiments.

Even in the absence of high-resolution structural data, sophisticated mechanistic theories for M2 function were proposed based on the first models of the transmembrane domain helical bundle, which were published in 1997. Two mechanistic hypotheses would dominate the literature for the next decade, with subsequent experimental results being interpreted to support one or the other.

As discussed in the previous section, Pinto *et al.* built a model of the M2 transmembrane domain based on parameterization of functional perturbations stemming from single-residue mutations in the TM sequence (Pinto, Dieckmann et al. 1997). The large N-terminal aqueous pore in the resulting bundle structure was occluded by His 37 imidazole rings aligned parallel to the membrane normal. Based on the (low) pH-cooperativity of M2 activation observed in early functional studies (Wang, Lamb et al. 1995), it was postulated that only a single His sidechain must be protonated to activate transport. Because the His sidechains were blocking the pore in the computed model, it was hypothesized that all protons transported must be shuttled across the constriction by an imidazole sidechain, and that a continuous water wire (bypassing the imidazoles) did not form throughout the pore upon channel activation. Thus, transported protons would be bound from water or hydronium by a neutral imidazole from the N-terminal side, and released to water on the C-terminal side. A ring flip or tautomerization would complete the cycle. An important corollary of this "proton shuttle" hypothesis is that, assuming relatively unimpeded diffusion through the rest of the channel, the rate of transport would be determined by the kinetics of proton interactions with the imidazole. With these assumptions, imidazole protonation on-rates would be diffusion-limited (near 10^9/(M sec)). The on-rates and off-rates can be related through the proton affinity constant, the $pK_a = -\log(K_a) = -\log([A^-]/[HA]) = -\log(k_{H+,off}/k_{H+on})$. This relationship implies that the maximum off-rate, and thus the transport speed limit, would be near 1000

protons/second assuming a typical His pK_a of ~6; this maximum speed is roughly consistent with estimates from functional studies.

A second widely accepted model was proposed from the first set of M2 TM molecular dynamics simulations by Sansom *et al*. (Sansom, Kerr et al. 1997). In this work, the His 37 imidazole rings were observed to sterically occlude the aqueous pore in the 0+, fully deprotonated state of the channel, but moved away from each other when one of them was protonated, creating a continuous water wire through the length of transmembrane section of M2. Thus, it was argued, the His 37 imidazoles regulate proton transport in an electrostatic fashion. As they become successively protonated with decreasing pH_{out}, the positive charges repel each other to permit proton transport along water wires. A corollary of this "electrostatic gate" mechanism is that with sufficient His 37 protonation and repulsion, the rate of proton transport becomes limited by diffusion along the water wires, and is thus substantially faster than in the shuttle model.

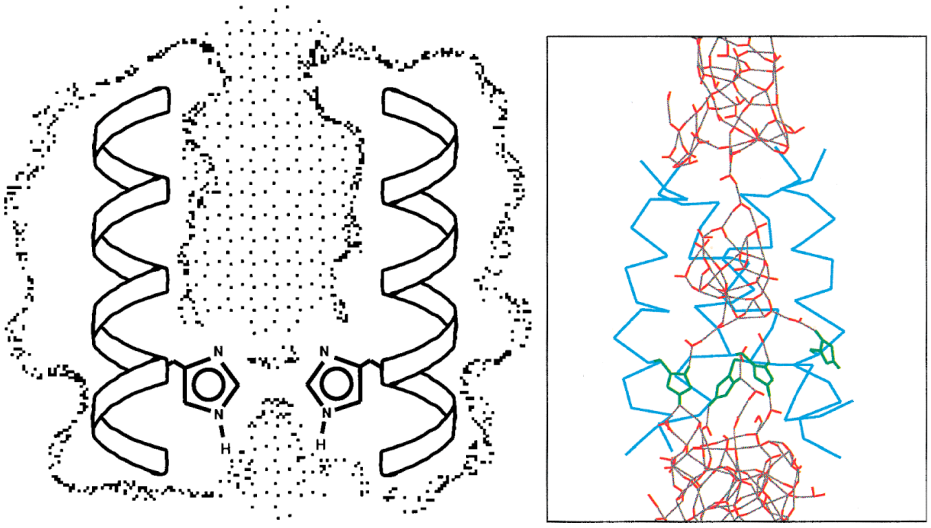

Figure 1.19. Schematics of proposed mechanisms of proton transport through M2. In the model proposed by Pinto *et al*. (Pinto, Dieckmann et al. 1997) (left), the His 37 imidazole rings occlude the pore and serve as shuttles for transiting protons which bind then dissociate from the imidazoles. The overall transport rate is predicted to be limited by the imidazole proton off-rate.

In the mechanism proposed by Sansom *et al.* (Sansom, Kerr et al. 1997) (right), protonation of His 37 sidechains leads to their steric separation and the formation of water wires through the entire aqueous pore. Figures obtained from respective references.

Subsequent functional and spectroscopic studies of M2 were carried out to determine which mechanism, if either, was more robust. The proton shuttle model of Pinto *et al.* was supported by numerous lines of evidence, including studies in oocytes using deuterated bathing buffer, where the noticeably slowed kinetics of transport suggested that His 37 directly interacts with transported protons in the M2 pore, and estimated maximum M2 currents at a relatively slow 1-10 fA (Mould, Li et al. 2000).

The matter became somewhat more complicated with the publication of data on pH-dependent activation of full length A/M2 in MEL cells from Chizhmakov et al., where the relationship of flux to pH_{out} and voltage was most consistent with a two-site model (Chizhmakov, Geraghty et al. 1996), unlike the single-site model earlier surmised in both mechanistic hypotheses. The first protonation step (with a pK_a of ~ 7) was suggested to activate the channel, and the second (with a pK_a of ~6) to lead to proton permeation, or conduction, without explicitly favoring the gate or the shuttle mechanism. Mathematical models of the His shuttle transport with a two-proton site (Salom, Hill et al. 2000) or a three-proton site mechanism (Lear 2003) with only protonation and deprotonation steps considered, fit well to the Chizhmakov data, supporting the shuttle hypothesis.

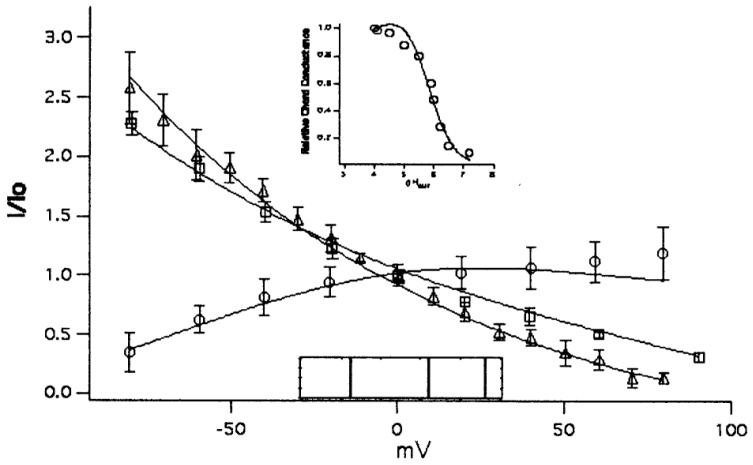

Figure 1.20. Quantitative mechanistic analysis (solid lines) of A/M2 functional data (raw data from ref. (Chizhmakov, Geraghty et al. 1996)) using a two site protonation-deprotonation model. Main panel: current-voltage ratios (current normalized to current at 0 mV) at a variety of pH_{in} and pH_{out} values (triangles, pH_{in} 5, pH_{out} 7; circles, pH_{in} 8, pH_{out} 6; squares, pH_{in} 6, pH_{out} 8). Upper inset: ratio of pH-dependent chord conductance g/g_{max} ($g=I/(V-E_{rev})$, where I is the observed current, V is the applied voltage, and E_{rev} is the proton reversal potential at a given pH calculated by the Nernst equation) where g_{max} is g at pH 4. Solid lines indicate fits of two-site model, where protonation at the first site activates the channel, and the transported proton binds the second site. The best fit lines are consistent with dissociation constants of pK_1=6.5 and pK_2=5.67. Figure from (Lear 2003).

Other evidence was interpreted to favor the electrostatic gate mechanism, including a series of molecular dynamics simulations with the M2 bundle solvated in an explicitly modeled lipid bilayer. In one study, protein “breathing” motions that at times permitted continuous water wires to span the entire transmembrane segment were seen, indicating that His 37 imidazoles may not always occlude the transport pathway (Forrest, Kukol et al. 2000). A subsequent modeling study (Smondyrev and Voth 2002) using an advanced, multi-state empirical valence bond potential to more accurately model electrostatic interactions, did find a partially His-blocked pore but showed that protons can hop between water molecules on either side of the His 37 occlusion without

being bound by the imidazole rings, thus disfavoring the shuttle mechanism. Also, the previously discussed UV resonance Raman results from M2 TM in liposomes suggested that all four histidines of the bundle are protonated in a noncooperative process, with a rather low pK_a of ~5.7 (Okada, Miura et al. 2001). The observation of fully protonated M2 was consistent with the electrostatic gate mechanism, since the shuttle mechanism presumably required less than complete protonation at pH_{out} values that facilitated conduction.

In summary, similarly to the pursuit of a structural understanding of M2 transport, uncertainty with respect to translocation mechanism remained the status quo for over a decade, with a handful of studies consistent with each of the two leading hypotheses. As will be outlined in the next section, the determination of the first high-resolution M2 structures suggested yet another paradigm for M2 proton transport.

1.8. Entering the high-resolution era: the first detailed structures of M2 TM.

Protein structure determination using X-ray diffraction from crystals has become a mainstay technique since Kendrew and Perutz's pioneering results on myoglobin and hemoglobin in the late 1950s, and the development of advanced nuclear magnetic resonance techniques (Fourier transform spectroscopy and 2-D NMR in the late 1970s and early 1980s, and multidimensional NMR in the late 1980s and early 1990s) led to the widespread use of solution NMR spectroscopy in structural biology. Membrane proteins constitute roughly one-third of the human genome, but the crystal structure of the first integral membrane protein, a holy grail for the field, was only obtained in the mid-1980s, and the second membrane protein crystal structure was determined only six years later. Even with the successful adaptation of solution NMR methods to detergent-solubilized membrane peptides (MacKenzie, Prestegard et al. 1997) and proteins (Arora, Abildgaard et al. 2001), membrane protein structure determination remains a daunting task. As of July 2009, the Protein Data Bank protein structure compendium contained over 50,000 entries, whereas subset databases of membrane and membrane-associated protein structures contain up

to 1,000 unique entries representing a much smaller number of nonredunant proteins. Therefore, to this day, membrane protein structural biology remains a difficult endeavor, with multiple experimental bottlenecks that include production of large amounts of stable protein samples, generation of high-quality crystals by optimizing detergent micelle or cubic phase bilayer conditions, or determining optimal fragments and experimental conditions for NMR spectroscopy.

Thus, it is of no surprise that the first high-resolution structures of influenza A/M2 were the result of years of painstaking trial and error. Two X-ray crystal structures (Stouffer, Acharya et al. 2008) and one solution NMR structure (Schnell and Chou 2008) were published simultaneously; the X-ray structures were of variants of the M2 transmembrane peptide (residues 22-46), while the NMR structure was of a longer fragment encompassing residues 18-60 (a domain diagram is provided in Figure 1.6).

The highest-resolution crystal structure, an Ile33SeMet variant, was crystallized at pH 7.3 from β-octylglucoside (OG) micelles. The crystal packing was in a bilayer-like environment, indicating a biologically relevant form. The resulting structure, at 2.05 Å resolution, was an asymmetric, teepee-shaped four-helix bundle (Figure 1.21) with the helices close together at the N-termini but further apart at the C-termini. Each helix had a similar tilt with respect to the membrane normal in its N-terminal half, but the orientation of the C-terminal half varied because of the presence or absence of kinking at the level of Gly 34. The helices whose C-terminal ends were furthest removed from the bundle central axis were almost completely straight, whereas those ending closer to the central axis were kinked up to 15 degrees. The overall structure was interpreted as a snapshot of several conformations that the protein could sample. The straight-helix extreme was labeled the “A” form, the most highly kinked helix became the “D” form, and the intermediate forms were named “B” and “C”. All four forms had His 37 side chains oriented nearly parallel to the membrane normal, and Trp 41 side chains faced either into the interhelical space (models A-C) or into the pore (model D). Confirming UVRR (Okada, Miura et al. 2001) and fluorescence

(Czabotar, Martin et al. 2004) observations, the His 37 imidazole from helix C interacted edge-on with the Trp 41 sidechain from helix D in the asymmetric bundle structure; additionally, an Asp 44 – Arg 45 interhelical salt bridge was observed between the C and D helices.

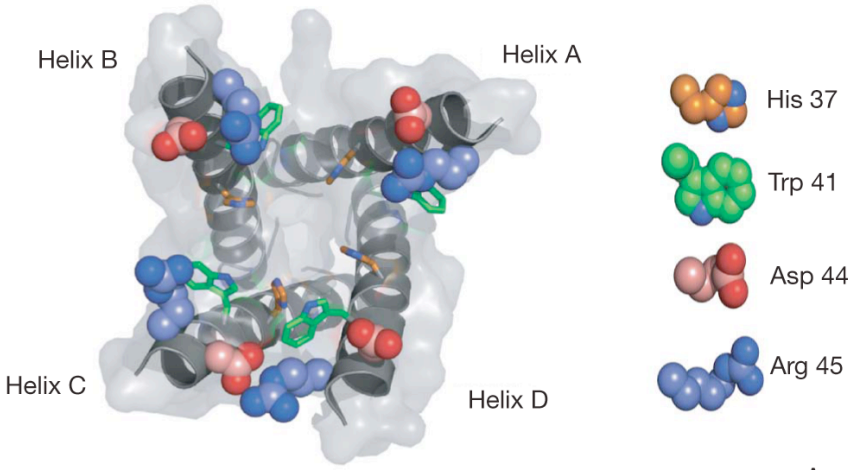

Figure 1.21. 2.05 Å resolution structure of M2TM, viewed along membrane normal from C-terminal side of the bundle. The conformation of each helix in the bundle is asymmetric: each helical form (A-D) was interpreted to represent an intermediate conformation sampled by the M2 tetramer. Key side chains are highlighted. Figure from (Stouffer, Acharya et al. 2008).

Models of the entire transmembrane domain in each conformation were constructed by applying four-fold symmetry to each of the asymmetrically packed helices in turn. In all cases, the resulting aqueous pore is tightly constricted near its N-terminus at the level of the Val 27 side chain, and widens substantially at subsequent pore-lining residues Ala 30, Ser 31, and Gly 34. In a tetramer made from the kinked, “D” form, the aqueous pore is also occluded by His 37 side chains, and is partially occluded by the Trp 41 indoles. The C-terminal ends of the helices are held together by Asp 44 – Arg 45 interhelical salt bridges. By contrast, in a tetramer constructed from the straight helix “A” form, the salt bridges are broken, and the His 37 side chains are sterically separated to allow a continuous pore from the C-terminal end of the bundle into the middle of the channel.

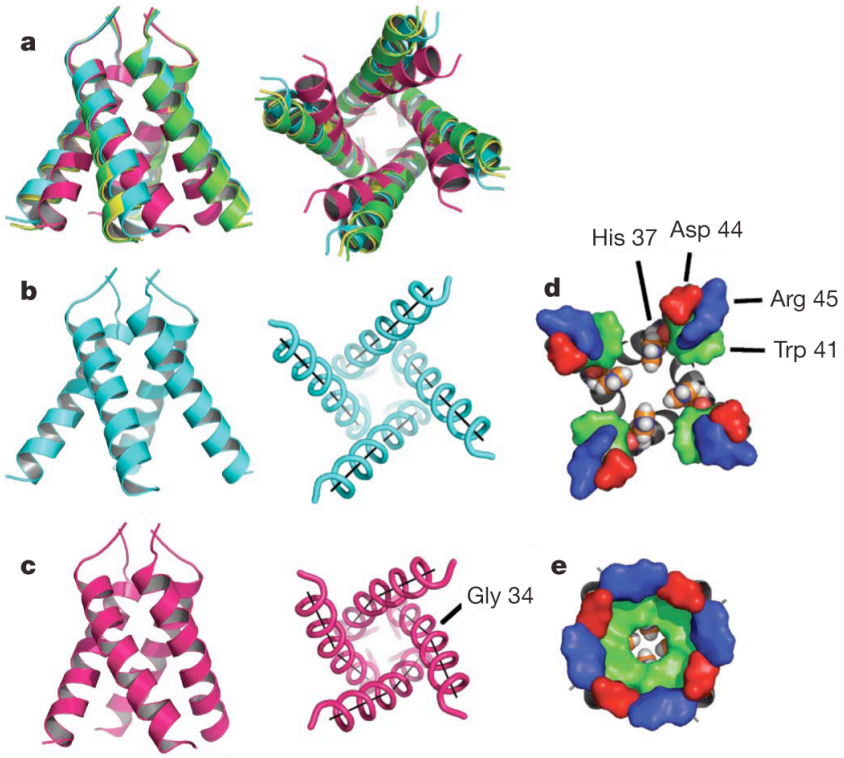

Figure 1.22. Models of M2TM built by imposing four-fold rotational symmetry on helical monomers from crystal structure. (a) Superimposition of the four resulting helical bundles showing range of conformations sampled by M2TM tetramer. (b),(d) Tetramer built from the "A" helix. (c),(e) Tetramer built from the "D" helix. Figure from (Stouffer, Acharya et al. 2008).

A second structure, shown in Figure 1.23, obtained from crystals of the Gly34Ala variant of M2 TM grown at pH 5.3 in the presence of the drug amantadine, was determined at a somewhat lower resolution of 3.5 Å. The overall helical bundle shape is symmetric and very similar in orientation to the straight-helix "A" form, with a large opening at the C-terminal end of the tetramer that narrows down to the Val 27 constriction. An electron density consistent with the size and shape of amantadine was observed in the center of the aqueous pore, with the drug's hydrophobic cage abutting against the Val 27 and Ser 31 side chains (the latter H-bonded to the protein backbone), and the amine group pointing into the open pore towards the C-terminus. The drug is located at the hotspot for most known amantadine resistance mutations (occurring at

Ser31 and Gly34), and its location is consistent with known 1:1 inhibitor:tetramer stoichiometry measured in other experiments (Wang, Takeuchi et al. 1993).

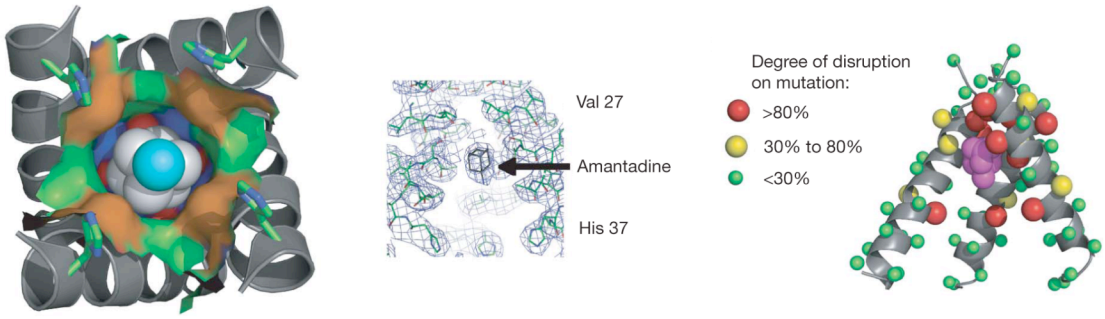

Figure 1.23. Low pH (5.3) structure of M2 TM bound to amantadine. Left panel: structure viewed along membrane normal from C-terminal side showing amantadine blocking the aqueous pore near residues Gly 34 (orange), Ser 31 (blue), Ala 30 (green), and Val 27 (red). The His 37 sidechain is shown in stick form. Middle panel: Electron density omit map ($2F_o$-F_c contoured at 1σ) showing density corresponding to amantadine molecule. Right panel: Results of Cys-scanning mutagenesis (from (Pinto, Dieckmann et al. 1997; Tang, Zaitseva et al. 2002)) showing position-specific effect of mutants on ability of amantadine to inhibit M2. Most disruptive, resistance-inducing mutants are at positions shown in red. Figure adapted from (Stouffer, Acharya et al. 2008).

The solution NMR structure (Schnell and Chou 2008) (shown in Figure 1.24) features a longer fragment of M2, encompassing the transmembrane domain and a C-terminal amphiphilic helix. (Schnell and Chou 2008) The structure was determined at high pH (7.5-8.0) in dihexanoylphosphatidylcholine micelles, in the presence of a large excess of the inhibitor rimantadine, which was required to stabilize the protein for structure determination. The transmembrane domain forms a tightly packed, symmetric four-helix bundle, shaped more like a cylinder rather than the cone seen in the crystal structures. An aqueous pore is present, lined by the same residues as in the crystal structure. There is a constriction at the N-terminal end formed

by the sidechains of Val 27, and two even narrower constrictions at the C-terminal end from the His 37 and Trp 41 sidechains. The His 37 sidechains are again oriented parallel to the membrane normal. However, the Trp 41 indoles assume a different rotamer state compared to the crystal structures, with the π-surface of the rings nearly aligned with the membrane normal and facing into the pore. An electrostatic, interhelical Arg 44 – Asp 45 interaction is again present. While no NOEs were observed for residues 47-50, the C-terminal amphiphilic helices formed a loosely packed tetrameric coiled coil, with the interhelical interactions mediated by hydrophobic sidechains on each helix.

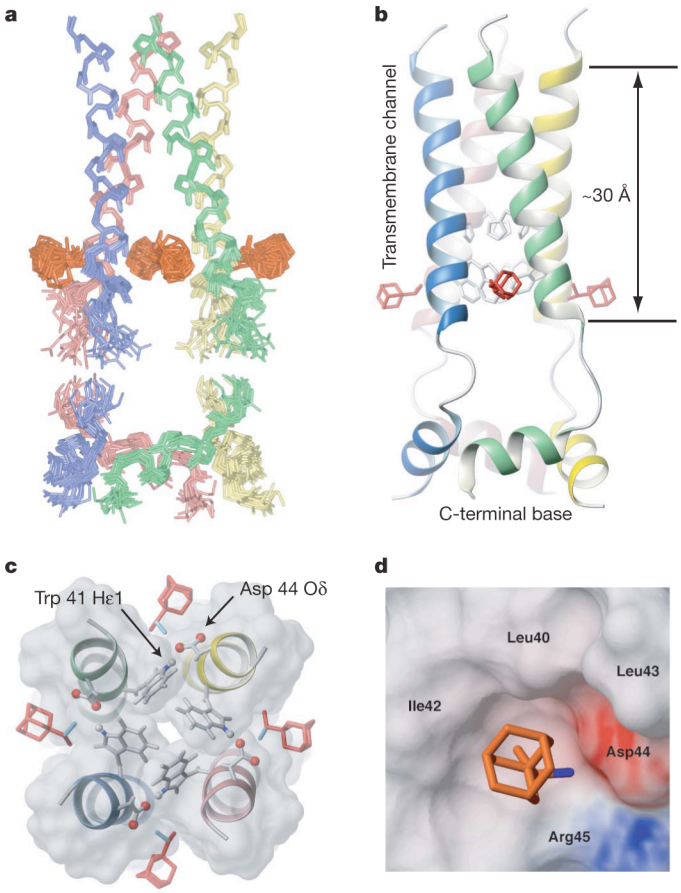

Figure 1.24. Solution NMR structure of M2 core (residues 18-60). Rimantadine (shown in orange-red) was observed to interact with the pore exterior. (a) Ensemble of low-energy models

derived from NMR restraints, viewed from side. (b) Ribbon view of typical structure from ensemble in (a). (c) View of transmembrane domain bundle along membrane normal from C-terminal end showing phenyl ring of Trp 41 sidechain facing into the pore and the external rimantadine binding site. (d) Space-filling view of external rimantadine binding site. The amine of the rimantadine was proposed to form an electrostatic interaction with the Asp 44 sidechain. Figure from (Schnell and Chou 2008).

Surprisingly, in this structure an external rimantadine binding site was found, and no definitive drug signal was obtained from the predicted internal amantadine site observed in the crystal structures. Instead, the C-terminal exterior of each transmembrane helix (near residues 43-46) is noncovalently interacting with a loosely ordered rimantadine molecule, at a site not typically associated with resistance mutations. While some membrane proteins are inhibited in such an allosteric fashion, the more likely explanation for this result is the enormous excess of rimantadine used with respect to the protein (40x) and to the detergent (~13 mol %), which leads to the population of weak, nonspecific binding sites. However, the absence of the drug from its expected, internal, location must also be explained, and is likely due to a combination of limitations of the NMR technique, including rotational averaging of drug-pore NOE signals (one drug to four symmetric helices), which reduces their amplitude four-fold. Furthermore, the magnitude and direction (positive or negative) of NOEs depends on the timescale of the target molecule motion, and transitions through a zero point at intermediate timescale regimes. Thus, it is possible that the internally bound rimantadine moves at a timescale at which drug-protein NOEs are undetectable; a possibility supported by the lack of water-protein NOEs in the area of the pore from the NMR structure that corresponds to the internal drug binding site. Very strong evidence for the inside-pore binding site was also provided by subsequent experiments from the Lamb and Pinto labs, where the homologous, naturally amantadine-insensitive influenza B BM2 protein was rendered partially amantadine-sensitive in *Xenopus* oocytes by replacing its N-

terminal TM sequence with that of A/M2, while leaving the proposed C-terminal, external binding site intact (Jing, Ma et al. 2008).

What new inferences can be made about transport mechanism from the high-resolution structures? To begin with, it is difficult to conclude whether the structures support either one of the two mechanistic hypotheses discussed above. While the neutral-high pH forms (NMR and the crystal "D" form) have the pore occluded by His residues and would therefore be consistent with the shuttle mechanism proposed by Pinto et al. (Pinto, Dieckmann et al. 1997), the low pH amantadine-bound structure, and the very similar, apo, "A" model from the neutral pH crystal, show a C-terminal open pore more consistent with the electrostatic gate (Sansom, Kerr et al. 1997) mechanism. A key question is the extent to which these forms are populated at the pH values at which conduction through M2 is observed. The answer is somewhat elusive, since the crystals took many months to grow (allowing for slow chemical changes in the crystallization buffer) and in some cases were grown in the presence of transition metals, which may influence pH in unpredictable ways. Thus, it is possible that these low pH conformations may be sampled by the protein rarely, if at all, under physiological conduction conditions.

However, a comparison of the pH-dependent helix configurations and pore water accessibilities of the different structures gives rise to another attractive hypothesis: that the M2 transmembrane domain functions not as a channel but as a classical transporter, as an extension of the shuttle model. As shown in Figure 1.25, the Val 27 constriction is somewhat more open at high pH, allowing access of water to the His 37 residues, at which point the pore is occluded and the helix bundle stabilized at the C-terminal end by Asp 44 - Arg 45 interhelical salt bridges. As the N-terminal pH is decreased, the His side chain is protonated, favoring a conformational transition to a form where the Val 27 sphincter is tightly closed, cutting off access to the N-terminal waters, but the His 37 sidechain is now highly exposed to water molecules from the C-terminal side of the membrane as the C-terminal helix ends (and the salt bridges holding them together) come apart.

The His 37 imidazole can now be deprotonated from the C-terminal side, which favors a return to the N-open form. This hypothesis was supported by the results of molecular dynamics simulations where the transmembrane domain crystal structures were placed into a lipid bilayer, and various protonation states of His 37 explored (Khurana, Dal Peraro et al. 2009). In the neutral, fully deprotonated state, M2 assumed an N_{open}-C_{closed} conformation, with His 37 residues occluding the pore at the C-terminal end, but the Val 27 sidechains loosely packed at the N-terminal end. As the protein protonation state increased to 2+ or greater, the Val 27 sidechains closed the N-terminal pore more tightly, while the His 37 and Trp 41 sidechains moved apart to open the pore on the C-terminal side. Additional support for this mechanism comes from disulfide cross-linking studies on transmembrane domain Cys mutants of full length M2 (Bauer, Pinto et al. 1999), where decreased cross-linking of residues at the C-terminal end of the TM domain was seen when pH was lowered.

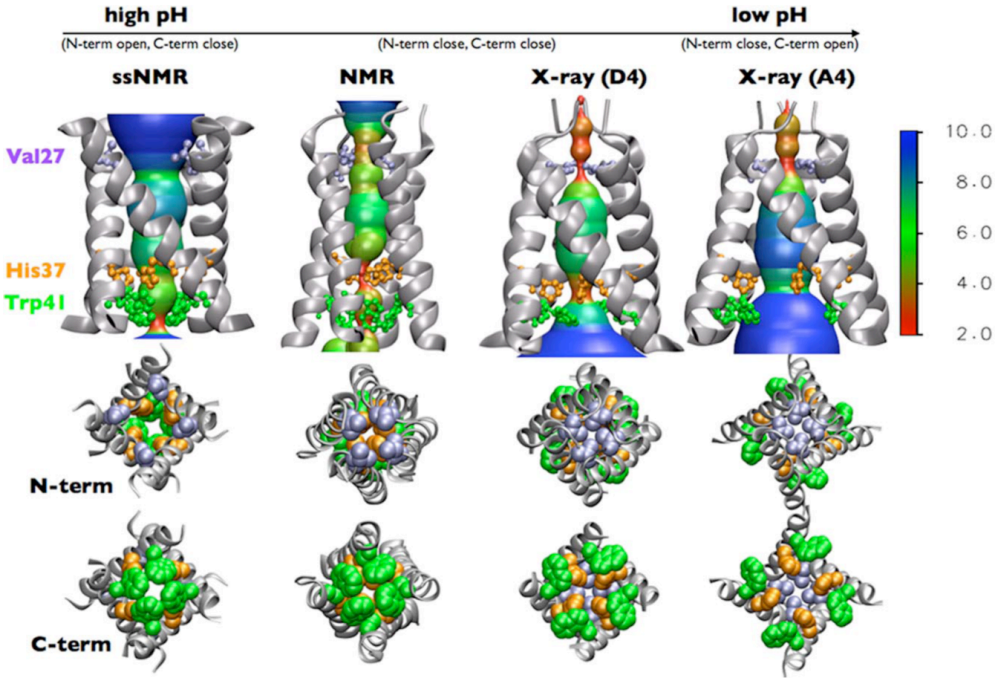

Figure 1.25. Analysis of helix tilt and pore water accessibility from structures and models of M2TM at various pH values. Top panel: as external pH is lowered, the pore radius at the level of

Val 27 decreases, while increasing at the level of His 37 and Trp 41. Bottom panels: view along membrane normal from N-terminal and C-terminal sides showing configuration of Val 27, His 37, and Trp 41 sidechains. Figure from (Khurana, Dal Peraro et al. 2009).

However, this hypothesis has a number of potential pitfalls: for one, the NMR structure was solved with an additional C-terminal amphiphilic helix, while the X-ray structures were of the transmembrane domain alone. It is possible that the presence of this second helix affects the conformational space that the transmembrane domain can sample, and this helix's role in transport, if any, is poorly defined. Secondly, the molecular dynamics simulations that supported this mechanism were of a duration (30 ns) that precluded direct observation of deprotonation and any slow conformational transitions. Finally, as will be explored in the following section, the force fields used in these simulations may not accurately model the process by which protons are bound and stabilized by the histidine residues of M2.

1.9. Solid state NMR pH titration of M2 TM in bilayers.

A landmark discovery was made in 2006 by the Cross *et al.*, who synthesized the M2 TM peptide with isotopic ^{15}N labeling at either nitrogen of the His 37 sidechain, reconstituted it in bilayers, and performed a pH titration of the system to monitor pK_a values and tautomer states of the His 37 imidazoles (Hu, Fu et al. 2006). A low pK_a value implies an unstably bound proton, and it was expected that a multi-protonated M2 would be highly unstable, since a large amount of positive charge would need to be confined to within a small, subnanometer space, and in addition be possibly exposed to the lower dielectic environment of a phospholipid membrane interior. In fact, Poisson-Boltzmann calculations on a structure obtained from a state of the art classical MD simulation (Chen, Wu et al. 2007) predicted that the pK_a values of the four His 37 residues would be 6.6 for the 1^{st} proton bound by the tetramer, and 6.0, 5.5 and 2.1 for the last three protons respectively. Surprisingly, the ssNMR titration showed that the first two protons are bound stably

with the unexpectedly high pK_a values of 8.2 for each, while the third and fourth protons are bound with pK_as of 6.3 and a value less than 5.0 that was not precisely ascertained.

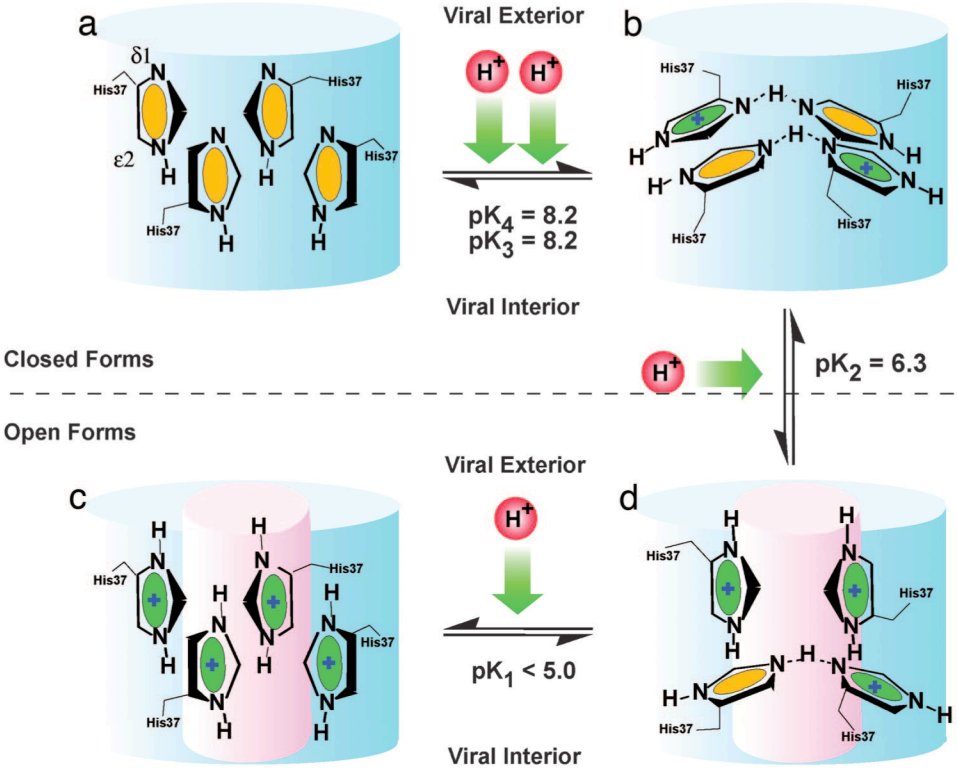

Figure 1.26. Results and interpretation of ssNMR pH titration of M2TM peptide. The protonation states of the His 37 imidazoles and the predicted imidazole-imidazolium dimers in the 2+ and 3+ states are shown. The first two protons are bound with a very high pK_a, whereas the 3rd proton is bound in the pH range where conduction is observed. Figure from (Hu, Fu et al. 2006).

Thus, in a stunning turn of events, the measured cumulative stability of the first three protons bound diverged from top of the line computational estimates by over four orders of magnitude! Cross *et al*. hypothesized that the first two protonation events lead to a symmetric pair of imidazole-imidazolium dimers that stabilize the two protons via low barrier hydrogen bonds, but the nature of the doubly protonated intermediate could not be precisely ascertained. In all

regards, this highly unusual degree of proton stabilization requires a structural and physico-chemical explanation, and adds another layer of complexity to any mechanistic theory.

1.10. Summary of the state of the field.

In summary, the past decade has seen enormous advances made in the functional characterization of proton transport through M2, as well as in the structure determination of its transmembrane domain. However, progress has been slower on the establishment of a comprehensive, structure-based transport mechanism to correlate the two knowledge domains. The recent results indicating unexpectedly high degrees of proton stabilization inside the M2 pore that cannot be explained by classical modeling, only served to deepen the mystery. However, before a detailed mechanism that accounts for the unusual degree of proton stability can be put forth, a more simple question must be addressed. The vast majority of functional assays have been performed on the full-length protein, whereas the almost all of the structural biology, spectroscopy and computational modeling has been done on the transmembrane domain. Therefore, before a structure-based mechanism can be proposed and tested, it becomes imperative to determine whether the transmembrane domain can be a valid model for the function, assembly, and inhibition of the full length protein. What, if any, are the contributions of the non-transmembrane segments of M2 (which make up over 70% of its sequence) to proton transport?

Chapter 2: Validation of the M2 transmembrane domain as a model for proton transport by full length A/M2.

Much of the material in this chapter has been published in the Proceedings of the National Academy of Sciences, 2009 Jul 28;106(30), 12283-12288. http://www.pnas.org/cgi/doi/10.1073/pnas.0905726106

2.1. Literature review of structural and functional characterization of A/M2 fragments.

The divergence of protein and environment model systems in the study of A/M2 structure, biophysics, and electrophysiology evolved naturally. In the classical, cell-based cargo trafficking and electrophysiological experiments that were initially used to determine M2 proton channel activity, the genetic approaches used were readily compatible with and indeed favored expression of the full-length protein, since little was known about the transport role of its non-transmembrane segments. In these assays, studying a larger, full-length construct was of no disadvantage as long as its expression was robust (conversely, very short transmembrane segments can often be difficult to express in these experimental systems). With most biophysical approaches, however, small model systems are clearly preferred: every added atom increases the processing time expense in computer simulations or leads to an additional signal in an already crowded protein NMR spectrum. Success in crystallographic studies depends enormously on choosing a well-ordered fragment that can assemble into a crystal lattice. In NMR experiments protein length and its dynamic properties affect the tumbling and magnetic relaxation times that determine whether an NMR experiment is interpretable. Peptides corresponding to desired fragments are often synthesized chemically, with a marked dropoff in synthesis yields when common methods are used for constructs longer than approximately 30 residues. Thus, it is of no surprise that studies of M2 using biophysics and electrophysiology employed almost exclusively the TM domain peptide or the full-length protein respectively.

Furthermore, there is often a natural divergence in the membrane “solvent” involved in structural and functional studies. While studies of transport function necessitate incorporation of the protein in a cell or artificial membrane, spectroscopic techniques used in biophysics often require an

optically transparent sample, and are more difficult to use with lipid bilayer vesicles that scatter light. Very few high-resolution membrane protein structures have been obtained from phospholipid bilayer or bicelle environments (Johansson, Wohri et al. 2009), the vast majority relying instead on solubilization in lipid-mimetic detergent micelles. Therefore, while all functional experiments were performed in bilayers, many biophysical and structural experiments on M2 were performed in detergent micelles, and those that were done in phospholipid membranes employed arbitrarily chosen, and sometimes non-native bilayer components.

This natural divergence in techniques, constructs, and reconstitution systems has impeded the path to a unified view of M2 structure and function. Clearly, some pharmacological questions – such as the location of the pharmacologically relevant drug-binding site – have been so critical that it has been essential to obtain biologically compelling answers by not only expressing the native protein in mammalian cells, but also by demonstrating the robustness of the results through the construction of live infectious viruses (Jing, Ma et al. 2008). However, it is not feasible to address all questions with this level of rigor, and structural studies often need to be conducted on fragments in membranes other than the viral envelope. It is thus important to determine the extent to which reconstituted fragments faithfully reproduce the assembly, proton transport and inhibition of the native protein, independent of other complicating variables such as expression, membrane-trafficking, engagement of the matrix protein, and virus incorporation.

The earliest functional studies of the M2 transmembrane domain were published in 1992, when Duff and Ashley (Duff and Ashley 1992) reconstituted the M2TM peptide in planar lipid bilayers and observed proton-selective single channel currents that were inhibited by amantadine. However, these experiments were carried out at extremely acidic pH values (~2.3 or even lower), and thus cannot be easily correlated to the M2 transport function observed under physiological conditions. Given the observations of Cross *et al.* (Hu, Fu et al. 2006), it is likely that all four His 37 residues of M2 were protonated under the conditions used by Duff and Ashley. Such highly

acidic conditions may favor a set of conformations not populated during physiological transport, or perhaps even lead to dissociation of the tetramer (potentially reversed by addition of amantadine) because of a high degree of accumulated positive charge (Salom, Hill et al. 2000).

The work of Duff and Ashley (shown in Figure 2.1) was repeated by Busath *et al*. (Hu, Fu et al. 2006), also at a very low pH of 2.3, along with a parallel experiment on the same peptide reconstituted in liposomes at more physiological pH values. While in both cases proton currents were observed, the estimated per-protein conductance varied enormously between the two systems: currents in the planar bilayer experiment (of a very similar magnitude to those seen by Duff and Ashley) were seven orders of magnitude larger than those for the same peptide in the liposome system (and approximately six orders of magnitude larger than those obtained for full length A/M2 in liposomes by a different group (Lin and Schroeder 2001)). Thus, the outcome was difficult to interpret and prompted further questions in the literature (Miller 2008).

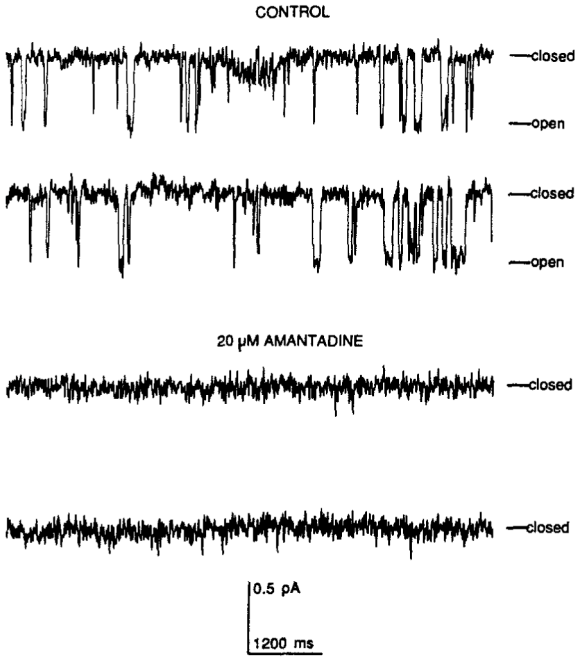

Figure 2.1. Single-channel currents observed by Duff and Ashley (Duff and Ashley 1992) upon incorporation of M2TM peptide (labeled “CONTROL”) into planar lipid bilayers. The currents are

inhibited upon application of amantadine (lower traces). Note that 1 pA (the approximate scale of the single channel currents shown) corresponds to approximately 10^7 protons per second, which is approximately 10^6-10^7 fold greater than estimated per-tetramer currents from liposome experiments on M2TM (Hu, Fu et al. 2006) and full-length A/M2 (Lin and Schroeder 2001) at physiological pH. Figure from (Duff and Ashley 1992).

A more systematic approach to investigate the function of shorter A/M2 fragments was undertaken by Tobler *et al*. (Tobler, Kelly et al. 1999), where the transport properties of C-terminally truncated M2 proteins were studied in *Xenopus* oocytes, and their surface expression and tetramerization were measured in HeLa T4 cells. (The reader is referred to Figure 1.6 for a domain diagram of M2.) Constructs spanning residues 1-72 and longer (1-77, 1-82, 1-87, 1-92, and full length A/M2) showed robust cell surface expression and formed mixtures of disulfide-linked dimers and tetramers. Shorter constructs consisting of residues 1-62 and 1-52 showed substantially lower cell surface expression levels, especially for the latter, but nevertheless formed dimers and tetramers. Expression of an even shorter fragment spanning only the ectodomain and TM domain (residues 1-45) could not be detected in the HeLa system and was not attempted in oocytes.

When expressed in oocytes, constructs of residues 1-72 and longer showed inwardly rectifying currents similar to those of full length A/M2, whereas rectification was less apparent for constructs 1-62 and 1-52. While most truncation mutants tested showed stable activity when exposed to slightly lowered pH (6.2) to trigger transport, the shortest two constructs (1-62 and 1-52), and somewhat unexpectedly, 1-82, showed progressive decreases in transport activity at this pH.

Protein specific activity was estimated by correlating flux measurements in oocytes with expression levels in HeLa cells. Using this method, it was found that constructs of residues 1-92, 1-77 and 1-72 had apparently similar activity to that of full length protein, while 1-82, and the

shorter 1-62 and 1-52 had lower activity. However, these measurements were not definitive, because instead of correlating whole-cell current and protein expression in each individual oocyte, the expression level was measured in a different cell line. Thus it is possible that differences in fragment expression between the oocyte and HeLa cell systems, and differences in the propensity of each construct to activate endogenous oocyte currents, confounded the results, especially for the shorter fragments.

From these experiments it became apparent that M2 transport function can tolerate deletions of at least some of the C-terminal domain. One may also approach the problem from a structural perspective, since unstructured extra-membrane segments not involved in assembly or drug binding are less likely to be relevant for function. From this point of view, it was observed that full length A/M2 has additional helical content not present in the transmembrane segment (Kochendoerfer, Salom et al. 1999; Tian, Gao et al. 2003), and upon limited trypsin proteolysis of A/M2 in dodecylphosphocholine micelles, protected fragments corresponding to residues 19-60 and 19-61 were isolated, indicating that the transmembrane domain and a domain immediately C-terminal to it form a tightly packed structure. The C-terminal end of this segment also roughly corresponded to the C-terminal end of the truncated segment in the work of Tobler *et al*. where reliable functional measurements became problematic (Tobler, Kelly et al. 1999). The presence of a helix just C-terminal to the transmembrane domain was confirmed in the high-resolution solution NMR structure (Schnell and Chou 2008), although its detailed conformation was less constrained than that of the TM domain due to a paucity of NOE signals in the C-terminal region. Comparison of thermodynamic stabilities of the transmembrane peptide and the full length protein in micelles showed that the latter was ~ 7 kcal/mol more stable (Kochendoerfer, Salom et al. 1999), indicating that structural elements outside of the transmembrane domain contribute to tetramer stability, though their functional role remained unclear. However, circular dichroism spectroscopy and analytical ultracentrifugation experiments performed by the author on a peptide corresponding to the M2 ectodomain (residues 2-24) with cysteines mutated to serines indicated

that this segment alone forms a monomeric random coil and does not bind amantadine with or without detergent, suggesting that the ectodomain is unlikely to strongly contribute to noncovalent M2 tetramer stability or drug binding (Polishchuk).

2.2. Model validation of the M2 TM domain: requirements for parity with full-length A/M2.

Prior to discussing experiments to determine whether the M2 TM domain can functionally represent the full-length protein, it is necessary to establish a set of criteria that must be fulfilled in order for the two constructs to be considered functionally equivalent in terms of proton transport.

First and foremost, the M2 transmembrane domain must transport protons at similar rates as full length A/M2. Transport must be selective for protons by a factor of 10^6 or more, as observed for full length A/M2 in mammalian cell (Chizhmakov, Geraghty et al. 1996) and liposome systems (Lin and Schroeder 2001), and inhibitable by amantadine at ~100 μM concentrations, as seen in oocyte (Wang, Takeuchi et al. 1993) and other experiments (Lin, Heider et al. 1997). The rate of transport should increase with decreasing pH_{out} at moderately acidic pH values, as it does in full length A/M2 (Pinto, Holsinger et al. 1992; Chizhmakov, Geraghty et al. 1996).

Secondly, evidence for the highly perturbed pK_a values observed for the His 37 residues in the M2 transmembrane peptide tetramer (Hu, Fu et al. 2006) should also be obtained from full length A/M2, in order for protonation kinetics and thermodynamics to be comparable between the two systems. While differences in baseline thermodynamic stabilities of A/M2 and M2TM tetramers are acceptable, these constructs must be studied under conditions where they are predominantly tetrameric, and their thermodynamic stabilities should respond similarly to changes in pH.

2.3. A two-pronged approach to assay function of the M2 transmembrane peptide.

Together with our collaborators at the Pinto lab, we set out to test the function of progressively shortened A/M2 constructs in two systems. The Pinto lab, with over 15 years of experience

studying M2 in *Xenopus* oocytes, again turned to this technique in the current endeavor. Oocytes are advantageous in permitting a thorough electrophysiological characterization of channel currents, given that the experimenter can control the membrane voltage via whole-cell clamping. However, there had previously been difficulties characterizing C-terminal truncation mutants of A/M2 in oocytes (Tobler, Kelly et al. 1999), most likely because short fragments of M2 were not efficiently expressed.

In contrast with oocyte experiments, proteoliposome flux measurements can in theory be performed with any peptide that spans the bilayer, if care is taken to verify efficient reconstitution. While detailed electrophysiological parameters such as reversal potentials are difficult to measure using this system, it is sufficiently robust to answer the functional criteria outlined in section two of this chapter. Therefore, the author of this thesis employed the proteoliposome assay, in parallel with the oocyte work of Pinto *et al.*. As will be discussed below, only the proteoliposome assay could be used to determine function of the 25 residue M2 TM peptide, but there was excellent agreement between the two systems with somewhat longer fragments, giving further validity to the results.

The oocyte assay methods and results will be described first in section four, followed by those from proteoliposomes in section five.

2.4. Evaluating activity of M2 deletion mutants in the *Xenopus* oocyte assay.

The expression, functional characterization, and determination of membrane insertion and specific activity of M2 deletion mutants were performed by Drs. Chunlong Ma and Yuki Ohigashi in the laboratory of Dr. Lawrence Pinto at Northwestern University. To build upon the results of Tobler *et al.* (Tobler, Kelly et al. 1999), each oocyte assayed electrophysiologically could also be tested for expression and correct orientation of the desired construct by immunofluorescence. To enable fluorescent detection of M2 molecules in the oocyte, a C-terminal FLAG epitope tag was

added to the protein. In order to determine the impact of the FLAG tag on M2 fragment function, oocytes injected with mRNA encoding FLAG-free constructs were also characterized. In addition, expression and orientation of the fragments of interest was also measured by immunofluorescence in mammalian cells.

2.4.a. Oocyte current measurements – materials and methods.

pGEMHJ plasmids were constructed to contain sequences encoding WT A/M2 protein and shortened fragments (residues 1-71, 21-71, 21-61, and 21-51) with or without a C-terminal FLAG tag (added to full length A/M2, and fragments 21-61 and 21-51). The plasmids were linearized using a downstream NotI restriction site. mRNA was generated from the linearized DNA by *in vitro* transcription with an Ambion T7 mMESSAGE mMACHINE kit. *Xenopus laevis* oocytes were obtained from surgically removed ovarian lobules of female frogs (Nasco, Fort Atkinson, WI). Following excision, the lobules were treated with collagenase B (2 mg/mL, Roche Applied Science) to dissociate the oocytes from follicle cells (Pinto, Holsinger et al. 1992). The oocytes were then cultured, injected with mRNA (~50 ng), and maintained as described in Ma *et al.* (Ma, Soto et al. 2008). Whole cell current was measured in oocytes 48-72 hours following mRNA injection using two-electrode voltage clamping, with details of instrumentation and buffer composition as described (Ma, Soto et al. 2008). During constant-voltage current measurements, oocytes were held at -20 mV and bathed with buffers at pH 8.5 or 5.5 with or without the drug amantadine. Voltage ramps to determine reversal potential (the voltage at which the measured current becomes zero) were also performed. It has previously been shown that erroneous proton reversal potentials can be obtained because of rapid local acidification of the area near the cytoplasmic leaflet of the oocyte membrane, leading to higher than expected apparent internal proton concentrations (Mould, Drury et al. 2000). To minimize this effect, the oocytes were bathed with pH 5.5 buffer and voltage ramps were performed after the measured inward current had reached a steady maximum. Membrane voltage-ramp measurements were also made at pH 8.5. Current-voltage relationships were plotted after subtracting the background current measured at

pH 8.5. Because oocytes do not withstand polarization to large positive voltages (>60 mV), the actual reversal potential could not be measured in all cells, and instead was estimated by extrapolation of current-voltage curves measured at lower voltages.

2.4.b. Determination of fragment specific activity and orientation by anti-FLAG immunofluorescence.

A detailed protocol of sample preparation for immunfluorescence is provided in Ma *et al*. (Ma, Soto et al. 2008). Briefly, individual oocytes on which current measurements had been performed were fixed with 2% paraformaldehyde. After membrane permeabilization with 0.1% saponin (parallel experiments were also performed without saponin) and blocking of nonspecific binding sites with nonfat milk, the FLAG tag was detected using ANTI-FLAG ® M2 monoclonal antibody (Sigma), followed with goat-anti mouse IgG1 (γ1), and labeling with AlexaFluor ® 546 (Molecular Probes). Fluorescence was quantified with a PTI Image Master microfluorometer (Photon Technologies) with an excitation wavelength of 540 nm. Fluorescence of non-injected oocytes lacking M2 was also determined to control for the autofluorescence effect from the oocyte yolk (Beumer, Veenstra et al. 2005).

Specific activity was calculated from the ratio of steady current that flowed at pH 5.5 to the relative amount of protein that was expressed at the surface of the oocyte for each cell studied. For each experiment, at least five oocytes expressing the FLAG-tagged full length A/M2 protein and three uninjected oocytes were measured. For each uninjected cell and for each cell expressing a given truncated mutant protein, the current was plotted against the oocyte surface immunofluorescence for that cell, and a straight line was fitted to the plot.

For expression experiments in mammalian cells, HeLa LTR CD4 βgal cells were maintained in Dulbecco's Modified Eagle's medium supplemented with 10% fetal bovine serum (FBS) at 37°C in 5% CO_2. Cells grown on cover glass were transfected with pCAGGS constructs using

Lipofectamine 2000 (Invitrogen, Carlsbad, CA) according to the manufacturer's protocol. At 16-20 hr. post-transfection, the cells were washed and incubated with anti-FLAG monoclonal antibody (Sigma-Aldrich, St. Louis, MO) followed by FITC conjugated goat anti-mouse antibody (Jackson ImmunoResearch Laboratories, Inc., West Grove, PA) in the presence and absence of 0.1% saponin. Labeled cells were fixed in 2% formaldehyde and mounted on a slide. Immunofluorescence images were obtained with Zeiss LSM 5 Pascal (Zeiss Inc., Thorndale, NY).

2.4.c. Oocyte current measurements – results.

To determine the minimal part of the A/M2 protein necessary for its ion transport function, a series of truncation mutants were constructed (Figure 2.2).

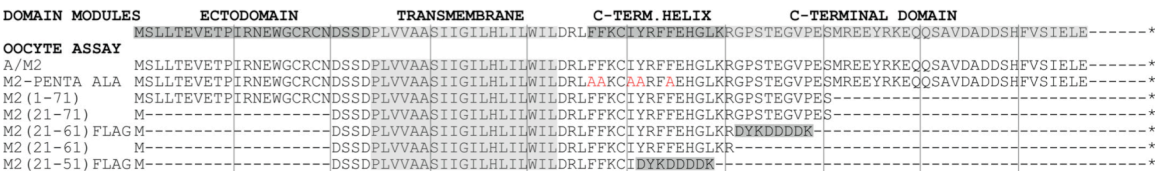

Figure 2.2. Full length and truncated construct sequences used in oocyte experiments. The Penta Ala construct has Ala mutations to structurally important hydrophobic residues in the C-terminal amphiphilic helix (see text). Figure published in (Ma, Polishchuk et al. 2009).

The wild type A/M2 and each of the A/M2 truncation mutant proteins were expressed in oocytes of *Xenopus laevis* and the amantadine-sensitive inward currents were measured using a two-electrode voltage clamp apparatus. Ion transport activity was induced by bathing oocytes in pH 5.5 solution (Ma, Soto et al. 2008; Stouffer, Ma et al. 2008). Previously, Tobler *et al*. found that the smallest construct with ion transport properties similar to those of full length A/M2 protein was trunc72 (residues 1-71) (Tobler, Kelly et al. 1999), and the activity of this fragment was re-confirmed (Figure 2.3). The majority of the ectodomain (1-20) could also be deleted without affecting proton transport (Figure 2.3); M2(21-71) has an inward current of equal amplitude to that of the wild-type A/M2 protein. We next created a fragment similar to one identified as protease-

resistant in micelles in a previous study (Kochendoerfer, Salom et al. 1999): M2(21-61), which contains the transmembrane domain and the cytoplasmic helix (residues 47-61). This construct still displayed the robust inward current of full length A/M2 protein, and of M2(21-71) protein (Figure 2.3). The amantadine sensitivity of all the A/M2 variants was determined by bathing the oocytes in pH 5.5 solution that contained 100 μM amantadine once the oocyte inward current had become maximal. As depicted in Figure 2.3, the inward currents of the truncation mutants were almost completely inhibited (~95%) by treatment with 100 μM amantadine, although the inhibition kinetics were faster for the proteins with a complete ectodomain, suggesting that the ectodomain may help funnel amantadine to the TM pore. The inhibition of neither wild-type A/M2 nor truncation mutant proteins was reversible within 2 min.

To probe further the role of the C-terminal helix (residues 47-60), a construct coding for A/M2(21-51) was examined, with most of this helix deleted. Although it was observed that oocytes injected with this mRNA did not show significant membrane current, it appeared likely that such a short fragment might not be expressed or reach the cell surface (*vide infra*). Thus, in an alternate approach we mutated five of the hydrophobic residues (F47, F48, I51, Y52, and F55) in this region to Ala residues. This construct exhibited activity virtually identical to wild-type A/M2 (Figure 2.3, M2-Penta Ala); a result which will be further discussed in the next chapter.

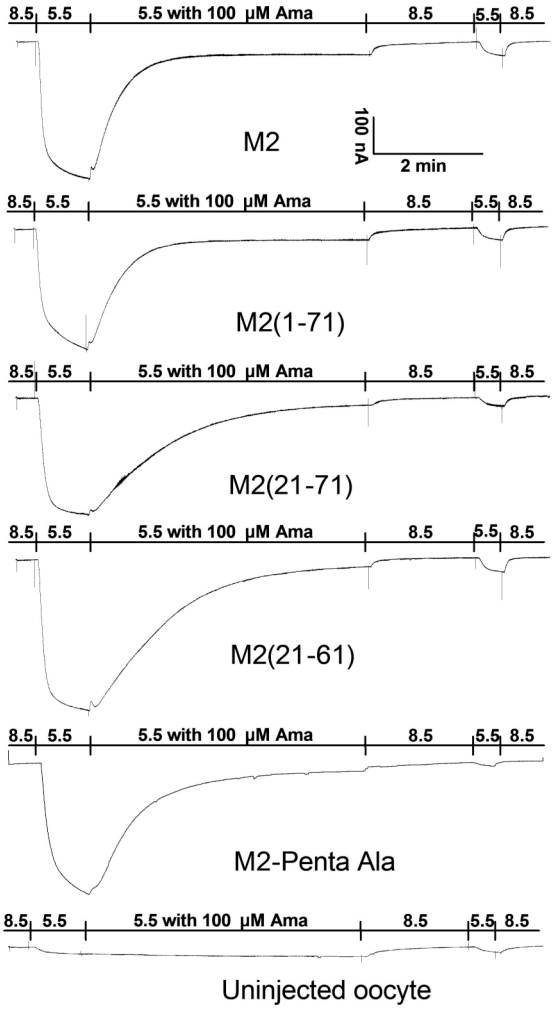

Figure 2.3. Proton transport through A/M2, its truncation mutants and the Penta Ala full length construct. Whole-cell currents (displayed) are induced by bathing oocytes in pH 5.5 buffer. All constructs are almost fully inhibited by 100 μM amantadine; the inhibition is irreversible within 2 minutes. Uninjected oocytes show minimal currents under these conditions. Figure published in (Ma, Polishchuk et al. 2009).

2.4.d. Specific activity measurements in oocytes and expression in mammalian cells - results.

To compare activities of ion channels single channel conductance and open probability are usually measured. However, the single channel conductance of the A/M2 protein is too low to permit single channel measurements at physiological pH ranges (Mould, Drury et al. 2000; Lin

and Schroeder 2001). As a surrogate measure of specific activity, A/M2 surface expression in oocytes was quantified by measuring fluorescence of immuno-stained epitope tagged A/M2 protein after recording the inward current (Ma, Soto et al. 2008; Stouffer, Ma et al. 2008). To measure the immunofluorescence of A/M2(21-61) protein and of wt A/M2 protein, a FLAG tag was attached to the C-termini. This modification has the added benefit of increasing the length of the very short 21-51 construct, which could possibly increase its expression. As shown in Figure 2.4, oocytes expressing both epitope-tagged M2(21-61)-FLAG and full length A/M2 protein displayed a robust pH activated inward current, similar to that seen for the untagged proteins. Moreover, the currents of oocytes expressing these FLAG-tagged proteins were amantadine sensitive. Interestingly, M2(21-51)-FLAG displayed an amantadine sensitive inward proton current (Figure 2.4), unlike the untagged version of this construct. To determine whether the low current observed for M2(21-51)-FLAG was a consequence of poor expression or low intrinsic activity, its expression level and surface orientation were observed.

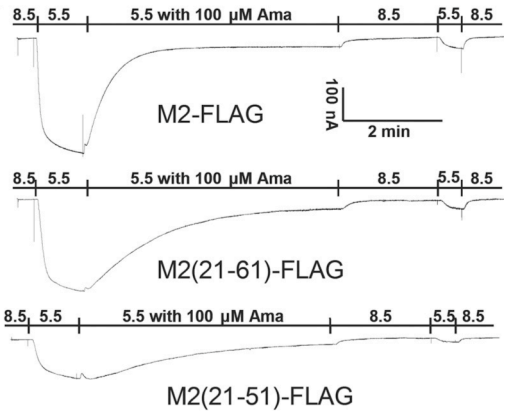

Figure 2.4. Proton transport by FLAG-tagged A/M2 and shortened constructs in oocytes. The FLAG tag does not appreciably affect function of full length A/M2 and M2(21-61), but may rescue expression of M2(21-51), leading to lower, but observable amantadine sensitive current. Figure published in (Ma, Polishchuk et al. 2009).

To determine whether the truncated proteins were expressed in the oocyte plasma membrane in the correct N_{out}/C_{in} orientation, oocytes expressing M2(21-51)-FLAG, M2(21-61)-FLAG, and A/M2-FLAG were observed by immunofluorescence by using anti-FLAG antibody (Figure 2.5 A). In the absence of saponin, there was almost no fluorescence, whereas, when 0.1% saponin was included to permeabilize the plasma membrane, bright fluorescence was observed for A/M2-FLAG and M2(21-61)-FLAG tagged proteins, especially at the edge of the oocytes. Staining for M2(21-51)-FLAG was less intense, consistent with lower expression. The FLAG-tagged M2 proteins were also expressed in mammalian cells and subjected to indirect immunohistochemistry using anti-FLAG antibody (Figure 2.5 B). The results were similar to those observed in oocytes. Moreover, when the mammalian cell membrane was permeabilized by saponin, it clearly showed that fluorescence was only at the membrane surface and not in the cytoplasm. These findings indicate that wt A/M2-FLAG, M2(21-61)-FLAG and M2(21-51)-FLAG proteins are expressed and appropriately inserted into the cytoplasmic membrane with the C-terminus, where the FLAG tag was positioned, facing inside the cells.

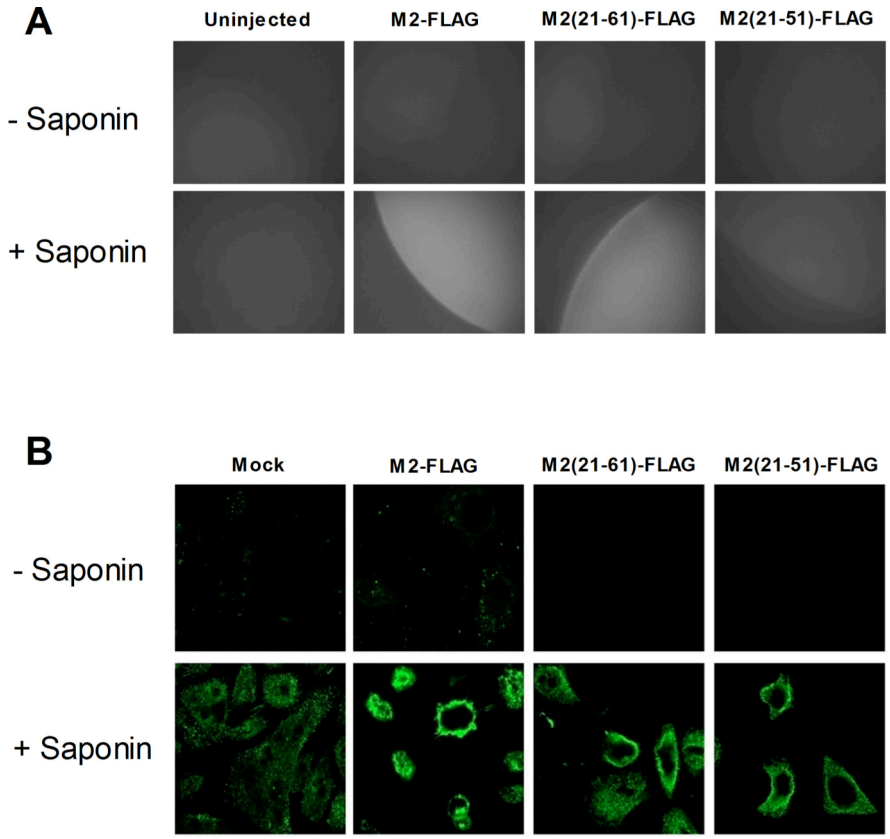

Figure 2.5. Immunofluorescent detection of FLAG-tagged A/M2 and deletion mutants expressed in oocytes (A) and mammalian cells (B). Strong fluorescence signal is observed at the cell surface and only upon saponin permeabilization, suggesting that the constructs are appropriately expressed and oriented. Figure published in (Ma, Polishchuk et al. 2009).

Since FLAG-tagged proteins were expressed in the plasma membrane in the correct orientation, it was feasible to normalize the current observed by the level of expression. The specific activity was calculated from the ratio of maximum inward current at pH 5.5 to the relative amount of protein that was expressed at the surface of the same oocyte, measured by immunofluorescence (Ma, Soto et al. 2008). This experiment was repeated in approximately ten cells for each construct, because the level of protein expression varies from cell to cell. For a given construct, the maximal conductance varies linearly with respect to the amount of protein expressed on the cell surface (Figure 2.6). The slope of the line, obtained by linear regression, reflects the change

in conductance with respect to surface concentration, and hence is a measure of the specific activity of a given A/M2 variant protein. The calculated specific activity for M2(21-61)-FLAG was the same as A/M2-FLAG (Figure 2.6) within experimental error (P = 0.17). The calculated specific activity of M2(21-51)-FLAG was about 50% of full length A/M2, although the expression level of M2(21-51)-FLAG was too low to do a fully quantitative assessment of its activity.

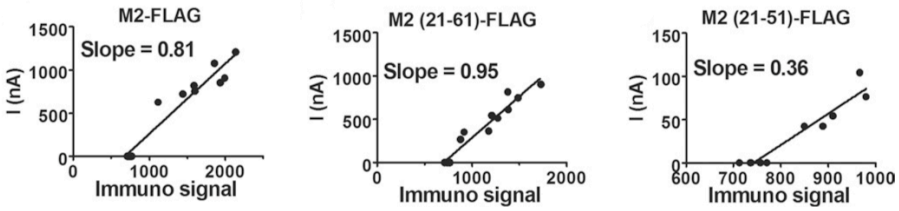

Figure 2.6. Specific activity of FLAG-tagged A/M2 (left panel), M2(21-61) (center panel), and M2(21-51) (right panel). Each point represents the maximum current obtained from a single oocyte (Y axis) plotted against that oocyte's immunfluorescence signal (X axis). The slope of the resulting regression line is the construct's specific activity. Figure published in (Ma, Polishchuk et al. 2009).

2.4.e. Ion selectivity of A/M2 fragments measured in oocytes – results.

The reversal voltage, which provides a measure of the ion selectivity of the protein, was measured to check for the altered ion selectivity of truncated mutant M2 constructs. The current-voltage relationship of M2(21-61)-FLAG and full length A/M2-FLAG were almost identical (Figure 2.7). Although the macro-conductance of M2(21-51)-FLAG was much lower than that of full length and M2(21-61)-FLAG proteins, the extrapolated I-V curve of M2(21-51)-FLAG intercepted the voltage-axis close to the intercepts for full length A/M2 and M2(21-61) proteins (Figure 2.7). These results indicate that these truncated M2 constructs have similar ion selectivity to the wild type, full length A/M2 protein.

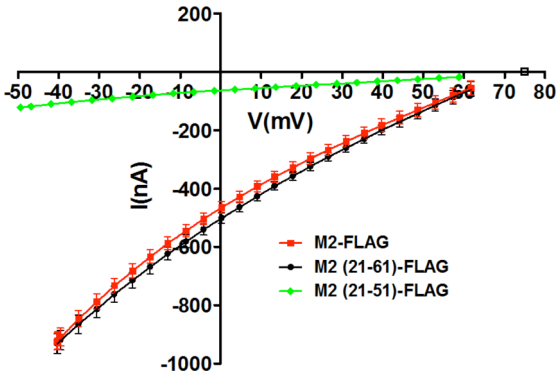

Figure 2.7. Current-voltage profiles of full length M2-FLAG and FLAG-tagged truncation mutants. The extrapolated reversal potential (voltage at which current is zero) is similar for all constructs. Figure published in (Ma, Polishchuk et al. 2009).

2.4.f. Oocyte results – conclusions.

In summary, expression of A/M2 fragments in *Xenopus* oocytes and mammalian cells showed that removal of the N-terminal ectodomain (residues 1-20) and of the C-terminal domain portion following residue 61 does not markedly affect transport rate, proton selectivity, and extent of amantadine inhibition (though a slight decrease in the drug's binding "on" rate was observed). Expression of C-terminally FLAG-tagged full length A/M2 and M2(21-61) constructs in oocytes and mammalian yielded similar functional properties as the FLAG-free constructs, and allowed confirmation of surface expression and correct orientation of constructs in the membrane. Addition of the C-terminal FLAG tag partially rescued deficient expression or insertion of M2(21-51). Full length A/M2-FLAG and M2(21-61)-FLAG had similar specific activities, while the specific activity of M2(21-51)-FLAG was 2-3 fold lower but could not be precisely quantified because of low immunofluorescence signal. Thus, while it was clearly shown that M2(21-61) retains the functional properties of full-length A/M2 and has a similar specific activity (the latter representing a major advance from the work of Tobler *et al*. (Tobler, Kelly et al. 1999), the data were less definitive for M2(21-51). Shorter fragments such as those corresponding to the M2TM peptide could not be studied, and the functional role of the C-terminal amphiphilic helix (residues 47-61)

remained ambiguous, although mutation of the hydrophobic residues in that helix to Ala in context of full-length A/M2 did not affect transport function in oocytes.

2.5. Determination of M2 fragment function in liposomes – experimental background.

While the proteoliposome assay system is less easily manipulated with respect to electrophysiological parameters (i.e. voltage clamping), it is advantageous in isolating the protein of interest from other cellular components. It is also useful in giving the experimenter control over bilayer composition, and the ability to use transport-mediating protein fragments from both biological as well as chemical (synthetic peptides or peptidomimetics) sources, with *in vitro* reconstitution that does not depend on cell-based expression and insertion machinery. The transport activity, inhibitor sensitivity, and, under appropriate conditions, ion selectivity of proteins of interest can be determined through proteoliposome reconstitution if the requisite controls are correctly performed.

Proteoliposomes and artificial membranes have been successfully used to study a wide-ranging array of ion channels (reviewed by Miller (Miller 1983; Miller 1984)), including full-length A/M2 from bacterial (Moffat, Vijayvergiya et al. 2008) and eukaryotic sources (Schroeder, Ford et al. 1994; Lin and Schroeder 2001), building on work by Dencher in developing experimental methods for measuring proton flux across lipid bilayers (Dencher, Burghaus et al. 1986). While there have been reports of M2 transmembrane peptide activity in liposomes and planar lipid bilayers (Duff and Ashley 1992; Hu, Fu et al. 2006; Pielak, Schnell et al. 2009), these experiments have several shortcomings. First of all, none of the groups measured the extent of peptide reconstitution, instead assuming stoichiometric protein incorporation when calculating specific activity. Not surprisingly, the magnitude of the measured currents differed substantially between systems and experimenters. Secondly, none of the reports rigorously probed the ion selectivity of M2 TM under physiological conditions, and finally, none of the work was performed in parallel with full-length A/M2 as an internal control (Duff and Ashley 1992; Hu, Fu et al. 2006;

Pielak, Schnell et al. 2009). The present work aims to definitively address these questions by characterizing full length A/M2 in parallel with the M2 TM peptide, M2(22-46), and intermediate length fragments when reconstituted in liposomes under similar experimental conditions.

2.5.a. Proteoliposome flux assay – summary of procedure.

A brief summary of the protein reconstitution procedure and the experimental protocol for the proteoliposome flux assay will be provided in this section; complete protocols for peptide synthesis and protein purification, details of reconstitution technique, and details of experimental procedure will be provided in the following sections.

Lipid films consisting of 25 μmol 4:1:2 POPC:POPG:cholesterol were made by drying component stocks dissolved in chloroform under a stream of nitrogen or argon gas. The films were re-dissolved in ethanol and mixed with ethanolic stocks of A/M2 or fragments (with a target protein:lipid ratio of approximately 1:1000 monomer:lipid), then immediately dried down a second time.

Protein/lipid films made as described above were immediately hydrated with 995 mL of "K" buffer (100 mM K_2SO_4, 15 mM K_xPO_4 pH ~7.5); the samples were then vortexed extensively and frozen. Upon thawing, the pH indicator dye pyranine (Invitrogen, Carlsbad, CA) was added, and the mixture was subjected to ten additional freeze-thaw cycles to form dye-containing liposomes. Liposomes were sized by extrusion to ~100 nm diameter and dialyzed against "K" buffer precisely pH adjusted to 7.4. XAD-4 Amberlite resin (Supelco, Bellefonte, PA) was added to the dialysis buffer to bind excess dye. Liposomes were stored at 4°C and used within a week.

Fluorescence proton flux assays were performed at 18°C in a buffer equivalent to "K" buffer except with Na^+ as the counterion ("Na" buffer), in the presence of a membrane-impermeable pyranine quencher (DPX, Invitrogen). The potassium ionophore valinomycin (Sigma Aldrich)

and/or amantadine hydrochloride were added to the assay buffer as indicated. Valinomycin selectively permeabilizes the liposome membrane to potassium, creating a negative potential inside the liposome as it leaks out. To restore electrical neutrality to the membrane, protons flow into the liposome if a proton transporting protein is present.

Liposomes (preincubated with desired concentration of inhibitor) were rapidly diluted into the assay buffer, and pH changes inside the liposome were tracked. The ion fluxes in the experiment are summarized in Figure 2.8.

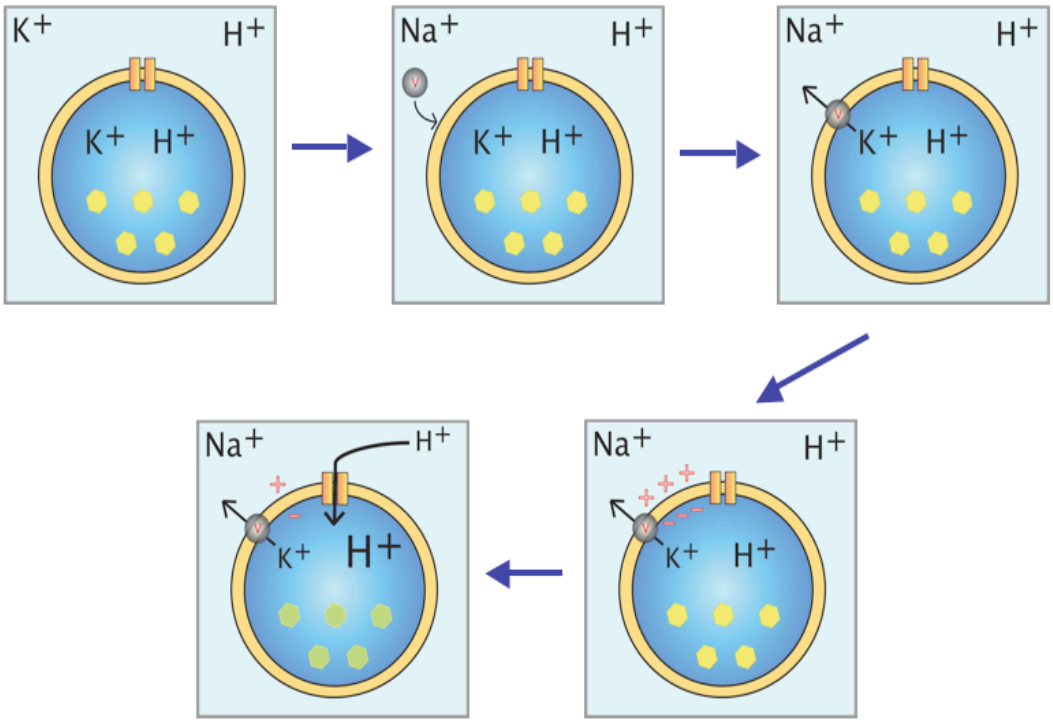

Figure 2.8. Summary of the proteoliposome proton flux assay. Proteoliposomes made in K+ containing buffer are diluted into Na^+ containing buffer with the K^+ ionophore valinomycin (V). Valinomycin-mediated K^+ efflux down its concentration gradient creates a net negative charge inside the liposome, providing a driving force for proton entry through M2. Changes in intraliposomal pH are monitored fluorimetrically through entrapped pH indicator dye (pyranine).

pH changes inside the liposome were measured by monitoring signal decay of the deprotonated indicator dye form, followed by recording of the signal at the pH-insensitive isosbestic point of the dye. Intraliposomal pH was calculated from a calibration curve of the deprotonated/isosbestic fluorescent signals shown in Figure 2.9. Proton flux was calculated by converting intraliposomal pH to total intraliposomal protons *vs*. time using the intraliposomal buffering capacity (Dencher, Burghaus et al. 1986) adjusted for liposome volume; the result was then divided by measured protein incorporation to obtain per tetramer proton transport.

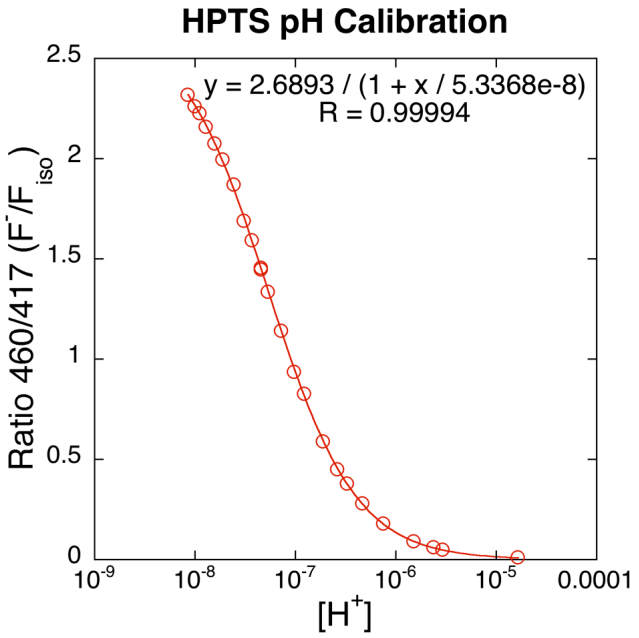

Figure 2.9. HPTS (pyranine) pH calibration. The ratio of the signal of the deprotonated form (F^-, ex 460 nm, em 515 nm) to the signal at the isosbestic point (F_{iso}, ex 417 nm, em 515 nm) is plotted vs. $[H^+]$. Figure published in (Ma, Polishchuk et al. 2009).

2.5.b. Chemical synthesis of M2 fragment peptides.

Significant progress has been made in the chemical synthesis of hydrophobic peptides (such as those corresponding to helical transmembrane segments of proteins) (Glover, Martini et al. 1999;

Fisher and Engelman 2001); nevertheless, these sequences are not trivial to synthesize because of their propensity to aggregate on the solid support resin, which reduces reaction yields and/or leads to poorly separable side products. Longer membrane spanning sequences (>40 amino acids) can be especially difficult to make with common synthesis procedures. Thus, while standard procedures (with double coupling for difficult parts of the sequence) could be used to synthesize the shorter M2 fragments, high-temperature microwave synthesis was employed for a longer fragment encompassing the transmembrane domain and the C-terminal helix. While full-length A/M2 has previously been synthesized using native chemical ligation of its fragments (Kochendoerfer, Salom et al. 1999), for this work we employed bacterial expression to produce large amounts of this protein (described in next section) for use in liposome activity measurements. For easy reference in the sections below, chemically synthesized peptides will be prefixed by "syn" to distinguish them from bacterially expressed constructs.

The 25-residue M2 transmembrane peptide synM2(22-46) and the 29 residue peptide synM2(22-50) were synthesized using standard solid-phase Fmoc chemistry manually on an Argonaut Technologies (Foster City, CA) Quest heated reaction/liquid handling system or on a Protein Technologies (Tucson, AZ) PTI Symphony automated synthesizer, and were C-terminally amidated. The 44-residue synM2(19-62) was synthesized manually with frequent double deprotection and double coupling cycles, and constant monitoring of coupling efficiency, in a CEM (Mathews, NC) Mars reactor with microwave heating during deprotection and coupling. synM2(19-62) was C-terminally amidated and N-terminally acetylated to protect the N-terminal Cys sidechain from modification. Sequences of the full length construct (*vide infra*) and the synthetic peptides used in the proteoliposome flux assay are provided in Figure 2.10.

```
DOMAIN MODULES      ECTODOMAIN          TRANSMEMBRANE       C-TERM.HELIX        C-TERMINAL DOMAIN
                 MSLLTEVETPIRNEWGCRCNDSSDPLVVAASIIGILHLILWILDRLFFKCIYRFFEHGLKRGPSTEGVPESMREEYRKEQQSAVDADDSHFVSIELE------*
LIPOSOME ASSAY
A/M2          -SLLTEVETPIRNEFGSRSNDSSDPLVVAASIIGILHLILWILDRLFFKSIYRFFEHGLKRGPSTEGVPESMREEYRKEQQSAVDADDSHFVSIEGRHHHHHH*
SYNM2(19-62)  ----------------CNDSSDPLVVAASIIGILHLILWILDRLFFKSIYRFFEHGLKRG----------|----------|----------|----------*
SYNM2(22-50)  ----------|----------|-SSDPLVVAASIIGILHLILWILDRLFFKS----------|----------|----------|----------|----------*
SYNM2(22-46)  ----------|----------|-SSDPLVVAASIIGILHLILWILDRL----|----------|----------|----------|----------|----------*
```

Figure 2.10. Sequences of A/M2 and synthetic fragments used in proteoliposome assay. The full length construct has a 6xHis tag for purification, and the following mutations that do not affect activity but improve culture yields: W15F, C17S, C19S, C50S (*vide infra*). Figure adapted from (Ma, Polishchuk et al. 2009).

Peptides were cleaved from the solid support by immersion and stirring in a cocktail of 90% trifluoroacetic acid, 5% water, and 5% triisopropylsilane (synM2(22-46) and synM2(22-50)), or 90% trifluoroacetic acid, 5% thioanisole, 3% ethanedithiol, and 2% anisole (synM2(19-62)). The reaction was allowed to proceed for 3-4 hours, after which the solid support was separated by filtration over glass wool, and the volume of the cleavage cocktail was reduced by evaporation under a stream of nitrogen gas. The crude peptide was precipitated by dripping the filtered cleavage reaction mixture into an excess of cold diethyl ether and hexanes. After centrifuging and washing the precipitate, and decanting the ether/hexanes supernatant, the white crude product was dissolved in buffer B (90% acetonitrile, 10% water, 0.1% trifluoroacetic acid), frozen thoroughly in liquid nitrogen, and lyophilized overnight to yield a fluffy, easily handled white or off-white solid, which was stored at -20 ºC prior to purification.

Peptides were purified by reverse-phase high performance liquid chromatography (HPLC) over a C4 silica column. Crude product was dissolved in trifluoroethanol (TFE, Acros Organics, 30-40% v/v final concentration depending on fragment hydrophobicity) and distilled, deionized water. To revert trifluoroacetyl adducts (observed by MALDI-mass spectrometry of crude product as series of peaks with masses of product + 96 Da, product + 192 Da, etc.), 1M ultra-pure aqueous Tris-HCl buffer pH 8 (Invitrogen) was added to a final concentration of 100 mM (10% v/v). For cysteine-containing synM2(19-62), an excess of the reducing agent triscarboxyethylphosphine (TCEP-HCl) was added to the final loading mixture. Following thorough mixing and filtration through a polypropylene syringe filter (Whatman), the crude product was loaded onto the HPLC column. It was important to keep the TFE concentration in the loading buffer as low as possible

without precipitating the peptide in order to ensure efficient peptide binding onto the column material. It was also necessary to keep the dissolved crude product and purified liquid fractions from the HPLC at or below ~0 ºC to avoid oxidation of the Trp 41 sidechain.

Peptides were eluted from column using linear gradients of the polar buffer A (0.1% TFA in water) and the hydrophobic buffer B or buffer B' (90% acetonitrile, 10% water, 0.1% TFA or 60% 2-propanol, 30% acetonitrile, 10% water, 0.1% TFA respectively), ramping from 30-50% to 100% hydrophobic buffer. Peptide fractions were frozen and lyophilized, and their purity assayed by analytical-scale reverse-phase HPLC, and MALDI or ESI mass spectrometry. Peptides were stored as solid trifluoracetate salts at -20 ºC or as ethanol stocks at -80 ºC.

2.5.c. Bacterial expression and purification of codon-optimized, cysteine-free A/M2.

A pET23D plasmid with a bacterial codon-optimized synthetic gene sequence encoding a variant of A/M2 (based on the sequence of A/Udorn/72, accession number CAD22815) followed by a six-residue C-terminal His tag was kindly provided by Dr. Joshua Rausch at the Pinto laboratory. This sequence further differs from A/Udorn/72 in that all of its cysteine residues (at positions 17, 19, and 50) have been mutated to serines, and a tryptophan in the N-terminal ectodomain at position 15 has been mutated to phenylalanine to enable spectroscopic studies of the remaining "gating" tryptophan at position 41 in the transmembrane domain. The mutation of Cys residues to Ser has no effect on M2 function (Nguyen, Soto et al. 2008), and, as described in section 4 of this chapter, the entire M2 ectodomain (containing residue 15) can be removed with minimal impact on proton transport. This form of full-length A/M2 is advantageous in its ~5-fold higher culture yields compared to the Cys-containing Udorn sequence, and was used as the full length construct in proteoliposome experiments.

Recombinant 6XHis-tagged A/M2 protein was produced from BL21(DE3)pLysS *E. coli* cells (Invitrogen, Carlsbad, CA) using the pET23D(+) plasmid (EMD Biosciences, San Diego, CA).

BL21 cells were chemically transformed with the pET23D(+) plasmid containing the M2 gene and grown in LB media containing 100 mg/ml ampicillin. When OD_{600} of 0.6-1.0 was achieved, protein production was induced by addition of 1 mM IPTG to the media. After 4-5 hours of induction, cells were harvested by centrifugation at 4 ^{o}C for 30 minutes. Pellets were resuspended in 25 ml of 50 mM Tris, pH 8, 0.25 mg/ml lysozyme, 0.02 mg/ml DNase I and 100 μM - 1 mM PMSF. Solutions were subjected to a minimum of three cycles of freezing and thawing in a dry ice / ethanol bath and a 37^{o}C water bath, followed by a further hour at 37^{o}C for full lysis of cells. This solution was then centrifuged at ~15,000 *g* for 30 minutes and the pellet resuspended in 50 mM Tris, pH 8, 150 mM NaCl, 40 mM OG, 1 mM DTT and 100 mM – 1 mM PMSF. The octylglucoside (nOG) solution was then centrifuged at ~15,000 *g* for 30 minutes and the supernatant was saved for purification on Ni-NTA columns.

The OG solubilized supernatant containing A/M2 protein was mixed with Ni-NTA agarose (Qiagen, Valencia, CA) and incubated overnight at 4^{o}C with constant agitation. Imidazole was added to a final concentration of 10 mM to block nonspecific interactions when purifying the Cys-free construct. Columns were washed successively 50 mM Tris, pH 8, 150 mM NaCl, 40 mM OG, 1 mM DTT, then 50 mM Tris, pH 8, 20 mM OG, 20 % (v/v) glycerol, followed by 50 mM Tris pH 8, 4 mM OG, 20% (v/v) glycerol. Finally, the proteins were eluted from the column using ~15 ml 50 mM Tris pH 8, 4 mM OG, 20% (v/v) glycerol and 300 mM imidazole. Fractions were evaluated for protein content by measuring absorbance at 280 nm or by a Bradford (Sigma-Aldrich, St. Louis, MO) protein assay. Centrifugal concentrators (Millipore, Billerica, MA) were utilized for concentrating and rinsing pooled protein fractions into a final solution of 50 mM Tris (pH 8), 4 mM OG and 20% (v/v) glycerol or 50 mM HEPES (pH 8), 4 mM OG, and 20% (v/v) glycerol. The protein was then purified from the final buffer by RP-HPLC and lyophilized similarly to the chemically synthesized peptides. HPLC and mass spectral analysis of the nickel column eluate showed a clean trace with a single peak corresponding to the protein of interest, and a late-eluting shoulder corresponding to the protein of interest + approximately 40 Da, which may be an

acetyl group. Trypsin digestion followed by MALDI-mass spectrometry indicated that the adduct formed at an ectodomain residue (N-terminal to residue 19) and thus was unlikely to influence function. Therefore, during preparative HPLC purification, the main peak and the +40 Da shoulder were collected together and used in further experiments.

2.5.d. Liposome flux assay – experimental considerations and challenges.

When proteoliposomes are formed, the natural machinery of membrane protein chaperones and translocons is bypassed for the final incorporation of purified membrane protein into the liposome membrane, and some form of artificial incorporation is instead used. A variety of commonly accepted strategies exist, including permeabilization of a membrane protein from its source in detergent micelles followed by transfer to hydrated phospholipids (Allen, Romans et al. 1980; Miller 1984), co-drying of organic stocks of phospholipids and protein followed by hydration of the resulting film (Cristian, Lear et al. 2003), or rapid injection of co-dissolved phospholipids and protein from an organic stock into aqueous buffer (Allen, Romans et al. 1980). In applying these approaches, great care must be taken to preserve the function of the membrane protein and to prevent aggregation of the sample components, since it is not uncommon for membrane proteins to lose a significant degree of function during e.g. detergent solubilization (Seddon, Curnow et al. 2004; Dahmane, Damian et al. 2009; Niu, Doctrow et al. 2009). A given reconstitution method may be adequate for some proteins but not for others: some detergents may not stably solubilize certain protein fragments, while organic solvent solubilization may not be applicable to longer, more complex membrane proteins which can be irreversibly denatured by such treatment.

Not surprisingly, in our trials of reconstitution methods for A/M2 and fragments, we found that the degree of protein incorporation varied substantially from one procedure to another in a fragment-specific manner. In previously published, successful, proteoliposome experiments, full-length A/M2 was introduced into liposomes from n-octylglucoside (nOG) micelles (Schroeder, Ford et al. 1994; Lin and Schroeder 2001), and this was the first method that we attempted. While

immediately successful in the case of synM2(22-46) and synM2(22-50), this method led to sample aggregation when applied to synM2(19-62). The aggregation usually manifested as clogging of the sizing membranes during liposome extrusion, where a non-uniformly sized unilamellar proteoliposome population is repeatedly filtered through pores to achieve a more uniform size distribution. This aggregation was not prevented by addition of reducing agent (TCEP HCl), dilution of sample prior to the extrusion step, gentle heating of the sample during extrusion, or brief sonication prior to extrusion.

An alternative reconstitution method described in detail below and involving co-drying of the protein and lipid out of ethanol, was found to be effective for all constructs tested, generally yielding reconstitution levels of 75% or greater when compared to starting amounts.

This experience reinforces the absolute necessity of verifying protein incorporation in the final product (e.g. by HPLC as described below) instead of relying on the input stoichiometries, since unsuccessful reconstitution methods such as the octylglucoside technique applied to synM2(19-62) often led to very low incorporation (10% of target value or below) and would have resulted in erroneous conclusions with respect to transport activity if a high level of incorporation was assumed.

Aside from carefully controlled reconstitution, the proteoliposome assay requires additional care to ensure reliable results, (Szoka Jr and Papahadjopoulos 1980) including: 1) using lipids free of oxidation products (e.g. by using presealed ampules of polar lipids stored as indicated by manufacturer); 2) minimizing the time that the protein and lipid are together in a dehydrated state; 3) confirming that a uniform vesicle population is obtained by using light-scattering and/or electron microscopy; 4) minimizing prolonged incubations below neutral pH. When functionally reconstituted, the reaction rate is relatively rapid, so we used a rapid mixing device and the

assays were conducted at pH 7.4 and 18°C to allow convenient measurement of the signal over 20 sec.

2.5.e. Detailed protocol for proteoliposome flux assay.

Sample preparation. Lipid films consisting of 4:1:2 POPC:POPG:cholesterol (25 μmol total) were made by mixing chloroform stocks of the phospholipids (POPC and POPG, 25 mg/mL, Avanti Polar Lipids, Alabaster, AL) taken from a freshly opened manufacturer ampule with a freshly made chloroform stock of powder cholesterol (25 mg/mL, Sigma Aldrich, St. Louis, MO). The combined chloroform solutions were evaporated without delay under a stream of nitrogen or argon gas; the resulting lipid films were dried on a lyophilizer for at least two hours.

All handling of chloroform stocks was performed in Teflon-capped glass vials and metal/glass/Teflon Hamilton (Reno, NV) syringes with Teflon needle hubs. Plastic components were not used to prevent leaching of plasticizers into the chloroform stocks. Exposure of chloroform lipid stocks to room temperature was kept as short as possible.

Protein and fragment concentration was quantified by using absorbance at 280 nm in an ethanol stock. The calculated extinction coefficient for synM2(22-46) and synM2(22-50) was 5,850 M^{-1} cm^{-1}. The extinction coefficient used for synM2(19-62) was 6,990 M^{-1} cm^{-1}, and for the Cys-free Trp15Phe A/M2 it was 8,480 M^{-1} cm^{-1}.

Lyophilized peptides and protein (as trifluoroacetate salts from HPLC purification) were dissolved in ethanol and the fragment concentration was determined. Stocks were maintained on dry ice or at -80°C until use. Peptide/protein in ethanol in an amount of 25 nmol monomer was added to a lipid film (target 1:1000 monomer:lipid ratio); additional ethanol was added to a total volume of approx. 300 μL. For protein-free control liposomes, only ethanol was added. The mixture was vortexed to dissolve the dried lipid, then immediately dried under an argon stream.

The resulting film was immediately hydrated with 995 μL "K" buffer (50 mM K_2SO_4, 15 mM K_xPO_4 pH ~7.5) by vortexing for 2 minutes. The mixture was frozen on dry ice and thawed. 5 μL of 100 mM hydroxypyrene trisulfonic acid trisodium salt (HPTS, pyranine from Invitrogen) was then added, and the mixture vortexed. Unilamellar liposomes were formed by 10 freeze-thaw cycles (dry ice/ethanol and 37°C water bath) and sized by repeated passage through 100 nM polycarbonate filter membranes (Whatman, Piscataway, NJ) in a mini-extruder (Avestin, Ottawa, Canada). Liposomes were then dialyzed for 8 hours-overnight in a 10K MWCO Pierce Slide-A-Lyzer cassette against 1.8 L of "K" buffer pH 7.40 (adjusted with H_3PO_4 or KOH) with 5 g Amberlite XAD-4 resin (Supelco, Bellefonte, PA) added to bind unincorporated dye. A second cycle of dialysis under identical conditions was performed for 2-3 hours. Dialyses were performed at 4°C. Liposomes were stored at 4°C for up to a week following the completion of dialysis. Results from a selectivity-probing experiment where the reconstitution and dialysis were performed at pH 6.5 will also be described.

Proton flux assay: Experiments were performed using an Aviv ATF-105 spectrofluorometer (Aviv Biomedical, Lakewood, NJ) in a 1x1 cm Hellma (Plainview, NY) QS fluorescence cell, thermostated at 18°C. The ratiometric pH indicator HPTS (pyranine, pK_a ~ 7.22) was used to determine intraliposomal pH. The ratio of fluorescent signal of the deprotonated form (excitation 460 nm, emission 515 nm, "F^-") to the pH-independent isosbestic point (excitation 417 nm, emission 515 nm, "F_{iso}") as a function of pH was used to calibrate the assay (Fig. 2.9), and was largely independent of the presence of liposomes. For all samples measured with amantadine, liposomes were pre-mixed with 100x aqueous amantadine HCl (Sigma Aldrich, St. Louis, MO) in a 100:1 v/v ratio and allowed to interact overnight so as to achieve equilibrium binding.

Assay buffers: 2.5 mL of assay buffer (50 mM Na_2SO_4, 15 mM Na_xPO_4 pH 7.40 adjusted with H_3PO_4 or NaOH, "Na buffer") was added to the fluorescence cuvette. It was critical to establish

that the “Na” buffer pH precisely matched that of the final dialysis “K” buffer to within 0.05 pH units. Experiments to probe selectivity and pH_{out} activation in which the same buffer composition but with different pH values was used, will also be described below.

To the assay “Na” buffer was added 37.5 μL of 1M *p*-xylene bis-pyridinium bromide (DPX; Invitrogen, Carlsbad, CA), a membrane impermeable quencher of pyranine fluorescence to restrict measured signal to intraliposomal dye. For experiments shown in Figure 2.11, 3.5 μL of 18 μM valinomycin (Fluka/Sigma Aldrich, St. Louis, MO) in ethanol and 25 μL of 100x aqueous amantadine hydrochloride (as indicated), were also added to the assay buffer. We also performed experiments without valinomycin to assess background K^+ leakage; no effect on transport was observed by adding 3.5 μL of ethanol alone. All fragments (synM2(22-46), synM2(22-50), synM2(19-62), A/M2) were tested with either no drug or a final drug concentration of 99 μM amantadine. Sample buffer conditions for a separate, additional amantadine titration experiment (shown in Figure 2.11 panel D) on synM2(22-46) are described next.

An amantadine titration experiment was performed on a second, independent synM2(22-46) liposome preparation in order to observe inhibition at a greater range of amantadine concentrations. Liposome preparation and overnight amantadine incubation for this data set were performed as described above. For these samples, 25 μL of 100x amantadine hydrochloride or water (no drug) was added to the assay buffer containing DPX and valinomycin as above to attain the desired amantadine concentration. This resulted in a duplicate amantadine-free data set for synM2(22-46), with assay buffer now diluted by <1% by the added water. The results of the two experiments were essentially identical and are averaged in the final figure. Two data sets were also obtained from the separate synM2(22-46) liposome preps under inhibition by 99 μM amantadine; these were also averaged in the final figure.

Data collection: Prior to data collection, the assay buffer (with DPX, valinomycin and drug as indicated) was allowed to equilibrate at 18°C for 5 minutes in the fluorometer cell holder. Liposomes (~20 μL) were injected into the cuvette containing assay buffer from a 1 mL Hamilton (Reno, NV) glass syringe fitted with a repeat-dispensing system. Injections (at t=0 sec) were performed through an adapter in the fluorometer cell holder cover that enabled immediate data acquisition following injection. The sample in the cuvette was vigorously stirred during the experiment. From t=0 sec, kinetic data monitoring the deprotonated form of HPTS (F^-, ex 460 nm, em 515 nm, bandwidths 3 nm) were collected for approximately 50 sec at one second intervals. The first three seconds following injection were omitted from analysis to allow for full mixing of the sample. At t=~90 sec, kinetic data monitoring the isosbestic point of HPTS (F_{iso}, ex 417 nm, em 515 nm, bandwiths 3 nm) were collected for approximately 20 sec at one second intervals. An excitation wavelength scan (ex 480-380 nm, em 515 nm, bandwiths 3 nm) was performed at the conclusion of each experiment for secondary confirmation of the result. Experiments on each condition were performed in triplicate. Two outlying runs from the entire data set of 75 runs were excluded from analysis.

Liposome Flux Assay Data Analysis: The measured isosbestic kinetic signal (F_{iso}, ex 417 nm, em 515 nm) was averaged to a single value, and each data point from the deprotonated HPTS signal kinetic (F^-, ex 460 nm, em 515 nm) was divided by the isosbestic signal average to obtain a signal ratio (deprotonated:isosbestic) as a function of time. The ratios at each time point were averaged between the three independent experiments run for each condition.

The averaged signal ratio vs. time was converted to intraliposomal pH vs. time based on the calibration curve (Fig. 2.9) obtained with free dye in “K” buffer.

Intraliposomal pH ($-\log[H^+_{free}]$) *vs*. time was converted to total intraliposomal [H+] vs time (including H^+ bound to buffer) by using an estimate of the internal buffering capacity (Dencher

1986) assuming an intraliposomal [phosphate] of 15 mM, and negligible contribution to buffering capacity by the dye given its much lower concentration.

Total intraliposomal [H+] vs. time was converted to the total intraliposomal proton count vs. time through multiplication by N_A and intraliposomal volume estimated from dynamic light scattering measurements (described below) assuming no phospholipid loss during preparation and a single phospholipid surface area of $6.3x10^{-19}$ m^2. Experiments with tracer amounts of radiolabeled lipid show that signal loss during typical preparations is <10%.

The initial number of total protons at t=3 sec was subtracted from successive measurements, and the result was divided by the number of peptide tetramers delivered per experiment, as estimated by integration of the 280 nm protein peak from chromatography of proteoliposome samples on an analytical RP-HPLC column (see below).

Results for protein-free control liposomes shown in Figure 2.11 were adjusted for differences in surface area with protein- or fragment-containing liposomes, and were normalized for the degree of protein reconstitution observed for the fragment in each panel (i.e. the difference total H^+ *vs*. time traces for the control liposomes were divided by the same number of peptide tetramers as determined for the corresponding protein-containing sample shown in each panel).

Estimate of protein reconstitution: Liposome samples were mixed in a 2:1 ratio with a lysis buffer containing 150 mM nOG and 150 mM Tris pH 8. 100 mM TCEP HCl (~6% v/v) was added to all samples. The mixture was then injected onto an analytical C4 RP-HPLC column and eluted with a linear gradient of 2:1 isopropanol:acetonitrile with 0.1% TFA and water with 0.1% TFA. Reconstitution was estimated by integration of the 280 nm protein peak in the chromatogram compared to a standard derived from loading synM2(22-46) peptide onto the same column in known amounts from a mixed organic-aqueous stock.

Using the peptide incorporation method described, reconstitution was nearly complete for synM2(22-46), synM2(22-50) and A/M2, and was ~20% reduced for synM2(19-62).

Determination of liposome volume and surface area: Liposome radii were determined using a Wyatt (Santa Barbara, CA) DynaPro dynamic light scattering instrument at 25°C. Liposomes were diluted ~1:1,000-1:10,000 into pre-filtered "K" buffer. Measurements were performed in triplicate for each sample, and the radius distribution peak maxima were averaged.

Volumes and surface areas were determined based on the averaged measured radius. The software of the instrument was set for analysis based on a Rayleigh sphere model, and the solvent model was set to phosphate buffered saline.

2.5.f. Proteoliposome flux assay results: flux magnitude and inhibition.

As described in detail in the previous sections, proton flux in proteoliposomes was evaluated in response to the generation of an electrochemical potential by diluting vesicles that contain K^+ buffer, into Na^+ buffer in the presence of the potassium-selective carrier valinomycin (Lin and Schroeder 2001). If a proton channel is present in the bilayer, protons will diffuse down the induced electrical field, acidifying the interior of the vesicle. The advantage of measuring proton flux in this manner (rather than by simply changing the pH of the buffer on the outside of the liposome and measuring acidification of the interior) (Pielak, Schnell et al. 2009) is that it requires ion-selectivity. If the channel is not selective for protons or the liposomes are non-selectively leaky, then Na^+, which is present in far greater concentration than the concentration of H^+, will diffuse into the vesicles as K^+ diffuses out, and no significant acidification occurs.

A number of reconstitution methods were evaluated to discover a single approach that would allow reconstitution of A/M2 and fragments of various lengths. Ultimately, we found that co-

solubilization of the peptide or protein with a 1000 to 2000-fold molar excess of polar lipids provided satisfactory results for the entire set of M2 protein analogues. The results presented in Figure 2.11 represent the average of three independent measurements, and are reproducible between different sample preparations to within 20%.

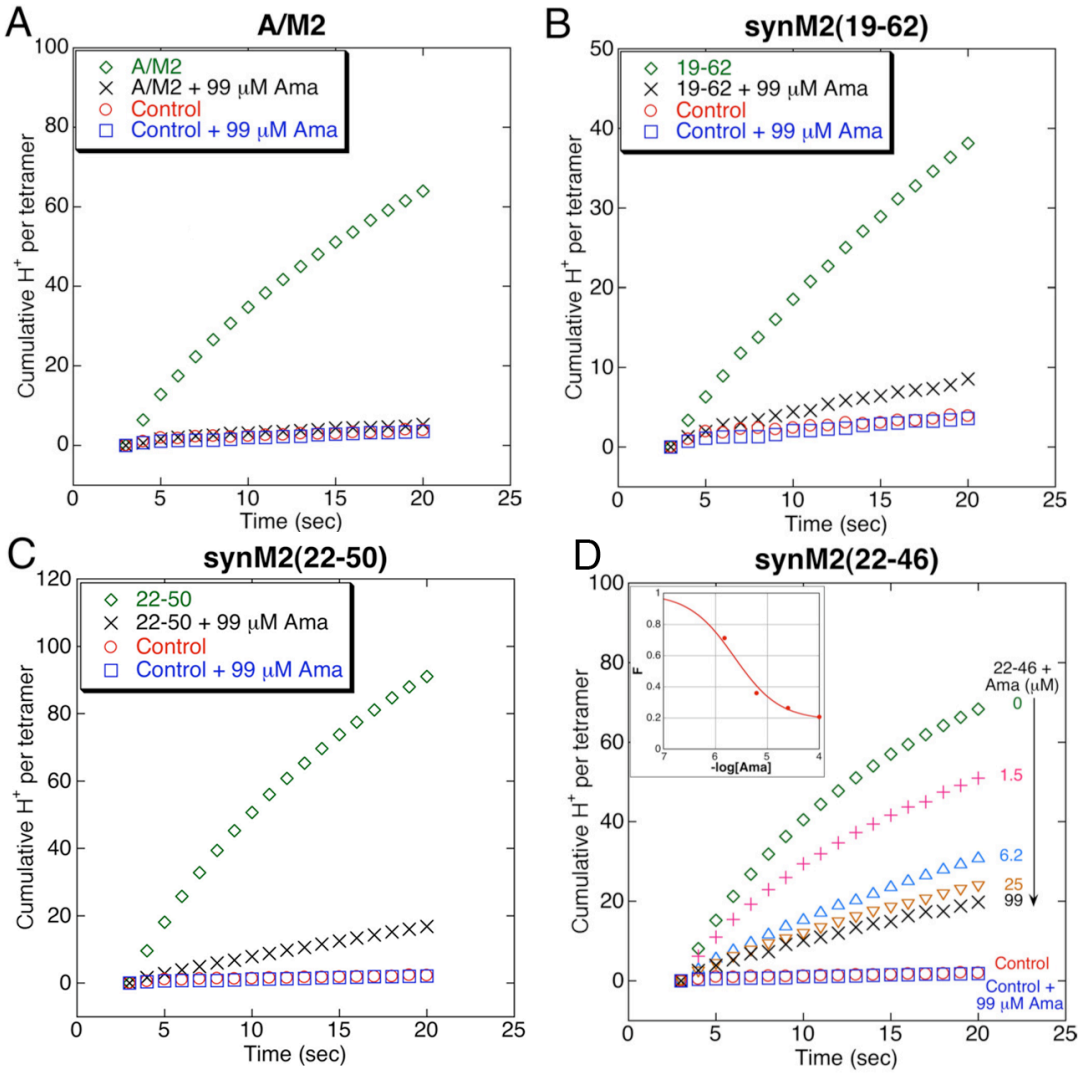

Figure 2.11. Cumulative per-protein H^+ flux in valinomycin-driven proteoliposome assay through A/M2 (A), synM2(19-62) (B), synM2(22-50) (C), and synM2(22-46) (D). Addition of 99 μM amantadine inhibits all constructs to 80+%. A more extensive amantadine dose-response

experiment on synM2(22-46) is shown in panel D and in panel D inset. Control liposomes show minimal flux with or without amantadine. Data published in (Ma, Polishchuk et al. 2009).

The rate of proton flux observed for full-length A/M2 (Figure 2.11 A) is 4.8 sec^{-1} per tetramer, in good agreement with the value of ~7.5 H^+/sec previously measured under almost identical conditions (Lin and Schroeder 2001), and also within an order of magnitude of the rate observed at neutral pH in a similar system (Moffat, Vijayvergiya et al. 2008), and comparable to rates obtained from electrophysiological measurements at this pH (Mould, Li et al. 2000). Very similar rates of proton transport were also observed for the synthetic fragments synM2(19-62), synM2(22-50), and synM2(22-46) (2.3, 7.6, and 6.1 sec^{-1} per tetramer, respectively), all of which are within a factor of ~2 of the value measured for the full-length protein (Figure 2.11 B,C,D). Typically, proteins reconstituted in this manner are randomly oriented $N_{in}C_{out}$ and $N_{out}C_{in}$. However, because of possible biases in the orientations, it is uncertain whether the two-fold difference in rate reflects differences in orientational preferences or genuine differences in conductivity.

The proton flux of A/M2 and the synthetic peptides is inhibited to near background levels by 100 μM amantadine (Figure 2.11). We examined the full dose-response behavior for the shortest construct, synM2(22-46) (Figure 2.11 D), corresponding to the M2 transmembrane peptide that has been the subject of extensive structural and biophysical characterization. It showed a half-maximal effect near 5 μM amantadine (inset Figure 2.11 D), within the range observed of A/M2 in oocytes (Wang, Takeuchi et al. 1993; Jing, Ma et al. 2008), reaching near completion (~80-90%) by 100 μM amantadine.

2.5.g. Proteoliposome flux assay: measurement of proton selectivity and pH activation.

Having established that the M2 transmembrane peptide and full length A/M2 have similar proton transport rates in the proteoliposome assay, and are both susceptible to inhibition by near-

physiological concentrations of amantadine, we must next determine whether the TM fragment shows a similar degree of proton selectivity as the full length protein, and whether both demonstrate an increasing proton transport rate in response to a lower pH_{out}.

In comparison with classical electrophysiological measurements in the oocyte system, it is more difficult to ascertain reversal potentials in liposomes, since the experimenter has little control over the protein's orientation in the membrane, and the starting voltage itself is determined by permeant ion concentration. For example, when valinomycin is used to provide the driving force by selectively permeabilizing the liposome membrane to potassium ions, the relative concentrations of K+ inside and outside the liposome largely determine the starting voltage according to the Nernst equation $E = \frac{RT}{zF} \ln \frac{[Out]}{[In]}$, assuming that the liposome is not intrinsically leaky to other ions. In the equation, E is the driving electrical potential, R is the gas constant, T is the temperature in Kelvin, z is the charge of the permeant ion, F is the Faraday constant, and [Out] and [In] are the concentrations of the permeant ion inside and outside the liposome respectively.

In oocyte experiments, the membrane voltage is precisely and rapidly controlled by electrode clamping, leading to straightforward measurements of reversal potential. In liposomes, the starting voltage can be theoretically be altered by changing the relative concentration of K^+ inside and outside the liposomes in a series of experiments with changing internal and external buffers, while controlling for osmolarity effects. However, a more rapid estimate of proton selectivity in this system can be obtained without measuring a reversal potential, by performing the flux experiments in the absence of valinomycin.

In the K^+ in, Na^+ out liposome buffer system such as the one used in this work, one would expect a *perfectly* proton-selective protein to result in no internal pH change in the absence of

valinomycin if the internal and external buffer pH values are equal. A similar result would also be expected for a perfectly *non-selective* protein, since K^+ and Na^+ would dissolve in and out of the liposome with equal probability, creating no driving force for net proton translocation. However, in this latter case, there would also be minimal acidification in the presence of valinomycin, given the very large excess of Na^+ ions over H^+ (greater than 10^6 in this system).

Let us now consider what would happen if the protein of interest was also permeable to K^+ or Na^+ but not both to the same extent. If the protein also transported K^+ in addition to H^+, then in the absence of valinomycin, K^+ would leak out of the liposome down its concentration gradient (as it is likely that the orientation of the protein in the membrane is random). This would create a negative potential inside the liposome, drawing protons in and leading to acidification. If, by contrast, the protein transported Na^+ and H^+, then, without valinomycin, Na^+ would diffuse from the outside into the liposome interior down its concentration gradient, leading to an accumulation of excess positive charge inside the liposome, the extrusion of H^+, and a more basic intraliposomal pH.

Experiments without valinomycin at neutral pH on full length A/M2, synM2(19-62), synM2(22-50), synM2(22-46) all resulted in significant acidification of the liposome interior (data shown for A/M2 and synM2(22-46) in left panel of Figure 2.12), although in every case less than the extent of acidification with valinomycin. synM2(19-62) showed the smallest degree of acidification, while synM2(22-50) had the largest. Confirmatory experiments on synM2(22-46) where Na^+ was in the inside buffer and K^+ was in the outside buffer led more basic intraliposomal pH as expected (data not shown). This would suggest that all of the M2 constructs tested are also capable of transporting K^+, at first glance in possible contradiction with other evidence indicating that A/M2 is highly proton selective (Chizhmakov, Geraghty et al. 1996; Lin and Schroeder 2001).

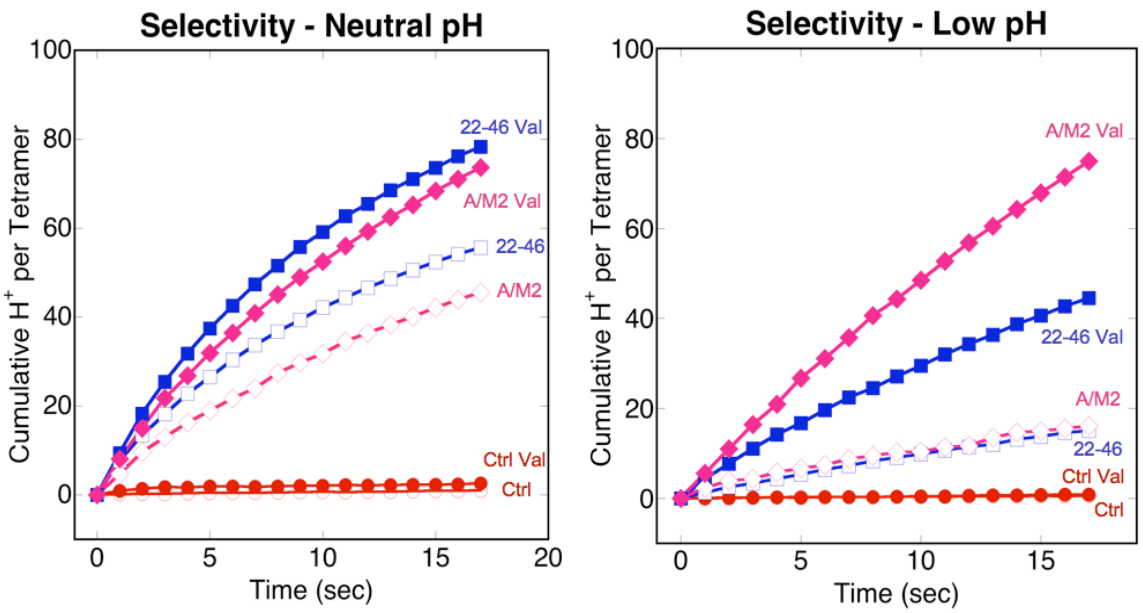

Figure 2.12. Probing selectivity of A/M2 and synM2(22-46) in proteoliposome system. Left panel: experiments with and without valinomycin, pHin and pHout ~ 7.4 Right panel, pH_{in} and pH_{out} ~ 6.5.

However, a more nuanced consideration of these findings has to take into account the very large excess of Na^+ and K^+ to H^+ in the experimental system at hand. The concentration of K^+ and Na^+ in the respective buffers and salts is ~120 mM, whereas at pH 7.4, the free proton concentration is $4x10^{-8}$, a difference of ~$3x10^6$ fold. Previous studies have determined the proton selectivity of A/M2 as approximately 10^6 fold (Chizhmakov, Geraghty et al. 1996; Lin and Schroeder 2001). Therefore, since the excess of non-proton cations to protons is in fact somewhat greater than the previously determined selectivity, the observed valinomycin-free are not inconsistent with the previously determined high proton selectivity of M2.

That the observed valinomycin-free current was due to the high excess of potassium to protons could be ascertained by decreasing the excess of Na^+ and K^+ to H^+ (e.g. by performing the measurement at somewhat lower pH). If the proton selectivity of M2 is high, then the ratio of

valinomycin-free proton flux (where passive leak of potassium drives liposome acidification) to proton flux with valinomycin (when protons are driven into the liposomes from an external potential) should be significantly lower when the proton concentration is higher. This hypothesis was tested on A/M2 and synM2(22-46), with both K^+ and Na^+ buffers now set at pH ~ 6.5.

As shown in the right panel of Figure 2.12, addition of valinomycin elicited proportionally larger inward proton currents through reconstituted A/M2 and synM2(22-46) at lower pH. Therefore, the results were consistent with high proton selectivities of A/M2 and the M2 TM peptide.

The final functional criterion that must be examined for validation of M2 transmembrane domain function is the pH_{out} activation of M2: inward currents increase in response to decreasing external pH (Chizhmakov, Geraghty et al. 1996). To this end, A/M2 and synM2(22-46) were reconstituted into proteoliposomes in K buffer at pH 7.4. The inward per-tetramer proton currents were measured with valinomycin upon dilution into Na buffer at pH 7.4, 7.0, 6.5, and 6.0. After subtraction of background current measured in protein-free liposomes under these conditions, the current ratios at the lower pH values vs. current at pH 7.4 for full length A/M2 and synM2(22-46) are plotted in Figure 2.13. Both A/M2 and the M2 TM peptide show a similar trend of increasing inward proton current with decreasing pH_{out}, indicating that the two have a similar pattern of pH_{out} activation.

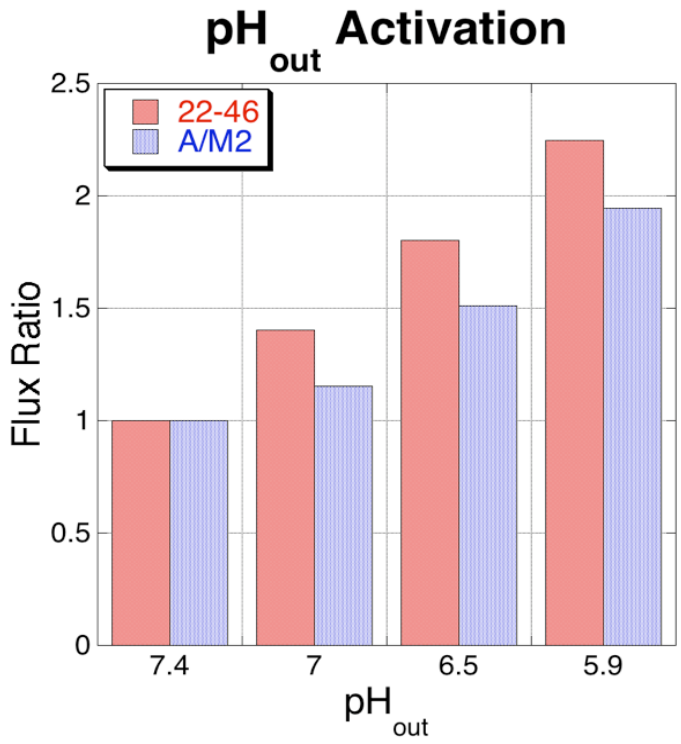

Figure 2.13. Activation of proton flux through A/M2 and synM2(22-46) by decreasing pHout. Current ratios are normalized to initial current at pH_{out} 7.4.

2.6. Comparison of pH-dependent thermodynamic stability of synM2(22-46) and A/M2.

As described in the introductory chapter, groundbreaking ssNMR experiments in bilayers established that the M2 TM peptide had unexpectedly high His 37 pK_a values (Hu, Fu et al. 2006), which are sure to play into any mechanistic model of proton transport through M2. However, no evidence of these perturbed pK_as has been obtained from the full length A/M2, or from any M2 constructs studied in micelles, as certain biophysical techniques favor or necessitate.

The ssNMR pH titration of synM2 22-46 showed that of the tetramer His 37 pK_a values (pK_a[1] through pK_a[4]); the first two, 8.2 and 8.2, were higher than that of the monomer (app. 6.5) (Salom, Hill et al. 2000), pK_a[3] was similar to that of the monomer at 6.3, and pK_a[4] was much

lower than that of the monomer at <5.0 (Hu, Fu et al. 2006). Thus, relative to the monomer, the tetramer has much greater affinity for binding the first two protons, approximately the same for the third and much lower affinity for the fourth. Because proton-binding and tetramerization are thermodynamically linked it therefore follows that the thermodynamic stability of the tetramer should peak when it is di- to tri-protonated (near pH 6 – 7), and that it should be destabilized as the pH is raised or lowered beyond this value. Although it might seem counterintuitive that protonation of two to three closely placed His residues buried in a membrane protein should stabilize the protein, this phenomenon is a consequence of thermodynamic coupling between ligand (proton) binding and its thermodynamic stability. Previously, the destabilization of tetrameric M2(22-46) at low pH has been well documented (Salom, Hill et al. 2000) by a circular dichroism spectroscopy assay in DPC micelles. Here, new work by Dr. Amanda Stouffer demonstrates that the stability reaches a maximum near pH 6.5, and falls off at higher pH. Furthermore, Amanda demonstrated that the full-length A/M2 shows a similar pH-dependence of tetramer stability in micelles; her findings are summarized below.

The stability between pH 6 and 9 of synM2(22-46) and A/M2 were determined by analytical ultracentrifugation as described previously (Stouffer, Nanda et al. 2005). The A/M2 construct used was a His-tagged A/72/Udorn sequence containing all the WT Cys residues and Trp at position 15, and was expressed and purified in a very similar fashion to the procedure provided in section 5.c of this chapter but with lower culture yields. synM2(22-46) was studied in dodecylphosphatidylcholine (DPC) micelles, chosen to allow comparison with previous studies (Stouffer, Nanda et al. 2005). However, full-length A/M2 shows a small degree of high-order aggregation in DPC (Kochendoerfer, Salom et al. 1999), which was alleviated by switching the detergent to C14-sulfobetaine whose lower critical micelle concentration allowed measurements over a larger range of protein/detergent ratios. The degree of association of M2 in micelles depends on the protein/detergent ratio so the tetramer-monomer dissociation constant (K_{app}) is expressed in units of MR^3 (MR is the mole ratio of peptide to detergent).

The pH dependence of M2 tetramerization involves multiple histidine protonation states in the monomeric and tetrameric forms of the protein. The observed equilibrium dissociation constant for tetramerization K_{obs} at a given pH is related to the corresponding dissociation constant (K_{tet}) for the tetramer observed at high pH by:

$$K_{obs} = \frac{[mon] + [mon \cdot H^+]}{[tet] + [tet \cdot H^+] + [tet \cdot H^+_2] + [tet \cdot H^+_3] + [tet \cdot H^+_4]}$$

$$K_{obs} = \frac{K_{tet}(1 + \frac{[H^+]}{K_{mon}})}{1 + \frac{[H^+]}{K(1)} + \frac{[H^+]^2}{K(1)K(2)} + \frac{[H^+]^3}{K(1)K(2)K(3)} + \frac{[H^+]^4}{K(1)K(2)K(3)K4)}}$$

in which K_{mon} is the equilibrium constant for protonation of the monomer, while K[1] through K[4] are for protonation of His37 in the tetramer. To allow the use of published acid dissociation constants (Hu, Fu et al. 2006), these were treated as ensemble averages as in previous work and were not corrected for statistical factors associated with the number of permutations of protonation states for a given charge state. Previously determined values of K[1] through K[4] were used in fitting curves to the data, leaving only the value of K_{tet} for synM2(22-46) or K_{tet} and K_{mon} for A/M2 as adjustable parameters.

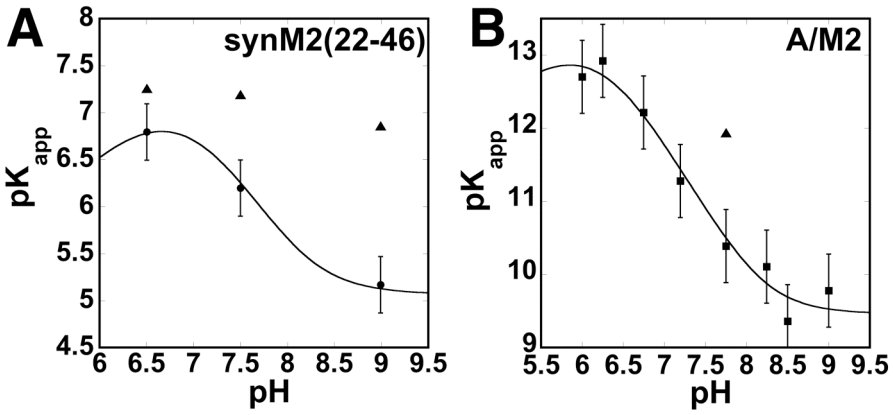

Figure 2.14. Thermodynamic stability of synM2(22-46) (panel A, circles) and full length A/M2 (panel B, squares) in micelles as a function of pH. Triangles indicate measurements in the presence of amantadine. The tetramer stability, plotted as the negative log of the tetramer-monomer dissociation constant, is shown to decrease with increasing pH above ~6-6.5. Lines indicate fits of a monomer-tetramer equilibrium model to the data using known, constrained values of tetramer (panel B) and monomer and tetramer pK_as (panel A). Figure published in (Ma, Polishchuk et al. 2009).

Plots of pK_{app} *vs.* pH for the TM peptide and full-length protein confirm that the tetramer strength reaches a maximum near pH 6.5 and decreases with increasing pH (Figure 2.14). The outstanding fit of the curve in Fig. 5A for synM2(22-46), which was generated using the literature values for pK_as of the monomer and tetramer (Salom, Hill et al. 2000; Hu, Fu et al. 2006), is most encouraging given that they were not treated as adjustable parameters. A more extensive set of data was collected for A/M2; the titration curve can again be fit using the pK_a values reported for tetrameric synM2(22-46). This finding confirms that the functionally relevant protonation behavior of His37 is constant over a range of fragment lengths and environments including both micelles and bilayers. The addition of amantadine to both synM2(22-46) and A/M2 shifts the equilibrium toward tetramers, as evidenced by an increase in pK_{app} (Figure 2.14). Consistent with previous findings (Wang, Takeuchi et al. 1993), the affinity of amantadine for the tetramer, which is reflected in the difference between the value of pK_{app} in the presence (▲) versus the absence (●) of amantadine (Salom, Hill et al. 2000), decreases with decreasing pH, indicating that the drug binds less strongly as the number of protons on His37 increases.

While the pH dependent assembly trends of synM2(22-46) and A/M2 are similar, the full-length protein is more thermodynamically stable at each pH studied. Part of the difference arises from reconstitution of A/M2 in C14-sulfobetaine, which favors the formation of tetramers by approximately an order of magnitude (relative to the DPC, the detergent used for the TM peptide).

In DPC the K_{app} at pH 7.5 of A/M2 and synM2(22-46) are 10^{-10} MR^3 *vs.* approximately $10^{-6.3}$ MR^3, respectively. These values indicate that A/M2 and synM2(22-46) are 50% dissociated at a peptide/DPC ratio of approximately 1/1700 (midpoint = $(2 \bullet K_{app})^{1/3}$) vs. 1/110 at this pH. Thus, by this measure, A/M2 is about 10 to 20-fold more stable than synM2(22-46), corresponding to approximately 1.6 kcal/mol of monomer.

In summary, Dr. Stouffer's analytical ultracentrifugation results and earlier work by Dr. David Salom (Salom, Hill et al. 2000) have shown that both A/M2 and synM2(22-46) in micelles also displayed the strongly perturbed pK_as of His37 observed in synM2(22-46) bilayers (Hu, Fu et al. 2006), demonstrating the conservation of functionally important properties over a range of constructs and solution conditions. Complementing the functional equivalency determined from liposome experiments and described in section 5, the evidence from this section indicates that pH-dependent protonation and assembly equilibria of these two constructs are also similar.

2.7. Conclusions: Validation of M2 TM peptide as a mechanistic model for full-length A/M2.

The evidence presented in this chapter definitively establishes the M2 transmembrane peptide as a model system for transport, protonation, and assembly of full-length A/M2. While oocyte experiments in the Pinto lab could not address the function of M2 TM because of poor expression of such a short construct on the oocyte surface, they showed that slightly longer constructs maintained key functional properties of the full length protein. In agreement with findings from the Pinto lab, proteoliposome flux experiments on full length A/M2 and intermediate fragments showed that all constructs were functional and sensitive to amantadine. Furthermore, results from proteoliposome assays showed that the transport rates, inhibition, ion selectivity and pH_{out} activation of the M2 TM peptide and full length A/M2 were very similar. This functional equivalence is further bolstered by thermodynamic analyses indicating a similar pH dependence of tetramer protonation and assembly in both micelles and bilayers. It is remarkable that a 25-residue peptide is capable of assembling into a ligand-activated proton transporter. The results of

biophysical studies in both micelle and bilayer systems on this functional core can now be merged with electrophysiological data on the full-length protein in pursuit of a unified transport mechanism. However, it should be kept in mind that as part of a multi-modular, multi-functional protein, non-transmembrane sections of M2 are nevertheless important for its non-transport functions in the viral life cycle (Chen, Leser et al. 2008).

Chapter 3: A high-resolution structure of the M2 transmembrane domain yields insights into proton transport pathway and conduction mechanism

3.1. Membrane protein structure determination – a still-daunting task.

While integral membrane proteins are the products of approximately one-third of known genes, the determination of their high-resolution structures continues to be a daunting task. The count of unique high-resolution membrane protein structures was only in the ~200 range as of 2009, according to one commonly used database (White). A telling analysis involves comparing the number of cumulative new structures solved vs. time for water soluble proteins (starting in 1960) and for membrane proteins (starting in 1985). When the temporal "head start" granted to water soluble proteins is removed and the two curves are synchronized at a single time point, it is clear that progress on membrane protein structural determination is being attained at a significantly slower rate (White 2004). As discussed in greater detail in the introduction, this finding is not surprising, since membrane protein structure determination adds substantial roadblocks: exceptional care must be taken to preserve protein function when extracting it from the source, bilayer mimetics such as detergent micelles must be used to generate crystals or allow for tractable NMR conditions, and high-quality crystals are difficult to obtain since detergent-solvated transmembrane domains rarely form favorable crystal contacts.

This problem becomes even more difficult for smaller membrane proteins or isolated transmembrane peptides. Many membrane protein crystals are stabilized by contacts formed by their water-soluble, extramembrane domains. In fact, successful approaches to ion channel crystallization have often relied on co-crystallizing the proteins with antibody fragments targeting their soluble domains in efforts to both stabilize their structure and increase their water-soluble crystal-packing "footprint" (Dutzler, Campbell et al. 2003; Jiang, Lee et al. 2003). For

transmembrane peptides lacking water-soluble sequences of significant length, the problem becomes even more pronounced. In fact, very few structures of such peptides exist, and most have been determined by solution NMR in micelles or bicelles at more modest resolution (MacKenzie, Prestegard et al. 1997; Arora, Abildgaard et al. 2001; Bocharov, Mineev et al. 2008). While antibodies are available to the N-terminal ectodomain of M2, this domain is intrinsically disordered (as discussed in Chapter 2). Furthermore, there is a substantial stretch of non-structured sequence between commonly targeted antibody epitopes (Zhang, Zharikova et al. 2006) and the well structured transmembrane domain, indicating that applying the antibody strategy to M2 crystallization would likely be difficult.

The DeGrado laboratory has been pursuing the high-resolution 3D structure of the M2 transmembrane domain since the late 1990s. While quality crystals of M2 TM (22-46) were obtained quite early on in the process, they tended to be anisotropic with weaker diffraction along the transmembrane "z" axis. Furthermore, phasing the collected crystallographic data sets presented a major bottleneck. Various approaches were attempted by previous lab members, including MAD (multiple anomalous diffraction) phasing *via* selenomethionine-derivatized peptides or NaBr soaked native peptide crystals. While anomalous diffraction signals were obtained from these constructs, the anomalously scattering heavy atoms could not be reliably located, most likely because of radiation damage, oxidation, or disordered packing. The crystallization work described below was started and well-diffracting crystals were obtained before any high resolution M2 structures became available. While the resulting data sets were solved after the initial X-ray and NMR structures were published (Schnell and Chou 2008; Stouffer, Acharya et al. 2008), the new structure described below is of substantially improved resolution, and represents not only a major advance in our understanding of proton transport by M2, but also sheds light on a new mechanism used by Nature to stabilize large amounts of electric charge in a small, subnanometer environment.

3.2. Toward better packed crystals: using bromophenyl-derivatized peptides.

To improve packing of M2 transmembrane peptide tetramers in the crystal lattice, we introduced an N-terminal 4-bromophenyl group on the M2 transmembrane helix. The reasons for this were three-fold: the electron-rich bromophenyl ring would stabilize the transmembrane helix dipole by "capping" the helix with an electronegative group, the bromine atom on the bromophenyl group is known for strong anomalous scattering and could be used for multiwavelength anomalous diffraction (MAD) phasing, and the electronegative N-terminal bromophenyl ring could interact with C-terminal positively charged residues (e.g. Arg 45) on vertically adjacent M2 tetramers to provide crystal contacts in the "z" direction and lead to thicker, better diffracting, less anisotropic crystals. The desired effect is shown in Figure 3.1.

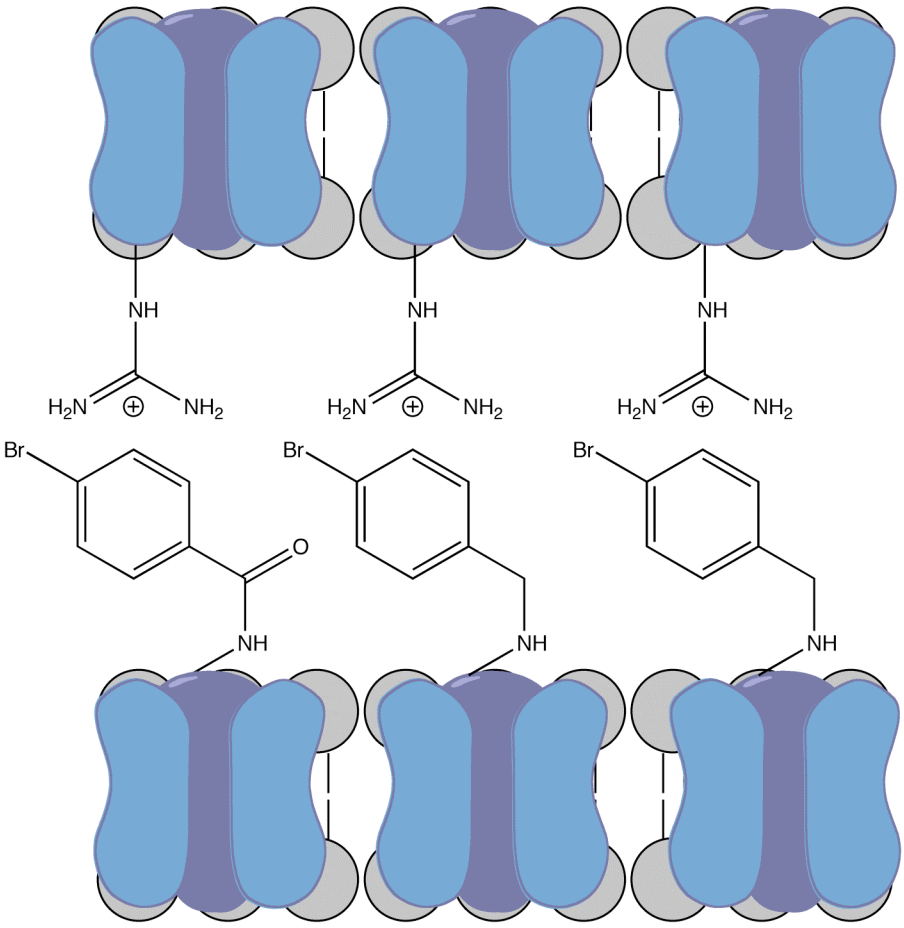

Figure 3.1. Engineering a cation-π interaction to stabilize crystal packing of M2 transmembrane peptide constructs.

To this end, constructs of two different lengths were synthesized and capped with 4-bromobenzoic acid on the N-terminus. Both constructs, M2 25-46 (M2TM') and M2 24-46 (M2TM' + 1), were a few residues shorter than the usual M2 TM peptide (22-46), but both encompassed the predicted transmembrane helical segment of M2 (residues 25-43). Both peptides in the initial trials had a G34A mutation, which in other constructs tested in the lab led to faster crystallization (a few months vs. a year), thus the sequences made were as follows:

M2TM' G34A
4-bromobenzoyl-PLVVAASIIAILHLILWILDRL-$CONH_2$

M2TM'+1 G34A
4-bromobenzoyl-DPLVVAASIIAILHLILWILDRL-$CONH_2$

The peptides were synthesized as C-terminal amides using strandard Fmoc chemistry methods either on an Applied Biosystems (Foster City, CA) 433A or on a Protein Technologies (Tucson, AZ) Symphony synthesizer as previously described (Stouffer, Acharya et al. 2008). For subsequent crystallization trials, the corresponding wild type M2TM' (25-46) G34 peptide, was also made in a similar fashion.

Following the addition and deprotection of the most N-terminal amino acid, 4-bromobenzoic acid (Sigma Aldrich, St. Louis, MO) was coupled to the amino terminus of the peptide on resin in N,N-dimethylformamide. The product was cleaved from the resin and purified as previously described to achieve a very high level of purity (98-99% or better) (Stouffer, Acharya et al. 2008). Purity was verified with analytical RP-HPLC and MALDI-TOF mass spectrometry.

To make aliquots for crystallization, peptide and n-octylglucoside (OG, Sigma Aldrich) were mixed in an aqueous:isopropanol (1:1) stock using ε_{280}peptide = 5853 M^{-1} cm^{-1}. To attempt co-

crystallization with inhibitor, amantadine HCl was added to the peptide-octylglucoside mixture. The mixture was evaporated under reduced pressure in an Eppendorf tube. The resulting film was dried on a lyophilizer, then taken up in 5% (w/v) xylitol and mixed with precipitant for crystallization trials. In some cases, the reconstituted peptide-detergent mixture was filtered prior to crystallization.

3.3. Crystallization trials of bromophenyl-derivatized peptides.

A wide array of crystallization conditions was sampled for the two bromophenyl-derivatized G34A (M2TM' and M2TM'+1) constructs. From experience of other lab members, the detergent octylglucoside was found to be effective in facilitating M2 TM crystal growth; thus this detergent was used as a first choice for the crystallization of the new M2TM' constructs. In the final reconstituted mix, the target concentration of M2TM' monomer was 0.8 mM; amantadine, if used, was added to a final concentration of 0.6 mM. A number of octylglucoside concentrations were employed, generally ranging from 1:25-1:45 peptide monomer:octylglucoside. Crystals were grown using the hanging drop method by mixing 1 μL of well solution with 1 μL of peptide:detergent stock; the well solution volume was 750 μL. Crystallization experiments were maintained at or slightly below ambient temperature.

From prior experience of other lab members, crystallization of the longer M2 TM was often facilitated using transition metal containing precipitant solutions (e.g. Mg, Co, Ni) along with polyethylene glycol and Tris buffer at moderately basic pH. However, these trials did not lead to high-quality crystals of the M2TM' constructs, indicating that successful crystallization conditions are extremely fragment-specific.

Sparse matrix screens, such as the Hampton Research (Aliso Viejo, CA) MembFac were also tested with the M2TM' and M2TM'+1 constructs. While no hits were obtained with M2TM' + 1 G34A, crude crystals of M2TM' G34A formed fairly rapidly (within a few weeks) in a number of

conditions. The best looking crystals were obtained out of condition #14, a mixture of sodium citrate and isopropanol at an overall pH of ~ 6.4. These were densely packed, multifaceted rock-like crystals that were not yet of diffraction quality.

Expansion of the citrate/isopropanol screen on M2TM' G34A generated crystals of improved appearance. Initially, fuzzy sphere-like precipitates formed, that eventually developed surface spicules which grew in size to thin, flat plates, that occasionally separated from the spherical centers. These plates were often difficult to cleanly isolate and were quite thin, but diffracted to a resolution limit of 3-4 Å on a home source CuKα X-ray generator.

Further attempts to improve crystal thickness and diffraction quality involved replacement of the isopropanol component of the well solution with ethanol, variation of the peptide:detergent ratio, and the addition of small amounts of other sparse matrix screen conditions to the citrate-isopropanol mixture that previously yielded the best results.

Thicker crystals of M2TM' G34A that diffracted to ~2.5Å on the home source generator were obtained from drops containing 0.8 mM M2TM' G34A peptide (as monomer), 28mM OG and 5% xylitol, mixed in the ratio of 1:1 with a reservoir solution mixture of 95% [100mM sodium citrate pH 5.6, 150mM tri-sodium citrate, 15% v/v isopropanol] and 5% [0.2M MgCl2 $6H_2O$, 0.1M Tris-hydrochloride pH 8.5, 30% w/v Polyethlene glycol 4000]. Crystals appeared in two weks, and were grown over a period of 2-5 months. Cryoprotection was effectively achieved by briefly immersing the crystals in 2-methyl-2,4-pentanediol (MPD).

For M2TM' G34, reconstituted similarly to M2TM' G34A, the best crystals were obtained from a precipitant solution of 100 mM sodium citrate pH 5.6, 100mM tri-sodium citrate, and 15% v/v isopropanol. M2TM' G34 crystals grew much more slowly, appearing after 5 months, and were

grown for an additional two months. These crystals were much smaller than those of M2TM' G34A and diffracted to a lower resolution. MPD was again used for cryoprotection.

3.4. Data collection and processing.

Many data sets were collected from several crystals of M2TM' G34A, with cryo-cooling to 100K during data collection. These include MAD data sets recorded at synchrotron beam lines (NSLS, Brookhaven, NY, USA) and data sets collected at a University of Pennsylvania home source. Data were collected by the author, and Drs. Steven Stayrook and Rudresh Acharya. The crystals were usually found to diffract to a maximum resolution of 2.6–1.65 Å. The diffraction images were indexed, integrated using MOSFLM (Leslie 1999; Powell 1999) and scaled using SCALA (Evans 2006). Table 3.2 shows the data collection statistics for the data sets (1.65 Å) used in the refinement.

Diffraction data sets for M2TM' G34 crystals were collected at synchrotron beam line X29 (NSLS, Brookhaven, NY, USA) by the author and Dr. Rudresh Acharya. The data sets could be processed up to ~68% completeness and were found to belong to the same unit cell as M2TM' G34A data sets (Table 3.2).

Data collection and processing	M2TM'G34A	M2TM'G34
Space group	$C222_1$	$C222_1$
Cell dimension a, b, c (Å)	48.67, 79.09, 48.56	48.74, 77.860, 48.61
Resolution (Å)	48.6-1.65(1.75-1.65)[1]	41.3-2.50 (2.64-2.5)
Rmerge	0.070 (0.45)	0.098(0.344)
I/σ(I)	19.4 (2.7)	7.1(2.3)
Completeness (%)	99.5 (96.6)	67.5(70.9)
Multiplicity	6.6 (4.5)	2.8(2.7)
Total number of (observation/unique)	76869/11567	6174/2230
Refinement		
Resolution (Å)	31.5-1.65	41.3-2.5
Number of reflections	10998	2130
R_{work}/R_{free}	0.196/0.205	0.299/0.333
Number of atoms		
Proteins	732[2]	728
Ligand/ion	31	0
Waters	25	0
B-factors (Å^2)		
Proteins	13.7	13.2
Ligand/ion	48.4	
Waters	24.9	
R.M.S. deviation		
Bond lengths (Å)	0.007	
Bond angle (°)	0.879	
Ramachandran plot		
Residues in Most favorable region (%) Additional allowed region (%) Generously allowed region (%)	 100.0 0.0 0.0	 100.0 0.0 0.0

[1]Highest resolution shell is shown in parenthesis.
[2]Including Bromo benzoyl group.
[3]$R_{work} = \Sigma \, ||F_{obs}|-|F_{calc}|| / \Sigma |F_{obs}|$ where F_{obs} and F_{calc} are calculated observed and calculated structure factor amplitudes respectively, R_{free} was calculated as R_{work} using 5.0% of the randomly selected unique reflections that were not included in the structure refinement.

Table 3.2. Statistics from data collection and structure determination of M2TM' G34A and M2TM'.

3.5. Structure determination, model building, and refinement of M2TM'.

Initial attempts to phase M2TM' G34A data sets using multiwavelength anomalous diffraction were unsuccessful. While a strong bromine signal was detected in an EXAFS experiment on M2TM' crystals, indicating the presence of the anomalously diffracting heavy atom, the location of the bromine atoms in the unit cell could not be reliably determined presumably because of disorder or radiation damage.

Following the successful solution of earlier M2 TM data sets from our laboratory using a molecular replacement approach based on the structure of a monomeric M2 TM helix (Stouffer, Acharya et al. 2008), Dr. Rudresh Acharya attempted to solve the M2TM' G34A data sets using molecular replacement with the newly solved M2 TM structure as a model. His successful approach to determine the structure of M2TM' G34A is described below.

Since initial attempts at molecular replacement using a single alpha-helix or tetramers from a previously solved structure (PDB code 3BKD) (Stouffer, Acharya et al. 2008) as model probes did not yield the structure solution, a more nuanced approach to model construction was pursued. By comparison of cell dimensions, it was intuitive to notice that helices forming the tetramer are more closely packed in the present data sets than those in 3BKD. Whereas in 3BKD (with cell dimensions *a* = 38.753 Å, *b* = 56.557 Å and *c* = 56.009Å), helices are oriented along the **a** crystallographic axis, and two tetramers lie in the **bc** plane, in the present data sets (Table 3.2), tetramer(s) lie(s) in the **ac** plane with helices oriented along the **b** axis. Based on this packing knowledge, tetramer models were generated to use as model probes in molecular replacement.

*Tetramer model generation***.** Using one of the helices of the previously published 2.0 Å resolution structure (3BKD, chain 'A'), tetramer models were generated with various helical orientations; -

30º < Xangle < -20º, 7º < Yangle < 10º, 160º < Zangle < 190º and radius of bundle 6.8 < r < 8.0 Å, where Xangle, Yangle and Zangle represents the angle formed by the helix with the X-axis, Y-axis and Z-axis respectively. During tetramer generation, the helix oriented along the Z-axis was first rotated around the Z-axis (Zangle), then about the X-axis (Xangle) and then about the Y-axis (Yangle). For this orientated helix, four copies were created by applying four fold symmetry along the Z- axis and each copy was translated to a radius distance in four fold symmetry on an XY-plane.

Among tetramer models generated as described above, only those models having orientation of Val27 close to that in the 3BKD structure were considered for molecular replacement calculations. The molecular replacement calculations were performed using the program PHASER (Read 2001; McCoy, Grosse-Kunstleve et al. 2005) for data in the resolution range of 15-4.0 Å. The data sets used for initial phasing were processed in the space group $P2_1$ with cell parameters *a* = 46.41 Å, *b* = 48.52 Å, *c* = 46.27 Å and β = 116.97° and were collected at the home source to a resolution limit of 2.6 Å. The Matthews coefficient (Matthews 1968) (Vm = 2.3 $Å^3$/Da) indicated the presence of two tetramers in the asymmetric unit. Initially molecular replacement calculations were performed using bundles with parameters: radius 8.0 Å, 7.5 Å [-26° (Xangle), 10° (Yangle), 160°-190° (Zangle)] and later, models were randomly selected for the calculations. In evaluating model quality during calculations, importance was given to recognizing an interpretable electron density map. In general, the resulting maps were not good, but the model with Xangle = -24°, Yangle = 10°, Zangle = 167°, and radius 7.0 Å had a very clear density for a dimer. The dimer was used as a model and two tetramers were located in the asymmetric unit, resulting in an excellent electron density map.

Of several M2TM' G34A crystals tested for diffraction at the synchrotron beam line (NSLS, X6A), a crystal belonging to the space group $C222_1$ with cell parameters *a* = 48.67 Å *b* = 79.09 Å and *c* = 48.56 Å was found to diffract to a maximum resolution of 1.65 Å. With the possibility of a

tetramer in the asymmetric unit as suggested by the Matthews coefficient (Vm = 2.4 $Å^3$/Da), the structure was solved by the molecular replacement technique using one of the above-determined tetramers as a model. Iterative refinement and model building were carried out, during which all side chains could be traced in the electron density map. As the refinement progressed water molecules were located in the map. When the refinement had converged, the model was refined to R_{work} = 19.7% and R_{free} = 20.5% (Table 3.2), with all the residues in allowed regions (100% favorable) of the Ramachandran plot. Details of refinement statistics are shown in Table 3.2. The refinement was carried out using the CCP4 program suite (Collaborative Computational Project 1994) (REFMAC) (Murshudov, Vagin et al. 1997) and all model building was done using COOT (Emsley and Cowtan 2004).

In general, solvent molecules were included only if they were visible at the 3σ level in an F_O–F_C map. All were found in full occupancy with the exception of the Br atoms in the bromobenzoyl group, which were disordered, presumably due to radiation damage. The dimer of water molecules in the outer cluster (in a region of the pore slightly N-terminal to His 37, described as the "MPSC" in the discussion below) had two alternate conformations that refined with occupancies of 0.6 and 0.4.

3.6. Comparison of M2TM' X-ray diffraction data: G34A and G34.

To assess the similarity between the structure of M2TM' G34A and M2TM' G34, the partial dataset from crystals of M2TM' G34 was submitted to molecular replacement using the structure of M2TM' G34A. A satisfactory solution (R_{cryst} = 0.41, CC = 0.65 (polyala)) was obtained, resulting in a map of good quality with clearly visible density at the location of the amino acid sidechains mutated to Ala in the model. In a second trial, initial rigid-body refinement of the M2TM' G34 dataset using the structure of M2TM' G34A with the Ala methyl and all solvent molecules removed led to a satisfactory initial solution (Table 3.2) with an interpretable density map showing density attributable to water in e.g. the area of the pore just N-terminal to His 37.

These findings strongly suggest that the overall structures are very similar, although it would be inappropriate to fully refine the structure of M2TM' G34 without collecting more complete data.

3.7. The high-resolution structure of M2TM': backbone conformation.

M2TM' G34A (from here on referred to as M2TM') was crystallized at pH ~ 6.5, under conditions more acidic than those of the solution NMR structure (pH 7.5-8) and likely more basic than the earlier, lower resolution X-ray crystal structures (the apo form M2 TM was crystallized with starting buffer near pH ~ 7, but due to the presence of transition metal ions in the precipitant buffer and the long time to crystal appearance, the exact pH of crystallization is unknown and likely lower; the lower-resolution drug-bound structure was crystallized with starting buffer near pH ~ 5 but similarly uncertain). Not surprisingly, the backbone conformation of M2TM' is intermediate between the solution NMR and previous crystal structures. The backbone of the C-terminal segment of the M2TM' helical bundle is almost completely superimposable on the solution NMR structure; whereas the N-terminal portion of the helices is more kinked in the crystal structure and more straight in the NMR structure (Figure 3.3). Overall, the Cα RMSD between the two structures is a low 1.4 Å. By contrast, in the lower resolution low-pH M2 TM crystal structure (starting buffer near pH ~ 5), the backbone helices once again straighten out, but now at a similar angle to the kinked N-terminal section of the pH 6.5 M2TM'. The low pH structure resembles a teepee or a cone, and the kinked conformation of the new, intermediate pH structure, forms a bridging intermediate conformation state between the high and the low pH forms, consistent with the proposed conformational changes in the M2 activation and transport mechanism (Stouffer, Acharya et al. 2008; Khurana, Dal Peraro et al. 2009).

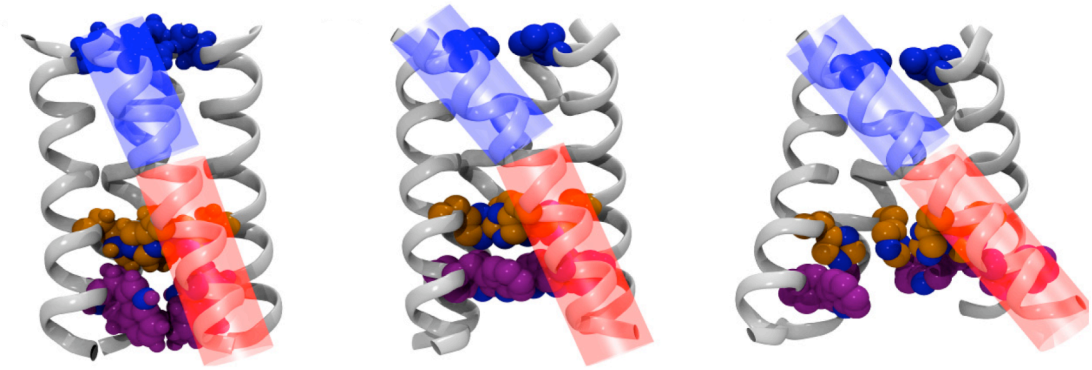

Figure 3.3. Comparison of the backbone and key sidechain structures of M2 obtained at different pH values. Left panel: solution NMR, pH 7.5-8 (PDB ID: 2RLF); middle panel: M2TM' X-ray; pH 6.5, right panel: M2TM X-ray pH ~5.3 (PDB ID: 3C9J). Val 27 sidechains are in blue, His 37 sidechains are in orange, Trp 41 sidechains are in purple.

3.8. The high-resolution structure of M2TM': structure of the aqueous pore.

M2TM' assembles into a nearly symmetrical helical bundle, structurally similar to previous lower-resolution models (Pinto, Dieckmann et al. 1997; Tian, Gao et al. 2003; Hu, Asbury et al. 2007; Schnell and Chou 2008; Stouffer, Acharya et al. 2008). However, the significantly greater resolution now shows that the pore is formed by five layers of sidechains and three intercalated water clusters stacked to form a continuous conduction pathway (Fig 3.4). Representative electron density maps are shown in Appendix A.

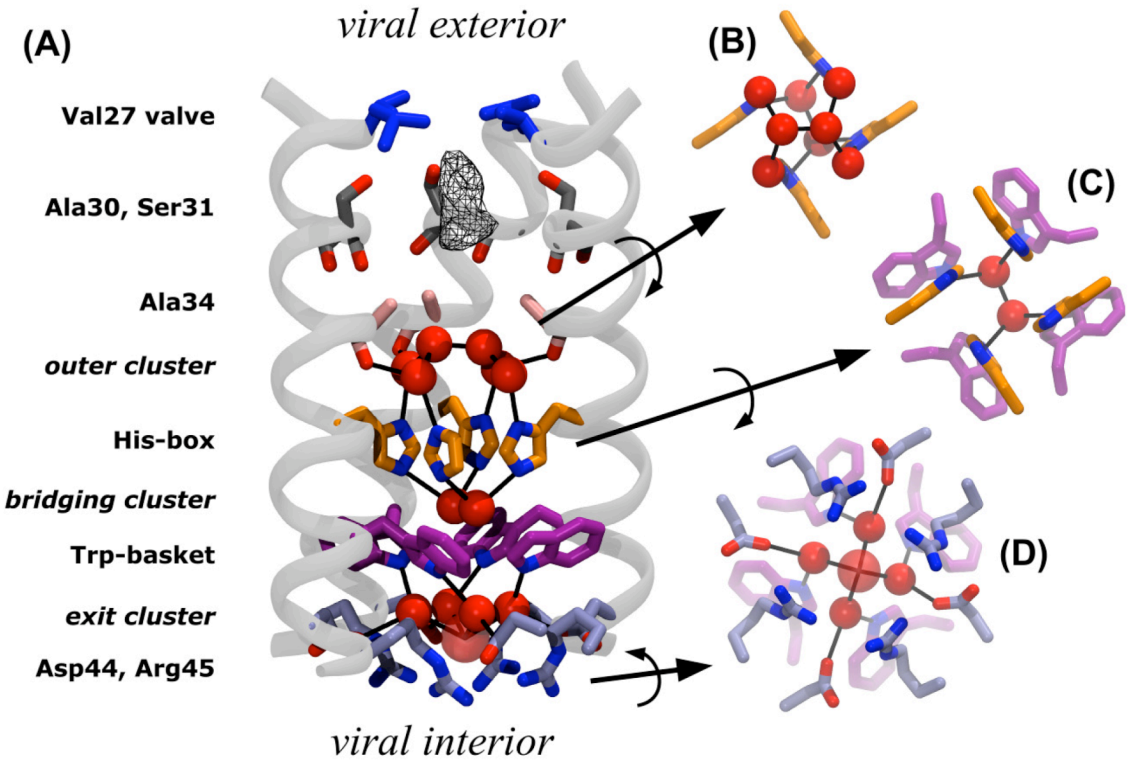

Figure 3.4. Pore lining residues and water molecules define the proton conduction pathway (A) in a new high-resolution structure of the M2 transmembrane segment. Key portions include a His box with an N-terminal water cluster (B), a Trp basket with a bridging water cluster (C), and an exit water cluster lined by Asp and Arg sidechains (D).

The outermost or "top" layer of side chains is composed by the four Val 27 residues, which form a nearly closed *Val 27 valve* (2 Å pore radius), leading to a central pore lined by small residues, Ala 30, Ser 31, and Gly/Ala 34. The conduction pathway is next interrupted by the His 37 residues (forming what we term a *His-box*, similar to aromatic boxes, but smaller in cross-section due to the smaller size of the imidazole ring). The His-box needs to expand only slightly (1-2 Å) to allow passage of a water-sized molecule. Below this motif the sidechains of Trp 41 form a basket (*Trp-basket*) with the aromatic rings angled by approximately 45° relative to the bundle axis. In a key difference, the Trp sidechains assume a different rotameric state compared to the high pH solution NMR structure. In the crystal structure, the indole nitrogens point into the pore as

opposed to the benzenoid portion of the indole ring in the NMR structure (Schnell and Chou 2008). The other lower-resolution crystal structures, likely corresponding to lower pH conformations, also have the indole nitrogen facing into the pore (Stouffer, Acharya et al. 2008). Finally, Asp 44 and Arg 45 line an *Asp/Arg box*, defining the cytoplasmic end of the channel. The planar faces of the guanidino groups of Arg 45 form a 7 to 8 Å box stabilized at the corners by interaction with an oxygen atom of Asp 44, confirming the Asp-Arg salt bridge seen in the NMR structure and in the predicted high pH forms of lower-resolution crystallographic models; the salt bridge is broken in the low-pH crystal forms. While the electron density for the Asp 44 residues is very well-defined, the Arg45 sidechains have higher Debye-Waller factors, suggestive of greater conformational mobility.

Right below the Val 27 valve is a region of diffuse density, indicative of dynamically or statically disordered solvent (Figure 3.4 A); beyond this point, the remainder of the pore is filled by three well-ordered water layers. Above the His-box is an *outer cluster* of 6 waters (Figure 3.4 A,B) that consists of a tight water dimer (O – O distance 2.4 Å) atop four waters, which in turn are H-bonded to the Nδ of His37 and the backbone carbonyl of residue 34. In the following, we refer to the outer cluster and the His-box together as the *"multi-proton storage" cluster* (MPSC). Connecting the His-box and Trp- basket is the *His 37/Trp 41 bridging cluster* of 2 waters (Figure 3.4 A,C), which H-bonds to the Nε of each His 37 residue. This dimer is well positioned to mediate a π-cation interaction (Okada, Miura et al. 2001) between charged His 37 residues and the electron-rich faces of Trp 41 residues. Finally, the *exit cluster* (Figure 3.4 A,D) consists of four waters that form H-bonds connecting the indole NH of Trp 41 to a carboxylate O of Asp 44. A fifth, poorly ordered solvent molecule (presumably water) lies below these four waters, displaced towards the interior of the virus. Throughout the structure, the four-fold symmetry is broken only by the water dimer found in the outer cluster and the His 37/Trp 41 bridging cluster (Figure 3.4 B,C). No counterion was detected in the structure, although the density in the central pore around Ala 30 and Ser 31, as well as the fifth solvent in the exit cluster is sufficiently diffuse that it

would be difficult to unambiguously rule out disordered chloride ions with partial occupancy at these positions.

In summary, the pore of M2TM' is populated by water molecules stably H-bonded to the protein, starting below the Val 27 valve, extending through the MPSC, and broken only at the π-face of Trp 41, near the interior of the virus. We next asked how charge is stabilized within the MPSC, as well as how passage of protons is allowed through the Val27 and Trp41 constriction regions.

3.9. Structure of M2TM' represents 2+ protonation state.

To draw the correct conclusions from the newly discovered water clusters in the structure of M2TM', it was important to determine the charge state of His 37 tetrad that the structure represents. Based on the two-fold symmetry of the water clusters, the most likely state was one of even protonation (0+, 2+ or 4+). As the crystals grew quite rapidly from a concentrated buffer at pH ~6.5, comparison to the experimental pK_a values determined by Cross *et al*. (Hu, Fu et al. 2006) indicated that the structure should represent the 2+ state, though quite near to the pK_a (6.3) for the 3rd proton. Theoretical analysis of the structure by our collaborators in the Klein lab, including quantum-chemical calculations of the magnetic shieldings of the MPSC in the 2+ and 3+ state, and classical simulations of the structure of the water cluster, showed that the state with two histidines with unprotonated Nδ and two doubly protonated histidines (each with a single positive charge) contributes most to the present structure. This is once again consistent with the backbone conformation, which is intermediate between the previously determined high-pH NMR (Schnell and Chou 2008) and low-pH crystal structures (Stouffer, Ma et al. 2008) (Figure 3.3).

3.10. Quantum mechanical simulations of MPSC suggest mechanism for charge stabilization in high protonation states.

It is remarkable that two to three His37 residues can be stably charged at near neutral pH, despite their mutual proximity in a region of presumably low dielectric. Indeed, Poisson-Boltzmann (Dutzler, Campbell et al.) calculations (performed by our collaborators in the Klein lab) on M2TM' embedded in a hydrophobic bilayer and a continuum solvent predict that the first three pK_a's are 7.0, 4.2, and 1.7 respectively, *vs.* the experimentally obtained pK_a values of 8.2, 8.2, and 6.3 (Hu, Fu et al. 2006). Thus, the product of the first two experimentally determined proton dissociation constants differs from the PB estimate by 10^5, indicating the need to consider proton mobility and protein polarization, absent in the PB method. The Klein lab therefore used quantum mechanical (QM) and quantum mechanical/molecular mechanical (QM/MM) methods to examine how the MPSC in the crystal structure is able to stabilize the 1+ and 2+ states and accept a third proton. Like a previous empirical valence bond study of a model structure (Smondyrev and Voth 2002), the QM/MM approach allowed them to examine the diffusion of the protons themselves, which cannot be treated with force-field based molecular mechanics (MM) models.

It is reasonable to suspect that the first and second protons accepted by the MPSC bind to histidine residues, and indeed geometry optimizations performed by the Klein lab at the QM/MM level of theory show that these structures are stable. However, the structure of the outer water cluster (Figure 3.4 A,B) suggests that a simple configuration with three charged His residues may not be the only significantly populated configuration of the 3+ state of the MPSC. In particular, this structure bears an intriguing resemblance to one of the preferred conformations of a $H^+(H_2O)_6$ cluster, in which the excess proton is shared by the two central water molecules in a barrierless fashion (Headrick, Diken et al. 2005). To gain further insight into this issue the Klein group carried out a QM/MM simulation of the 2+ state with a third excess proton moving along a Grotthuss hopping path across one of the C2 symmetry-related halves of the MPSC.

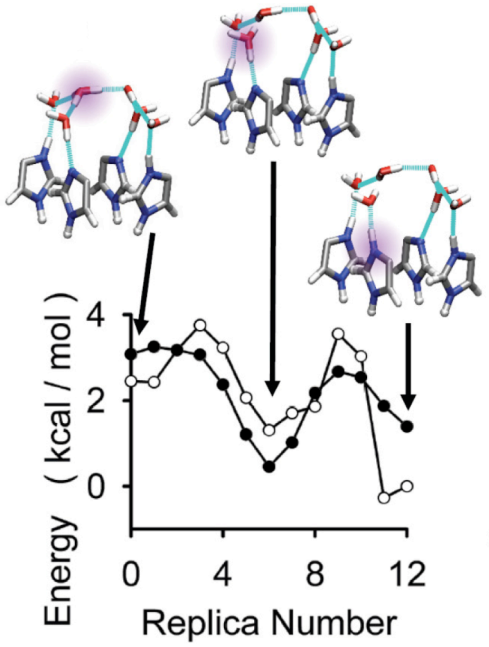

Figure 3.5. Energetics of proton transfer across the MPSC. (A) The potential energy surface for one possible proton transfer pathway is calculated using an MP2 model of the MPSC (filled circles) and a QM/MM model of M2TM' (empty circles). The MP2 model included the MPSC, the Ala34-Ile35 peptide groups, the bridging cluster below the His-box, and one additional water molecule above the MPSC (so that a complete solvation shell is included for any position of the hydronium). The QM/MM model extended the MP2 model by including the entire peptide tetramer, lipid, and solvent environment at the MM level of theory. All of the Nε atoms, and the Nδ of 2nonadjacent histidines are protonated. We added an extra proton at three different positions (modeling a Grotthuss hopping path from a central water to a nearby water and then to a histidine), and optimized these 3 structures and interpolated 10 intermediate structures. The state with the hydronium adjacent to a neutral histidine (replica 6) is stabilized by two nearby large dipole groups: the Ala34-Ile35 peptide group and the neutral histidine.

The resulting energy profile (Figure 3.5) encompasses two proton transfer events (the first

between two water molecules; the second from a water molecule to a His residue), and exhibits low barriers for proton transport, similar to those in bulk water. A first calculation was performed at the MP2/cc-pvdz level of theory for a cluster system. The resulting surface (Figure 3.5, filled circles) spans an energy range of 3 kcal/mol, with a maximum barrier of 3 kcal/mol, suggesting a fast diffusion of protons across the water molecules of the cluster. Particularly noteworthy is the unexpectedly low energy of the state in which a hydronium is located adjacent to the neutral His, which is attributed to the local electrostatic environment. The dipoles stabilizing the cation (the His 37 side chain and the peptide group of Ala 34-Ile 35) are even larger than those provided by H-bonded water molecules, which themselves stabilize a hydronium state by tens of kcal/mol (Lill and Helms 2001). A second source of stabilization is that the positive charge keeps a distance of ~5.5 Å from the histidine bound protons when bound to this water. This is about halfway between a purely His-bound 3+ state (4.5 Å) and the 2+ state (6.5 Å diagonal distance between His residues).

The inclusion of the remainder of the protein-lipid-water environment may alter the stability of the hydronium states relative to the His-bound ones. The Klein lab examined this effect by calculating a QM/MM model based on a DFT-BLYP (quantum mechanical) description of the MPSC and its surrounding area (the Ala34-Ile35 peptide groups, the bridging cluster below the His-box, and one additional water molecule above the MPSC) and the rest of the peptide tetramer, lipid and solvent at the MM (molecular mechanical) level of theory, which predicted a total energy drop of 2 kcal/mol over the course of the path (Figure 3.5, empty circles). However, the barriers were not greatly affected and were never higher than 4 kcal/mol. Furthermore, additional room temperature QM/MM MD simulations performed by the Klein lab support the prediction of fast proton transport kinetics: during a total of 60 ps of simulated time, many proton transfer events were observed, both between water molecules and from a water molecule to a neutral His (Appendix B). Consistent with the QM/MM energies, no jumps were observed from the His residues to the water cluster on the timescale of the simulations.

Thus, state of the art computational analysis of the His 37 sidechains, the N-terminal water cluster (the multi-proton storage cluster) and the surrounding areas provides a structural and physical explanation for the unusually perturbed pK_a values previously recorded in ssNMR experiments (Hu, Fu et al. 2006) with, the emerging detailed structural being more complex than the imidazole-imidazolium dimers proposed in the ssNMR study. Based on the crystal structure and QM modeling, the ordered water molecules forming the multi-proton storage cluster delocalize protons incoming toward the 2+ state in a nearly barrierless fashion, providing increased entropic terms underlying the unexpected energetic ease with which these excess protons bind, and giving further credence to mechanistic hypotheses where the slow, rate-determining step of proton transport is deprotonation. As will be discussed in the next section, classical simulations show an additional mechanism for charge stabilization in M2TM' by the means of reorienting water dipoles. In summary, the highly tuned arrangement of the His 37 box and the MPSC water cluster form an unprecedented system that stabilizes bound protons by as many as five orders of magnitude. It is perhaps not surprising that this very simple yet remarkably effective nanodevice for charge storage is found in one of the smallest yet most fascinating membrane transport proteins known to date.

3.11. Modulation of pore water dipoles may contribute to charge stabilization and unidirectional transport by A/M2.

To determine how protonation states of the His 37 box affect the pore water structure in M2TM', the Klein lab performed a thorough exploration of the configurational space of water molecules by classical MD simulations on M2TM' systems with an increasing number of protons added to the His-box. The water density distribution from classical MD simulations was always in good agreement with the positions of the crystallographic waters in the various clusters, in particular in the 2ε state. The only water that was not stable was the central water in the exit cluster, which had been observed experimentally to have a high Debye-Waller factor (Figure 3.4 A).

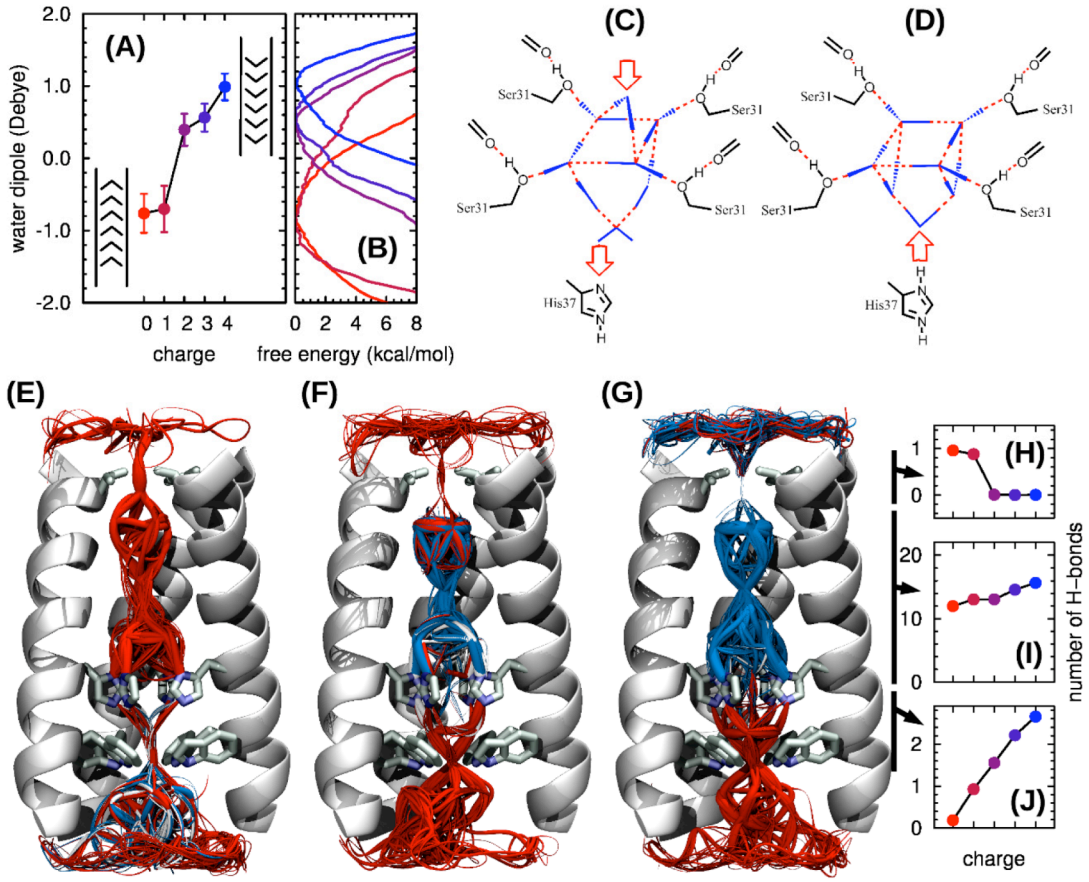

Figure 3.6. Switching mechanism of the pore waters in the M2TM' bundle, across five protonation states, postulated to be the sequence of M2 activation (0, 1+, 2+, 3+, 4+). We considered an order parameter, *d*, as the average projection along the pore axis of the water dipole (defined between -2.35 and 2.35 Debye). (A) Average and standard deviation of *d* at each state, and (B) free energy profiles *f*(*d*), computed by metadynamics MD runs (each ca. 50 ns long). (C-D) Schematic structures of the pore waters (shown in blue) immediately below the Val27 valve, in the under-protonated (C) and over-protonated (D) states. In the under-protonated state (C) the four water molecules adjacent to Ser31 can saturate their H-bond network only if an additional water molecule enters the valve. When protons accumulate at the His-box, water molecules reorient towards it (see (A)) and the H-bond network with the protein becomes fully satisfied: without free acceptors, the valve dehydrates. (E-G) Distribution of the H-bonded water wires in the neutral (E), 2+ (F), and 4+ (G) states, constructed by joining all of the neighboring H-bonds observed in classical MD simulations. To make the rarely populated wires more visible, line thicknesses in the picture are proportional to the square root of their population. *Red* indicates water wires oriented towards the viral interior (inward wires), *blue* wires run in the opposite direction (back-flow wires) and *white* wires connect adjacent His37 side chains. Three regions with different behavior can be identified: the Val27 valve, which always features inward wires of decreasing intensity; the region between the valve and the His-box, where the equilibrium switches (see also (A)) from inward wires connected to the Val27 valve and back-flow wires that are disconnected from it; the region between the His-box and the Trp-basket, always

featuring inward wires of increasing intensity. (H-J) Average count of H-bonds within each of the three regions.

The H-bonded water clusters in the channel pore (including the MPSC) exhibited a well-concerted response to increasing charge (Figure 3.6 A) suggestive of a global control of the proton flow. The most prominent feature of this mechanism was observed directly at the Val 27 valve. Although the backbone atoms were restrained in the simulations and therefore the radius of the valve was approximately constant across the different charge states, a sudden drop in the water density was observed in this region when the MPSC reached a total charge of 2+ (Figure 3.6 H).

This behavior is explained by the electrostatic interactions between the charged residues and the water molecules: as already observed in similar systems (de Groot and Grubmuller 2001; Tajkhorshid, Nollert et al. 2002; Chakrabarti, Roux et al. 2004) the orientation of the dipole moments of the water molecules filling a hydrophobic pore is highly sensitive to the magnitude and the position of the charges lying within the pore. In M2TM', the total dipole moment of the water molecules correlates with the total charge of the His-box, and, in particular, changes its sign as soon as this charge increases to 2+ (Figure 3.6 A) The two apparent alternate states (positive or negative) feature different H-bond networks, which, in turn, determine the solvation properties of the Val valve: in the under-protonated states (neutral, 1+) each of the four water molecules adjacent to Ser31 can form 4 H-bonds (a complete first solvation shell) only by binding a water molecule further up towards the top in the Val valve region (Figure 3.6 C,D), while in the over-protonated states (2+, 3+, 4+) the H-bonding capability of these water molecules is fully satisfied by intra-cluster H-bonds.

This switch between two different H-bond networks turns out to dramatically affect the population and the directionality of *water wires,* required by the Grotthuss hopping mechanism as proton transport pathways (Agmon 1995). In the neutral and 1+ states, most such water wires connect

the bulk at the N-terminal part of the protein with the His-box, consistent with the fact that the channel is activated upon acidification of the medium outside the virus. As the charge is increased (2+, 3+ and 4+), their relative population decreases by several orders of magnitude. Instead, wires originating at the His-box and oriented in the back-flow direction become dominant, but cannot reach the exterior, because they terminate at the Val27 valve (2+ and 3+), or flow through it with a smaller probability than that of the incoming, forward-flow wires (4+ state). That is, even when the His-box grows richer in H-bond donor groups looking towards the N-terminal end, the connectivity of the water wires prevents the protons from easily reaching the exterior, and the conditions for a net proton influx are always preserved.

At the C-terminal end, instead, water wires from His 37 are connected to the viral interior in all of the protonation states except the neutral one. Interestingly all these water wires are always directed toward the virus interior: the H-bonds donated by the indole amino groups of Trp41 impose a stable orientation on the water molecules in the lower cluster. Thus, as for the configuration like the NMR structure (in which the indole group physically occludes the pore) the proton accessibility from the viral interior is low and back-flow currents are prevented. Unlike the N-terminal end, the effect of increasing charge is to intensify the existing water wires and set the stage for a prompt release of excess protons from the Nε sites towards the interior. This outcome appears most favorable at the 4+ state, when each His has an acceptor water molecule at the C-terminal side, constantly connected by a short H-bond (< 3 Å).

In these simulations, the M2TM' backbone was constrained, preventing additional ratchet-like gating motions that have been proposed to underlie its conduction mechanism. Nevertheless, since the backbone conformation obtained from the pH 6.5 crystal structure is likely to be populated by a significant fraction of M2 tetramers at a range of conducting pH values, the formation, dehydration, and reorientation of pore water wires described above not only contributes to the unusual proton stability in the MPSC and His 37 box, but also complements the

ratchet mechanism in maintaining the unidirectional, inward proton flow through the M2 transmembrane segment. In particular, the dehydration of water density at the Val 27 valve at high protonation states is consistent with a secondary gating role proposed for those residues from molecular dynamics simulations performed on other M2 models, where under certain conditions water wires at the N-terminal pore were interrupted by Val 27 (Yi, Cross et al. 2008).

3.12. Correlation of molecular dynamics results and channel function by modulating pore radius.

To correlate the computational model predictions with M2 function, we can compare calculated pore water densities from Klein lab molecular dynamics simulations on M2TM' variants at position 34 with specific activity measurements on full-length protein carrying the same mutations, determined by Dr. Victoria Balannik in the Pinto Lab.

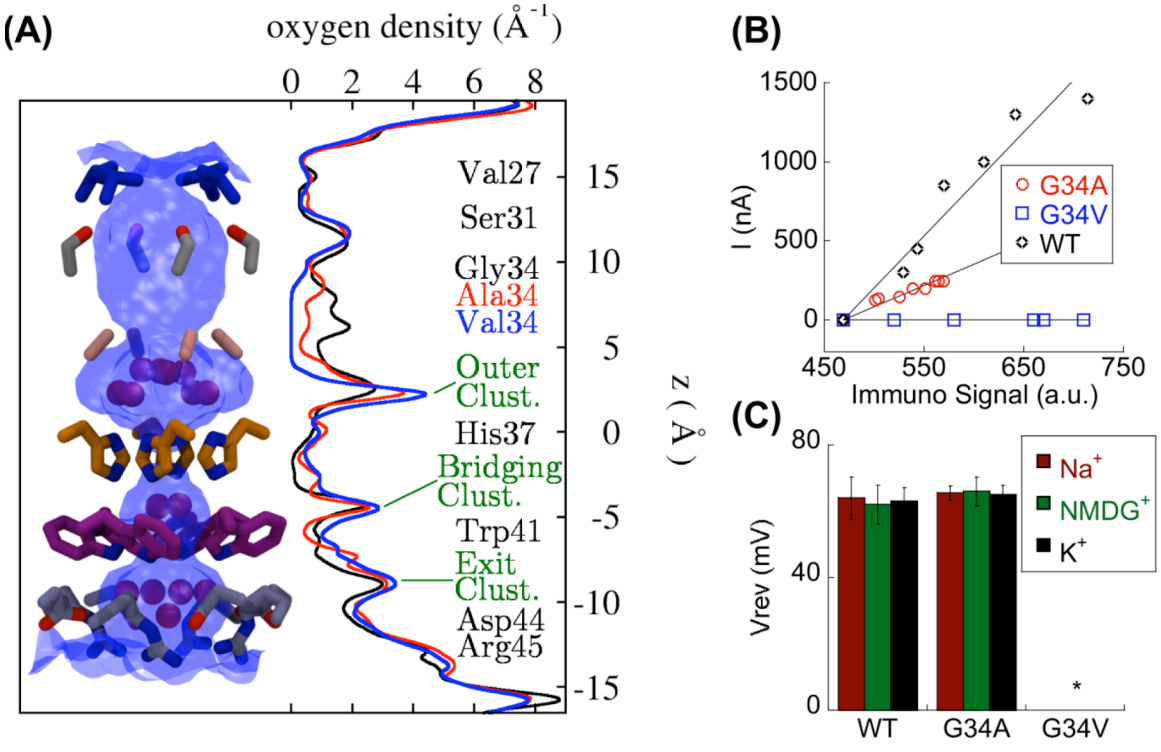

Figure 3.7. Effect of mutations of pore-lining residues. (A) The density of water oxygens as a function of the location in the channel pore (z) for the wild type (WT) and 2 mutants (G34A and G34V) taken from classical molecular dynamics simulations of the 2ε state is reported in black,

red, and blue respectively. The shape of the channel pore is depicted in light-blue shading along with the sidechains of pore-lining residues (color coded as in Fig. 3.4). The density in the region adjacent to residue 34 decreases with the increased size of the sidechain and drops to zero for the G34V mutant. (B) Specific activity measurements for M2 wild type, G34A and G34V. The amplitude of the channel activity (I) was plotted as a function of the immunosignal intensity for each tested oocyte and a straight line was fitted to the data. The slope of each plot represents the relative specific activity for the protein: 6.6±1.5 for M2; 2.7 ±0.4 for M2-G34A. M2-G34V showed membrane expression comparable to the wild type, but no detectable channel activity. (C) Comparison of channel activity and proton selectivity between full-length M2, and the G34A and G34V mutants. The channel activity was evoked by rapid exchange of non-activating solution (pH 8.5) with activating solution (pH 5.5). The reversal voltages were measured in Na+, K+ and NMDG+ - based activating solutions showing no significant differences in the ion selectivity and channel properties between the M2 wild type and the G34A mutant. G34V mutant (marked with *) did not show any pH induced channel activity. Each bar is the mean (± SD) of 5 independent experiments.

With respect to WT M2, the introduction of Val at position 34 in computer models sharpened the distribution of waters attached to His37, and more importantly introduced a 5 Å gap in the water profile surrounding residue 34 (Fig. 3.7 A). G34A showed intermediate behavior between WT and G34V in simulations, retaining significant water density through this region of the channel. Thus, G34V would be predicted to be unable to conduct protons; G34A might have a lower conductance if the restriction of the channel diameter causes the rate of diffusion of protons to the MPSC to become slower than the rate of dissociation of protons from this cluster.

The proton conductivity, ion selectivity and surface expression of these mutant channels was assayed and compared to that of the wild type protein. The specific activity, determined from the slope of the proton current vs. the amount of protein expressed on the surface, was approximately 2.5 fold lower for the M2-G34A mutant channel than for the wild type (Fig. 3.7 B). Although expressed normally, the M2-G34V mutant protein did not show any detectable channel activity (Fig. 3.7 B). The ion selectivity was assayed by measuring the reversal voltage (V_{rev}) in recording solutions containing different cations (Na+, NMDG+, or K+). The reversal voltage of M2-G34A mutant was comparable to that of the wild type protein indicating that the mutant channel retains very high proton selectivity (Fig. 3.7 C). We therefore conclude that the G34V mutation blocks the channel by occluding the conduction pathway, and postulate that the diffusion

through the Gly34/Ala34 region to the MPSC is permitted, but becomes partially rate-limiting in the G34A mutant.

These results impart experimental support for the computational techniques used by the Klein lab to model the water structure of M2TM', and also provide evidence that the G34A mutation in M2 (as present in the best medium- and low-pH structural models thereof currently available) (Stouffer, Acharya et al. 2008) has only a minor effect on transport rate and does not affect the protein's ion selectivity. This, along with the similarity in crystal parameters from a WT M2TM' peptide, reinforces the notion that the Ala at position 34 imparts only a local structural change, and can be mutated to Gly in silico for mechanistic studies or inhibitor docking trials.

3.13. Why was amantadine not observed in the pore of the M2TM' structure?

A brief digression is warranted to comment on the absence of amantadine in the newly solved M2TM' structures. For M2TM' G34A, crystal growth in the absence and in the presence of amantadine was similar, and high-quality diffraction data was obtained for crystals grown in the presence of the drug. For M2TM' G34, highest-quality crystals were obtained in drops without amantadine; experiments with amantadine led to crystals that were too small to manipulate and mount.

Electron density maps for M2TM' G34A crystals grown in the absence and presence of amantadine were essentially identical, with no evidence of the drug. Two possibilities underlying this observation need to be examined. The first is that G34A mutants bind amantadine poorly because of additional steric crowding imposed by Ala 34 methyl sidechains in the pore. This notion is weakened somewhat by the observation of electron density corresponding to amantadine in a lower-resolution, low pH crystal structure of a G34A variant of M2TM (Stouffer, Acharya et al. 2008), although it is possible that the more closely-packed conformation adopted by M2TM' G34A destabilizes amantadine at more neutral pH values.

A second reason is evidenced by the lack of high quality M2TM' G34 crystals grown in the presence of amantadine. There is ample evidence that amantadine binding stabilizes the M2 TM tetramer (Salom, Hill et al. 2000), which would presumably facilitate crystallization. However, all M2TM' crystals were grown in precipitant solution that contained 2-propanol (crystals were also obtained from similar well solutions that instead contained ethanol, suggesting that an alkyl alcohol contributed to crystal formation). Examination of the M2TM' pore near Ala 30 and Ser 31 (Figure 3.4 A) shows a poorly ordered density that may be consistent with rotationally averaged 2-propanol. This suggests that 2-propanol (or similar alcohols) bind to the aqueous pore, occluding the amantadine site. Such an interaction would be consistent with the observations of Schroeder et al. that fairly short alkylamines inhibit transport through M2 in liposomes (Lin, Heider et al. 1997). While the binding affinity of M2 for 2-propanol would certainly be much lower than that for amantadine, the enormous excess of 2-propanol in the crystallization experiment may have precluded the stable binding of the drug in the protein's pore; therefore, it appears that the most likely reason for amantadine's absence from the crystal is an unfortunate quirk of the crystallization experiment.

Further work to co-crystallize amantadine with M2TM' may well start from the neutral pH citrate conditions that have been successful here, but may avoid short-chain alkyl alcohols and instead use longer polyethyleneglycols that would be less likely to bind inside the pore.

3.14. Conclusions: lessons learned from a high-resolution structure of the M2 transmembrane domain.

The new, high-resolution view of the M2 transmembrane domain and the aqueous proton transport pathway contained therein that was unveiled from M2TM' crystals represents a major advance in our understanding of not only the protein and its biological mechanism, but also of the elegantly simple methods employed by Nature to achieve charge stabilization within membranes

and membrane proteins. From the mechanistic perspective, we have garnered greater evidence that changes in helix tilt as a function of pH and the pore's alternating accessibility to internal and external water molecules play a role in a transporter-like mechanism of proton conduction by M2. Focusing in on specific portions of the protein, we see evidence for rotameric switching of the Trp 41 side chain between the high pH and intermediate pH conformations, which perhaps prime or activate the protein for conduction at lower pH values. Interhelical Asp 44 – Arg 45 salt bridges stabilize M2 bundle conformations where the C-terminal helix ends are close together and must be broken to transition to a conformation favored at low pH where these helix ends move apart. Most importantly, a symmetric network of highly ordered water molecules interacts with incoming protons and His 37 residues to provide a structural explanation for the highly perturbed His 37 pK_a values measured by solid state NMR (Hu, Fu et al. 2006), and points to a transport pathway where the protons transition through water molecules that bridge clusters of pore-lining residues. The unusual degree of charge stabilization afforded by the N-terminal water cluster sheds light on a nanoelectric charge storage device previously unseen in Nature. Computational studies of how the pore water molecules respond to changing His 37 protonation states point to a highly tuned but structurally simple system that regulates and imparts directionality on proton transport, and suggest an important role for the Val 27 secondary gate (Yi, Cross et al. 2008). With these new insights in hand, we can now put forth a comprehensive mechanistic hypothesis that links changes in protein and pore water structures with proton binding and release in the M2 transport cycle.

Chapter 4: Evidence for pH-driven structural transitions of M2 transmembrane and C-terminal helices in bilayers

4.1. Proposed mechanism requires dynamic evidence of pH-driven structural changes in bilayers that are consistent with structural snapshots in micelles.

The currently available high-resolution structures of M2, as discussed in Chapters 1 and 3, suggest that the transmembrane domain of the protein undergoes pH-driven conformational changes of its helical backbone structure and also of key residues lining its aqueous pore, such as His 37 and Trp 41. The former notion is consistent with early cross-linking experiments on full-length A/M2 performed at two pH points (Bauer, Pinto et al. 1999). There, the pattern of cross-link formation favored the N-terminal portion of the bundle when the experiment was performed at low pH, suggesting that the C-terminal ends of the TM helices separate in this regime, as seen in the pH ~ 5 crystal structure (Stouffer, Acharya et al. 2008).

However, there has been more limited evidence obtained from non-static experiments in bilayers that suggests that the core amino acids of the aqueous pore – namely, His 37 and Trp 41 – populate discrete, pH-dependent conformational states. The high-resolution structures available thus far represent either conformational snapshots that may or may not be favored at equilibrium (crystallography) or averaged conformations but only from a very narrow pH range (solution NMR); therefore, it is important to experimentally demonstrate that the protein can significantly populate and switch between the proposed conformations at equilibrium. That the evidence come from protein reconstituted in bilayers is important since it has been previously demonstrated that the M2 TM bundle can have substantially different conformational stability in micelle and bilayer systems (Stouffer, Ma et al. 2008).

Previous spectroscopic experiments in bilayers to this end have either been interpreted to indicate a two-state pH-dependent structural transition, or monitored the protonation of His 37 directly or indirectly with a limited ability to describe the immediate environment of that sidechain (Okada, Miura et al. 2001; Czabotar, Martin et al. 2004).

An experiment to measure the effect of pH on specific sidechains or domains of the protein necessitates that the pH-driven structural transitions be rapid on the timescale of the experiment. Fortunately, strong evidence to this end was obtained experimentally by Schnell and Chou, who monitored the NMR dynamics of Trp 41 in micelles at high pH and observed conformational transitions on the millisecond timescale (Schnell and Chou 2008). In addition, molecular dynamics simulations by Klein on the M2 TM bundle in bilayers showed that certain pH-driven conformational changes occurred on the nanosecond timescale, indicating that changing the protonation state of His 37 drives a very rapid structural transition to equilibrium (Khurana, Dal Peraro et al. 2009).

We therefore set out to observe whether the environment around Trp 41 (probed by its accessibility to polar small molecule quenchers in fluorescence Stern-Volmer quenching experiments (Lakowicz 2006)) when M2 is reconstituted in bilayers undergoes distinct pH-dependent state changes as the structural snapshots obtained in micelles would indicate. We also used spectroscopic methods to study the C-terminal amphiphilic helix of M2, where we found further evidence of pH-driven conformational changes transmitted from the TM domain.

4.2. pH-dependent Stern-Volmer quenching of full length A/M2 in bilayers: materials, methods and experimental considerations.

Data Collection: For Trp 41 fluorescence quenching experiments, we used the single-Trp, Cys-free full length A/M2 construct, obtained from *E. coli* cultures as described in Chapter 2. The WT A/Udorn/72 sequence has two Trp residues (at positions 15 and 41), which would have

complicated spectral analysis; the single-Trp variant retaining the sidechain at position 41 and having a Trp15Phe mutation enabled unambiguous interpretation of the results without compromising protein function (see Chapter 2); in addition, this construct provided the high culture yields of protein necessary for these experiments.

To enable detection of Trp 41 fluorescence, a target protein monomer:lipid ratio of 1:100 was used. Lipid films (25 μmol 4:1:2 POPC:POPG:cholesterol, made from chloroform stocks as described in Chapter 2) were thoroughly hydrated with ~ 400 μL of MilliQ water and 100 μL of 10x buffer (at 10x, 500 mM potassium phosphate, 100 mM NaCl, pH-adjusted to 7.0 with HCl). The actual volume of water added was adjusted so that following the subsequent addition of protein, the total volume of the sample would be 1 mL. The sample was vigorously vortexed, and the hydrated, protein-free lipid suspensions were subjected to five freeze-thaw cycles (dry ice-ethanol bath and 37°C water bath).

Full length A/M2 (non-HPLC purified eluate from nickel column in 50 mM HEPES pH 8 buffer, 4 mM OG, 20% v/v glycerol) was next added dropwise to the experimental sample. The stock concentration of protein was ~500 μM. For the control liposome sample, an equal volume of protein-free HEPES/OG/glycerol buffer was added. The mixtures were freeze-thawed an additional five times and sized to 100 nm liposome target diameter by 33+ passes through a mini-extruder (Avestin, Ottawa, Canada). To remove residual octylglucoside from the samples, the mixtures were dialyzed for 1-2 cycles in 1L of 1x buffer (50 mM potassium phosphate pH 7.0, 10 mM NaCl) in the presence of the detergent-binding resin Amberlite XAD-4 (Supelco, Bellefonte, PA).

For experiments, 20 μL of liposome suspension was added to 2 mL of buffer set at the desired pH in a 1cm x 1cm Hellma QS fluorescence cell. 10 μL of a 4 μM ethanolic stock of the proton uncoupler FCCP (Fluka/Sigma-Aldrich, St. Louis, MO) was added to dissipate the pH gradient.

The mixture was stirred for five minutes prior to the experiment. A reference cuvette similarly configured but with control liposomes added at pH ~7 was used for on-line background signal subtraction from scatter induced by the vesicles.

Experiments were performed while stirring in an Aviv ATF-105 spectrofluorometer at 25°C by measuring a baseline Trp fluorescence value at the end of the five minute equilibration period, then adding 50 μL aliquots of a 5 M NaI solution (with 1 mM $Na_2S_2O_3$ added to prevent I^- photooxidation) and taking measurements following the addition of every aliquot. An automated titrator (Hamilton, Reno, NV) was used to allow for high precision of titrant addition and for careful control of the timing of titrant addition, equilibration time, and scan time. No titrant was added to the control cuvette, and the subtracted background signal was not corrected for the small dilution effect (~10% maximum) that addition of titrant would have caused. To account for any deviation from the pre-set buffer pH as a result of adding other sample components, pH of the cuvette contents was measured at the conclusion of each titration and that value was used as the experimental pH.

To avoid exciting Tyr residues in the protein, fluorescence excitation was performed at 295 nm rather than the standard Trp wavelength of 280 nm. At 295 nm, the spectrum of Trp shows substantial absorption while the absorption of Tyr is near zero. Fluorescence emission was measured at 340 nm, near the average emission maximum of indole in both hydrophobic and polar environments.

The measurement of intrinsic Trp fluorescence in bilayers can be complicated by substantial scatter artifacts from the liposome sample, as analyzed in detail by White *et al*. (Ladokhin, Jayasinghe et al. 2000). In initial experiments with this system, very intense periodic scatter peaks were visible in the emission spectrum (perhaps complicated by an uncommonly high lamp power on the Aviv instrument), making spectral interpretation difficult and leading to physically

unreasonable calculated quenching constants. The problem was resolved by installing polarizers in a cross-polarized configuration (excitation polarizer horizontal, emission polarizer vertical) and adding an emission filter that blocked light at wavelengths below 300 nm from reaching the detector. The excitation bandwidth was kept low (2-3 nm) and the emission bandwidth was allowed to be higher (6-7 nm). Experiments using this configuration with model Trp-like small molecule compounds quenched by acrylamide and iodide quenching yielded quenching constant values consistent with those available in the literature (Dvorin, Mantulin et al. 1985; Stoeva, Dolashka et al. 1995; Alston 2004), and the scatter peaks were substantially diminished. Experiments on the M2 proteoliposomes were performed with the fluorometer in this configuration and led to physically reasonable Stern-Volmer quenching constants similar in scale to those observed in unpublished experiments from the Pinto lab.

A final complicating factor in this experiment was the observation that the steady-state Trp fluorescence of M2 in liposomes was somewhat unstable (and declining) as a function of time, especially at certain pH values. A variety of factors were adjusted in an attempt to account for this phenomenon, including the length and frequency of sample irradiation (to rule out photooxidation), length of temperature equilibration, as well as the presence and absence of various ionophores such as FCCP and valinomycin. None of these appeared to be causally involved. It is also possible that under certain conditions, the liposomes are more likely to more strongly adhere to the cuvette walls, reducing the signal intensity, but this variable was not explored. Instead, the experiment was performed under very stringent and consistent timing, and a constant “noise” parameter obtained from the data set was introduced in the data analysis, as will be described in the next section.

Data Analysis: Fluorophores such as the indole group of tryptophan, when in their excited electronic state (which normally leads to fluorescence), can instead non-radiatively transition back to their ground state through a close encounter (collision or static binding) of a quencher. There

is a multitude of known quenchers of indole of varying potency, including molecular oxygen, protonated imidazole (as observed by Hay *et al*., for the M2 system (Czabotar, Martin et al. 2004)), acrylamide, cationic cesium, and anionic iodide (Lakowicz 2006). The latter was chosen for this study because of its charged nature and thus lower accessibility to hydrophobic environments.

The relative potency of the quencher or, conversely, the relative accessibility of the fluorophore being quenched, can be determined through Stern-Volmer analysis, where the fluorescence lifetimes of the fluorophore in the absence of quencher (τ_0) and in the presence (τ) of a certain concentration of quencher [Q] are used to calculate a quenching constant k_Q:

$$\frac{\tau_0}{\tau_Q} = 1 + k_Q[Q]$$

Assuming that the quenching is purely collisional or dynamic (i.e. that no stable, long-lived complexes form between the quencher and the fluorophore), the fluorescence lifetime can be linearly correlated to the fluorescence intensity (F): $\tau \alpha F$, leading to the following relationship:

$$\frac{F_0}{F_Q} = 1 + k_Q[Q]$$

To account for the uncertainty in the measurement of F_0 (as described in the previous section), the following equation was fitted to the pH-dependent quenching data sets, now incorporating a linear error correction:

$$F_Q = \frac{F_0}{1 + k_Q[Q]} - k_E[Q]$$

This equation represents a rearranged Stern-Volmer equation, with an added quencher-dependent error constant k_E. In this equation, the $k_E[Q]$ term represents the time-dependent variation in baseline fluorescence, where time is represented by the quencher concentration, which, in the experimental titration, increases by the same amount at evenly spaced timepoints.

These data were analyzed and the error parameter obtained from the fit was plotted against the initial fluorescence F_0, as shown in Figure 4.1.

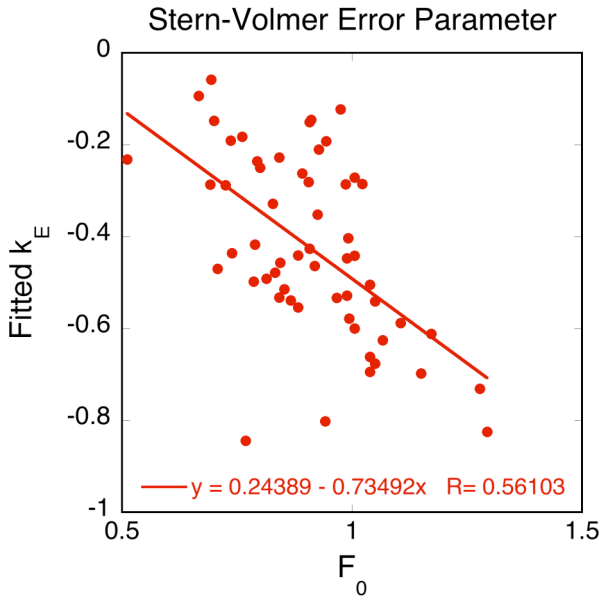

Figure 4.1. Fitted error parameter k_E from Stern-Volmer experiments plotted vs. initial fluorescent signal F_0. A linear regression function is fitted to the data.

Based on these data, the initial (and experimentally most variable and difficult to measure) fluorescence value F_0 was excluded from further analysis, by finding the predicted value of the error parameter k_E where F_0=1 (which based on figure 4.1 is -0.491) and fitting the following equation to each experiment, where F_0 is set to 1, and k_E is fixed at $k_E(F_0=1)$:

$$F_Q = \frac{1}{1 + k_Q[Q]} + 0.491[Q]$$

The resulting data are shown in Figure 4.2. A protonation equilibrium function, defined by the following two equations, was fit to the data (solid line). The protein was assumed to be fully tetrameric under every condition studied.

$$k_{Q,obs} = \frac{k_{q0}M_0 + k_{q2}M_2 + k_{q3}M_3 + k_{q4}M_4}{M_0 + M_2 + M_3 + M_4}$$

In the above equation, k_{q0}, k_{q2}, k_{q3} and k_{q4}. represent the quenching constant of the fully deprotonated, doubly protonated, etc. species of the protein. M_0, M_2, M_3 and M_4 represent the relative population of each species. When the pK_a values governing the protonation events are considered, the equation is expanded as shown below.

$$k_{Q,obs} = \frac{k_{q0} + \frac{k_{q2}[H^+]^2}{K_{a12}{}^2} + \frac{k_{q3}[H^+]^3}{K_{a12}{}^2 K_{a23}} + \frac{k_{q4}[H^+]^4}{K_{a12}{}^2 K_{a23} K_{a34}}}{1 + \frac{[H^+]^2}{K_{a12}{}^2} + \frac{[H^+]^3}{K_{a12}{}^2 K_{a23}} + \frac{[H^+]^4}{K_{a12}{}^2 K_{a23} K_{a34}}}$$

In this function, it is assumed that every protonation state of the tetramer has a preferred equilibrium structure and therefore a unique k_Q determined by that conformation's Trp 41 sidechain accessibility to water. Therefore, the observed k_Q is deconvoluted into components made up by k_{Q0}, k_{Q2}, k_{Q3}, and k_{Q4} (assuming that the first two protons bind with the same pK_a as shown by Cross *et al*. (Hu, Fu et al. 2006)); the contribution of each component depends on the relative population of that structural state at the pH of the experiment, which the function computes. The denominator is used as to normalize the value for the total amount of protein present.

4.3. Stern-Volmer quenching: evidence for pH-driven conformational transitions involving Trp 41 in bilayers.

The Stern-Volmer quenching data in the physiologically relevant pH range of 8-5, collected from full length M2 reconstituted in bilayers, is shown in Figure 4.2. As discussed in the previous section, the $k_{Q,obs}$ shown on the y-axis of the plot represents the population-averaged accessibility of the Trp 41 sidechain to the ionic iodide quencher. A higher k_Q indicates greater accessibility.

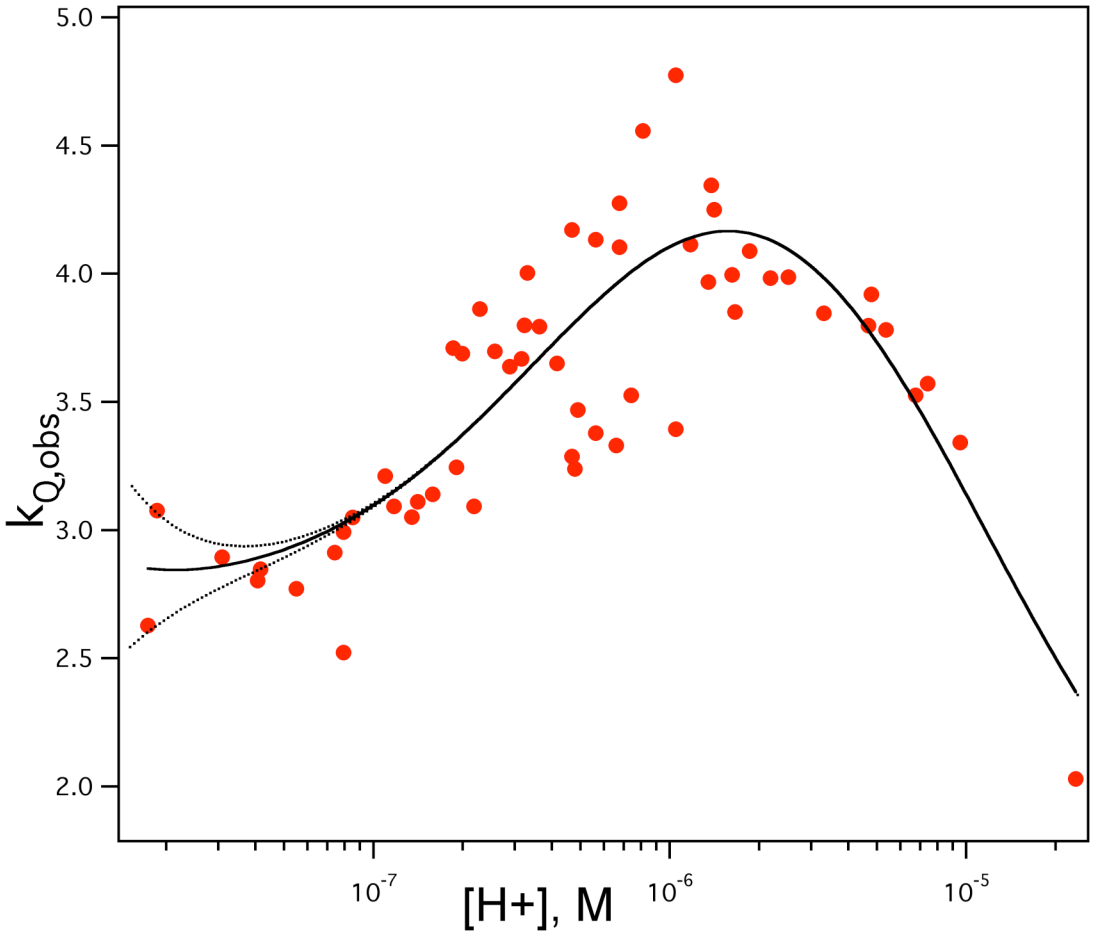

Figure 4.2. pH-dependent Stern-Volmer quenching of Trp 41 by iodide. The fitted black line represents a protonation equilibrium function with pK_a values constrained to those observed by Cross *et al*. (Hu, Fu et al. 2006)

The curve fit line shown in Figure 4.2 (solid line) was used to deconvolute the population-averaged $k_{Q,obs}$ from the experiment into a sum of population-weighted component k_Q values representing each protonation state of the tetramer (where k_{Q0} is the quenching constant for the fully deprotonated state of the protein, k_{Q2} for the 2+ state, etc). The hypothesis being explored was that different protonation states of the protein correspond to different equilibrium conformational ensembles that are reflected in the quenching accessibility of Trp 41 (k_{Q0}, k_{Q2}, etc.), and that the protein is able to transition between these conformational ensembles at equilibrium in a bilayer environment.

To this end, the pK_a values observed by Cross *et al*. (Hu, Fu et al. 2006) are used as constraints governing the protonation events in the curve fit (n.b. Cross *et al*. were unable to precisely determine the lowest pK_a value of the tetramer, but it was suggested to be <5; a pK_a of 5 was used in the curve fit, but a similar pattern of results could be obtained using slightly lower values for the 4^{th} pK_a). A good curve fit was obtained using these constraints, suggesting that protonation events and conformational changes around Trp 41 may be linked. The Stern-Volmer quenching experiments were performed over the physiological pH range that a virus may encounter in an infection cycle, therefore few data points were collected at pH ranges where the fully deprotonated state is significantly populated (given that the pK_a of first two protonations is 8.2 (Hu, Fu et al. 2006)). However, the k_Q values for the physiologically relevant 2+, 3+ and 4+ states were very well defined and substantially different from each other. A summary of the computed parameters from the fit is shown in Table 4.3. As will be discussed below, these results show that changing the protonation state of M2 His 37 residues in bilayers over the physiological pH range does indeed result in discrete structural transitions of the environment near Trp 41, consistent with the mechanistic hypothesis being developed in this thesis.

k_{Q0}	3.4 ± 2.2
k_{Q2}	2.7 ± 0.1
k_{Q3}	5.1 ± 0.2
k_{Q4}	1.2 ± 0.4

Table 4.3. Computed conformation-specific Stern-Volmer quenching constants.

The data in Figure 4.2 indicate that the accessibility of the Trp 41 sidechain to aqueous quencher changes dramatically as a function of pH between pH 5 and 8. The overall Trp accessibility (represented by the observed k_Q) is relatively lower at high pH values, then rises as pH decreases, peaking at approximately pH 6, before declining again at lower pH values. Further insights can be gleaned by a comparison of the protonation-state specific quenching constants

calculated from the curve fit (Table 4.3) with the high-resolution structures of M2 TM determined at similar pH values.

We did not perform Stern-Volmer experiments under the rather basic conditions where the fully deprotonated, 0+ state, would predominate, since this pH range would not be encountered by a virus *in vivo*. There is thus relatively greater uncertainty for the value of k_{Q0} calculated in the fitting (dotted lines in the plot show the fitting function with k_{Q0} fixed at the high and low ends of its fitting confidence limit in Table 4.3). Comparing the pH 8 solution NMR structure (Schnell and Chou 2008) (which would likely correspond to the 0+ state) and the pH 6.5 high resolution crystal structure (Chapter 3, corresponding to the 2+ state), we note that the rotameric conformation of Trp 41 is different in these structures in the context of an otherwise well-packed C-terminal aspect of the bundle. This structural difference likely underlies whatever accessibility differences are present between these two states, but we are unable to analyze these physiologically less important changes further because of noise in k_{Q0}. We therefore focus our discussion on the physiologically encountered transitions between the 2+, 3+ and 4+ states, where the bulk of our data were collected.

In the high resolution structure (Chapter 3) that we assign to the 2+ state, the Trp sidechains are exposed to solvent largely through the central pore, and are otherwise located in a tightly packed area of the helical bundle that restricts solvent access from other directions. It would be unlikely that a large ion could access the Trp 41 sidechains from the N-terminal side of the aqueous pore, (Figure 3.4) as it would need to penetrate the constrictions created by the Val 27 and His 37 sidechains. Thus, the predominant means of access is likely from the C-terminal side of the protein's aqueous pore. The detailed view of the proton transport pathway in the structure of the 2+ state indicates that the C-terminal face of the Trp basket interacts with four ordered water molecules in the exit cluster, that are further stabilized by interactions with Arg 45 sidechains that

line the pore exit. This ordered structural unit may act to restrict access to the sidechain by quencher, consistent with the relatively low k_Q calculated for the 2+ state.

There is less structural certainty with regard to the conformation that is favored in the 3+ and 4+ protonation states of the protein, for which the k_Q increases substantially then decreases dramatically, respectively. The "A" helix structural model from the published pH ~ 7 crystal structure (Stouffer, Acharya et al. 2008) was proposed to represent a conformation favored at low pH based on its structural similarity with a lower resolution structure determined from crystals grown at a starting pH near 5. However, in light of the previously discussed uncertainty with respect to the actual pH of crystallization for both crystals, it is unclear whether these structures represent a conformation favored in the 3+ or the 4+ state. In comparison to the doubly protonated state represented by the high-resolution structure, the helices making up the transmembrane domain straighten out, with their C-terminal ends undergoing a dramatic separation. The overall shape of the transmembrane helical bundle changes from a cylinder in the 2+ state to a cone at lower pH, and the water accessibility of the C-terminal aqueous pore where the Trp 41 sidechains reside is dramatically increased. Thus, it is likely that these structures represent the 3+ state with its correspondingly high calculated Stern-Volmer constant (Table 4.3); this argument would also suggest that at least in the lower pH structure (Stouffer, Acharya et al. 2008), the actual pH of crystal formation was close to that set at the beginning of the experiment. This hypothesis is also consistent with earlier cross-linking results showing greatly decreased TM helix cross-linking on the C-terminal end at pH 5.2 (where the protein would be predominantly in the 3+ state) than at neutral pH (Bauer, Pinto et al. 1999).

While a relatively high degree of Trp 41 solvent accessibility is calculated for the 3+ state, this value drops off dramatically with binding of the 4th proton (Table 4.3). The pH-chord conductance curve of M2 saturates around a pH_{out} of 4 (Chizhmakov, Geraghty et al. 1996), suggesting that the 4+ state is likely active in conduction. We can only speculate as to its structural identity, but

some clues may be provided by the structure of the 3+ state, where the Trp 41 sidechain turns away from facing the center of the pore to pointing into the (now very large) interhelical space. Perhaps a continuation of this trajectory leads to more complete burrowing of the Trp indole into the membrane, and/or its occlusion from solvent by neighboring pore-lining residues His 37, Asp 44, and Arg 45, both of which would explain a state with dramatically reduced quencher accessibility.

In summary, the bilayer Stern-Volmer quenching results presented here are in good agreement with the structural snapshots of M2 obtained thus far in micelles, and describe a series of shifting conformational equilibria of the protein that are driven by His 37 protonation at pK_a values that were previously determined by spectroscopy (Hu, Fu et al. 2006). To reinforce this view, we can visualize the pH-induced changes in the conformational ensembles of M2 as an energy landscape that shifts with pH, weighting the ensemble toward one predominant conformation or another (Figure 4.4).

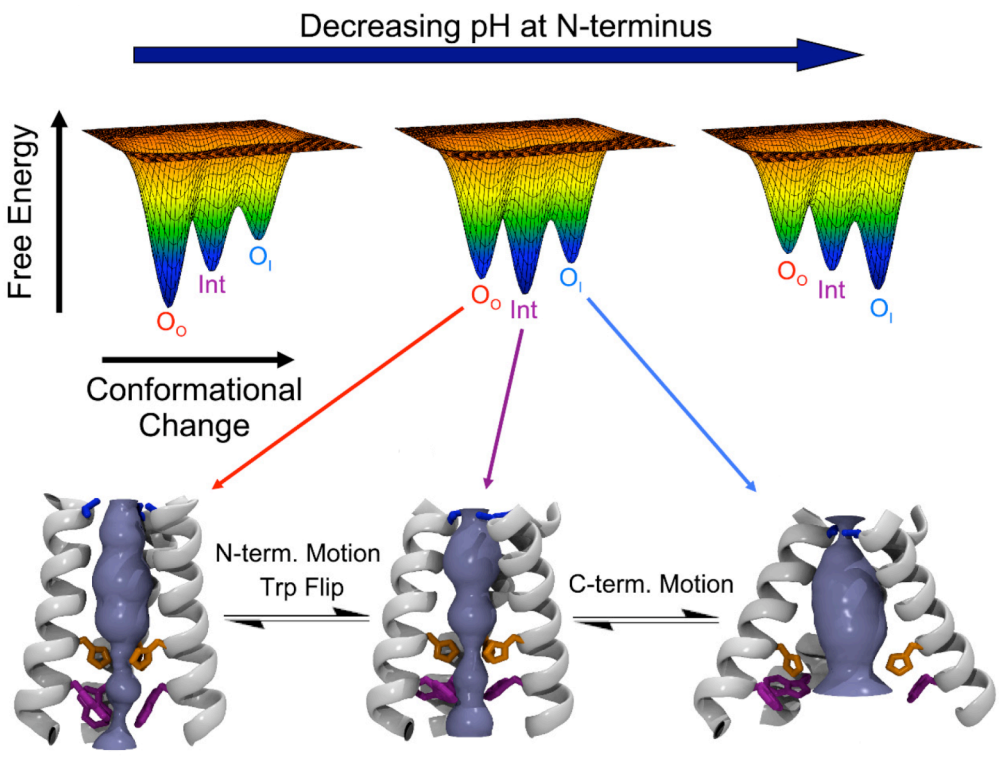

Figure 4.4. An energy landscape perspective of the pH-driven changes in the structural ensemble of M2 conformational states. The Out Open form (O_O, solution NMR, (Schnell and Chou 2008)) predominates at high pH, the Intermediate form (Int, high-resolution structure from Chapter 3) at pH just below neutral, and the Open In form (O_I, lower-resolution crystal structre, (Stouffer, Acharya et al. 2008)) at low pH.

4.4 The C-terminal amphiphilic helix undergoes pH-driven structural transitions coupled to transitions of transmembrane domain.

In Chapter 2, we demonstrated that the C-terminal amphiphilic helix is not required for the transmembrane domain to achieve functionally equivalent proton transport to the full length protein. Removal of this helix did not significantly affect rate of proton transport, amantadine inhibition, pH activation of transport, and ion selectivity. Furthermore, the His 37 pK_a values were similar between the TM peptide alone and the full length protein.

There is evidence, however, that this helix may play a structural role in stabilizing the protein tetramer and anchoring it in the membrane (via e.g. a palmitoylation site at Cys 50 (Sugrue, Belshe et al. 1990)). Sedimentation measurements show that the full-length protein is substantially more stable than the TM helix alone, (Kochendoerfer, Salom et al. 1999) and the C-terminal helix is the only other known portion of M2 with a well ordered structure. In this section, we show that the C-terminal helix interacts with the phospholipid bilayer via its hydrophobic sidechains and changes conformation in response to changes in pH transmitted by the TM domain helices.

The structural changes of the C-terminal helix in bilayers were studied by electron paramagnetic resonance spectroscopy in the context of spin labeled 38-residue peptides (M2TMC) consisting of residues 23-60, and thus encompassing the transmembrane domain and the C-terminal helix of the protein. Peptides were chemically synthesized as C-terminal carboxamides using standard

solid-state methods by the author and other members of the DeGrado lab, Dr. Gregory Caputo and Dr. Chad Tatko. A wild-type, cysteine-free sequence was used for dilute spin labeling experiments, where a small amount of spin-labeled peptide is added to a predominantly non-labeled population. Peptides for labeling were made as site-specific Cys mutants.

Peptides were purified, spin-labeled with MTSSL (1-oxyl-2,2,5,5-tetramethyl-3-pyrroline-3-methyl methanethiosulfonate), reconstituted in POPC:POPG (4:1) bilayers and observed spectroscopically by Phong Nguyen and Dr. Kathleen Howard at Swarthmore College. More detailed methods of this work have been previously described (Nguyen, Soto et al. 2008). The effects of cysteine mutations (with no spin-label) at the residues of interest in the C-terminal helix were also studied by Dr. Chunlong Ma in the Pinto laboratory, who measured the activity and the reversal potential of full-length Cys-free A/M2 and site-specific Cys mutants in *Xenopus* oocytes using techniques described in Chapter 2. The electrophysiology results are shown in Figure 4.5.

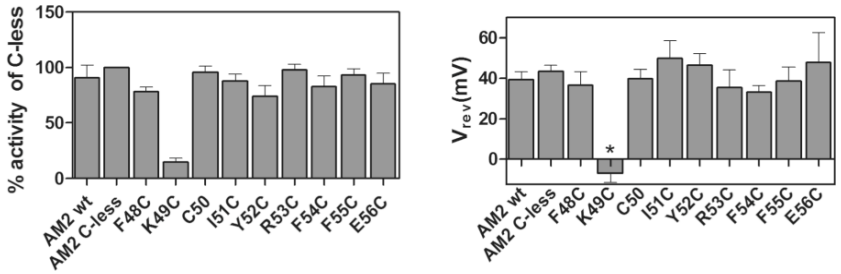

Figure 4.5. Activity and reversal potential (ion selectivity) of M2 C-terminal amphiphilic helix Cys mutants expressed in *Xenopus* oocytes. All mutants except K49C showed similar activity to WT; K49C was almost completely inactive and its reversal potential could not be precisely determined. However, K49A (not shown) had WT-like properties, suggesting that the loss of activity is specific to certain amino acid sidechains. Figure published in (Nguyen, Soto et al. 2008).

The electrophysiology data shown in Figure 4.5 are largely consistent with results presented in Chapter 2, where it was shown that the C-terminal helix was not required for M2 TM activity. All

mutants except one exhibit largely unchanged transport activity and ion selectivity (reversal potential). The exception, at Lys49Cys, results in an almost total loss of channel activity, although similar experiments on a Lys49Ala mutant (Pinto lab, unpublished) find that its functions similarly to WT protein. Therefore, introduction of a Cys residue at position 49 (which is normally a charged Lys) seems to affect M2 structure and function in a highly specific way. Based on EPR results that will be discussed next, we hypothesize that this mutation may lead to some form of a structural collapse of the aqueous pore at the C-terminal mouth of the channel.

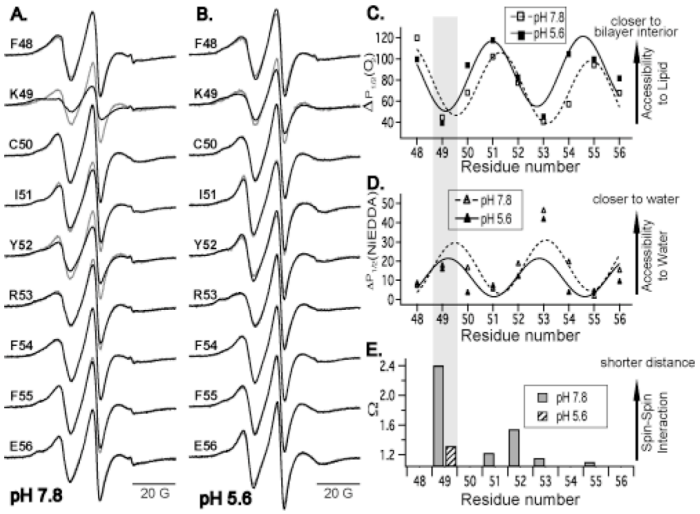

Figure 4.6. Electron paramagnetic resonance spectroscopy of site-directed spin-labeled M2TMC. Panel A and B show EPR spectra of each mutant determined at pH 7.8 (panel A) and pH 5.6 (panel B). Dark lines indicate signal from a fully-labeled sample, whereas lighter lines represent a dilute labeled sample where a small amount of labeled peptide is added to a wild-type, unlabeled peptide sample. Panel C, label accessibility to lipid and Panel D, label accessibility to water as a function of pH and labeled site, as measured by interaction with paramagnetic molecular probes. A sine function is fit to each data set. Panel E, measured spin-spin interaction between peptide monomers in fully labeled samples. Figure published in (Nguyen, Soto et al. 2008).

The results of the pH-dependent EPR spectroscopy of spin-labeled M2TMC variants are shown in Figure 4.6. The EPR spectra of fully labeled or dilute labeled samples are shown in panels A (pH 7.8) and B (pH 5.6). The accessibilities of the label to lipid and water were measured by the label's interaction with a lipid-soluble and a water-soluble paramagnetic molecular probe (molecular oxygen, and nickel (II) ethylenediaminediacetate (NiEDDA), respectively). Sine functions (to represent an alpha helical periodicity) were fit to the pH-and residue specific accessibility profiles in Panels C and D. The results show that one face of the helix, which is predominantly lined with hydrophobic sidechains, interacts with the phospholipid bilayer (as shown by a higher lipid accessibility and a lower water accessibility), whereas the other face, lined with more polar groups, interacts preferentially with water, with the reverse accessibility profile.

Interestingly, the lipid-interacting surface of the helix changes somewhat as a function of pH, a phase shift of approximately one residue or one-third to one-fourth of a helical turn. Furthermore, at low pH the C-terminal helix penetrates somewhat deeper into the bilayer, likely pulled in that direction by the decreased transmembrane projection of the TM helix, which is now straightened and more tilted relative to the membrane normal, as shown in Figure 4.7.

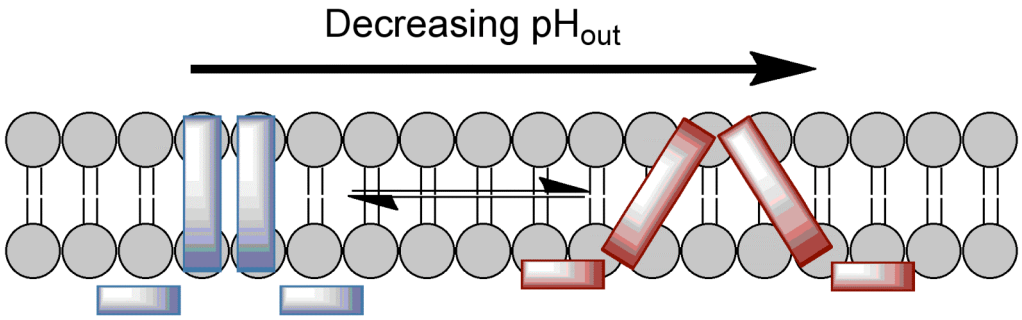

Figure 4.7. Proposed structural mechanism for increased lipid embedding of C-terminal amphiphilic helix of M2 at lower pH.

In Figure 4.6 E, comparisons of EPR data from fully-labeled and dilute-labeled samples were used to determine the extent of interaction between spin labels within the protein tetramer. With the exception of the highly perturbed result for Cys49Lys that is difficult to interpret given the functional implication of that mutation, there is a degree of sidechain-sidechain interaction (the range of detection is 8-20 Å) observed for residues 51, 52, 53, and 55, corresponding to Ile, Tyr, Arg, and Phe, respectively, falling on one face of the helix, and dropping off in intensity at more C-terminal residues. This indicates that the helix-helix interaction is most likely hydrophobic/van der Waals in nature and occurs predominantly at Tyr 52 and its nearest neighbors. The inter-subunit interaction past residue 49 can no longer be detected at low pH, suggesting that the C-terminal helices move away from each other in more acidic environments.

In conclusion, the EPR data show that the C-terminal amphiphilic helix of M2 interacts with the phospholipid bilayer along one face and with water along its other face, consistent with its amino acid sequence. Inter-subunit interactions are observed at high pH corresponding primarily to the 2+ state of the TM tetramer, but are disrupted at low pH corresponding primarily to the 3+ state, as the helix twists clockwise along its axis and embeds itself deeper into the membrane. These conformational transitions are presumably driven by the pH-dependent conformational changes of the M2 TM helix bundle, where the helices straighten out and take on an increased tilt relative to the membrane normal at low pH. Structurally, the EPR results indicate a different conformation of the C-terminal helices as compared to that observed by solution NMR in micelles (Schnell and Chou 2008). Whereas in the NMR study, the C-terminal helices interact only with other C-terminal helices in a four-membered coiled coil, and have no interaction with the micelle, in the present study the helices interact extensively with the bilayer and have more limited intersubunit contacts. We attribute this difference to the sample conditions (bilayer vs. short-chain micelle) in the two experiments.

4.5. Conclusions: Trp 41 and the C-terminal amphiphilic helices of M2 undergo pH-driven changes of their conformational equilibria in bilayers.

The evidence presented in this chapter allows the reader to put together the high-resolution structural snapshots of the M2 transmembrane domain obtained in micelle systems into an equilibrium ensemble that represents conformations in bilayers. The changing accessibility profile of Trp 41 to a polar quencher as a function of pH is consistent with its position in M2 structures obtained at high (Schnell and Chou 2008), intermediate (Chapter 3), and low pH (Stouffer, Acharya et al. 2008), and is furthermore well described by a protonation equilibrium determined by the known His 37 pK_a values (Hu, Fu et al. 2006). The C-terminal amphiphilic helix, shown in Chapter 1 to be dispensable from the point of view of transport function, is shown here to interact with the inner face of the lipid bilayer, and undergoes its own conformational changes in response to the protonation-induced structural transitions of the TM domain.

Chapter 5: Developing and testing structure-based mechanistic models of proton transport through influenza A/M2

5.1. Overview of exercise.

In the previous chapters, we have established that the M2 transmembrane domain is functionally equivalent to the full length protein (Chapter 2), and that protonation of histidine 37 residues in this domain leads to significant changes in the protein's conformational equilibrium in the membrane (Chapter 4 and Chapter 3). It has been previously hypothesized from molecular dynamics simulations that the transmembrane domain of M2 may function in a transporter-like fashion (Khurana, Dal Peraro et al. 2009), by switching between conformations that are able to bind protons from the N-terminal side of the aqueous pore, and others that are accessible only to the C-terminal side.

In this chapter, we develop mathematical models of ion transporters that sample multiple conformational states, each with its own level of proton binding affinity (pK_a). We find that a very simple, two-conformation single-proton model describes most features of transport by the wild-type protein, then build up complexity so that that the model parameters accurately reflect the pK_a values and multiple protonation states observed by Cross *et al*. (Hu, Fu et al. 2006). From these exercises, we find that only a model in which the first two protons bound can participate in conduction (in addition to the third) can describe the entirety of flux data from wild-type A/M2 at physiologically relevant pH values. This more complex model can also best account for the rather unusual flux features observed in certain mutant variants of the protein.

5.2. Transport model construction and implementation.

Transporter models were developed to describe flux at steady-state kinetic regimes (i.e. immediately following the imposition of a driving force for proton transport). Each model was

constructed as a kinetic cycle of interconverting conformational and protonation states, with the simplest arrangement shown in Figure 5.1. Each transition is defined by its own rate constant, as shown.

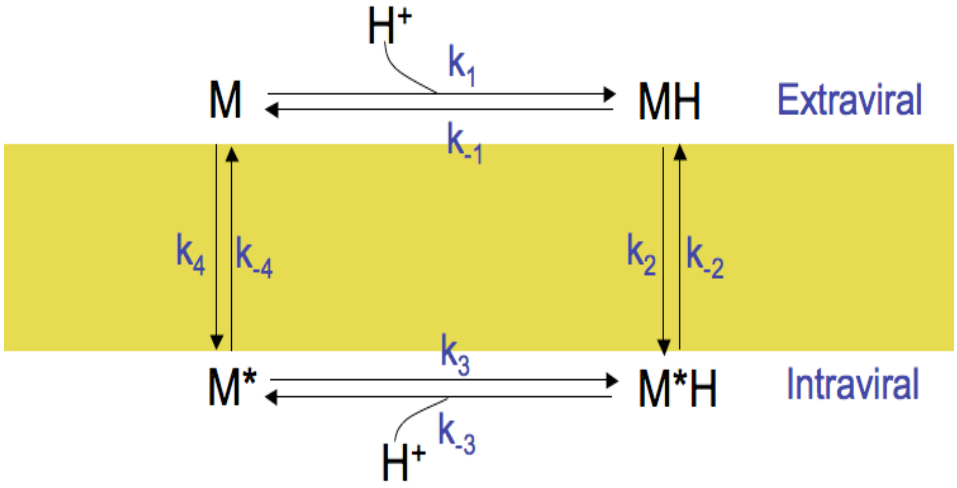

Figure 5.1. Simplified proton transporter model. The "M" conformation is accessible to extraviral waters, while the "M*" conformation is accessible to intraviral waters.

The normalized population of each state under steady state conditions was then calculated by first setting the total rate of change of each state to zero,

$$\frac{d[M]}{dt} = \frac{d[MH]}{dt} = \frac{d[M^*]}{dt} = \frac{d[M^*H]}{dt} = 0$$

which yields the following system of linear equations:

$$0 = \frac{d[M]}{dt} = k_{-1}[MH] - k_1[M][H_{out}] + k_{-4}[M^*] - k_4[M]$$

$$0 = \frac{d[MH]}{dt} = k_1[M][H_{out}] - k_{-1}[MH] + k_{-2}[M^*H] - k_2[MH]$$

$$0 = \frac{d[M^*H]}{dt} = k_3[M^*][H_{in}] - k_{-3}[M^*H] + k_2[MH] - k_{-2}[M^*H]$$

$$0 = \frac{d[M^*]}{dt} = k_{-3}[M^*H] - k_3[M^*][H_{in}] + k_4[M] - k_{-4}[M^*]$$

Solving the system by hand and or with online solver applications (Gang 1997), or for more complex models, more advanced mathematical software such as Maxima (2009) or Mathematica (Wolfram Research 2008), provided the populations of each state of the protein under steady-state kinetic conditions; the populations were normalized to reflect an unchanging amount of total protein.

Proton flux at a given condition was defined by subtracting the difference of extraviral proton release and binding rates from the difference of intraviral proton release and binding rates, as follows:

$$Flux = (Release,in - Binding,in) - (Release,out - Binding,out)$$

Or, more specifically for this system:

$$Flux = (k_{-3}[M*H]_{ss} - k_3[M*][H^+]_{in}) - (k_{-1}[MH] - k_1[M][H^+]_{out})$$

where the protein terms are the normalized steady-state populations obtained from solving the linear system described above. In more complex models, flux was described similarly by summing all possible internal deprotonation event rates as the “Release, in” term, all possible internal protonation event rates as the “Binding, in” term, etc.

The resulting flux equation was then globally fit to M2 functional data from a variety of sources, including the experiments of Chizhmakov *et al*. ((Chizhmakov, Geraghty et al. 1996; Chizhmakov, Ogden et al. 2003), where M2 was expressed in CV-1 cells) and Balannik *et al*. (unpublished, where M2 was expressed in *Xenopus* oocytes). Global fitting was performed using the Levenberg-Marquardt algorithm implemented in Igor Pro 6.0 (Wavemetrics, Lake Oswego, OR). Igor Pro procedure files used in the fitting are provided in Appendix C. Rate constants involving a charged species were modeled as voltage-dependent (unless otherwise indicated), using the single-conformation electrical distance/barrier model developed by Lear as shown in Figure 5.2, but extended to provide an additional energy minimum and barrier for a second binding site conformational state prior to deprotonation.

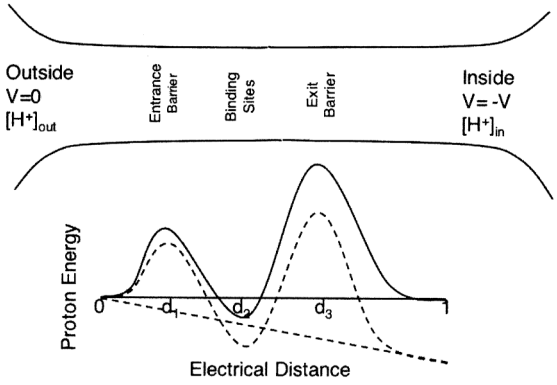

Figure 5.2. Approximating electrical distances as geometrical distances in the M2 pore. When a voltage V is applied, the rate constant for outside protonation is multiplied by $e^{-d1*V/25.7}$, where 1/25.7 is the Nernst equation (eF/RT) constant for protons at 25°C, with the electrical potential expressed in millivolts. By contrast, reversing the outside protonation process would require the proton to transit an electrical distance in the opposite direction approximated as (d2-d1); thus the respective rate constant would be multipled by $e^{-((d2-d1)*V/25.7)}$; the remaining rate constants are treated similarly with the electrical distance at the protein exit being set to 1. Figure from Lear (Lear 2003).

Wherever a complete kinetic cycle was present, the zero-voltage value of one of the rate constants making up the cycle was calculated from the other zero-voltage rate constants in order to maintain microscopic reversibility.

5.3. Results and discussion: building up from a first-principles transport model to account for known M2 conformational changes and pK_a values.

Since the flux activation profile of M2 ultimately depends on the titration of its His 37 residues, even a single-proton titration curve (ignoring additional protonation states and all conformational transitions) such as the one shown in Figure 5.3 can capture the essential features of the protein's pH activation; however, this approach breaks down dramatically when attempting to capture the features of more esoteric A/M2 mutants such as Ser31Gly. In the following discussion, we will examine conformation-based transporter models (as described in the methods section, 5.2) of increasing complexity, with the target of arriving at a model that fully describes the

features of WT transport and is consistent with its known His pK_a values (Hu, Fu et al. 2006), and also better approximates transport by the unusual pore-lining residue mutant variants of M2.

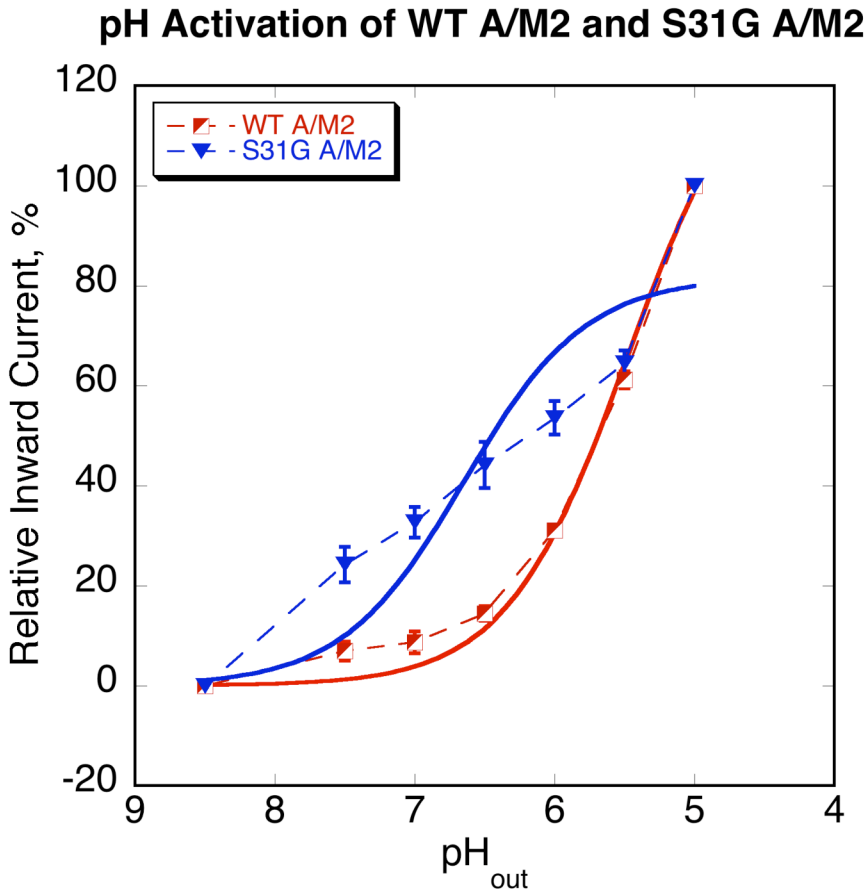

Figure 5.3. Fitting (solid lines) a single protonation-deprotonation event ($Current = \frac{\frac{k_{off}[H^+]}{K_a}}{1+\frac{[H^+]}{K_a}}$) to the pH activation profile of WT A/M2 and S31G A/M2 . Data from Victoria Balannik, Pinto Lab.

We begin our discussion with the simplest, four-state transporter model described in the methods section (see Figure 5.1), which was developed by the author together with Dr. James Lear. All subsequent models discussed were implemented and tested by the author alone. This simplified transporter model was created to test the general applicability of the transporter hypothesis to M2 function. As shown in Figures 5.4 and 5.5, this mechanism fits reasonably well to pH-dependent

conductance and current-voltage voltage data obtained by Chizhmakov *et al*. (Chizhmakov, Geraghty et al. 1996; Chizhmakov, Ogden et al. 2003) for M2 proteins from two commonly studied influenza A strains, Weybridge (with properties similar to Udorn) and Rostock.

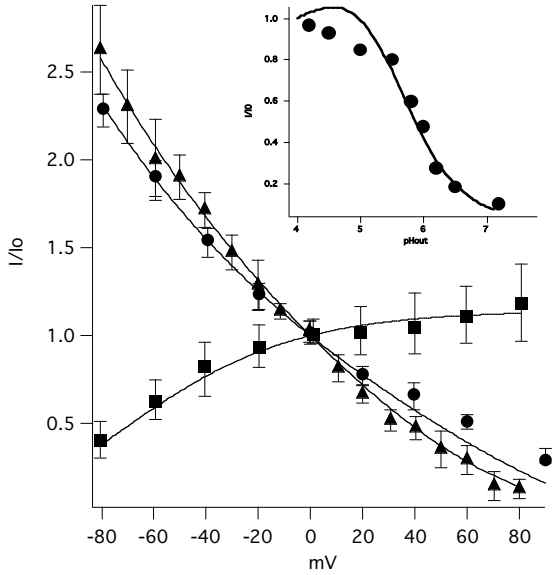

Figure 5.4. Curve fits (lines) to Weybridge strain current-voltage data obtained from (Chizhmakov, Ogden et al. 2003) for different pH gradients: pH_{in}/pH_{out} = 6/8 (circles), 7/5 (triangles), and 8/6 (squares). Inset is fit (line) and data (points) of chord conductance versus external pH from an earlier reference (Chizhmakov, Geraghty et al. 1996). Current-voltage and current-pH data were fit together using common (global) model parameters. The best fit outside (conformation "M") and inside (conformation "M*") pK_a's were 7.9 and 5.1 respectively; the rates of structural interconversion were assumed to be rapid and not rate-limiting. Site electrical distances *d1, d2, d3, d4* and *d5* were 0.24, 0.24, 0.5 (fixed), 0.23 and 0.49 respectively.

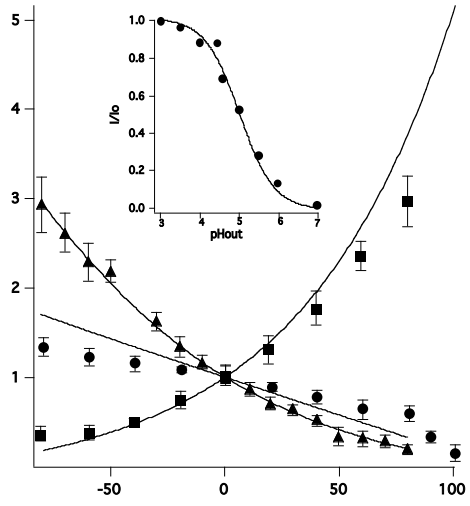

Figure 5.5. Curve fits (lines) to Rostock strain M2 current-voltage data obtained from (Chizhmakov, Ogden et al. 2003) for different pH gradients: pHin/pHout = 6/8 (circles), 7/5 (triangles), and 8/6 (squares). Inset is fit (line) and data (points) of 0 mV current normalized to pH_{out}=3 versus external pH. IV and current-pH data were fit together using common (global) model parameters. As with Figure 4.4, the "M" and "M*" pK_a's were fixed at 7.9 and 5.1 respectively. The site electrical distances could not be stably fit, but setting them to 0.5, 0.5, and 0.5, and 0.9 allowed a reasonable fit. Alternatively, an equally good fit could be gotten with "M" and "M*" pK_a's of 8.9 and 5.4 respectively and different "on" rate constants for protonation.

From Figures 5.4 and 5.5, we conclude that even a simplified two-conformation, one-proton transporter model can be globally fit to electrophysiological data from WT A/M2 strains with reasonable output parameters. Of particular interest are the fitted pK_a values "M" and "M*" for the "open-out" and "open-in" conformation respectively. The "M" pK_a is high at ~8-9 depending on the strain and fit, indicating that the out-open state binds protons very stably. This is generally consistent with the high pK_a values observed for the first two protons bound by Cross *et al. (Hu, Fu et al. 2006)*, and with the high pK_a conformation being a combination of the open-out structures observed at pH 8 (solution NMR (Schnell and Chou 2008)) and pH 6.5 (high-resolution X-ray, Chapter 3), the latter with its proton-stabilizing water clusters. By contrast, the "M*" pK_a is much lower at ~5, indicating that once the "open-in" conformation (represented by the low pH crystal structure (Stouffer, Acharya et al. 2008)) is assumed, the proton is readily released to the viral interior. Interestingly, these pK_a values also imply that the stable and rapid binding of protons by the "open-out" form is enough to facilitate what appears structurally to be a high-barrier conformational transition to the "open-in" form, where Arg 44-Asp 45 salt bridges have been broken. At the minimum, this transition takes place at a fast enough rate so as not to interfere with conduction. Note also that while the current-pH curve (Figures 5.4 and 5.5, insets) is not fit above pH 7.5, the curve fit line tends to slightly underestimate the flux at the high pH limit. This feature of the model will become more apparent in its next iteration, where higher pH_{out} values are explored.

We now extend the simple transporter model to one that better reflects our understanding of the multiple conformational states and proton binding events that M2 undergoes. Chizhmakov *et al*. (Chizhmakov, Geraghty et al. 1996) postulated that M2 is activated with the first proton it binds, and the second (or, according to the measurements of Cross *et al*. (Hu, Fu et al. 2006), third) protonation event is required for conduction. This hypothesis is supported by the observation that outward (reverse) proton transport through M2 is much slower at pH_{in} 6, pH_{out} 8 then at pH_{in} 6, pH_{out} 6.5, in both cases with an outward-driving electrical potential (Chizhmakov, Ogden et al. 2003). Therefore, according to the hypothesis, the accelerating effects of the outward proton gradient are negated since more of the protein is trapped in an inactive conformation at higher pH_{out}. We thus constructed a more complex transporter model (Figure 5.6) where the first protonation step (a double protonation according to Cross *et al*. (Hu, Fu et al. 2006)) activates or primes the protein to enter the transport cycle. We hypothesized that the inactive, "A" state is represented by the solution NMR structure at pH 8 (Schnell and Chou 2008), whereas the "B" and "C" states are represented by the high-resolution pH 6.5 (Chapter 3) and lower-resolution pH ~5 crystal structures (Stouffer, Acharya et al. 2008), respectively.

Importantly, the activating protons in this variant of the model can only be bound from or released to the outside, extraviral compartment, and therefore are nonconducting in the analysis. For the remaining "open-out" and "open-in" states, we allowed a secondary pathway for protonation and deprotonation from the non-favored compartment to be fully consistent with the water accessibility profiles of the crystal structures (see e.g. Chapter 3), although in our fits the contribution of these pathways was kept very minor and was essentially negligible unless otherwise indicated.

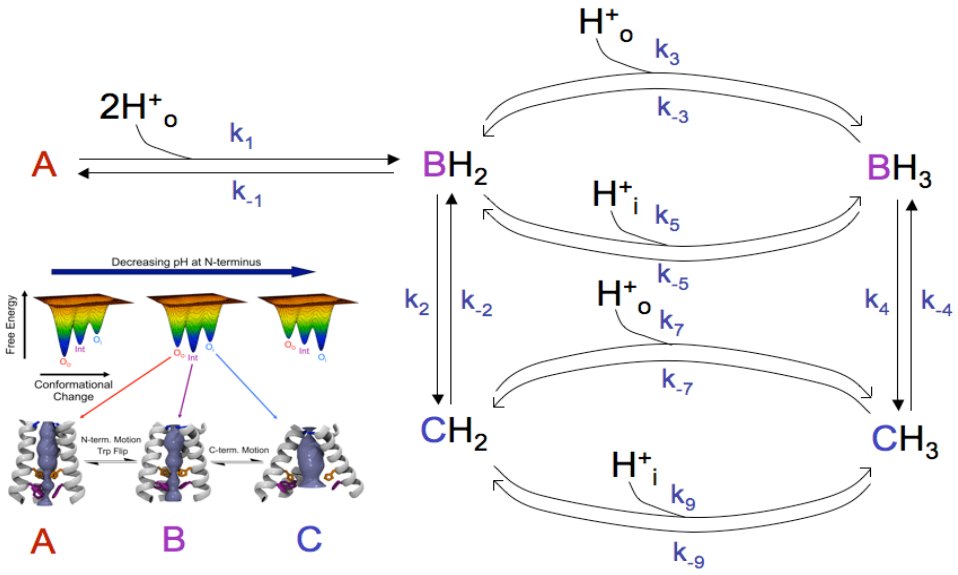

Figure 5.6. Transporter model with added activation step (A - BH_2). H^+_o designates outside protons, H^+_i designates inside protons. The M2 TM structures proposed to describe the A, B, and C conformational states are shown together with the mechanistic hypothesis in the inset on the lower left. The rate constants of minor pathways defined by k_5, k_{-5}, k_7, and k_{-7} were kept to at most one-tenth the value of those corresponding to the major pathways defined by k_3, k_{-3}, k_9, and k_{-9} when fitting WT flux data.

The global fitting results of the expanded transporter model to wild type protein flux data are shown in Figure 5.7.

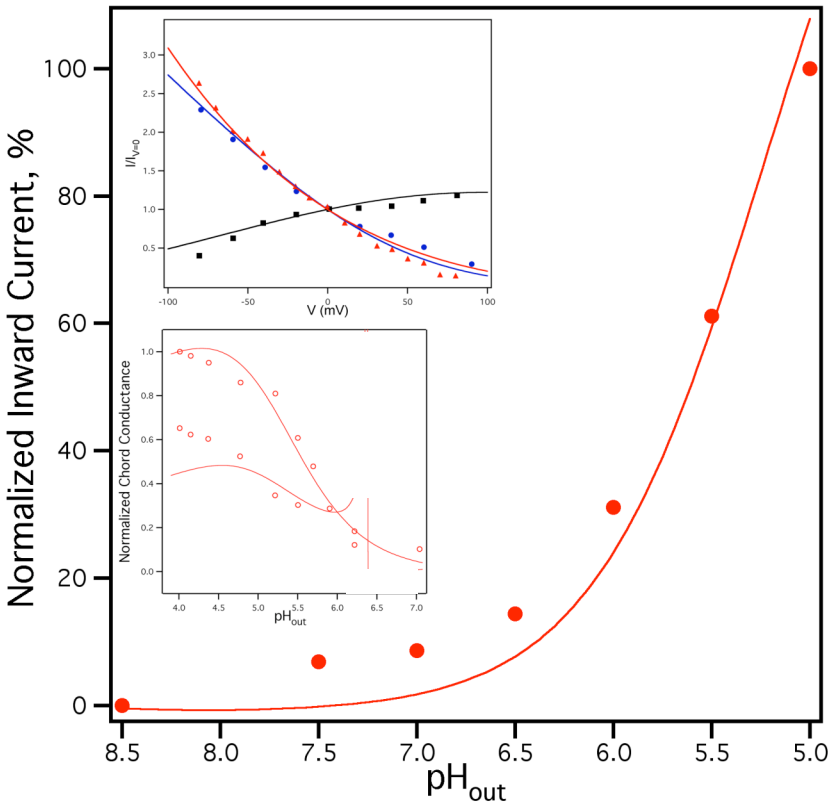

Figure 5.7. Combined global fit of activating transporter model to Udorn and Weybridge electrophysiological data. Main panel, pH-dependent inward fluxes of Udorn A/M2 (data from Victoria Balannik, Pinto Laboratory). Upper inset, current-voltage data from Weybridge A/M2 (Chizhmakov, Ogden et al. 2003) plotted with symbols as in Figure 4.4. Lower inset, pH-dependent chord conductance data at -60 mV (upper trace) and +60 mV (lower trace), normalized to -60 mV, pH 4 (Chizhmakov, Geraghty et al. 1996). The chord conductance function at +60 mV has a discontinuity that is reflected in the fitted line.

Again, the curve fitting exercise was largely successful in recapitulating the principal functional trends exhibited by the protein. Changes in the pK_a values for binding the first two protons (modeled as a fully cooperative process) did not significantly influence the fitting results if the sum of the two pK_as was higher than ~15.5. Lower sum values slightly altered the predicted I-V curves but not the chord conductance and flux-pH relationships, as expected for a non-

conducting process. These pK_a values were therefore held at 8.2 each, as measured by Cross *et al.*(Hu, Fu et al. 2006). Changes to the combined two-proton on-rate did not significantly influence the fit results; this value was held at $5x10^{17}$ $M^{-2}s^{-2}$ reflecting average individual on-rates of ~$7x10^{8}$ $M^{-1}sec^{-1}$, consistent with an unimpeded, near diffusion-limited protonation event. Because this activation process was non-conducting, the on and off rates for the first two protons were modeled as voltage-independent, as were the minor rate processes.

A number of pK_a values for the "B" and "C" state gave good fits to the data; the rate constants for conformational transitions k_2 and k_{-4} were fixed at 10^7 sec^{-1} so as not to be rate-determining; k_4 was allowed to float in the fit and k_{-2} was calculated by applying microscopic reversibility to the cycle. Multiple minima were found that provided adequate fits to the data. To select the process most representative of reality, an additional constraint was applied to select a combination of "B" and "C" pK_as and k_4 values such that the population-weighted pK_a of the "B" and "C" states at equilibrium was near 6.3, the pK_a value observed for the third protonation of the M2 bundle by Cross *et al*. (Hu, Fu et al. 2006). A well-fitting solution satisfying this constraint was found, with a "B" state pK_a of 6.6 and a "C" state pK_a of 4.4. These results show a similar pK_a trend to what was seen with the basic transporter model discussed above. The pK_a values are thus consistent with the argument that the intermediate pH "open-out" state has a higher affinity for protons than the low pH favored "open-in" state, thus facilitating inward proton transport over outward.

Electrical distances were fit as for the previous model, with the addition of two more parameters for the BH_2-CH_2 transition; in imposing voltage dependence, k_2 was multiplied by e^{-d6*V}, while k_{-2} was multiplied by e^{d7*V}, with the best fit values for d6 and d7 at 0.26 and 0.23 respectively. For the BH_2-BH_3-CH_3-CH_2 cycle, d1 was 0.59, d2-d4 were 0.69, and d5 was 1. On rates for principal pathways were allowed to float within reasonable ranges expected for diffusion-limited processes (10^7-10^9 M^{-1} sec^{-1}).

While successful in capturing the key trends in M2 behavior, the fit results from this model also show a number of limitations. The voltage-current fits in Figure 5.7 are slightly worse than those in Figure 5.4, most likely because data sets from two similar but not identical M2 strains were combined in the global fitting. A good fit is seen for the chord conductance at -60 mV, but the fit to chord conductance at +60 mV is worse, likely because that function involves a discontinuity in the middle of the data being fit, and also because a fourth protonation state, not considered in the model, is probably involved at very low pH_{out} values. Finally, the fit to the flux-pH relationship shown in the main panel significantly underestimates flux at low pH regimes, a problem that persists even when the rest of the data, plotted in the insets (and obtained from a different M2 strain) are excluded from the fitting. The discrepancy is also not resolved when small changes in the pH_{in} parameter are permitted (to allow for deviations from the assumed intra-oocyte pH).

In summary, while providing an adequate fit to multi-strain functional data, this model cannot be made to account for the small degree of conductance that takes place at high pH_{out} regimes, for which additional pathways must be added. We hypothesized that by allowing the activating two protons in our model to be conducted, and thus bound and removed from both inside and outside the membrane, better agreement would be achieved with the WT Udorn flux-pH trace.

We therefore augmented the transporter model as shown in Figure 5.8 to allow the A and B states to conduct the first two protons bound.

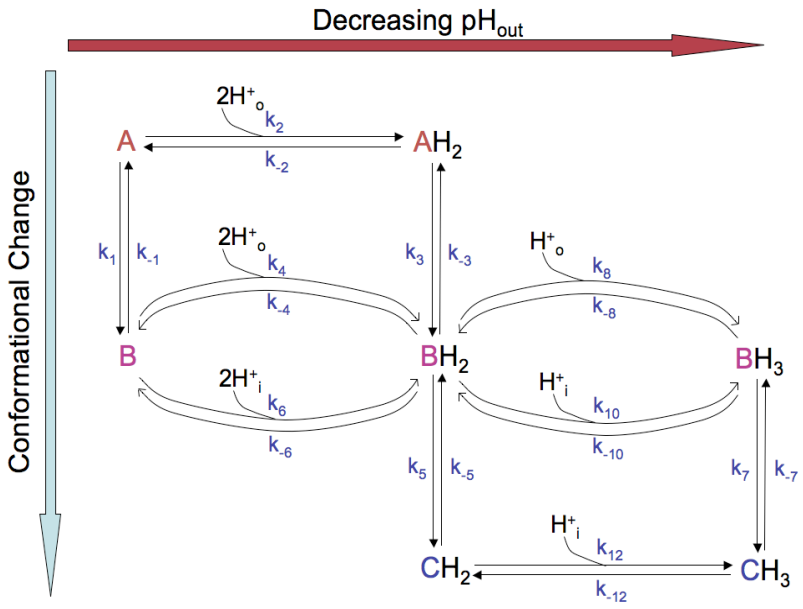

Figure 5.8. Augmented structure-based M2 transport mechanism. Note that the first two protons can now be conducted via the A-AH$_2$-BH$_2$-B-A and B-BH$_2$-B cycles.

The augmented model was globally fit to the same mixed Udorn/Weybridge data shown in Figure 5.7 in a similar fashion to the previous mechanism. The results of the fit are shown in Figure 5.9.

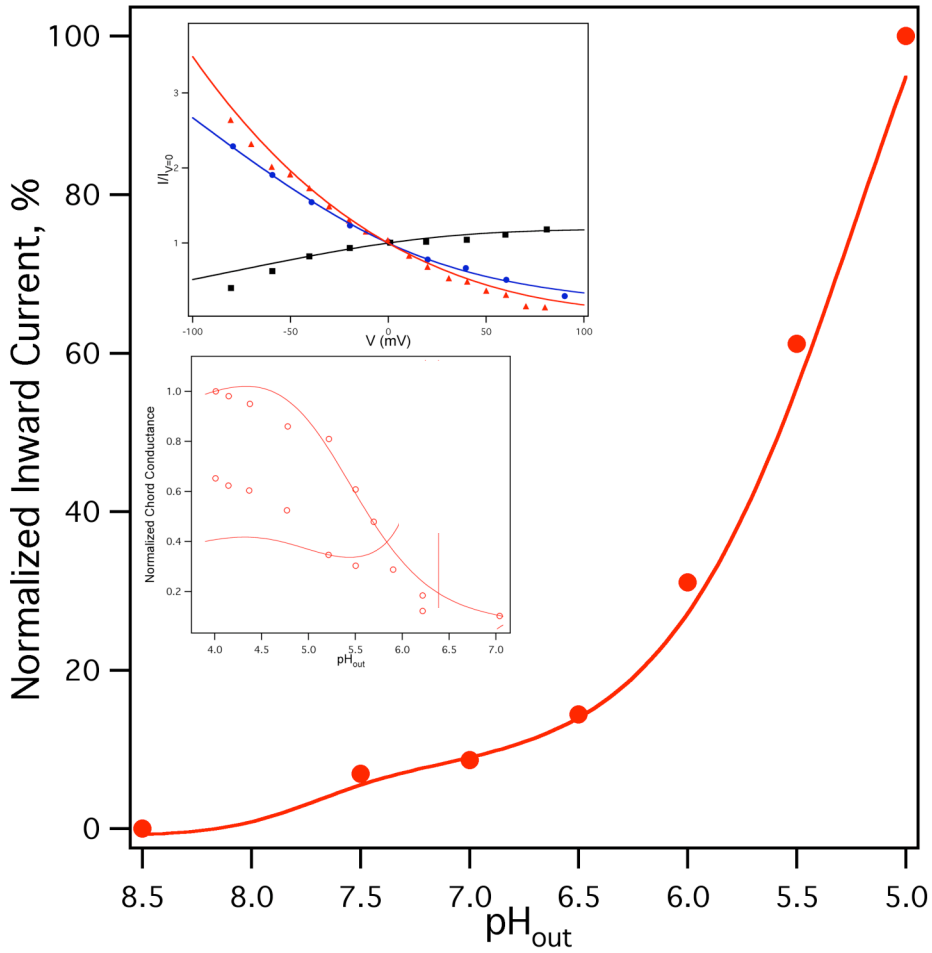

Figure 5.9. Combined global fit of augmented transporter model to functional data, displayed as in Figure 5.7. The assumed oocyte pH_{in} value for the flux-pH relationship shown in the main panel was allowed to vary slightly (by ¾ of one unit) to obtain optimal fitting results, as described in the text.

The rate constants for minor circuits, defined by k_4, k_{-4}, k_{10}, and k_{-10}, were again constrained to be at most $1/10^{th}$ of the values of the corresponding major pathways and were modeled as voltage-independent. A good fit to the data was obtained with k_2 and k_6 set to 10^{17} $M^{-2}s^{-2}$, indicating a diffusion-limited process. k_1, k_3, k_{-3}, k_5, and k_{-7} were set to 10^7 s^{-1} to represent rapid conformational transitions. The pK_a values for A, B, BH_2, and CH_2 were 16.4, 15.9 (both cooperative double protonations), 6.6, and 4.4 respectively, and were again constrained to agree

with the population-normalized pK_a values observed by Cross *et al*. (Hu, Fu et al. 2006). k_7, k_8, and k_{12} were 70,000 s^{-1}, $3x10^7$ $M^{-1}s^{-1}$ and $2x10^8$ $M^{-1}s^{-1}$ respectively. Electrical distances for the BH_2-BH_3-CH_2-CH_3 circuit were 0.59,0.68,0.69,0.69 and 1, in agreement with those fit by the simpler activation model. Electrical distances for the A-AH_2-BH_2-B circuit were 0, 0.05, 0.3, 0.3, and 0.3, lower than those for the three-proton circuit reflecting the decreased charge of the species involved. Similarly to the case of the previous model, k_5 was multiplied by $e^{-0.24*V}$, while k_{-5} was multiplied by $e^{0.25*V}$ for best-fit voltage dependence.

An improved fit was obtained to the voltage-current curves from the Weybridge protein, and the fit was again good for the -60 mV chord conductance-pH relationship. Similarly to the previous model, the +60 mV chord conductance was more difficult to fit, most likely because of the involvement of a fourth protonation site at the very low pH regimes where the fit is especially poor, and a discontinuity in the function at higher pH. Notably, an excellent fit was obtained to the Udorn flux-pH relationship in oocytes shown in the main panel in Figure 5.9. Since the oocyte internal pH is not precisely measured during every experiment and instead is based upon a previously measured reference value, its assigned value in the fit was allowed to vary slightly. Setting pH_{in} to 7.5 instead of 7.25 resulted in a good curve fit that captured the biphasic nature of the activation curve with a rise in flux at high pH, and an excellent fit as shown above was obtained by setting pH_{in} to 8.

By incorporating the ability to conduct the first two protons bound (though at a low level, with correspondingly high pK_a values), the augmented model was able to account for the previously unexplained current observed at high pH in the flux-pH curve. The pK_a values are again higher for the outside protonation events than for the inside ones, explaining the unidirectional proton flow facilitated by M2. This structure-based model, unifying conformational changes of the protein with protonation events governed by spectroscopically defined pK_a values (Hu, Fu et al. 2006), is now successfully able to describe all of the tested electrophysiological data on M2 obtained above pH

5 with a relatively simple kinetic scheme. The successful fit of the model reinforces the mechanistic hypothesis being developed in this and previous chapters, that M2 conducts protons by pH-driven shifts in its structural equilibrium to select conformations that favor outer proton binding and inward proton release.

To test our hypothesis further, we attempted to fit the augmented model to the unusual pH activation profiles observed for certain pore-lining residue mutants of M2, such as the Ser31Gly variant shown in Figure 5.3. This model was able to give an adequate fit to the mutant data as shown in Figure 5.10, after changes in protonation rates, pK_a values and voltage dependences.

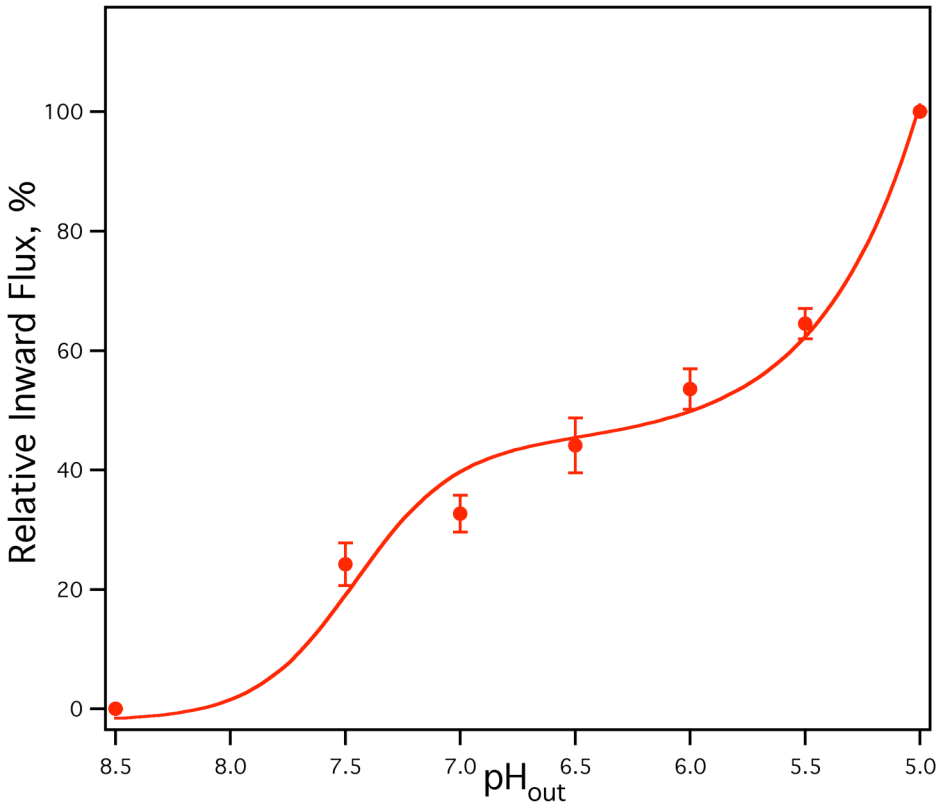

Figure 5.10. Fit of augmented structure-based model to Ser31Gly mutant data (Victoria Balannik, Pinto lab, unpublished). pH_{in} was set to 8.0, as in the previous example.

As shown in Figures 5.9 and 5.10, the augmented model is not only able to fully account for the electrophysiological properties of wild-type A/M2, but can also shed light on the unusual behavior of Ser31Gly, which has a pH-activation profile similar to that of a number of other pore-lining residue mutants. The key differences include lower pK_a values for A (double pK_a of 14) and B (double pK_a of 13.3), BH_2 (4.9) and CH_2 (3.4) that are consistent with higher off-rates. Also required was a faster minor pathway protonation rate constant (k_4) for the B species from outside the protein, indicating that a large portion of the high pH conductance must take place across the B species in the mutant protein. This change accounts for the significantly greater flux observed through the mutant at higher pH_{out}. The results suggest that the "B" state of the mutant variants is leakier and less rectifying than that of wildtype, allowing for facile protonation and deprotonation of the His residues on either side of the membrane. Therefore, for the intermediate pH B conformation in both the WT (releases first two protons inside, binds 3rd outside) and the mutant protein, the strict "open-in" – "open-out" ratchet mechanism as previously proposed appears to be violated, since the His residues in this conformation must be significantly accessible to waters from both inside and outside the pore in order to fit the data well. This phenomenon was also suggested by the water wire analysis of the high-resolution crystal structure in Figure 3.6.

5.4. Conclusions: lessons learned from modeling function of WT A/M2 and functionally perturbed mutants.

In this chapter, we constructed a structure-based model of A/M2 proton transport, informed by our findings in the previous sections of the thesis that have set the stage for quantitative mechanistic analysis. Even a simple, two-conformation one-proton model can capture many of the key functional properties of M2 and return qualitatively meaningful parameters. However, we needed to expand our analysis to a three-conformation, three-proton model to reflect our understanding of the pH-driven structural transitions of the protein, and to take account of the experimentally observed pK_a values for its histidine 37 residues (Hu, Fu et al. 2006). A model that allows for

conduction of the first two protons bound performs substantially better than one treating these protons as channel activators only, shedding light on the structural basis of the high-pH flux observed for WT A/M2 and indicating that certain conformations in the equilibrium may be significantly accessible to both external and internal waters. The validity of our modeling approach was further confirmed by its ability to describe a highly perturbed flux profile of a mutant A/M2 variant, where the intermediate pH conformational state was found to be considerably less rectifying.

In summary, we have quantitatively combined our understanding of the structural changes and protonation events of M2 into a simple, testable kinetic mechanism that performs very well in describing key attributes of the protein's structure and function. In the future, these and similar models can be correlated to the yet-to-be determined structures of functionally interesting mutant variants to further understand the structure-function correlates of this amazing, minimalistic, membrane protein.

Chapter 6: Testing the geometric and electronic determinants of function at the A/M2 histidine 37 residue

6.1. Review of literature on His 37 mutagenesis and rationale for unnatural amino acid substitutions.

As discussed throughout this thesis, histidine 37 is the most important residue of the A/M2 protein from the standpoint of its ion transport function. Its sidechain mediates the external pH activation of the protein (Wang, Lamb et al. 1995) and its high degree of proton selectivity (Chizhmakov, Geraghty et al. 1996), while forming a part of a highly tuned proton transport pathway within the protein's transmembrane domain through interactions with ordered water molecules in the aqueous pore (Chapter 3). This unique arrangement underlies the highly perturbed pK_a values of the His 37 sidechains in the protein (Hu, Fu et al. 2006), which enable the tetramer to remain assembled while stably accommodating at least three positive charges on the imidazole sidechains.

It has been demonstrated early on that mutations at the His 37 residue abrogate the protein's pH regulation and sometimes lead to dramatically altered channel behavior that results in oocyte death (Wang, Lamb et al. 1995). More detailed experiments with several mutant constructs where His 37 was mutated to a small residue (Gly, Ser, Thr) established that the mutant proteins had markedly decreased proton selectivity; in particular His37Gly was shown to conduct Na^+ and K^+, but not Cl^- (Venkataraman, Lamb et al. 2005). Remarkably, native-like electrophysiological properties could be largely restored to this mutant by using free imidazole (a molecule of the same chemical structure as the ring in the His side chain) in the oocyte bathing buffer (Figure 6.1). Partial success in this "chemical rescue" experiment was also observed when adding methylimidazole (which has a similar solution pK_a value). However, adding much larger, substituted heterocyclic buffers (morpholine- and pyridine-based) of similar pK_a did not result in

increased currents at low pH; and the use of a triazole ring with a much lower pK_a was inhibitory to both WT and His37Gly proteins.

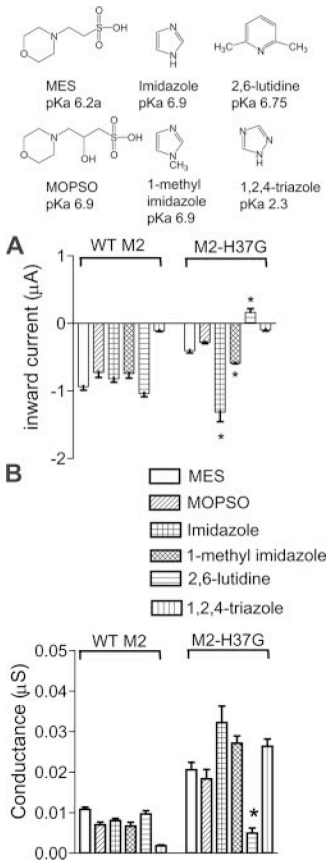

Figure 6.1. Chemical rescue of M2 His37Gly expressed in *Xenopus* oocytes with imidazole bathing buffer. Panel A: Inward currents at pH_{out} 5.5 through WT A/M2 and M2 His37Gly using the buffers indicated. Panel B: Conductance of WT A/M2 and M2 His37Gly measured under the same conditions as in panel A. Figure from (Venkataraman, Lamb et al. 2005).

The successful chemical rescues observed with imidazole and methylimidazole indicate that the M2 aqueous pore is precisely tuned for the His 37 sidechain, but can tolerate some amount of steric variability, since the methyl substitution in methylimidazole originated from a nitrogen and not a carbon as in histidine. The lack of rescue observed from much larger heterocycles is not surprising given the highly tuned arrangement of the imidiazoles in e.g. the high resolution crystal structure described in Chapter 3; there is most likely not enough room for these molecules to assume the required conformation for transport. The result with the triazole is difficult to interpret

given its observed inhibition of the wild type protein when added to bathing buffer, but one might expect that substituting a heterocycle with a significantly lower pK_a would require lower activating pH values to observe transport activity.

In this chapter, we describe experiments building upon the chemical rescue results that are designed to test the functional consequences of very subtle geometric alterations at the His 37 sidechain, as well as of changes in the pK_a at the imidazole ring of His 37. Peptide chemistry is used to introduce histidine-like unnatural amino acids (shown in Figure 6.2.) at position 37 into an M2 fragment. As shown in Figure 6.2, the His 37 sidechain in the wild-type protein is involved in bilateral hydrogen-bonding interactions with the water molecules that are hypothesized to make up the proton transport pathway. We must therefore take into account the consequences of the mutation upon these interactions as well as on the properties of the sidechain itself.

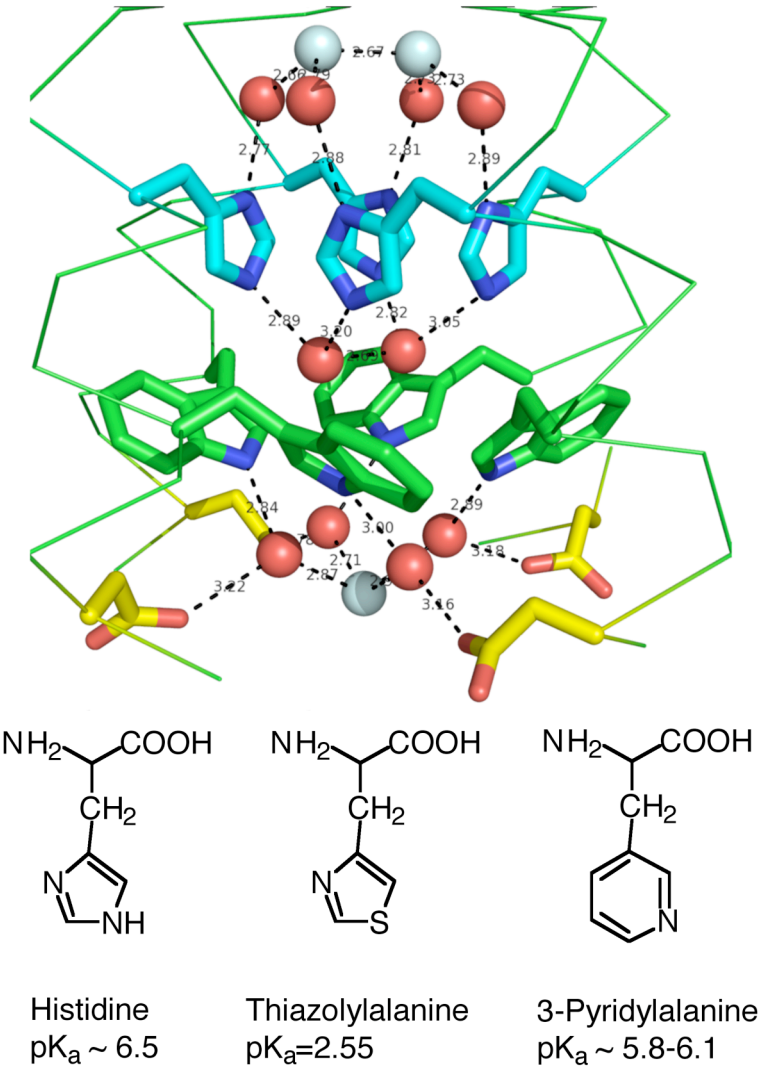

Figure 6.2. Upper panel, His 37 residue in the high-resolution crystal structure (Chapter 3) and its interactions with adjacent water clusters (distances are shown). Note that according to calculations described in Chapter 3, the C-terminal facing nitrogens of the His 37 imidazoles are fully protonated in this structure. Lower panel, histidine and unnatural amino acids introduced at position 37, with the approximate solution pK_a values of their heterocyclic rings.

As will be discussed below, the substitution of a 3-pyridine ring, with similar size and pK_a but with slightly altered geometry leads to relatively inactive protein, at all but very low activating pH values. This finding argues against the thermodynamic gate mechanism proposed earlier by

Sansom *et al*. (Sansom, Kerr et al. 1997), and indicates that the geometrical nature of the imidazole sidechain is optimal for effective transport, potentially because of its ability to form bilateral interactions with water molecules in the aqueous pore. However, when one of the imidazole nitrogens is replaced with sulfur, maintaining the geometry of the ring but dramatically lowering its pK_a and changing its ability to form bilateral hydrogen bonds, the result is a functional, amantadine-sensitive protein with a similarly lowered pK_a of activation. This result further supports the notion that sidechain geometry is key for mediating transport function, and suggests that the thiazole sidechain is able to take part in the requisite water interactions even though only its nitrogen atom can be protonated and donate hydrogen bonds.

6.2. Thermodynamic and functional studies of unnatural amino acid substituted M2 variants: materials and methods.

Peptides (M2 constructs of length 19-46 and 19-62 using the A/Udorn/72 sequence with the C50S mutation; see Fig. 2.10 for sequences) were synthesized by Fmoc solid-phase chemistry as C-terminal carboxamides, and were N-terminally amidated to protect the Cys 19 sidechain. Peptides were synthesized on an Applied Biosystems 433A synthesizer, or, for the longer constructs, manually using a CEM Mars microwave heated reactor, with frequent reaction monitoring. Fmoc-protected L-4-thiazolylalanine and L-3-pyridylalanine were purchased from Synthetech (Albany, OR) and used without further purification in place of Fmoc-His(Trt)-OH at position 37 in the mutant peptides. Peptides were cleaved from the resin and purified according to the procedure used for synM2(19-62) in Chapter 2.5.b.

Functional studies of the WT synM2(19-62) constructs and the corresponding histidine mutants were performed by the author largely according to the protocol outlined in Chapter 2.5.d-e, with the exception of the following minor changes: 990 μL of 1x “K” buffer was used to hydrate the protein/lipid films, and 10 μL of 100 mM HPTS was added; a single overnight cycle of dialysis against pH 7.4 “K” buffer was performed; a newer, more powerful Ushio (Cypress, CA) lamp on

the Aviv fluorometer led to the use of narrower excitation and emission bandwidths during experiments (2 nm instead of 3 nm). All experiments were performed in the presence of valinomycin and DPX (amounts as previously specified); experiments with amantadine were on samples preincubated for at least 3 hours in the presence of the drug, and with drug added to the sample buffer, both as previously described. Sample buffers during the experiments were "Na" buffers set at pH 7.4, 4.9, and 2.4 using phosphoric acid and NaOH.

During experiments in this study done at pH_{out} 4.9 and 2.4, noticeable decreases in the isosbestic signal F_{iso} (ex 417 nm, em 515 nm) were observed compared to runs performed at pH_{out} 7.4, which suggests that some dye may be leaking out of the liposomes at low pH conditions, or that the isosbestic wavelength may not be set with sufficiently high precision. To correct for this effect, the F_{iso} signal for a given set of liposomes determined in low pH experiments (e.g. control, WT, ThiazolylAla) was linearly normalized to its value determined from experiments performed at pH_{out} 7.4, since a similar volume of liposomes was added for each run.

More specifically, the time-averaged F_{iso} signals (obtained at ~90-120 seconds following experiment start) from triplicate runs under each condition were further averaged amongst themselves, and ratios of these values obtained at pH 4.9 vs. pH 7.4 and pH 2.4 vs. pH 7.4 were calculated. Recording of the F_{iso} signal began approximately 90 (t=90-120s) seconds following the start of each run, and the F^- signal was recorded for the first ~45 seconds (t=0-45s) of each run. The time-averaged F_{iso} signal for each low pH run was extrapolated to earlier timepoints with the following operation:

$$F_{iso}(t, pH(X)) = F_{iso(t=90 to 120, pH(X))}[1 + (\frac{AvgF_{iso}(pH7.4)}{AvgF_{iso}(pH(X))} - 1)(1 - \frac{t}{90})]$$

To determine intraliposomal pH, F^- at a given time t was divided by the calculated value of $F_{iso}(t)$, and the ratio used to calculate the pH according to the calibration curve shown in Figure 2.9.

Liposome size was measured using dynamic light scattering as described, and peptide incorporation was quantified using analytical HPLC. However, the incorporation assays were run on a different C4 HPLC column and were standardized using injections of known amounts of synM2(19-62) WT in detergent rather than synM2(22-46) in a mixed aqueous/organic solvent, resulting in a somewhat different calibration setting compared to that obtained previously (Chapter 2). The peptide extinction coefficients at 280 nm used for synM2(19-62) constructs were 6990 $M^{-1}cm^{-1}$ for WT and thiazole constructs, and 7329 $M^{-1}cm^{-1}$ for the pyridylalanine construct. The NIST WebBook entry for 3-ethylpyridine (NIST 2008) was used to calculate the additional contribution of the pyridyl ring to the ε_{280}.

6.3. Mutant constructs form stable tetramers in bilayers at high pH.

Thermodynamic studies of tetramer stability of the synM2(19-46) WT and mutant constructs in DPLC bilayers were performed by Dr. Lidia Cristian according to a previously described protocol (Cristian, Lear et al. 2003). The shorter constructs and thin bilayer were used for this experiment so that some amount of dissociated protein was present, in order that the equilibrium constant be quantified. Longer constructs such as synM2(19-62) and/or thicker bilayers such as POPC result in virtually complete M2 tetramerization and thus cannot be used to determine dissociation constants.

The results of thiol-disulfide equilibrium experiments on synM2(19-46) WT and His mutant constructs in bilayers are shown in Table 6.3.

Construct	pK_{tet} at pH 8
synM2(19-46) Wild Type	8.4
synM2(19-46) 4-Thiazolylalanine	7.8
synM2(19-46) 3-Pyridylalanine	8.3

Table 6.3. Thermodynamic stabilities of wild type and His37-mutant synM2(19-46) constructs. pK_{tet} is $-\log(K_{tet})$, where K_{tet} is the tetramer dissociation equilibrium constant.

The data show that at pH 8 in bilayers, the wild-type and mutant constructs have roughly similar tetramer stabilities (within an order of magnitude), indicating that the introduction of the unnatural amino acid does not substantially destabilize the tetrameric assembly of the protein. This finding paves the way for functional experiments that will determine the impact of the mutations of proton transport, activation, and inhibition.

6.4. Results: Proton transport through His-mutant synM2(19-62) constructs in liposomes.

The proteoliposome flux assay described in Chapter 2.5 and modified as discussed in Chapter 6.2 was used by the author to assay function of the histidine mutant constructs. Because of the requirement for unnatural amino acids, this experiment would be much more difficult to carry out in cell-based systems that rely on protein expression, such as *Xenopus* oocytes. A pH gradient approach is used here because the dynamic range of the indicator dye used precludes reliable measurements below pH ~ 6. Therefore, liposomes are formed at pH 7.4, and diluted into buffer of varying pH for experiments. Fluxes through protein free control liposomes under similar conditions, corrected for differences in surface area and peptide incorporation, are subtracted to isolate currents through the wild type and mutant M2 constructs.

Because the first few data points in the experiment are acquired while sample mixing takes place and cannot be reliably analyzed, it is important to first examine the calculated intraliposomal pH as a function of time to determine whether the fluxes of interest are measurable on the timescale of the experiment. It is possible that under especially large pH gradients, the fastest proton transport regime may be complete before the mixing time is over. If this were the case, transport rates calculated by comparing subsequent timepoints (as is typically done in this experiment) would significantly underestimate the actual velocities. The results of this analysis are presented in Figure 6.4.

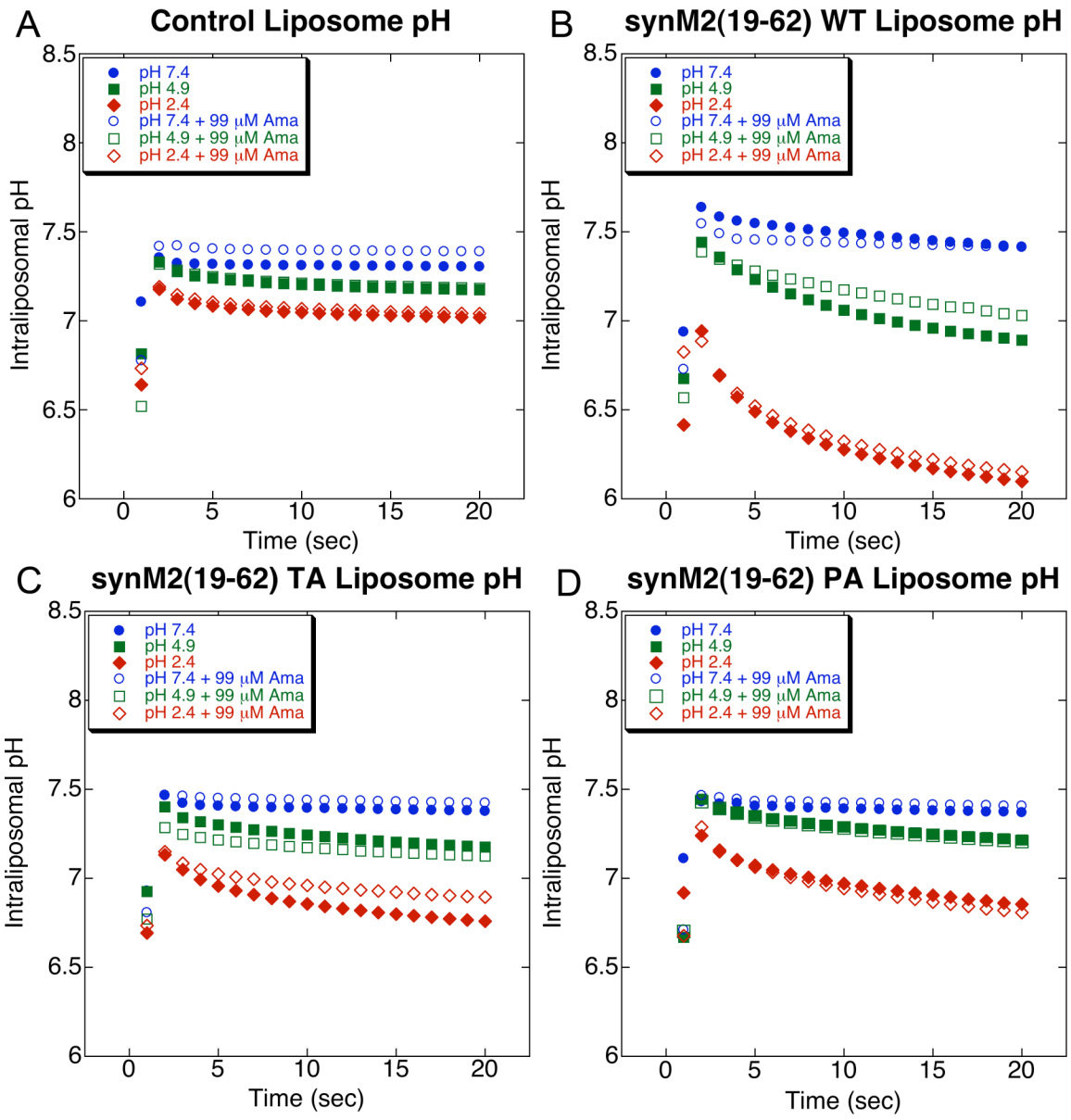

Figure 6.4. Calculated intraliposomal pH in control (A), synM2(19-62) WT (B), and the His 37 mutants synM2(19-62) 4-thiazolylalanine (C) and 3-pyridylalanine (D) proteoliposome experiments.

As seen in Figure 6.4, following mixing, the calculated pH values fall within the dynamic range of the dye, indicating reliable measurements. The starting pH values for thiazolylalanine (Figure 6.4 C) and pyridylalanine (Figure 6.4 D) liposomes do not deviate significantly from those of control

liposomes (Figure 6.4 A) under similar conditions, indicating that the fluxes can be calculated from measurements obtained immediately following mixing. The same holds true for measurements of wild-type M2 proteoliposomes at pH 7.4 and 4.9; however, a significant drop in starting pH (to below 7) is observed for the samples studied at pH 2.4.

The pK_a of the intraliposomal buffer (taken into account in per-tetramer flux calculations presented below) is approximately 7.2; this is where the buffering capacity of the liposome is highest under experimental conditions. Therefore, pH changes in the pH 7.4-7.0 range are consistent with relatively higher proton transport rates than pH changes of equivalent magnitude outside this range, since the buffering becomes less effective. This logic indicates that the wild-type samples observed at pH 2.4 have undergone a very significant and rapid proton uptake during the mixing period (from a starting pH of ~ 7.5 as observed in other WT samples). Therefore, per-tetramer fluxes cannot be reliably calculated for the WT, pH 2.4 sample by comparing post-mixing data points, and are instead to be estimated by quantifying the pH change from ~ 7.5 to the first post-mixing data point with account for buffering capacity and control liposome flux.

The calculated per-tetramer fluxes for the remaining experimental conditions are shown in Figures 6.5, 6.6, and 6.7.

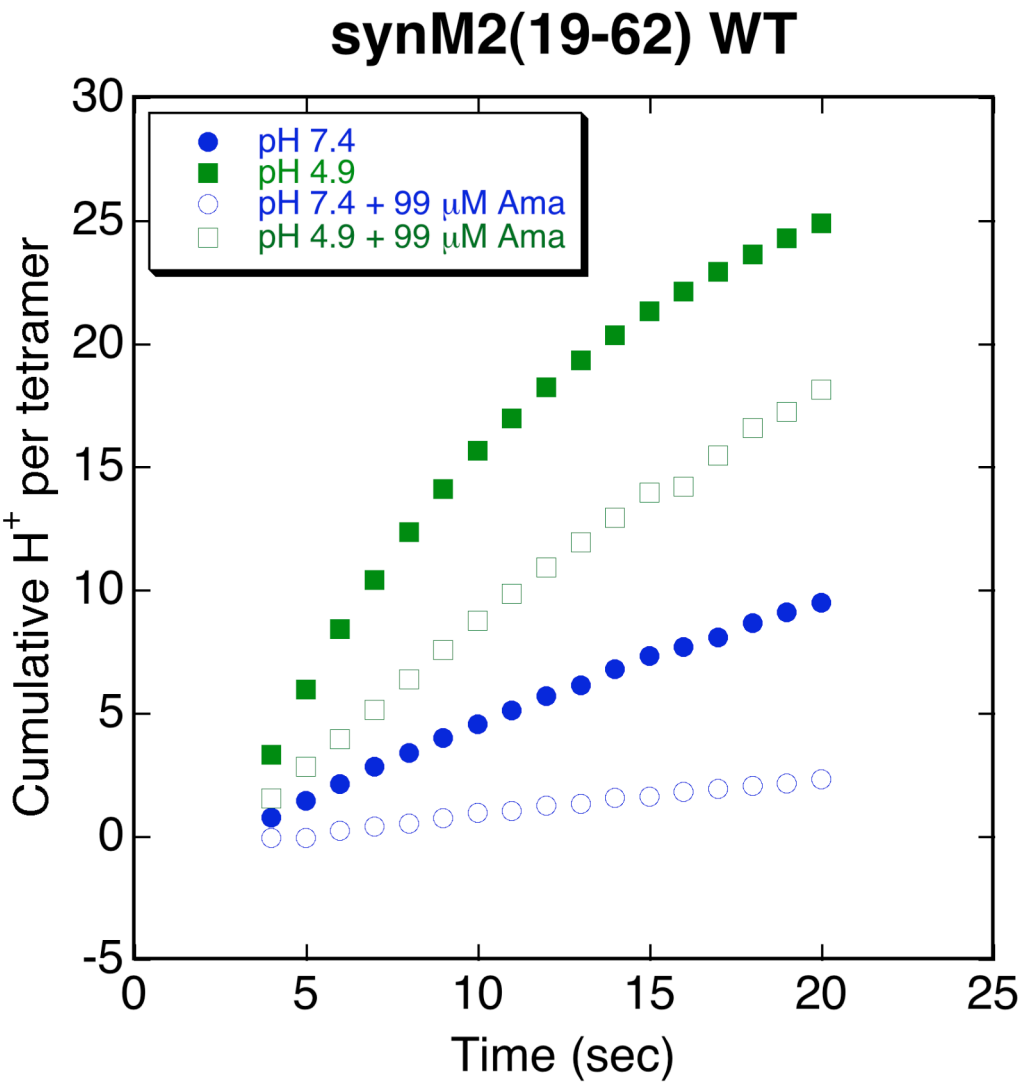

Figure 6.5. Control-corrected fluxes through synM2(19-62) WT proteoliposomes.

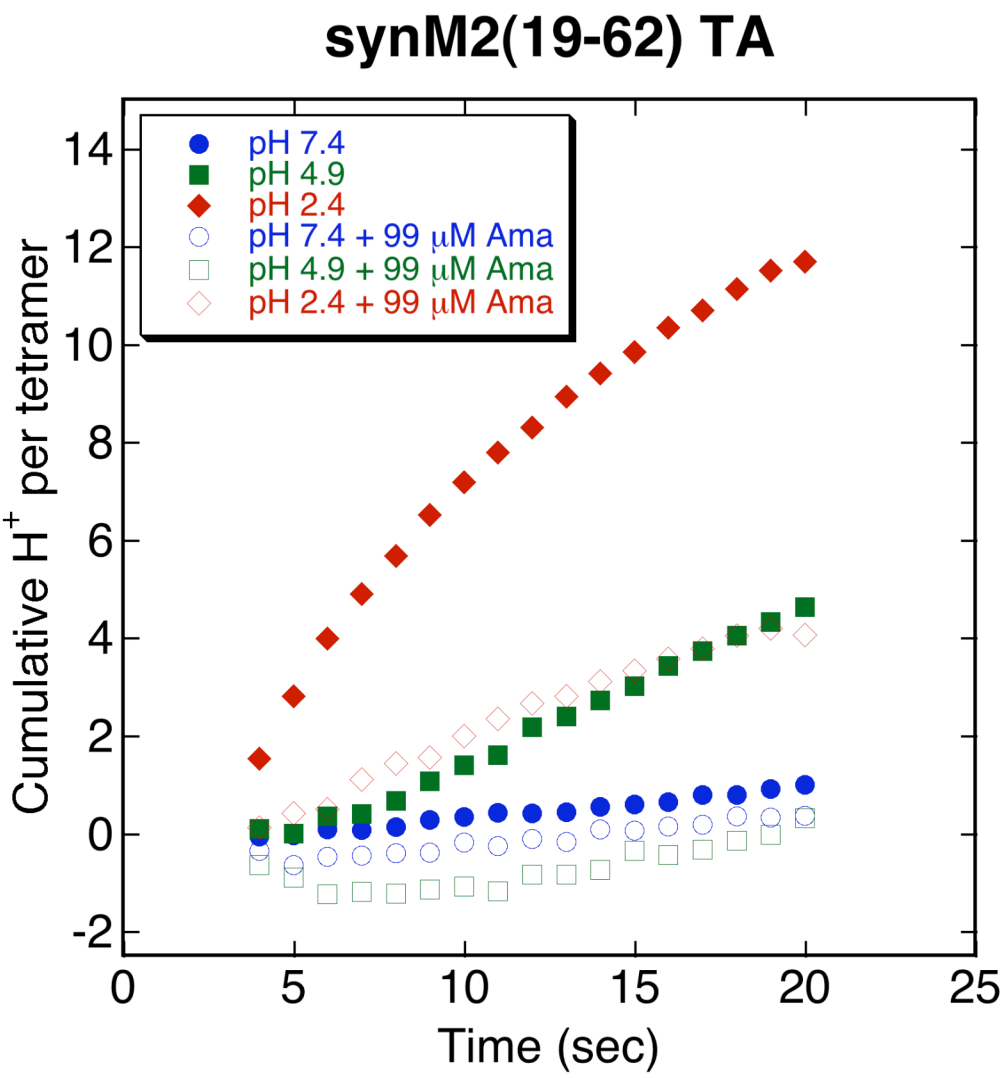

Figure 6.6. Control-corrected fluxes through synM2(19-62) 4-thiazolylalanine proteoliposomes.

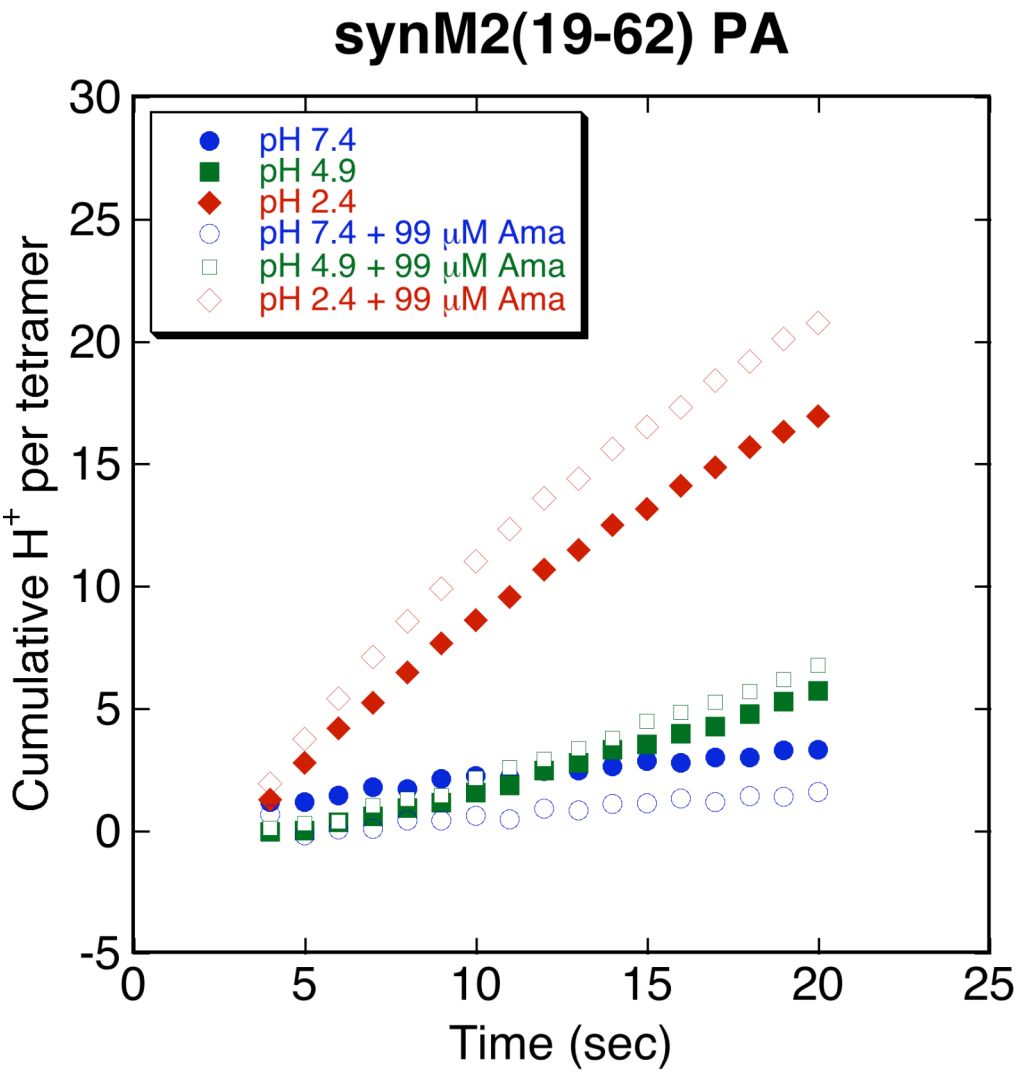

Figure 6.7. Control-corrected fluxes through synM2(19-62) 3-pyridylalanine proteoliposomes.

The results for synM2(19-62) proteoliposomes (Figure 6.5) show that the construct forms a functional, amantadine-sensitive tetramer at bathing buffer pH values of 7.4 and 4.9. An initial transport rate of approximately 1 proton per tetramer is observed at pH 7.4, and increases to approximately 3 protons per tetramer at pH 4.9. The amantadine sensitivity at ~100 μM is nearly complete at pH 7.4, but is decreased at pH 4.9. While the initial transport rate at pH 2.4 could not be calculated from the post-mixing flux curve, it is estimated to be ~15-20 protons per second per tetramer during the mixing process. This rate is significantly lower than expected from other

estimates of maximum M2 current in the literature (Mould, Li et al. 2000), and may reflect dissociation (Salom, Hill et al. 2000) or inactivation of the wild type protein at very acidic pH values. Flux limitation by the amount of valinomycin used (~30 nM, peptide:valinomycin ~10:1) must also be considered but is less likely given the high (10^4) per second turnover rate of valinomycin (Franklin and Snow 2005) and saturating potassium concentrations. No inhibitory effect of amantadine on flux was observed under these conditions.

The synM2(19-62) thiazolylalanine construct (Figure 6.6) was largely inactive at pH 7.4, as may be expected given the much lower pK_a of this sidechain as compared to histidine. However, progressive activation was observed at pH 4.9 and especially pH 2.4, where significant proton currents (~1.5 per second per tetramer) were observed. At all pH values tested, the currents were almost fully amantadine sensitive, indicating a native-like conformation of the tetramer and its N-terminal aqueous pore where amantadine binds.

The synM2(19-62) pyridylalanine construct has a sidechain pK_a similar to that of histidine, but was essentially inactive (Figure 6.7) at pH 7.4, had low activity at pH 4.9, but was more active at pH 2.4 (~1.3 protons per second per tetramer). Furthermore, all currents through this construct were not sensitive to amantadine inhibition at 100 μM.

6.5. Discussion: functional consequences of geometric and electronic changes at His 37 sidechain.

While mutating the His 37 imidazole sidechain to a thiazole or pyridyl ring did not significantly alter M2 tetramer stability at high pH (Table 6.3), the changes led to dramatic functional consequences.

In particular, substitution of the pyridyl ring, with a solution pK_a that is similar or slightly lower than that of imidazole, led to a very slow channel at all but the lowest pH_{out} values (Figure 6.7), where

the current was completely insensitive to amantadine inhibition. This result suggests that the pore of M2 is highly sensitive to the geometry of the sidechain at position 37. The pyridyl is not substantially larger than an imidazole, and a 3-pyridyl group was deliberately used to introduce the nitrogen atom on the side rather than the distal end (4-position) of the ring, so as to mimic the atomic arrangement of a histidine. Nevertheless, the protein was essentially inactive, perhaps because the non-nitrogen edge of the ring did not contain a polar group to interact with the bridging water cluster and Trp 41, or because the pyridine was unable to form the requisite hydrogen bond interactions with the N-terminal water cluster (Chapter 3). A steric clash seems less likely, since the high-resolution crystal structure indicates sufficient room for a slightly enlarged His 37 sidechain.

This finding argues against the mechanistic hypothesis proposed by Sansom *et al*. in 1997 (Sansom, Kerr et al. 1997), where successive protonation of the M2 tetramer leads to the establishment of continuous water wires in the M2 pore as the positively charged His 37 sidechains repel each other. In such a mechanism, channel opening would be dictated by sidechain pK_a, largely irrespective of the precise nature of the substituent. The pyridylalanine variant, with its similar solution pK_a, results in inactive channels at the pH range where WT M2 is active, indicating that transport is sensitive not only to the sidechain pK_a, but to the particulars of its geometry as well. The caveat with this interpretation is that it is unknown whether the pK_a values of the pyridine groups in the protein are similarly perturbed as those of the imidazoles (Hu, Fu et al. 2006). Thus, an alternate explanation is that the pyridines do not experience the charge stabilization afforded by the N-terminal water cluster (perhaps by disrupting it) and therefore bind successive protons much less favorably than imidazoles in the context of the assembled protein.

By contrast, the calculated fluxes through the thiazolylalanine-substituted protein (Figure 6.6) are essentially as expected if the geometrically similar thiazole group adopts a similar conformation and experiences an equivalent extent of charge stabilization as the imidazole, but at an

appropriately lowered pH. In essence, the M2 pH activation profile is shifted lower by 3-4 pH units, corresponding to the difference in the pK_a of the two rings in solution. The currents observed are sensitive to amantadine, indicating that the drug's binding site in the N-terminal aqueous pore is intact. Although the thiazole ring has two polar atoms (nitrogen and sulfur), it can only be protonated on the nitrogen, unlike the histidine imidazole, that can be protonated on either or both nitrogens, and switch between different tautomeric states. The observed activity of the thiazole-containing protein indicates that the water-Trp 41 network on the C-terminal side of the His 37 basket may be stabilized by a polarizable group or atom (e.g. sulfur) but not exclusively a hydrogen bond donor, as is observed for histidine in the high-resolution crystal structure (Chapter 3). This argument is consistent with the observation by Pinto *et al*. (Venkataraman, Lamb et al. 2005) that methylimidazole partially rescues function of a His37Gly M2 mutant, since the methyl group is attached to one of the imidazole nitrogens and eliminates that site as a hydrogen bond donor.

In summary, the findings with His 37-substituted constructs show that the protein is highly sensitive to small changes in geometry at this critical residue; since substitution of a similarly sized heterocyclic ring with a similar solution pK_a results in an inactive protein at the physiological pH range. However, the finding of pK_a-dependent activation upon introduction of a similarly shaped thiazole group result indicates that as long as an imidazole-like geometry and arrangement of polar atoms is maintained, the electronic properties of the ring can be changed to predictably alter the functional properties of the protein.

Chapter 7: Conclusions, lessons learned, and further directions.

Through data presented in this thesis, we have built a bridge between the structural biology, biophysics, and functional electrophysiology of influenza A M2, and unified findings from these scientific domains into a single, comprehensive proton transport mechanism.

First, we have established that a very simple model system consisting of the M2 transmembrane peptide faithfully reproduces the complex electrophysiological properties observed by electrophysiologists with the full length protein. This finding enabled us to correlate the results of structural and biophysical studies on this peptide with the known functional parameters of M2.

We obtained high-resolution crystals of the M2 transmembrane fragment, which yielded a highly detailed picture of the proton transport pathway through the protein's functional core. In conjunction with other structures of M2, the new structure was suggestive of a hypothesis where changes in pH lead to well-defined structural changes in the M2 helical bundle. From these crystals, we also discovered the structural basis for the unexpected stability of bound protons in the M2 tetramer, and learned that highly ordered pore waters play a key functional role in mediating proton transport and stabilization.

We next put our mechanistic hypothesis to the test in an equilibrium bilayer system to determine whether the micelle-derived "snapshot" M2 structures were representative of pH-driven changes in the M2 conformational ensemble in bilayers. We found that the protein indeed undergoes significant changes in its favored conformation, driven by protonation events that take place according to previously determined pK_a values.

As a final test of our mechanism, we constructed mathematical models of proton flux representing our hypothesis and fit them to electrophysiological data collected on M2. We found that the complex functional properties of this protein can be explained by pH-mediated changes in its

conformational ensemble, where the conformations differ in their accessibility to water molecules on either side of the membrane, and in the degree of stability with which they bind protons.

Finally, we zeroed in on the structural and electronic properties of the functionally critical His 37 residues. From our high-resolution crystal structure, these sidechains appeared to be precisely tuned and positioned to mediate interactions with water molecules that we found to be important for function. Using unnatural amino acids, we subtly changed either the geometry or the proton affinity of the His 37 sidechains, and determined that the protein's function and drug sensitivity is highly dependent on the ring structure, but that the ring's pK_a can be changed with predictable functional consequences.

As next steps, our transport mechanism model can be further extended to include the binding of a fourth proton by the M2 tetramer, although the pH ranges at which this process takes place would be rarely encountered in Nature. We can also apply our transport model to help inform a structural basis for the unusual functional properties of certain M2 mutants, as we began to do with the Ser31Gly variant.

Importantly, we can use the mechanism model results to inform drug design, so that the shapes of candidate inhibitors can be well-matched to the predominant protein conformation that the drug will encounter at a given stage of the viral infection cycle. The highly ordered water molecules that are observed near the amantadine binding site in our new crystal structure, and the drug resistance imparted by one of the His 37 mutations that we tested indicate that these water molecules are important from the perspective of transport inhibition, and must be considered along with the protein itself in the design of a new generation of antivirals.

Appendix A: Electron density maps from high resolution structure of M2TM' G34A

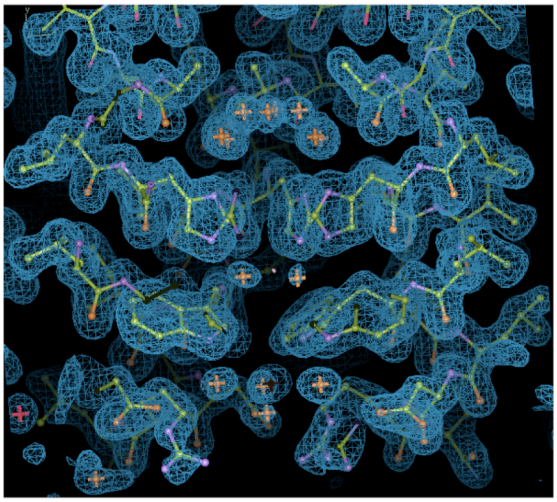

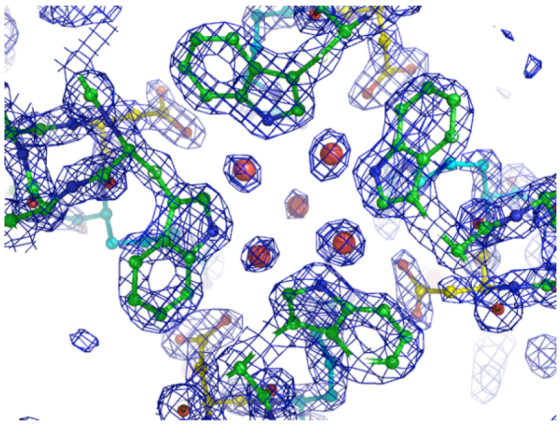

(left) $2F_0 - F_C$ map contoured at 1.1 σ, showing density from solvent molecules above and below the His37 residues. (right) $2F_0 - F_C$ map showing the Trp basket and the exit water cluster. The protein atoms are countered at 1.5 σ. The density from the solvent molecules is contoured at 1.1 σ. Note the poorer density for the middle water, which refined with a higher β-factor (53 $Å^2$).

Appendix B: Proton mobility in the MPSC

The mobility of the proton in the QM/MM simulations is quantified in figure B1 which shows the RMSD of the approximate location of the excess proton for the various simulations presented in this work. The large jumps observed in some trajectories correspond to collective Grothuss hopping motions where several protons jump simultaneously.

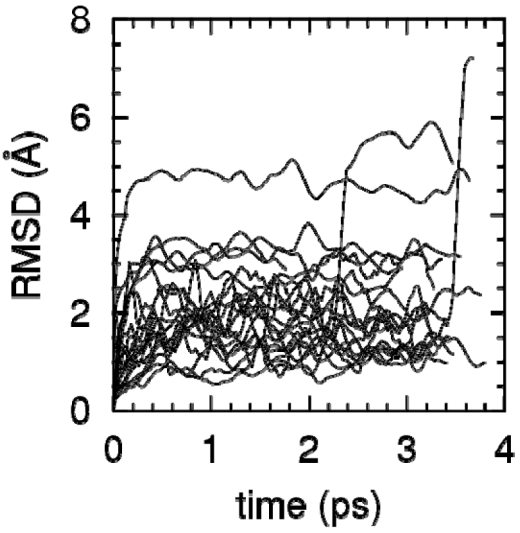

Fig. B1. Root mean square displacement (RMSD) of the three excess protons in QM/MM MD simulations.

Appendix C: Representative Igor Pro procedure files used in global fitting of mechanistic models

Single-proton, two state model:

```
#pragma rtGlobals=1		// Use modern global access method.
#include "JimsmodifiedGlobalFit"
Function xer()
Variable a=.088
Variable b=-.00488
Variable c=-.674
Variable d=-.00488
Variable e=0.008672
Variable f=-.0055

Variable x=(b*f-c*e)/(a*e-b*d)
Variable y=(c*d-a*f)/(a*e-b*d)
print x,y
end

Function AnyFunction(w,xx)
Wave w
Variable xx
if (xx>200)
	xx-=200
	return M2pH(w,xx)
else
	return CurRat(w,xx)
endif
end

Function CurRat(w,xx)
Wave w
Variable xx
Variable k0,k1,k2,k3,k4,k5,k6,k7,Hout,Hin,d1,d2,d3,d4,d5,V,k00,k10,k20,k30,k40,k50,k60,k70
k0=w[0];k1=k0*10^(-w[1]);k2=w[2];k3=w[3];k4=w[5]*10^(-w[4]);k5=w[5];k6=w[6];Hout=exp(-
2.303*w[8]);Hin=exp(-2.303*w[9]);d1=w[10];d2=w[11];d3=w[12];d4=w[13];d5=w[14]
k00=w[0];k10=k0*10^(-w[1]);k20=w[2];k30=w[3];k40=w[5]*10^(-
w[4]);k50=w[5];k60=w[6];k70=(k00*k20*k40*k60)/(k10*k30*k50);k7=k70
V=xx/25.7
k0*=exp(-d1*V);k1*=exp((d2-d1)*V);k2*=exp((d2-d3)*V);k3*=exp((d4-d3)*V);k4*=exp((d4-
d5)*V);k5*=exp((1-d5)*V)

Variable a,b,c,d,e,f,g,h,i,j,k,l
Variable a0,b0,c0,d0,e0,f0,g0,h0,i0,j0,ko,l0
a= -(k0*Hout+k6+k7);b=(k1-k6);c=-k6;d=k6;e=k0*Hout;f=-(k1+k2);g=k3;h=0;i=-k5*Hin;j=(k2-
k5*Hin);k=-(k3+k4+k5*Hin);l=k5*Hin
a0= -(k00*Hout+k60+k70);b0=(k10-k60);c0=-k60;d0=k60;e0=k00*Hout;f0=-
(k10+k20);g0=k30;h0=0;i0=-k50*Hin;j0=(k20-k50*Hin);ko=-(k30+k40+k50*Hin);l0=k50*Hin
//print  a,b,c,d,e,f,g,h,i,j,k,l
Variable S0,S1,S2,S3,S00,S10,S20,S30
S0 = -(b*(h*k-g*l)+c*(f*l-h*j)+d*(g*j-f*k))/(a*(g*j-f*k)+b*(e*k-i*g)+c*(i*f-e*j))
```

```
S00 = -(b0*(h0*ko-g0*l0)+c0*(f0*l0-h0*j0)+d0*(g0*j0-f0*ko))/(a0*(g0*j0-f0*ko)+b0*(e0*ko-
i0*g0)+c0*(i0*f0-e0*j0))

S1=(a*(h*k-g*l)+c*(e*l-i*h)+d*(i*g-e*k))/(a*(g*j-f*k)+b*(e*k-i*g)+c*(i*f-e* j))
S10=(a0*(h0*ko-g0*l0)+c0*(e0*l0-i0*h0)+d0*(i0*g0-e0*ko))/(a0*(g0*j0-f0*ko)+b0*(e0*ko-
i0*g0)+c0*(i0*f0-e0* j0))

S2 =-(a*(h*j-f*l)+b*(e*l-i*h)+d*(i*f-e*j))/(a*(g*j-f*k)+b*(e*k-i*g)+c*(i*f-e*j))
S20 =-(a0*(h0*j0-f0*l0)+b0*(e0*l0-i0*h0)+d0*(i0*f0-e0*j0))/(a0*(g0*j0-f0*ko)+b0*(e0*ko-
i0*g0)+c0*(i0*f0-e0*j0))

S3=1-S0-S1-S2
S30=1-S00-S10-S20
variable curr=(k0*S0*Hout-k1*S1-k5*S3*Hin+k4*S2)
variable curr0=(k00*S00*Hout-k10*S10-k50*S30*Hin+k40*S20)
//print k10,k40
//Print S0,S1,S2,S3,S0+S1+S2+S3
//return curr

return  abs(curr/curr0)
end



Function M2pH(w,xx)
Wave w
Variable xx
variable V=w[7]
w[8]=xx
variable V0=2.303*25.7*(w[9]-w[8])
//print v0
variable cond=IV(w,(V))/(V-V0)
w[8]=4
variable V1=2.303*25.7*(w[9]-4)
variable cond0=IV(w,(V))/(V-V1)
return cond/cond0

end

Function IV(w,xx)
Wave w
Variable xx
Variable k0,k1,k2,k3,k4,k5,k6,k7,Hout,Hin,d1,d2,d3,d4,d5,V,k00,k10,k20,k30,k40,k50,k60,k70
k0=w[0];k1=k0*10^(-w[1]);k2=w[2];k3=w[3];k4=w[5]*10^(-w[4]);k5=w[5];k6=w[6];Hout=exp(-
2.303*w[8]);Hin=exp(-2.303*w[9]);d1=w[10];d2=w[11];d3=w[12];d4=w[13];d5=w[14]
k00=w[0];k10=k0*10^(-w[1]);k20=w[2];k30=w[3];k40=w[5]*10^(-
w[4]);k50=w[5];k60=w[6];k70=(k00*k20*k40*k60)/(k10*k30*k50);k7=k70
//print k70
V=xx/25.7
k0*=exp(-d1*V);k1*=exp((d2-d1)*V);k2*=exp((d2-d3)*V);k3*=exp((d4-d3)*V);k4*=exp((d4-
d5)*V);k5*=exp((1-d5)*V)

Variable a,b,c,d,e,f,g,h,i,j,k,l
```

```
Variable a0,b0,c0,d0,e0,f0,g0,h0,i0,j0,ko,l0
a= -(k0*Hout+k6+k7);b=(k1-k6);c=-k6;d=k6;e=k0*Hout;f=-(k1+k2);g=k3;h=0;i=-k5*Hin;j=(k2-
k5*Hin);k=-(k3+k4+k5*Hin);l=k5*Hin
a0= -(k00*Hout+k60+k70);b0=(k10-k60);c0=-k60;d0=k60;e0=k00*Hout;f0=-
(k10+k20);g0=k30;h0=0;i0=-k50*Hin;j0=(k20-k50*Hin);ko=-(k30+k40+k50*Hin);l0=k50*Hin
//print  a,b,c,d,e,f,g,h,i,j,k,l
Variable S0,S1,S2,S3,S00,S10,S20,S30
S0 = -(b*(h*k-g*l)+c*(f*l-h*j)+d*(g*j-f*k))/(a*(g*j-f*k)+b*(e*k-i*g)+c*(i*f-e*j))
S00 = -(b0*(h0*ko-g0*l0)+c0*(f0*l0-h0*j0)+d0*(g0*j0-f0*ko))/(a0*(g0*j0-f0*ko)+b0*(e0*ko-
i0*g0)+c0*(i0*f0-e0*j0))

S1=(a*(h*k-g*l)+c*(e*l-i*h)+d*(i*g-e*k))/(a*(g*j-f*k)+b*(e*k-i*g)+c*(i*f-e* j))
S10=(a0*(h0*ko-g0*l0)+c0*(e0*l0-i0*h0)+d0*(i0*g0-e0*ko))/(a0*(g0*j0-f0*ko)+b0*(e0*ko-
i0*g0)+c0*(i0*f0-e0* j0))

S2 =-(a*(h*j-f*l)+b*(e*l-i*h)+d*(i*f-e*j))/(a*(g*j-f*k)+b*(e*k-i*g)+c*(i*f-e*j))
S20 =-(a0*(h0*j0-f0*l0)+b0*(e0*l0-i0*h0)+d0*(i0*f0-e0*j0))/(a0*(g0*j0-f0*ko)+b0*(e0*ko-
i0*g0)+c0*(i0*f0-e0*j0))

S3=1-S0-S1-S2
S30=1-S00-S10-S20

variable curr=-(k0*S0*Hout-k1*S1-k5*S3*Hin+k4*S2)
variable curr0=-(k00*S00*Hout-k10*S10-k50*S30*Hin+k40*S20)//Currebt at zero applied voltage
return  (3*9.65*1e5/6.023)*curr
end
Function States(w,xx)
Wave w
Variable xx
Variable k0,k1,k2,k3,k4,k5,k6,k7,Hout,Hin,d1,d2,d3,d4,d5,V,k00,k10,k20,k30,k40,k50,k60,k70
k0=w[0];k1=k0*10^(-w[1]);k2=w[2];k3=w[3];k4=w[5]*10^(-w[4]);k5=w[5];k6=w[6];Hout=exp(-
2.303*w[8]);Hin=exp(-2.303*w[9]);d1=w[10];d2=w[11];d3=w[12];d4=w[13];d5=w[14]
k00=w[0];k10=k0*10^(-w[1]);k20=w[2];k30=w[3];k40=w[5]*10^(-
w[4]);k50=w[5];k60=w[6];k70=(k00*k20*k40*k60)/(k10*k30*k50);k7=k70
V=xx/25.7
k0*=exp(-d1*V);k1*=exp((d2-d1)*V);k2*=exp((d2-d3)*V);k3*=exp((d4-d3)*V);k4*=exp((d4-
d5)*V);k5*=exp((1-d5)*V)

Variable a,b,c,d,e,f,g,h,i,j,k,l
Variable a0,b0,c0,d0,e0,f0,g0,h0,i0,j0,ko,l0
a= -(k0*Hout+k6+k7);b=(k1-k6);c=-k6;d=k6;e=k0*Hout;f=-(k1+k2);g=k3;h=0;i=-k5*Hin;j=(k2-
k5*Hin);k=-(k3+k4+k5*Hin);l=k5*Hin
a0= -(k00*Hout+k60+k70);b0=(k10-k60);c0=-k60;d0=k60;e0=k00*Hout;f0=-
(k10+k20);g0=k30;h0=0;i0=-k50*Hin;j0=(k20-k50*Hin);ko=-(k30+k40+k50*Hin);l0=k50*Hin
//print  a,b,c,d,e,f,g,h,i,j,k,l
Variable S0,S1,S2,S3,S00,S10,S20,S30
S0 = -(b*(h*k-g*l)+c*(f*l-h*j)+d*(g*j-f*k))/(a*(g*j-f*k)+b*(e*k-i*g)+c*(i*f-e*j))
S00 = -(b0*(h0*ko-g0*l0)+c0*(f0*l0-h0*j0)+d0*(g0*j0-f0*ko))/(a0*(g0*j0-f0*ko)+b0*(e0*ko-
i0*g0)+c0*(i0*f0-e0*j0))

S1=(a*(h*k-g*l)+c*(e*l-i*h)+d*(i*g-e*k))/(a*(g*j-f*k)+b*(e*k-i*g)+c*(i*f-e* j))
S10=(a0*(h0*ko-g0*l0)+c0*(e0*l0-i0*h0)+d0*(i0*g0-e0*ko))/(a0*(g0*j0-f0*ko)+b0*(e0*ko-
i0*g0)+c0*(i0*f0-e0* j0))
```

```
S2 =-(a*(h*j-f*l)+b*(e*l-i*h)+d*(i*f-e*j))/(a*(g*j-f*k)+b*(e*k-i*g)+c*(i*f-e*j))
S20 =-(a0*(h0*j0-f0*l0)+b0*(e0*l0-i0*h0)+d0*(i0*f0-e0*j0))/(a0*(g0*j0-f0*ko)+b0*(e0*ko-
i0*g0)+c0*(i0*f0-e0*j0))

S3=1-S0-S1-S2
S30=1-S00-S10-S20
print k7
return S3
end



Window Surface1() : SurfacePlot
	// Mac V. 0.8.0

	PauseUpdate; Silent 1	// Building window...

	// Do nothing if the Surface Plotter XOP is not available.
	if (exists("CreateSurfer") !=4)
		DoAlert 0, "Surface Plotter XOP must be installed"
		return
	endif

	CreateSurfer
	MoveWindow 419,189,1014,725
	ModifySurfer  FactoryDefaults, Update=0
	ModifySurfer/N=Surface1
	ModifySurfer srcWave=root:fit_wave9
	ModifySurfer  srcType=1,plotType=2
	ModifySurfer  setControlView=3
	ModifySurfer  theta=15,  phi=317,  zScale=1,  xStep=1,  yStep=2
	ModifySurfer  frame=3967,  drawFrame=1
	ModifySurfer  drawTicks=5,  axisLabels=88
	ModifySurfer topRGB={0,0,0},  bottomRGB={0,0,0},  backRGB={65535,65535,65535}
	ModifySurfer palette=Grays
	ModifySurfer topContourRGB={0,0,0},  bottomContourRGB={0,0,0}
	ModifySurfer gridRGB={0,0,0}
	ModifySurfer  numContourLevels=15,  contour=3
	ModifySurfer  marker=19,  markerSize=6
	ModifySurfer  fillFrame=0,  imageInterpolation=1,  imageType=1
	ModifySurfer  Update
End


Window Surface0() : SurfacePlot
	// Mac V. 0.8.0

	PauseUpdate; Silent 1	// Building window...

	// Do nothing if the Surface Plotter XOP is not available.
	if (exists("CreateSurfer") !=4)
		DoAlert 0, "Surface Plotter XOP must be installed"
```

```
            return
        endif

        CreateSurfer
        MoveWindow 519,318,1114,854
        ModifySurfer  FactoryDefaults, Update=0
        ModifySurfer/N=Surface0
        ModifySurfer srcWave=(root:wave10,root:wave11,root:wave9)
        ModifySurfer  srcType=4,plotType=5
        ModifySurfer  setControlView=3
        ModifySurfer  theta=15,  phi=317,  zScale=1,  xStep=1,  yStep=2
        ModifySurfer  frame=3967,  drawFrame=1
        ModifySurfer  drawTicks=5,  axisLabels=88
        ModifySurfer topRGB={0,0,0},  bottomRGB={0,0,0},  backRGB={65535,65535,65535}
        ModifySurfer palette=Grays
        ModifySurfer topContourRGB={0,0,0},  bottomContourRGB={0,0,0}
        ModifySurfer gridRGB={0,0,0}
        ModifySurfer  numContourLevels=15,  contour=3
        ModifySurfer  marker=19,  markerSize=6
        ModifySurfer  fillFrame=0,  imageInterpolation=1,  imageType=1
        ModifySurfer  Update
End
```

Three-proton, three state model (first two protons nonconducting)

```
#pragma rtGlobals=1             // Use modern global access method.
#include "JimsmodifiedGlobalFit"

Function AnyFunction(w,xx)
Wave w
Variable xx

if (xx>400)
    xx-=400
    return specact(w,xx)

elseif (xx>300)
    xx-=300
    return M2pH(w,xx)

elseif (xx>200)
        xx-=200
        return M2pH1(w,xx)

else
        return CurRat(w,xx)
endif
end


Function specact(w,xx)
Wave w
Variable xx
```

```
Variable c1,c2,c3,c4,c5,c6,c7,c8,c9,c10,c11,c12
Variable  cm1,cm2,cm3,cm4,cm5,cm6,cm7,cm8,cm9
Variable c1o,c2o,c3o,c4o,c5o,c6o,c7o,c8o,c9o
Variable  cm1o,cm2o,cm3o,cm4o,cm5o,cm6o,cm7o,cm8o,cm9o
Variable Ho,Hi,ed0,ed1,ed2,ed3,ed4,ed5,ed6,ed7,ed8,ed9,ed10,V
Ho=exp(-2.303*xx);Hi=5.62341E-08

c1o=w[2];cm1o=c1o*exp(-2.303*w[3]);c2o=w[4];c3o=w[6];cm3o=c3o*exp(-2.303*w[7])
c4o=w[8];cm4o=w[9];c5o=w[10];c6o=w[12];cm6o=w[13]
c7o=w[14];cm8o=w[16];cm8o=w[17];c9o=w[18];cm9o=c9o*exp(-2.303*w[19])
cm2o=(c2o*c9o*cm4o*cm3o)/(c3o*c4o*cm9o)
w[5]=c10
cm5o=c5o*cm3o/c3o
w[11]=c11
cm7o=c7o*cm9o/c9o
w[15]=c12

ed0=w[20]
ed1=w[21]
ed2=w[22]
ed3=w[23]
ed4=w[24]
ed5=w[25]
ed6=w[26]
ed7=w[27]
ed8=w[28]
ed9=w[29]
ed10=w[30]

V=-20/25.7

c1=c1o
cm1=cm1o
c2=c2o*exp(-ed6*v)
cm2=cm2o*exp(ed7*v)
c3=c3o*exp(-ed1*V)
cm3=cm3o*exp((ed2-ed1)*v)
c4=c4o*exp((ed2-ed3)*v)
cm4=cm4o*exp((ed4-ed3)*v)

c5=c5o
cm5=cm5o

c7=c7o
cm7=cm7o
c9=c9o*exp((1-ed5)*V)
cm9=cm9o*exp((ed4-ed5)*V)

variable A1=c4+cm4
variable A2=cm3+cm5
variable A3=(c5*c7+c3*c9)
variable A4=(c4+cm3+cm4+cm5)
variable A5=(c4+cm5)
```

```
variable A6=(cm7+cm9)
variable A7=(cm4+cm7+cm9)
variable A8=(cm2+cm7+cm9)

variable current
current=-
(2*ho^2*c1*(hi^2*c5*c9*(cm3*cm4+c4*cm7)+hi*(c2*c9*((c4+cm5)*cm7+cm3*(cm4+cm7))+c5*cm
2*(c4*cm7+cm3*(cm4+cm7+cm9))+ho*(c3*c9*(-cm4*cm5+c4*cm7)+c5*c7*(cm3*cm4-c4*cm9)))-
ho*(c2*c7*(cm4*cm5+(c4+cm3+cm5)*cm9)+c3*(ho*c7*(cm4*cm5+c4*cm9)+cm2*(cm4*cm5+c4*c
m9+cm5*(cm7+cm9))))))
variable current2
current2=current/(ho^4*c1*c3*c7*A1+ho*c7*cm1*cm4*A2+ho^3*c1*(c3*c4*cm2+c3*cm2*cm4+c7
*cm3*cm4+hi*A3*A1+c7*cm4*cm5+c2*c7*A4+c3*c4*cm7+c3*cm2*cm7+c3*c4*cm9+c3*cm2*cm9
)+cm1*(hi*c9*cm4*A2+cm2*(cm4*cm5+A5*A6+cm3*A7))+ho^2*c1*(hi^2*c5*c9*A1+hi*(c5*cm2*c
m4+c9*cm3*cm4+c9*cm4*cm5+c2*c9*A4+c5*cm2*cm7+c5*cm2*cm9+c4*c5*A8)+(c2+cm2)*(cm
4*cm5+A5*A6+cm3*A7)))
return current2/100
end




Function CurRat(w,xx)
Wave w
Variable xx
Variable c1,c2,c3,c4,c5,c6,c7,c8,c9,c10,c11,c12
Variable  cm1,cm2,cm3,cm4,cm5,cm6,cm7,cm8,cm9
Variable c1o,c2o,c3o,c4o,c5o,c6o,c7o,c8o,c9o
Variable  cm1o,cm2o,cm3o,cm4o,cm5o,cm6o,cm7o,cm8o,cm9o
Variable Ho,Hi,ed0,ed1,ed2,ed3,ed4,ed5,ed6,ed7,ed8,ed9,ed10,V
Ho=exp(-2.303*w[0]);Hi=exp(-2.303*w[1])

c1o=w[2];cm1o=c1o*exp(-2.303*w[3]);c2o=w[4];c3o=w[6];cm3o=c3o*exp(-2.303*w[7])
c4o=w[8];cm4o=w[9];c5o=w[10];c6o=w[12];cm6o=w[13]
c7o=w[14];cm8o=w[16];cm8o=w[17];c9o=w[18];cm9o=c9o*exp(-2.303*w[19])
cm2o=(c2o*c9o*cm4o*cm3o)/(c3o*c4o*cm9o)
w[5]=c10
cm5o=c5o*cm3o/c3o
w[11]=c11
cm7o=c7o*cm9o/c9o
w[15]=c12

ed0=w[20]
ed1=w[21]
ed2=w[22]
ed3=w[23]
ed4=w[24]
ed5=w[25]
ed6=w[26]
ed7=w[27]
ed8=w[28]
```

```
ed9=w[29]
ed10=w[30]

V=xx/25.7

c1=c1o
cm1=cm1o
c2=c2o*exp(-ed6*v)
cm2=cm2o*exp(ed7*v)
c3=c3o*exp(-ed1*V)
cm3=cm3o*exp((ed2-ed1)*v)
c4=c4o*exp((ed2-ed3)*v)
cm4=cm4o*exp((ed4-ed3)*v)

c5=c5o
cm5=cm5o

c7=c7o
cm7=cm7o
c9=c9o*exp((1-ed5)*V)
cm9=cm9o*exp((ed4-ed5)*V)

variable A1=c4+cm4
variable A2=cm3+cm5
variable A3=(c5*c7+c3*c9)
variable A4=(c4+cm3+cm4+cm5)
variable A5=(c4+cm5)
variable A6=(cm7+cm9)
variable A7=(cm4+cm7+cm9)
variable A8=(cm2+cm7+cm9)

variable current
current=-
(2*ho^2*c1*(hi^2*c5*c9*(cm3*cm4+c4*cm7)+hi*(c2*c9*((c4+cm5)*cm7+cm3*(cm4+cm7))+c5*cm
2*(c4*cm7+cm3*(cm4+cm7+cm9))+ho*(c3*c9*(-cm4*cm5+c4*cm7)+c5*c7*(cm3*cm4-c4*cm9)))-
ho*(c2*c7*(cm4*cm5+(c4+cm3+cm5)*cm9)+c3*(ho*c7*(cm4*cm5+c4*cm9)+cm2*(cm4*cm5+c4*c
m9+cm5*(cm7+cm9))))))
current/=(ho^4*c1*c3*c7*A1+ho*c7*cm1*cm4*A2+ho^3*c1*(c3*c4*cm2+c3*cm2*cm4+c7*cm3*c
m4+hi*A3*A1+c7*cm4*cm5+c2*c7*A4+c3*c4*cm7+c3*cm2*cm7+c3*c4*cm9+c3*cm2*cm9)+cm1*
(hi*c9*cm4*A2+cm2*(cm4*cm5+A5*A6+cm3*A7))+ho^2*c1*(hi^2*c5*c9*A1+hi*(c5*cm2*cm4+c9*
cm3*cm4+c9*cm4*cm5+c2*c9*A4+c5*cm2*cm7+c5*cm2*cm9+c4*c5*A8)+(c2+cm2)*(cm4*cm5+
A5*A6+cm3*A7)))


V=0
c1=c1o
cm1=cm1o
c2=c2o*exp(-ed6*v)
cm2=cm2o*exp(ed7*v)
c3=c3o*exp(-ed1*V)
cm3=cm3o*exp((ed2-ed1)*v)
c4=c4o*exp((ed2-ed3)*v)
cm4=cm4o*exp((ed4-ed3)*v)
```

```
c5=c5o
cm5=cm5o

c7=c7o
cm7=cm7o
c9=c9o*exp((1-ed5)*V)
cm9=cm9o*exp((ed4-ed5)*V)

A1=c4+cm4
A2=cm3+cm5
A3=(c5*c7+c3*c9)
A4=(c4+cm3+cm4+cm5)
A5=(c4+cm5)
A6=(cm7+cm9)
A7=(cm4+cm7+cm9)
A8=(cm2+cm7+cm9)
variable current0
current0=-
(2*ho^2*c1*(hi^2*c5*c9*(cm3*cm4+c4*cm7)+hi*(c2*c9*((c4+cm5)*cm7+cm3*(cm4+cm7))+c5*cm
2*(c4*cm7+cm3*(cm4+cm7+cm9))+ho*(c3*c9*(-cm4*cm5+c4*cm7)+c5*c7*(cm3*cm4-c4*cm9)))-
ho*(c2*c7*(cm4*cm5+(c4+cm3+cm5)*cm9)+c3*(ho*c7*(cm4*cm5+c4*cm9)+cm2*(cm4*cm5+c4*c
m9+cm5*(cm7+cm9))))))
current0/=(ho^4*c1*c3*c7*A1+ho*c7*cm1*cm4*A2+ho^3*c1*(c3*c4*cm2+c3*cm2*cm4+c7*cm3*c
m4+hi*A3*A1+c7*cm4*cm5+c2*c7*A4+c3*c4*cm7+c3*cm2*cm7+c3*c4*cm9+c3*cm2*cm9)+cm1*
(hi*c9*cm4*A2+cm2*(cm4*cm5+A5*A6+cm3*A7))+ho^2*c1*(hi^2*c5*c9*A1+hi*(c5*cm2*cm4+c9*
cm3*cm4+c9*cm4*cm5+c2*c9*A4+c5*cm2*cm7+c5*cm2*cm9+c4*c5*A8)+(c2+cm2)*(cm4*cm5+
A5*A6+cm3*A7)))
variable relcurr=current/current0
return abs(relcurr)
end


Function M2pH(w,xx)
Wave w
Variable xx
variable Vt=-60
w[0]=xx
variable V0=2.303*25.7*(w[1]-w[0])
//print v0
variable cond=phflux(w,(xx))/(Vt-V0)
w[0]=4
variable V1=2.303*25.7*(w[1]-4)
variable cond0=phflux(w,(4))/(Vt-V1)
return cond/cond0

end

Function M2pH1(w,xx)
Wave w
Variable xx
variable V=60
w[0]=xx
```

```
variable V0=2.303*25.7*(w[1]-w[0])
//print v0
variable cond=phflux1(w,(xx))/(V-V0)
w[0]=4
variable V1=2.303*25.7*(w[1]-4)
variable cond0=phflux(w,(4))/(-60-V1)
return cond/cond0

end



Function phflux(w,xx)
Wave w
Variable xx
Variable c1,c2,c3,c4,c5,c6,c7,c8,c9,c10,c11,c12
Variable  cm1,cm2,cm3,cm4,cm5,cm6,cm7,cm8,cm9
Variable c1o,c2o,c3o,c4o,c5o,c6o,c7o,c8o,c9o
Variable  cm1o,cm2o,cm3o,cm4o,cm5o,cm6o,cm7o,cm8o,cm9o
Variable Ho,Hi
Variable ed0,ed1,ed2,ed3,ed4,ed5,ed6,ed7,ed8,ed9,ed10,V
Ho=exp(-2.303*xx);Hi=exp(-2.303*w[1])

c1o=w[2];cm1o=c1o*exp(-2.303*w[3]);c2o=w[4];c3o=w[6];cm3o=c3o*exp(-2.303*w[7])
c4o=w[8];cm4o=w[9];c5o=w[10];c6o=w[12];cm6o=w[13]
c7o=w[14];cm8o=w[16];cm8o=w[17];c9o=w[18];cm9o=c9o*exp(-2.303*w[19])
cm2o=(c2o*c9o*cm4o*cm3o)/(c3o*c4o*cm9o)
w[5]=c10
cm5o=c5o*cm3o/c3o
w[11]=c11
cm7o=c7o*cm9o/c9o
w[15]=c12

ed0=w[20]
ed1=w[21]
ed2=w[22]
ed3=w[23]
ed4=w[24]
ed5=w[25]
ed6=w[26]
ed7=w[27]
ed8=w[28]
ed9=w[29]
ed10=w[30]

V=-60/25.7
c1=c1o
cm1=cm1o
c2=c2o*exp(-ed6*v)
cm2=cm2o*exp(ed7*v)
c3=c3o*exp(-ed1*V)
cm3=cm3o*exp((ed2-ed1)*v)
```

```
c4=c4o*exp((ed2-ed3)*v)
cm4=cm4o*exp((ed4-ed3)*v)

c5=c5o
cm5=cm5o

c7=c7o
cm7=cm7o
c9=c9o*exp((1-ed5)*V)
cm9=cm9o*exp((ed4-ed5)*V)

variable A1=c4+cm4
variable A2=cm3+cm5
variable A3=(c5*c7+c3*c9)
variable A4=(c4+cm3+cm4+cm5)
variable A5=(c4+cm5)
variable A6=(cm7+cm9)
variable A7=(cm4+cm7+cm9)
variable A8=(cm2+cm7+cm9)

variable current1
current1=-
(2*ho^2*c1*(hi^2*c5*c9*(cm3*cm4+c4*cm7)+hi*(c2*c9*((c4+cm5)*cm7+cm3*(cm4+cm7))+c5*cm
2*(c4*cm7+cm3*(cm4+cm7+cm9))+ho*(c3*c9*(-cm4*cm5+c4*cm7)+c5*c7*(cm3*cm4-c4*cm9)))-
ho*(c2*c7*(cm4*cm5+(c4+cm3+cm5)*cm9)+c3*(ho*c7*(cm4*cm5+c4*cm9)+cm2*(cm4*cm5+c4*c
m9+cm5*(cm7+cm9))))))
variable current2
current2=current1/(ho^4*c1*c3*c7*A1+ho*c7*cm1*cm4*A2+ho^3*c1*(c3*c4*cm2+c3*cm2*cm4+c
7*cm3*cm4+hi*A3*A1+c7*cm4*cm5+c2*c7*A4+c3*c4*cm7+c3*cm2*cm7+c3*c4*cm9+c3*cm2*cm
9)+cm1*(hi*c9*cm4*A2+cm2*(cm4*cm5+A5*A6+cm3*A7))+ho^2*c1*(hi^2*c5*c9*A1+hi*(c5*cm2*
cm4+c9*cm3*cm4+c9*cm4*cm5+c2*c9*A4+c5*cm2*cm7+c5*cm2*cm9+c4*c5*A8)+(c2+cm2)*(c
m4*cm5+A5*A6+cm3*A7)))
return -current2
end



Function phflux1(w,xx)
Wave w
Variable xx
Variable c1,c2,c3,c4,c5,c6,c7,c8,c9,c10,c11,c12
Variable  cm1,cm2,cm3,cm4,cm5,cm6,cm7,cm8,cm9
Variable c1o,c2o,c3o,c4o,c5o,c6o,c7o,c8o,c9o
Variable  cm1o,cm2o,cm3o,cm4o,cm5o,cm6o,cm7o,cm8o,cm9o
Variable Ho,Hi
Variable ed0,ed1,ed2,ed3,ed4,ed5,ed6,ed7,ed8,ed9,ed10,V
Ho=exp(-2.303*xx);Hi=exp(-2.303*w[1])

c1o=w[2];cm1o=c1o*exp(-2.303*w[3]);c2o=w[4];c3o=w[6];cm3o=c3o*exp(-2.303*w[7])
c4o=w[8];cm4o=w[9];c5o=w[10];c6o=w[12];cm6o=w[13]
c7o=w[14];cm8o=w[16];cm8o=w[17];c9o=w[18];cm9o=c9o*exp(-2.303*w[19])
cm2o=(c2o*c9o*cm4o*cm3o)/(c3o*c4o*cm9o)
w[5]=c10
```

```
cm5o=c5o*cm3o/c3o
w[11]=c11
cm7o=c7o*cm9o/c9o
w[15]=c12

ed0=w[20]
ed1=w[21]
ed2=w[22]
ed3=w[23]
ed4=w[24]
ed5=w[25]
ed6=w[26]
ed7=w[27]
ed8=w[28]
ed9=w[29]
ed10=w[30]


V=60/25.7
c1=c1o
cm1=cm1o
c2=c2o*exp(-ed6*v)
cm2=cm2o*exp(ed7*v)
c3=c3o*exp(-ed1*V)
cm3=cm3o*exp((ed2-ed1)*v)
c4=c4o*exp((ed2-ed3)*v)
cm4=cm4o*exp((ed4-ed3)*v)

c5=c5o
cm5=cm5o

c7=c7o
cm7=cm7o
c9=c9o*exp((1-ed5)*V)
cm9=cm9o*exp((ed4-ed5)*V)

variable A1=c4+cm4
variable A2=cm3+cm5
variable A3=(c5*c7+c3*c9)
variable A4=(c4+cm3+cm4+cm5)
variable A5=(c4+cm5)
variable A6=(cm7+cm9)
variable A7=(cm4+cm7+cm9)
variable A8=(cm2+cm7+cm9)

variable current1
current1=-
(2*ho^2*c1*(hi^2*c5*c9*(cm3*cm4+c4*cm7)+hi*(c2*c9*((c4+cm5)*cm7+cm3*(cm4+cm7))+c5*cm
2*(c4*cm7+cm3*(cm4+cm7+cm9))+ho*(c3*c9*(-cm4*cm5+c4*cm7)+c5*c7*(cm3*cm4-c4*cm9)))-
ho*(c2*c7*(cm4*cm5+(c4+cm3+cm5)*cm9)+c3*(ho*c7*(cm4*cm5+c4*cm9)+cm2*(cm4*cm5+c4*c
m9+cm5*(cm7+cm9))))))
variable current2
current2=current1/(ho^4*c1*c3*c7*A1+ho*c7*cm1*cm4*A2+ho^3*c1*(c3*c4*cm2+c3*cm2*cm4+c
```

```
7*cm3*cm4+hi*A3*A1+c7*cm4*cm5+c2*c7*A4+c3*c4*cm7+c3*cm2*cm7+c3*c4*cm9+c3*cm2*cm
9)+cm1*(hi*c9*cm4*A2+cm2*(cm4*cm5+A5*A6+cm3*A7))+ho^2*c1*(hi^2*c5*c9*A1+hi*(c5*cm2*
cm4+c9*cm3*cm4+c9*cm4*cm5+c2*c9*A4+c5*cm2*cm7+c5*cm2*cm9+c4*c5*A8)+(c2+cm2)*(c
m4*cm5+A5*A6+cm3*A7)))
return -current2
end


Window SetGuessTable() : Table
        PauseUpdate; Silent 1           // building window...
        String fldrSav0= GetDataFolder(1)
        SetDataFolder root:Packages:GlobalFit:
        Edit/W=(596,169,1395,620) 'Data Sets and Coefficients',AllCoefs,holds,ConWave as "Set
Initial Guesses"
        ModifyTable format(Point)=1,width('Data Sets and Coefficients')=200,alignment(holds)=1
        ModifyTable width(holds)=40,alignment(ConWave)=1
        SetDataFolder fldrSav0
EndMacro
```

Three-proton, three-state model (first two protons conducting)

```
#pragma rtGlobals=1             // Use modern global access method.
#include "JimsmodifiedGlobalFit"

Function AnyFunction(w,xx)
Wave w
Variable xx

if (xx>500)
   xx-=500
   return invchord (w,xx)


elseif (xx>400)
    xx-=400
    return specact(w,xx)

elseif (xx>300)
    xx-=300
    return M2pH(w,xx)

elseif (xx>200)
        xx-=200
        return M2pH1(w,xx)

else
        return CurRat(w,xx)
endif
end


Function specact(w,xx)
Wave w
```

```
Variable xx
Variable c1,c2,c3,c4,c5,c6,c7,c8,c9,c10,c12
Variable  cm1,cm2,cm3,cm4,cm5,cm6,cm7,cm8,cm9,cm10,cm12
Variable c1o,c2o,c3o,c4o,c5o,c6o,c7o,c8o,c9o,c10o,c12o
Variable  cm1o,cm2o,cm3o,cm4o,cm5o,cm6o,cm7o,cm8o,cm9o,cm10o,cm12o
Variable Ho,Hi,ed0,ed1,ed2,ed3,ed4,ed5,ed6,ed7,ed8,ed9,ed10,ed11,ed12,V
Ho=exp(-2.303*xx);Hi=5.62341E-08

c1o=w[2];
c2o=w[3];cm2o=c2o*exp(-2.303*w[4]);
c3o=w[5];cm3o=w[6];
c4o=w[7];
c5o=w[8];
c6o=w[9];cm6o=c6o*exp(-2.303*w[10]);
c7o=w[11];cm7o=w[12];
c8o=w[13];cm8o=c8o*exp(-2.303*w[14]);
c10o=w[15];
c12o=w[16];cm12o=c12o*exp(-2.303*w[17]);


cm1o=(c1o*c6o*cm3o*cm2o)/(c2o*c3o*cm6o);
cm4o=c4o*cm6o/c6o;
cm5o=(c5o*c12o*cm7o*cm8o)/(c8o*c7o*cm12o);
cm10o=c10o*cm8o/c8o;


ed0=w[20]
ed1=w[21]
ed2=w[22]
ed3=w[23]
ed4=w[24]
ed5=w[25]
ed6=w[26]
ed7=w[27]
ed8=w[28]
ed9=w[29]
ed10=w[30]
ed11=w[31]
ed12=w[32]


V=-20/25.7

c1=c1o;cm1=cm1o;
c2=c2o*exp(-ed1*v);cm2=cm2o*exp((ed2-ed1)*v);
c3=c3o*exp((ed2-ed3)*v);cm3=cm3o*exp((ed4-ed3)*v);
c4=c4o;cm4=cm4o;
c5=c5o*exp(-ed6*v);cm5=cm5o*exp(ed7*v);
c6=c6o*exp((1-ed5)*v);cm6=cm6o*exp((ed4-ed5)*v);
c7=c7o*exp((ed9-ed10)*v);cm7=cm7o*exp((ed11-ed10)*v);
c8=c8o*exp(-ed8*v);cm8=cm8o*exp((ed9-ed8)*v);
c10=c10o;cm10=cm10o;
c12=c12o*exp((1-ed12)*v);cm12=cm12o*exp((ed11-ed12)*v);
```

variable a1= hi^2*ho*c1*c6*c8*(c3+cm2)*(c7*cm12*cm5+cm10*(cm12*cm5+(hi*c12+cm5)*cm7))

variable a2=-ho^5*c2*c3*c4*c8*(c7*cm12*cm5+cm10*(cm12*cm5+(hi*c12+cm5)*cm7))

variable a3=ho^3*c8*(c2*c3*(hi^2*c6+cm1)+c1*c4*(c3+cm2))

variable a4=(c7*cm12*cm5+cm10*(cm12*cm5+(hi*c12+cm5)*cm7))

variable a5=cm12*cm5+(hi*c12+cm5)*cm7

variable a6=hi^2*c10*c12*cm7-cm5*cm6*(cm12+cm7)

variable a7=cm5*(cm12+cm7)

variable a8=c7*cm12*(c3*cm4+cm2*(cm3+cm4))

variable a9=c5*(c7+cm10+cm7+cm8)

variable a10=hi^4*c10*c12*c2*c3*c6*cm7*cm8

variable a11=c3*cm4+cm2*(cm3+cm4)

variable a12=hi^2*c10*c12*(c3+cm2)

variable a13=cm5*cm6*(c7*cm12+(cm12+cm7)*(cm10+cm8))

variable a14=c12*(c3*(c5+cm4)+cm2*(c5+cm3+cm4))*cm7

variable a15=hi^3*c2*c3*c6*(c10*a7*cm8+c12*cm7*(cm10*cm4+(c5+cm4)*cm8))

variable a16=c7*cm12+(cm12+cm7)*(cm10+cm8)

variable a17=c7*cm12*cm5*cm6

variable a18= c7*(cm12+cm5)

variable a19= cm7*(cm10+cm8)

variable a20= hi^4*c10*c12*c6*(ho^2*c2*c3+c1*(c3+cm2))*(c7+cm7)

variable a21=ho^5*c2*c3*c4*c8

variable a22=(cm3*cm5+c3*(c5+cm5))

variable a23= cm4+cm6

variable a24= cm2+cm3

variable a25=ho^3*c8*(c2*c3*cm1+c1*c4*(c3+cm2))

variable a26= ho^4*c10*c12*c2*c3*c4

```
variable a27= c1*c10*c12*c4

variable a28= c7+cm7

variable b1=
c12*(ho*c7*c8*cm2+ho*c8*cm2*cm7+cm10*cm2*cm7+cm10*cm3*cm7+cm2*cm7*cm8+cm3*cm
7*cm8+c5*cm2*(c7+cm10+cm7+cm8)+c3*(ho*c8*(a28)+a19+a9))

variable a29= c3+cm2

variable a30= c5+cm5

variable b2= ho^5*c12*c2*c3*c4*c8*(a28)+ho^3*c12*c8*(c2*c3*cm1+c1*c4*(a29))*(a28)

variable b3= c2*(cm1*cm5*(cm3+a23)+c3*(c5*cm1+cm5*(cm1+a23)))

variable b4= c6*(cm2*cm3*cm5+c1*(c5*cm2+(a24)*cm5+c3*(a30)))

variable b5=
ho^3*c12*c2*c3*c8*(a28)+c12*cm2*cm3*a19+ho^2*c2*(c10*c3*(a18+a7)+c12*(cm3*a19+c3*(a1
9+a9)))

variable b6=((a24)*a19+c5*cm2*(c7+cm10+cm7+cm8)+c3*(a19+a9))

variable b7=a26*(a28)+ho^3*c2*c3*c6*c8*(a18+a7)+ho*c1*c6*c8*(a29)*(a18+a7)+b4*(a16)

variable b8= ho^4*c2*c4*(c10*c3*(a18+a7)+c12*(cm3*a19+c3*(a19+a9)))

variable b9=
c12*(c4*cm2*cm3*a19+c2*(cm1*(cm3+a23)*a19+c3*((cm1+a23)*a19+c5*cm1*(c7+cm10+cm7+c
m8))))

variable b10= c10*c2*c3*cm1*(a18+a7)+c1*c4*(c10*(a29)*(a18+a7)+c12*b6)



variable current
current=-(2*(a2-a1-a3*a4-ho^4*c2*c3*c4*(a17+cm10*cm6*(a5)-(a6+hi*(c12*(c5-
cm6)*cm7+c10*a7))*cm8)+hi^2*c1*c6*(a8*cm5+cm10*(a11)*(a5)+(a12*cm7+(a11)*a7+hi*(a14+c
10*(a29)*a7))*cm8)+ho^2*(a10-(c2*c3*cm1+c1*c4*(a29))*a13+a15-
hi*(c2*c3*cm1+c1*c4*(a29))*(-c10*a7*cm8+c12*cm7*(cm10*cm6+(-
c5+cm6)*cm8))+hi^2*(a27*(a29)*cm7*cm8+c2*c3*(c10*c12*cm1*cm7*cm8+c6*cm4*cm5*(a16))))
))
variable current2
current2=(a20+a21*(a18+a7)+a25*(a18+a7)+ho^4*c2*c4*a22*(a16)+(c1+cm1)*cm5*(c3*(a23)+c
m2*(cm3+a23))*(a16)+ho^2*(c4*cm2*cm3*cm5+c1*c4*(c5*cm2+(a24)*cm5+c3*(a30))+b3)*(a16)
+hi^2*(b7+ho^2*(a27*(a29)*(a28)+c2*(c10*c12*c3*cm1*(a28)+c6*a22*(a16))))+hi^3*c6*(b5+c1*(c
10*(a29)*(a18+a7)+b1))+hi*(b2+c12*(c1+cm1)*(c3*(a23)+cm2*(cm3+a23))*a19+b8+ho^2*(b10+b
9)))
return current/(100*current2)
end
```

```
Function CurRat(w,xx)
Wave w
Variable xx
Variable c1,c2,c3,c4,c5,c6,c7,c8,c9,c10,c12
Variable  cm1,cm2,cm3,cm4,cm5,cm6,cm7,cm8,cm9,cm10,cm12
Variable c1o,c2o,c3o,c4o,c5o,c6o,c7o,c8o,c9o,c10o,c12o
Variable  cm1o,cm2o,cm3o,cm4o,cm5o,cm6o,cm7o,cm8o,cm9o,cm10o,cm12o
Variable Ho,Hi,ed0,ed1,ed2,ed3,ed4,ed5,ed6,ed7,ed8,ed9,ed10,ed11,ed12,V
Ho=exp(-2.303*w[0]);Hi=exp(-2.303*w[1])

c1o=w[2];
c2o=w[3];cm2o=c2o*exp(-2.303*w[4]);
c3o=w[5];cm3o=w[6];
c4o=w[7];
c5o=w[8];
c6o=w[9];cm6o=c6o*exp(-2.303*w[10]);
c7o=w[11];cm7o=w[12];
c8o=w[13];cm8o=c8o*exp(-2.303*w[14]);
c10o=w[15];
c12o=w[16];cm12o=c12o*exp(-2.303*w[17]);


cm1o=(c1o*c6o*cm3o*cm2o)/(c2o*c3o*cm6o);
cm4o=c4o*cm6o/c6o;
cm5o=(c5o*c12o*cm7o*cm8o)/(c8o*c7o*cm12o);
cm10o=c10o*cm8o/c8o;


ed0=w[20]
ed1=w[21]
ed2=w[22]
ed3=w[23]
ed4=w[24]
ed5=w[25]
ed6=w[26]
ed7=w[27]
ed8=w[28]
ed9=w[29]
ed10=w[30]
ed11=w[31]
ed12=w[32]

V=xx/25.7

c1=c1o;cm1=cm1o;
c2=c2o*exp(-ed1*v);cm2=cm2o*exp((ed2-ed1)*v);
c3=c3o*exp((ed2-ed3)*v);cm3=cm3o*exp((ed4-ed3)*v);
c4=c4o;cm4=cm4o;
c5=c5o*exp(-ed6*v);cm5=cm5o*exp(ed7*v);
```

```
c6=c6o*exp((1-ed5)*v);cm6=cm6o*exp((ed4-ed5)*v);
c7=c7o*exp((ed9-ed10)*v);cm7=cm7o*exp((ed11-ed10)*v);
c8=c8o*exp(-ed8*v);cm8=cm8o*exp((ed9-ed8)*v);
c10=c10o;cm10=cm10o;
c12=c12o*exp((1-ed12)*v);cm12=cm12o*exp((ed11-ed12)*v);


variable a1= hi^2*ho*c1*c6*c8*(c3+cm2)*(c7*cm12*cm5+cm10*(cm12*cm5+(hi*c12+cm5)*cm7))

variable a2=-ho^5*c2*c3*c4*c8*(c7*cm12*cm5+cm10*(cm12*cm5+(hi*c12+cm5)*cm7))

variable a3=ho^3*c8*(c2*c3*(hi^2*c6+cm1)+c1*c4*(c3+cm2))

variable a4=(c7*cm12*cm5+cm10*(cm12*cm5+(hi*c12+cm5)*cm7))

variable a5=cm12*cm5+(hi*c12+cm5)*cm7

variable a6=hi^2*c10*c12*cm7-cm5*cm6*(cm12+cm7)

variable a7=cm5*(cm12+cm7)

variable a8=c7*cm12*(c3*cm4+cm2*(cm3+cm4))

variable a9=c5*(c7+cm10+cm7+cm8)

variable a10=hi^4*c10*c12*c2*c3*c6*cm7*cm8

variable a11=c3*cm4+cm2*(cm3+cm4)

variable a12=hi^2*c10*c12*(c3+cm2)

variable a13=cm5*cm6*(c7*cm12+(cm12+cm7)*(cm10+cm8))

variable a14=c12*(c3*(c5+cm4)+cm2*(c5+cm3+cm4))*cm7

variable a15=hi^3*c2*c3*c6*(c10*a7*cm8+c12*cm7*(cm10*cm4+(c5+cm4)*cm8))

variable a16=c7*cm12+(cm12+cm7)*(cm10+cm8)

variable a17=c7*cm12*cm5*cm6

variable a18= c7*(cm12+cm5)

variable a19= cm7*(cm10+cm8)

variable a20= hi^4*c10*c12*c6*(ho^2*c2*c3+c1*(c3+cm2))*(c7+cm7)

variable a21=ho^5*c2*c3*c4*c8

variable a22=(cm3*cm5+c3*(c5+cm5))

variable a23= cm4+cm6
```

```
variable a24= cm2+cm3

variable a25=ho^3*c8*(c2*c3*cm1+c1*c4*(c3+cm2))

variable a26= ho^4*c10*c12*c2*c3*c4

variable a27= c1*c10*c12*c4

variable a28= c7+cm7

variable b1=
c12*(ho*c7*c8*cm2+ho*c8*cm2*cm7+cm10*cm2*cm7+cm10*cm3*cm7+cm2*cm7*cm8+cm3*cm
7*cm8+c5*cm2*(c7+cm10+cm7+cm8)+c3*(ho*c8*(a28)+a19+a9))

variable a29= c3+cm2

variable a30= c5+cm5

variable b2= ho^5*c12*c2*c3*c4*c8*(a28)+ho^3*c12*c8*(c2*c3*cm1+c1*c4*(a29))*(a28)

variable b3= c2*(cm1*cm5*(cm3+a23)+c3*(c5*cm1+cm5*(cm1+a23)))

variable b4= c6*(cm2*cm3*cm5+c1*(c5*cm2+(a24)*cm5+c3*(a30)))

variable b5=
ho^3*c12*c2*c3*c8*(a28)+c12*cm2*cm3*a19+ho^2*c2*(c10*c3*(a18+a7)+c12*(cm3*a19+c3*(a1
9+a9)))

variable b6=((a24)*a19+c5*cm2*(c7+cm10+cm7+cm8)+c3*(a19+a9))

variable b7=a26*(a28)+ho^3*c2*c3*c6*c8*(a18+a7)+ho*c1*c6*c8*(a29)*(a18+a7)+b4*(a16)

variable b8= ho^4*c2*c4*(c10*c3*(a18+a7)+c12*(cm3*a19+c3*(a19+a9)))

variable b9=
c12*(c4*cm2*cm3*a19+c2*(cm1*(cm3+a23)*a19+c3*((cm1+a23)*a19+c5*cm1*(c7+cm10+cm7+c
m8))))

variable b10= c10*c2*c3*cm1*(a18+a7)+c1*c4*(c10*(a29)*(a18+a7)+c12*b6)



variable current
current=-(2*(a2-a1-a3*a4-ho^4*c2*c3*c4*(a17+cm10*cm6*(a5)-(a6+hi*(c12*(c5-
cm6)*cm7+c10*a7))*cm8)+hi^2*c1*c6*(a8*cm5+cm10*(a11)*(a5)+(a12*cm7+(a11)*a7+hi*(a14+c
10*(a29)*a7))*cm8)+ho^2*(a10-(c2*c3*cm1+c1*c4*(a29))*a13+a15-
hi*(c2*c3*cm1+c1*c4*(a29))*(-c10*a7*cm8+c12*cm7*(cm10*cm6+(-
c5+cm6)*cm8))+hi^2*(a27*(a29)*cm7*cm8+c2*c3*(c10*c12*cm1*cm7*cm8+c6*cm4*cm5*(a16))))
))
current/=(a20+a21*(a18+a7)+a25*(a18+a7)+ho^4*c2*c4*a22*(a16)+(c1+cm1)*cm5*(c3*(a23)+cm
2*(cm3+a23))*(a16)+ho^2*(c4*cm2*cm3*cm5+c1*c4*(c5*cm2+(a24)*cm5+c3*(a30))+b3)*(a16)+h
i^2*(b7+ho^2*(a27*(a29)*(a28)+c2*(c10*c12*c3*cm1*(a28)+c6*a22*(a16))))+hi^3*c6*(b5+c1*(c10
*(a29)*(a18+a7)+b1))+hi*(b2+c12*(c1+cm1)*(c3*(a23)+cm2*(cm3+a23))*a19+b8+ho^2*(b10+b9)
```

))

V=0

c1=c1o;cm1=cm1o;
c2=c2o*exp(-ed1*v);cm2=cm2o*exp((ed2-ed1)*v);
c3=c3o*exp((ed2-ed3)*v);cm3=cm3o*exp((ed4-ed3)*v);
c4=c4o;cm4=cm4o;
c5=c5o*exp(-ed6*v);cm5=cm5o*exp(ed7*v);
c6=c6o*exp((1-ed5)*v);cm6=cm6o*exp((ed4-ed5)*v);
c7=c7o*exp((ed9-ed10)*v);cm7=cm7o*exp((ed11-ed10)*v);
c8=c8o*exp(-ed8*v);cm8=cm8o*exp((ed9-ed8)*v);
c10=c10o;cm10=cm10o;
c12=c12o*exp((1-ed12)*v);cm12=cm12o*exp((ed11-ed12)*v);

a1= hi^2*ho*c1*c6*c8*(c3+cm2)*(c7*cm12*cm5+cm10*(cm12*cm5+(hi*c12+cm5)*cm7))

a2=-ho^5*c2*c3*c4*c8*(c7*cm12*cm5+cm10*(cm12*cm5+(hi*c12+cm5)*cm7))

a3=ho^3*c8*(c2*c3*(hi^2*c6+cm1)+c1*c4*(c3+cm2))

a4=(c7*cm12*cm5+cm10*(cm12*cm5+(hi*c12+cm5)*cm7))

a5=cm12*cm5+(hi*c12+cm5)*cm7

a6=hi^2*c10*c12*cm7-cm5*cm6*(cm12+cm7)

a7=cm5*(cm12+cm7)

a8=c7*cm12*(c3*cm4+cm2*(cm3+cm4))

a9=c5*(c7+cm10+cm7+cm8)

a10=hi^4*c10*c12*c2*c3*c6*cm7*cm8

a11=c3*cm4+cm2*(cm3+cm4)

a12=hi^2*c10*c12*(c3+cm2)

a13=cm5*cm6*(c7*cm12+(cm12+cm7)*(cm10+cm8))

a14=c12*(c3*(c5+cm4)+cm2*(c5+cm3+cm4))*cm7

a15=hi^3*c2*c3*c6*(c10*a7*cm8+c12*cm7*(cm10*cm4+(c5+cm4)*cm8))

a16=c7*cm12+(cm12+cm7)*(cm10+cm8)

a17=c7*cm12*cm5*cm6

a18= c7*(cm12+cm5)

a19= cm7*(cm10+cm8)

a20= hi^4*c10*c12*c6*(ho^2*c2*c3+c1*(c3+cm2))*(c7+cm7)

a21=ho^5*c2*c3*c4*c8

a22=(cm3*cm5+c3*(c5+cm5))

a23= cm4+cm6

a24= cm2+cm3

a25=ho^3*c8*(c2*c3*cm1+c1*c4*(c3+cm2))

a26= ho^4*c10*c12*c2*c3*c4

a27= c1*c10*c12*c4

a28= c7+cm7

b1=
c12*(ho*c7*c8*cm2+ho*c8*cm2*cm7+cm10*cm2*cm7+cm10*cm3*cm7+cm2*cm7*cm8+cm3*cm7*cm8+c5*cm2*(c7+cm10+cm7+cm8)+c3*(ho*c8*(a28)+a19+a9))

a29= c3+cm2

a30= c5+cm5

b2= ho^5*c12*c2*c3*c4*c8*(a28)+ho^3*c12*c8*(c2*c3*cm1+c1*c4*(a29))*(a28)

b3= c2*(cm1*cm5*(cm3+a23)+c3*(c5*cm1+cm5*(cm1+a23)))

b4= c6*(cm2*cm3*cm5+c1*(c5*cm2+(a24)*cm5+c3*(a30)))

b5=
ho^3*c12*c2*c3*c8*(a28)+c12*cm2*cm3*a19+ho^2*c2*(c10*c3*(a18+a7)+c12*(cm3*a19+c3*(a19+a9)))

b6=((a24)*a19+c5*cm2*(c7+cm10+cm7+cm8)+c3*(a19+a9))

b7=a26*(a28)+ho^3*c2*c3*c6*c8*(a18+a7)+ho*c1*c6*c8*(a29)*(a18+a7)+b4*(a16)

b8= ho^4*c2*c4*(c10*c3*(a18+a7)+c12*(cm3*a19+c3*(a19+a9)))

b9=
c12*(c4*cm2*cm3*a19+c2*(cm1*(cm3+a23)*a19+c3*((cm1+a23)*a19+c5*cm1*(c7+cm10+cm7+cm8))))

b10= c10*c2*c3*cm1*(a18+a7)+c1*c4*(c10*(a29)*(a18+a7)+c12*b6)

variable current0
current0=-(2*(a2-a1-a3*a4-ho^4*c2*c3*c4*(a17+cm10*cm6*(a5)-(a6+hi*(c12*(c5-

```
cm6)*cm7+c10*a7))*cm8)+hi^2*c1*c6*(a8*cm5+cm10*(a11)*(a5)+(a12*cm7+(a11)*a7+hi*(a14+c
10*(a29)*a7))*cm8)+ho^2*(a10-(c2*c3*cm1+c1*c4*(a29))*a13+a15-
hi*(c2*c3*cm1+c1*c4*(a29))*(-c10*a7*cm8+c12*cm7*(cm10*cm6+(-
c5+cm6)*cm8))+hi^2*(a27*(a29)*cm7*cm8+c2*c3*(c10*c12*cm1*cm7*cm8+c6*cm4*cm5*(a16))))
))
current0/=(a20+a21*(a18+a7)+a25*(a18+a7)+ho^4*c2*c4*a22*(a16)+(c1+cm1)*cm5*(c3*(a23)+c
m2*(cm3+a23))*(a16)+ho^2*(c4*cm2*cm3*cm5+c1*c4*(c5*cm2+(a24)*cm5+c3*(a30))+b3)*(a16)
+hi^2*(b7+ho^2*(a27*(a29)*(a28)+c2*(c10*c12*c3*cm1*(a28)+c6*a22*(a16))))+hi^3*c6*(b5+c1*(c
10*(a29)*(a18+a7)+b1))+hi*(b2+c12*(c1+cm1)*(c3*(a23)+cm2*(cm3+a23))*a19+b8+ho^2*(b10+b
9)))

variable relcurr=current/current0
return abs(relcurr)
end


Function M2pH(w,xx)
Wave w
Variable xx
variable Vt=-60
w[0]=xx
variable V0=2.303*25.7*(w[1]-w[0])
//print v0
variable cond=phflux(w,(xx))/(Vt-V0)
w[0]=4
variable V1=2.303*25.7*(w[1]-4)
variable cond0=phflux(w,(4))/(Vt-V1)
return cond/cond0

end

Function M2pH1(w,xx)
Wave w
Variable xx
variable V=60
w[0]=xx
variable V0=2.303*25.7*(w[1]-w[0])
//print v0
variable cond=phflux1(w,(xx))/(V-V0)
w[0]=4
variable V1=2.303*25.7*(w[1]-4)
variable cond0=phflux(w,(4))/(-60-V1)
return cond/cond0

end


Function invchord(w,xx)
Wave w
Variable xx
variable Vt=60
w[0]=xx
variable V0=2.303*25.7*(w[1]-w[0])
```

```
//print v0
variable cond=phflux(w,(xx))/(Vt-V0)
w[0]=6
variable V1=2.303*25.7*(w[1]-6)
variable cond0=phflux(w,(6))/(Vt-V1)
return cond/cond0

end

Function phflux(w,xx)
Wave w
Variable xx
Variable c1,c2,c3,c4,c5,c6,c7,c8,c9,c10,c12
Variable  cm1,cm2,cm3,cm4,cm5,cm6,cm7,cm8,cm9,cm10,cm12
Variable c1o,c2o,c3o,c4o,c5o,c6o,c7o,c8o,c9o,c10o,c12o
Variable  cm1o,cm2o,cm3o,cm4o,cm5o,cm6o,cm7o,cm8o,cm9o,cm10o,cm12o
Variable Ho,Hi,ed0,ed1,ed2,ed3,ed4,ed5,ed6,ed7,ed8,ed9,ed10,ed11,ed12,V
Ho=exp(-2.303*xx);Hi=exp(-2.303*w[1])


c1o=w[2];
c2o=w[3];cm2o=c2o*exp(-2.303*w[4]);
c3o=w[5];cm3o=w[6];
c4o=w[7];
c5o=w[8];
c6o=w[9];cm6o=c6o*exp(-2.303*w[10]);
c7o=w[11];cm7o=w[12];
c8o=w[13];cm8o=c8o*exp(-2.303*w[14]);
c10o=w[15];
c12o=w[16];cm12o=c12o*exp(-2.303*w[17]);


cm1o=(c1o*c6o*cm3o*cm2o)/(c2o*c3o*cm6o);
cm4o=c4o*cm6o/c6o;
cm5o=(c5o*c12o*cm7o*cm8o)/(c8o*c7o*cm12o);
cm10o=c10o*cm8o/c8o;



ed0=w[20]
ed1=w[21]
ed2=w[22]
ed3=w[23]
ed4=w[24]
ed5=w[25]
ed6=w[26]
ed7=w[27]
ed8=w[28]
ed9=w[29]
ed10=w[30]
ed11=w[31]
ed12=w[32]
```

```
V=-60/25.7

c1=c1o;cm1=cm1o;
c2=c2o*exp(-ed1*v);cm2=cm2o*exp((ed2-ed1)*v);
c3=c3o*exp((ed2-ed3)*v);cm3=cm3o*exp((ed4-ed3)*v);
c4=c4o;cm4=cm4o;
c5=c5o*exp(-ed6*v);cm5=cm5o*exp(ed7*v);
c6=c6o*exp((1-ed5)*v);cm6=cm6o*exp((ed4-ed5)*v);
c7=c7o*exp((ed9-ed10)*v);cm7=cm7o*exp((ed11-ed10)*v);
c8=c8o*exp(-ed8*v);cm8=cm8o*exp((ed9-ed8)*v);
c10=c10o;cm10=cm10o;
c12=c12o*exp((1-ed12)*v);cm12=cm12o*exp((ed11-ed12)*v);


variable a1= hi^2*ho*c1*c6*c8*(c3+cm2)*(c7*cm12*cm5+cm10*(cm12*cm5+(hi*c12+cm5)*cm7))

variable a2=-ho^5*c2*c3*c4*c8*(c7*cm12*cm5+cm10*(cm12*cm5+(hi*c12+cm5)*cm7))

variable a3=ho^3*c8*(c2*c3*(hi^2*c6+cm1)+c1*c4*(c3+cm2))

variable a4=(c7*cm12*cm5+cm10*(cm12*cm5+(hi*c12+cm5)*cm7))

variable a5=cm12*cm5+(hi*c12+cm5)*cm7

variable a6=hi^2*c10*c12*cm7-cm5*cm6*(cm12+cm7)

variable a7=cm5*(cm12+cm7)

variable a8=c7*cm12*(c3*cm4+cm2*(cm3+cm4))

variable a9=c5*(c7+cm10+cm7+cm8)

variable a10=hi^4*c10*c12*c2*c3*c6*cm7*cm8

variable a11=c3*cm4+cm2*(cm3+cm4)

variable a12=hi^2*c10*c12*(c3+cm2)

variable a13=cm5*cm6*(c7*cm12+(cm12+cm7)*(cm10+cm8))

variable a14=c12*(c3*(c5+cm4)+cm2*(c5+cm3+cm4))*cm7

variable a15=hi^3*c2*c3*c6*(c10*a7*cm8+c12*cm7*(cm10*cm4+(c5+cm4)*cm8))

variable a16=c7*cm12+(cm12+cm7)*(cm10+cm8)

variable a17=c7*cm12*cm5*cm6

variable a18= c7*(cm12+cm5)

variable a19= cm7*(cm10+cm8)
```

variable a20= hi^4*c10*c12*c6*(ho^2*c2*c3+c1*(c3+cm2))*(c7+cm7)

variable a21=ho^5*c2*c3*c4*c8

variable a22=(cm3*cm5+c3*(c5+cm5))

variable a23= cm4+cm6

variable a24= cm2+cm3

variable a25=ho^3*c8*(c2*c3*cm1+c1*c4*(c3+cm2))

variable a26= ho^4*c10*c12*c2*c3*c4

variable a27= c1*c10*c12*c4

variable a28= c7+cm7

variable b1=
c12*(ho*c7*c8*cm2+ho*c8*cm2*cm7+cm10*cm2*cm7+cm10*cm3*cm7+cm2*cm7*cm8+cm3*cm7*cm8+c5*cm2*(c7+cm10+cm7+cm8)+c3*(ho*c8*(a28)+a19+a9))

variable a29= c3+cm2

variable a30= c5+cm5

variable b2= ho^5*c12*c2*c3*c4*c8*(a28)+ho^3*c12*c8*(c2*c3*cm1+c1*c4*(a29))*(a28)

variable b3= c2*(cm1*cm5*(cm3+a23)+c3*(c5*cm1+cm5*(cm1+a23)))

variable b4= c6*(cm2*cm3*cm5+c1*(c5*cm2+(a24)*cm5+c3*(a30)))

variable b5=
ho^3*c12*c2*c3*c8*(a28)+c12*cm2*cm3*a19+ho^2*c2*(c10*c3*(a18+a7)+c12*(cm3*a19+c3*(a19+a9)))

variable b6=((a24)*a19+c5*cm2*(c7+cm10+cm7+cm8)+c3*(a19+a9))

variable b7=a26*(a28)+ho^3*c2*c3*c6*c8*(a18+a7)+ho*c1*c6*c8*(a29)*(a18+a7)+b4*(a16)

variable b8= ho^4*c2*c4*(c10*c3*(a18+a7)+c12*(cm3*a19+c3*(a19+a9)))

variable b9=
c12*(c4*cm2*cm3*a19+c2*(cm1*(cm3+a23)*a19+c3*((cm1+a23)*a19+c5*cm1*(c7+cm10+cm7+cm8))))

variable b10= c10*c2*c3*cm1*(a18+a7)+c1*c4*(c10*(a29)*(a18+a7)+c12*b6)

variable current1
current1=-(2*(a2-a1-a3*a4-ho^4*c2*c3*c4*(a17+cm10*cm6*(a5)-(a6+hi*(c12*(c5-cm6)*cm7+c10*a7))*cm8)+hi^2*c1*c6*(a8*cm5+cm10*(a11)*(a5)+(a12*cm7+(a11)*a7+hi*(a14+c10*(a29)*a7))*cm8)+ho^2*(a10-(c2*c3*cm1+c1*c4*(a29))*a13+a15-hi*(c2*c3*cm1+c1*c4*(a29))*(-c10*a7*cm8+c12*cm7*(cm10*cm6+(-

```
c5+cm6)*cm8))+hi^2*(a27*(a29)*cm7*cm8+c2*c3*(c10*c12*cm1*cm7*cm8+c6*cm4*cm5*(a16))))
))
variable current2
current2=current1/(a20+a21*(a18+a7)+a25*(a18+a7)+ho^4*c2*c4*a22*(a16)+(c1+cm1)*cm5*(c3*
(a23)+cm2*(cm3+a23))*(a16)+ho^2*(c4*cm2*cm3*cm5+c1*c4*(c5*cm2+(a24)*cm5+c3*(a30))+b3
)*(a16)+hi^2*(b7+ho^2*(a27*(a29)*(a28)+c2*(c10*c12*c3*cm1*(a28)+c6*a22*(a16))))+hi^3*c6*(b
5+c1*(c10*(a29)*(a18+a7)+b1))+hi*(b2+c12*(c1+cm1)*(c3*(a23)+cm2*(cm3+a23))*a19+b8+ho^2
*(b10+b9)))
return -current2

end



Function phflux1(w,xx)
Wave w
Variable xx
Variable c1,c2,c3,c4,c5,c6,c7,c8,c9,c10,c12
Variable  cm1,cm2,cm3,cm4,cm5,cm6,cm7,cm8,cm9,cm10,cm12
Variable c1o,c2o,c3o,c4o,c5o,c6o,c7o,c8o,c9o,c10o,c12o
Variable  cm1o,cm2o,cm3o,cm4o,cm5o,cm6o,cm7o,cm8o,cm9o,cm10o,cm12o
Variable Ho,Hi,ed0,ed1,ed2,ed3,ed4,ed5,ed6,ed7,ed8,ed9,ed10,ed11,ed12,V
Ho=exp(-2.303*xx);Hi=exp(-2.303*w[1])


c1o=w[2];
c2o=w[3];cm2o=c2o*exp(-2.303*w[4]);
c3o=w[5];cm3o=w[6];
c4o=w[7];
c5o=w[8];
c6o=w[9];cm6o=c6o*exp(-2.303*w[10]);
c7o=w[11];cm7o=w[12];
c8o=w[13];cm8o=c8o*exp(-2.303*w[14]);
c10o=w[15];
c12o=w[16];cm12o=c12o*exp(-2.303*w[17]);


cm1o=(c1o*c6o*cm3o*cm2o)/(c2o*c3o*cm6o);
cm4o=c4o*cm6o/c6o;
cm5o=(c5o*c12o*cm7o*cm8o)/(c8o*c7o*cm12o);
cm10o=c10o*cm8o/c8o;



ed0=w[20]
ed1=w[21]
ed2=w[22]
ed3=w[23]
ed4=w[24]
ed5=w[25]
ed6=w[26]
ed7=w[27]
ed8=w[28]
```

```
ed9=w[29]
ed10=w[30]
ed11=w[31]
ed12=w[32]


V=60/25.7

c1=c1o;cm1=cm1o;
c2=c2o*exp(-ed1*v);cm2=cm2o*exp((ed2-ed1)*v);
c3=c3o*exp((ed2-ed3)*v);cm3=cm3o*exp((ed4-ed3)*v);
c4=c4o;cm4=cm4o;
c5=c5o*exp(-ed6*v);cm5=cm5o*exp(ed7*v);
c6=c6o*exp((1-ed5)*v);cm6=cm6o*exp((ed4-ed5)*v);
c7=c7o*exp((ed9-ed10)*v);cm7=cm7o*exp((ed11-ed10)*v);
c8=c8o*exp(-ed8*v);cm8=cm8o*exp((ed9-ed8)*v);
c10=c10o;cm10=cm10o;
c12=c12o*exp((1-ed12)*v);cm12=cm12o*exp((ed11-ed12)*v);


variable a1= hi^2*ho*c1*c6*c8*(c3+cm2)*(c7*cm12*cm5+cm10*(cm12*cm5+(hi*c12+cm5)*cm7))

variable a2=-ho^5*c2*c3*c4*c8*(c7*cm12*cm5+cm10*(cm12*cm5+(hi*c12+cm5)*cm7))

variable a3=ho^3*c8*(c2*c3*(hi^2*c6+cm1)+c1*c4*(c3+cm2))

variable a4=(c7*cm12*cm5+cm10*(cm12*cm5+(hi*c12+cm5)*cm7))

variable a5=cm12*cm5+(hi*c12+cm5)*cm7

variable a6=hi^2*c10*c12*cm7-cm5*cm6*(cm12+cm7)

variable a7=cm5*(cm12+cm7)

variable a8=c7*cm12*(c3*cm4+cm2*(cm3+cm4))

variable a9=c5*(c7+cm10+cm7+cm8)

variable a10=hi^4*c10*c12*c2*c3*c6*cm7*cm8

variable a11=c3*cm4+cm2*(cm3+cm4)

variable a12=hi^2*c10*c12*(c3+cm2)

variable a13=cm5*cm6*(c7*cm12+(cm12+cm7)*(cm10+cm8))

variable a14=c12*(c3*(c5+cm4)+cm2*(c5+cm3+cm4))*cm7

variable a15=hi^3*c2*c3*c6*(c10*a7*cm8+c12*cm7*(cm10*cm4+(c5+cm4)*cm8))

variable a16=c7*cm12+(cm12+cm7)*(cm10+cm8)

variable a17=c7*cm12*cm5*cm6
```

variable a18= c7*(cm12+cm5)

variable a19= cm7*(cm10+cm8)

variable a20= hi^4*c10*c12*c6*(ho^2*c2*c3+c1*(c3+cm2))*(c7+cm7)

variable a21=ho^5*c2*c3*c4*c8

variable a22=(cm3*cm5+c3*(c5+cm5))

variable a23= cm4+cm6

variable a24= cm2+cm3

variable a25=ho^3*c8*(c2*c3*cm1+c1*c4*(c3+cm2))

variable a26= ho^4*c10*c12*c2*c3*c4

variable a27= c1*c10*c12*c4

variable a28= c7+cm7

variable b1=
c12*(ho*c7*c8*cm2+ho*c8*cm2*cm7+cm10*cm2*cm7+cm10*cm3*cm7+cm2*cm7*cm8+cm3*cm7*cm8+c5*cm2*(c7+cm10+cm7+cm8)+c3*(ho*c8*(a28)+a19+a9))

variable a29= c3+cm2

variable a30= c5+cm5

variable b2= ho^5*c12*c2*c3*c4*c8*(a28)+ho^3*c12*c8*(c2*c3*cm1+c1*c4*(a29))*(a28)

variable b3= c2*(cm1*cm5*(cm3+a23)+c3*(c5*cm1+cm5*(cm1+a23)))

variable b4= c6*(cm2*cm3*cm5+c1*(c5*cm2+(a24)*cm5+c3*(a30)))

variable b5=
ho^3*c12*c2*c3*c8*(a28)+c12*cm2*cm3*a19+ho^2*c2*(c10*c3*(a18+a7)+c12*(cm3*a19+c3*(a19+a9)))

variable b6=((a24)*a19+c5*cm2*(c7+cm10+cm7+cm8)+c3*(a19+a9))

variable b7=a26*(a28)+ho^3*c2*c3*c6*c8*(a18+a7)+ho*c1*c6*c8*(a29)*(a18+a7)+b4*(a16)

variable b8= ho^4*c2*c4*(c10*c3*(a18+a7)+c12*(cm3*a19+c3*(a19+a9)))

variable b9=
c12*(c4*cm2*cm3*a19+c2*(cm1*(cm3+a23)*a19+c3*((cm1+a23)*a19+c5*cm1*(c7+cm10+cm7+cm8))))

variable b10= c10*c2*c3*cm1*(a18+a7)+c1*c4*(c10*(a29)*(a18+a7)+c12*b6)

```
variable current1
current1=-(2*(a2-a1-a3*a4-ho^4*c2*c3*c4*(a17+cm10*cm6*(a5)-(a6+hi*(c12*(c5-
cm6)*cm7+c10*a7))*cm8)+hi^2*c1*c6*(a8*cm5+cm10*(a11)*(a5)+(a12*cm7+(a11)*a7+hi*(a14+c
10*(a29)*a7))*cm8)+ho^2*(a10-(c2*c3*cm1+c1*c4*(a29))*a13+a15-
hi*(c2*c3*cm1+c1*c4*(a29))*(-c10*a7*cm8+c12*cm7*(cm10*cm6+(-
c5+cm6)*cm8))+hi^2*(a27*(a29)*cm7*cm8+c2*c3*(c10*c12*cm1*cm7*cm8+c6*cm4*cm5*(a16))))
))
variable current2
current2=current1/(a20+a21*(a18+a7)+a25*(a18+a7)+ho^4*c2*c4*a22*(a16)+(c1+cm1)*cm5*(c3*
(a23)+cm2*(cm3+a23))*(a16)+ho^2*(c4*cm2*cm3*cm5+c1*c4*(c5*cm2+(a24)*cm5+c3*(a30))+b3
)*(a16)+hi^2*(b7+ho^2*(a27*(a29)*(a28)+c2*(c10*c12*c3*cm1*(a28)+c6*a22*(a16))))+hi^3*c6*(b
5+c1*(c10*(a29)*(a18+a7)+b1))+hi*(b2+c12*(c1+cm1)*(c3*(a23)+cm2*(cm3+a23))*a19+b8+ho^2
*(b10+b9)))
return -current2
end


Window SetGuessTable() : Table
	PauseUpdate; Silent 1		// building window...
	String fldrSav0= GetDataFolder(1)
	SetDataFolder root:Packages:GlobalFit:
	Edit/W=(596,169,1395,620) 'Data Sets and Coefficients',AllCoefs,holds,ConWave as "Set
Initial Guesses"
	ModifyTable format(Point)=1,width('Data Sets and Coefficients')=200,alignment(holds)=1
	ModifyTable width(holds)=40,alignment(ConWave)=1
	SetDataFolder fldrSav0
EndMacro
```

BIBLIOGRAPHY

Books and Book Sections:

Brooks, G., J. Butel, et al. (2004). Jawetz, Melnick & Adelberg's Medical Microbiology. New York, McGraw-Hill Medical.

Crosby, A. (1976). Epidemic and Peace, 1918. Part IV. Westport, CT, Greenwood Press.

Franklin, T. and G. Snow (2005). Biochemistry and molecular biology of antimicrobial drug action. New York, Springer**:** 56.

Hirsch, A. (1883). Handbook of Geographical and Historical Pathology, 2nd Ed. London, New Sydenham Society.

Lakowicz, J. (2006). Quenching of Fluorescence. Principles of Fluorescence Spectroscopy. New York, NY, Springer**:** 278-330.

Schonenbaum, S. (1996). Impact of influenza in persons and populations. Options for the Control of Influenza. L. Brown, A. Hampson and R. Webster. New York, Elsevier Science B.V. **III:** 17-25.

Tang, Y., P. Venkataraman, et al. (2005). The M2 Proteins of Influenza A and B Viruses are Single-Pass Proton Channels. Viral Membrane Proteins: Structure, Function, and Drug Design. W. Fischer. New York, Kluwer Academic.

Thomson, D. and R. Thomson (1933). Influenza. New York, Ann Pickett-Thomas Research Labs.

Treanor, J. (2005). Influenza Virus. Principles and Practice of Infectious Diseases. G. Mandell, J. Bennett and R. Dolin. Philadelphia, Elsevier.

Wood, J. (1998). Standardization of inactivated influenza vaccine. Textbook of Influenza. K. Nicholson, R. Webster and A. Hay. London, Blackwell Science**:** 333-345.

Computer Software:

(2009). Maxima, a Computer Algebra System.

Wolfram Research, Inc. (2008). Mathematica. Champaign, IL, Wolfram Research, Inc.

Dissertations:

Alston, R. (2004). Probing the denatured state ensemble with fluorescence. Biochemistry. College Station, Texas A&M University. **Doctor of Philosophy Dissertation:** 227.

Journal Articles:

Agmon, N. (1995). "The Grotthuss mechanism." Chem Phys Lett **244**(5-6): 456-462.

Allen, T., A. Romans, et al. (1980). "Detergent removal during membrane reconstitution." Biochim Biophys Acta **601**(2): 328-342.

Arora, A., F. Abildgaard, et al. (2001). "Structure of outer membrane protein A transmembrane domain by NMR spectroscopy." Nat Struct Biol **8**(4): 334-338.

Barker, W. and J. Mullooly (1980). "Impact of epidemic type A influenza in a defined adult population." Am J Epidemiol **112**: 798-813.

Bauer, C., L. Pinto, et al. (1999). "The Influenza Virus M2 Ion Channel Protein: Probing the Structure of the Transmembrane Domain in Intact Cells by Using Engineered Disulfide Cross-Linking." Virology **254**: 196-209.

Beumer, T., G. Veenstra, et al. (2005). "Whole-mount immunohistochemistry on Xenopus embryos using far-red fluorescent dyes." Trends Genet. **11**(1): 9.

Blaine, W., J. Luby, et al. (1980). "Severe illness with influenza B." Am J Med **68**: 181-189.

Bocharov, E., K. Mineev, et al. (2008). "Spatial structure of the dimeric transmembrane domain of the growth factor receptor ErbB2 presumably corresponding to the receptor active state." J Biol Chem **283**(11): 6950-6956.

Bragstad, K., L. Nielsen, et al. (2008). "The evolution of human influenza A viruses from 1999 to 2006: a complete genome study." Virol J **5**: 40.

Bright, R., D. Shay, et al. (2006). "Adamantane resistance among influenza A viruses isolated early during the 2005-2006 influenza season in the United States." JAMA **295**(8): 891-894.

Chakrabarti, N., B. Roux, et al. (2004). "Structural determinants of proton blockage in aquaporins." J Mol Biol **343**: 493-510.

Chen, B., G. Leser, et al. (2008). "The influenza virus M2 protein cytoplasmic tail interacts with the M1 protein and influences virus assembly at the site of virus budding." J Virol **82**(20): 10059-10070.

Chen, H., Y. Wu, et al. (2007). "Proton Transport Behavior through the Influenza A M2 Channel: Insights from Molecular Simulation." Biophys J **93**: 3470-3479.

Chizhmakov, I., F. Geraghty, et al. (1996). "Selective proton permeability and pH regulation of the influenza virus M2 channel expressed in mouse erythroleukaemia cells." J Physiol **494**(2): 329-336.

Chizhmakov, I., D. Ogden, et al. (2003). "Differences in conductance of M2 proton channels of two influenza viruses at low and high pH." J Physiol **546**(2): 427-438.

Collaborative Computational Project, N. (1994). "The CCP4 suite: programs for protein crystallography." Acta Cryst **D50**: 760-763.

Colman, P., J. Varghese, et al. (1983). "Structure of the catalytic and antigenic sites in influenza virus neuraminidase." Nature **303**: 41-44.

Compans, R., N. Dimmock, et al. (1969). "Effect of antibody to neuraminidase on the maturation and hemagglutinating activity of an influenza A2 virus." J Virol **4**(4): 528-534.

Cristian, L., J. Lear, et al. (2003). "Use of thiol-disulfide equilibria to measure the energetics of assembly of transmembrane helices in phospholipid bilayers." Proc Natl Acad Sci U S A **100**(25): 14772-14777.

Czabotar, P., S. Martin, et al. (2004). "Studies of structural changes in the M2 proton channel of influenza A virus by tryptophan fluorescence." Virus Res **99**: 57-61.

Dahmane, T., M. Damian, et al. (2009). "Amphipol-assisted in vitro folding of G protein-coupled receptors." Biochemistry **48**(27): 6516-6521.

Davies, W., R. Grunert, et al. (1962). "Antiviral activity of 1-adamantanamine (amantadine)." Science **144**: 862-863.

de Groot, B. and H. Grubmuller (2001). "Water permeation across biological membranes: mechanism and dynamics of Aquaporin-1 and GlpF." Science **294**(5550): 2353-2357.

de Jong, M. (2008). "H5N1 transmission and disease: observations from the frontlines." Pediatr Infect Dis J **27**(10 Suppl): S54-S56.

de Jong, M., T. Tran, et al. (2005). "Oseltamivir resistance during treatment of influenza A (H5N1) infection." N Engl J Med **353**(25): 2667-2672.

Decoursey, T. (2003). "Voltage-gated proton channels and other proton transfer pathways." Physiol Rev **83**: 475-579.

Dencher, N., P. Burghaus, et al. (1986). "Determination of the net proton-hydroxide ion permeability across vesicular lipid bilayers and membrane proteins by optical probes." Methods Enzymol **127**: 746-760.

Dowdle, W. and G. Schild (1976). "Influenza: its antigenic variation and ecology." Bull Pan Am Health Organ **10**(3): 193-195.

Duff, K. and R. Ashley (1992). "The transmembrane domain of influenza A M2 protein forms amantadine-sensitive proton channels in planar lipid bilayers." Virology **190**(1): 485-489.

Duff, K., S. Kelly, et al. (1992). "The secondary structure of influenza A M2 transmembrane domain. A circular dichroism study." FEBS Lett **311**: 256-258.

Dutzler, R., E. Campbell, et al. (2003). "Gating the selectivity filter in ClC chloride channels." Science **300**(5616): 108-112.

Dvorin, E., W. Mantulin, et al. (1985). "Conformational properties of human and rat apolipoprotein A-IV." J Lipid Res **26**: 38-46.

Emsley, P. and K. Cowtan (2004). "Coot: model-building tools for molecular graphics." Acta Cryst **D60**: 2126-2132.

Evans, P. (2006). "Scaling and assessment of data quality." Acta Cryst **D62**: 72-82.

Fiore, A., D. Shay, et al. (2008). "Prevention and control of influenza: recommendations of the Advisory Committee on Immunization Practices (ACIP), 2008." MMWR Recomm Rep **57 (RR-7)**(1-60).

Fisher, L. and D. Engelman (2001). "High-Yield Synthesis and Purification of an alpha-Helical Transmembrane Domain." Anal Biochem **293**: 102-108.

Forrest, L., A. Kukol, et al. (2000). "Exploring Models of the Influenza A M2 Channel: MD Simulations in a Phopholipid Bilayer." Biophys J **78**: 55-69.

Francis Jr, T. (1940). "A new type of virus from epidemic influenza." Science **92**: 405-408.

Galbraith, A., J. Oxford, et al. (1971). "Therapeutic effect of 1-adamantanamine hydrochloride in naturally occurring influenza A 2 -Hong Kong infection. A controlled double-blind study." Lancet **2**(7716): 113-115.

Glezen, W., W. Keitel, et al. (1991). "Age Distribution of Patients with Medically-Attended Illnesses Caused by Sequential Variants of Influenza A/H1N1: Comparison to Age-Specific Infection Rates, 1978–1989 " Am J Epidemiol **133**(3): 296-304.

Glover, K., P. Martini, et al. (1999). "Preparation of Insoluble Transmembrane Peptides: Glycophorin-A, Prion (110-137), and FGFR (368-397)." Anal Biochem **272**: 270-274.

Govaert, T., C. Thijs, et al. (1994). "The efficacy of influenza vaccination in elderly individuals. A randomized double-blind placebo-controlled trial." JAMA **272**(21): 1661-1665.

Hay, A., A. Wolstenholme, et al. (1985). "The molecular basis of the specific anti-influenza action of amantadine." EMBO J **4**(11): 3021-3024.

Hayden, F. (2009). "Developing new antiviral agents for influenza treatment: what does the future hold?" Clin Infect Dis **48 Suppl 1**: S3-S13.

Headrick, J., E. Diken, et al. (2005). "Spectral Signatures of Hydrated Proton Vibrations in Water." Science **308**(5729): 1765-1769.

Helenius, A. (1992). "Unpacking the incoming influenza virus." Cell **69**: 577-578.

Holsinger, L., D. Nichani, et al. (1994). "Influenza A Virus M2 Ion Channel Protein: a Structure-Function Analysis." J Virol **68**(3): 1551-1563.

Hong, M. (2007). "Structure, topology, and dynamics of membrane peptides and proteins from solid-state NMR spectroscopy." J Phys Chem B **111**(35): 10340-10351.

Hu, J., T. Asbury, et al. (2007). "Backbone structure of the amantadine-blocked trans-membrane domain M2 proton channel from Influenza A virus." Biophys J **92**(12): 4335-4343.

Hu, J., R. Fu, et al. (2006). "Histidines, heart of the hydrogen ion channel from influenza A virus: Toward an understanding of conductance and proton selectivity." Proc Natl Acad Sci U S A **103**(18): 6865-6870.

Hurt, A., H. Ho, et al. (2006). "Resistance to anti-influenza drugs: adamantanes and neuraminidase inhibitors." Expert Rev Anti Infect Ther **4**(5): 795-805.

Jiang, Y., A. Lee, et al. (2003). "X-ray structure of a voltage-dependent K+ channel." Nature **423**(6935): 33-41.

Jing, X., C. Ma, et al. (2008). "Functional studies indicate amantadine binds to the pore of the influenza A virus M2 channel." Proc Natl Acad Sci U S A **105**(31): 10967-10972.

Johansson, L., A. Wohri, et al. (2009). "Membrane protein crystallization from lipidic phases." Curr Opin Struct Biol **19**(4): 372-378.

Kaiser, J. (2006). "A One-Size-Fits-All Flu Vaccine?" Science **312**: 380-382.

Kavet, J. (1977). "A perspective on the significance of pandemic influenza." Am J Public Health **67**(1063-1070).

Khurana, E., M. Dal Peraro, et al. (2009). "Molecular dynamics calculations suggest a conduction mechanism for the M2 proton channel from influenza A virus." Proc Natl Acad Sci U S A **106**(4): 1069-1074.

Knossow, M. and J. Skehel (2006). "Variation and infectivity neutralization in influenza." Immunology **119**(1): 1-7.

Kochendoerfer, G., D. Salom, et al. (1999). "Total Chemical Synthesis of the Integral Membrane Protein Influenza A Virus M2: Role of Its C-Terminal Domain in Tetramer Assembly." Biochemistry **38**(37): 11905-11913.

Kolocouris, N., G. Zoidis, et al. (2007). "Design and synthesis of bioactive adamantane spiro heterocycles." Bioorg Med Chem Lett **17**(15): 4358-4362.

Kowdley, G., S. Ackerman, et al. (1994). "Hyperpolarization-activated chloride currents in Xenopus oocytes." J Gen Physiol **103**(2): 217-230.

Kurtz, S., G. Luo, et al. (1995). "Growth impairment resulting from expression of influenza virus M2 protein in Saccharomyces cerevisiae: identification of a novel inhibitor of influenza virus." Antimicrob Agents Chemother **39**(10): 2204-2209.

Lackenby, A., C. Thompson, et al. (2008). "The potential impact of neuraminidase inhibitor resistant influenza." Curr Opin Infect Dis **21**(6): 626-638.

Ladokhin, A., S. Jayasinghe, et al. (2000). "How to measure and analyze tryptophan fluorescence in membranes, and why bother?" Anal Biochem **285**(2): 235-245.

Lagoja, I. and E. De Clercq (2008). "Anti-Influenza Virus Agents: Synthesis and Mode of Action." Med Res Rev **28**(1): 1-38.

Lamb, R., S. Zebedee, et al. (1985). "Influenza Virus M2 Protein Is an Integral Membrane Protein Expressed on the Infected-Cell Surface." Cell **40**: 627-633.

Langmuir, A., T. Worthen, et al. (1985). "The Thucydides syndrome. A new hypothesis for the cause of the plague of Athens." N Engl J Med **313**(16): 1027-1030.

Lear, J. (2003). "Proton conduction through the M2 protein of the influenza A virus; a quantitative, mechanistic analysis of experimental data." FEBS Lett **552**: 17-22.

Leslie, A. (1999). "Integration of macromolecular diffraction data." Acta Cryst **D55**(1696-1702).

Lill, M. and V. Helms (2001). "Compact parameter set for fast estimation of proton transfer rates." J Chem Phys **114**(1125-1132).

Lin, T., H. Heider, et al. (1997). "Different modes of inhibition by adamantane amine derivatives and natural polyamines of the functionally reconstituted influenza virus M2 proton channel protein." J Gen Virol **78**: 767-774.

Lin, T. and C. Schroeder (2001). "Definitive assignment of proton selectivity and attoampere unitary current to the M2 ion channel protein of influenza A virus." J Virol **75**(8): 3647-3656.

Luo, W., R. Mani, et al. (2007). "Side-Chain Conformation of the M2 Transmembrane Peptide Proton Channel of Influenza A Virus from 19F Solid-State NMR." J Phys Chem B **111**: 10825-10832.

Ma, C., A. Polishchuk, et al. (2009). "Identification of the functional core of the influenza A virus A/M2 proton-selective ion channel." Proc Natl Acad Sci U S A **106**(30): 12283-12288.

Ma, C., C. Soto, et al. (2008). "Identification of the Pore-lining Residues of the BM2 Ion Channel Protein of Influenza B Virus." J Biol Chem **283**(23): 15921-15931.
MacKenzie, K., J. Prestegard, et al. (1997). "A transmembrane helix dimer: structure and implications." Science **276**: 131-133.
Matthews, B. (1968). "Solvent Content of Protein Crystals." J Mol Biol **33**: 491-497.
McCoy, A., R. Grosse-Kunstleve, et al. (2005). "Likelihood-enhanced fast translation functions." Acta Cryst **D61**: 458-464.
McDermott, A. (2009). "Structure and dynamics of membrane proteins by magic angle spinning solid-state NMR." Annu Rev Biophys **38**: 385-403.
Memoli, M., D. Morens, et al. (2008). "Pandemic and seasonal influenza: therapeutic challenges." Drug Discov Today **13**: 590-595.
Miller, C. (1983). "Integral Membrane Channels: Studies in Model Membranes." Physiol Rev **63**(4): 1209-1242.
Miller, C. (1984). "Ion channels in liposomes." Annu Rev Physiol **46**: 549-558.
Miller, C. (2008). "Ion channels: coughing up flu's proton channels." Nature **451**(7178): 532-533.
Moffat, J., V. Vijayvergiya, et al. (2008). "Proton Transport through Influenza A Virus M2 Protein Reconstituted in Vesicles." Biophys J **94**: 434-445.
Mogabgab, W. (1963). "Virus association with upper respiratory illnesses in adults." Ann Intern Med **59**: 306-311.
Monto, A. (2008). "Antivirals and influenza: frequency of resistance." Pediatr Infect Dis J **27**(10 Suppl): S110-S112.
Morens, D., J. Taubenberger, et al. (2009). "The Persisent Legacy of the 1918 Influenza Virus." N Engl J Med **361**(3): 225-229.
Mould, J., J. Drury, et al. (2000). "Permeation and Activation of the M2 Ion Channel of Influenza A Virus." J Biol Chem **275**(40): 31038-31050.
Mould, J., H.-C. Li, et al. (2000). "Mechanism for Proton Conduction of the M2 Ion Channel of Influenza A Virus." J Biol Chem **275**(12): 8592-8599.
Murshudov, G., A. Vagin, et al. (1997). "Refinement of Macromolecular Structures by the Maximum-Likelihood Method." Acta Cryst **D53**: 240-255.
Neher, E. and B. Sakmann (1976). "Single-channel currents recorded from membrane of denervated frog muscle fibres." Nature **260**(5554): 799-802.
Nguyen, P., C. Soto, et al. (2008). "pH-induced conformational change of the influenza M2 protein C-terminal domain." Biochemistry **47**(38): 9934-9936.
Nicholson, K., F. Aoki, et al. (2000). "Efficacy and safety of oseltamivir in treatment of acute influenza: a randomised controlled trial. Neuraminidase Inhibitor Flu Treatment Investigator Group." Lancet **355**(9218): 1845-1850.
Nigg, C., C. Ecklund, et al. (1942). "Study of epidemics of influenza B." Am J Hyg **35**: 265-275.
Nishimura, K., S. Kim, et al. (2002). "The Closed State of a H+ Channel Helical Bundle Combining Precise Orientational and Distance Restraints from Solid State NMR." Biochemistry **41**: 13170-13177.
Niu, S., B. Doctrow, et al. (2009). "Rhodopsin activity varies in proteoliposomes prepared by different techniques." Biochemistry **48**(1): 156-163.

Okada, A., T. Miura, et al. (2001). "Protonation of Histidine and Histidine-Tryptophan Interaction in the Activation of the M2 Ion Channel from Influenza A Virus." Biochemistry **40**: 6053-6060.

Pielak, R., J. Schnell, et al. (2009). "Mechanism of drug inhibition and drug resistance of influenza A M2 channel." Proc Natl Acad Sci U S A **106**(18): 7379-7384.

Pinto, L., G. Dieckmann, et al. (1997). "A functionally defined model for the M2 proton channel of influenza A virus suggests a mechanism for its ion selectivity." Proc Natl Acad Sci U S A **94**: 11301-11306.

Pinto, L., L. Holsinger, et al. (1992). "Influenza Virus M2 Protein Has Ion Channel Activity." Cell **69**: 517-528.

Pinto, L. and R. Lamb (2006). "The M2 Proton Channels of Influenza A and B Viruses." J Biol Chem **281**(14): 8997-9000.

Pinto, L. and R. Lamb (2007). "Controlling influenza virus replication by inhibiting its proton channel." Mol Biosyst **3**: 18-23.

Powell, H. (1999). "The Rossmann Fourier autoindexing algorithm in MOSFLM." Acta Cryst **D55**: 1690-1695.

Powers, D. and R. Belshe (1993). "Effect of age on cytotoxic T lymphocyte memory as well as serum and local antibody responses elicited by inactivated influenza vaccine." J Infect Dis **197**: 584-592.

Read, R. (2001). "Pushing the boundaries of molecular replacement with maximum likelihood." Acta Cryst **D57**: 1373-1382.

Sagakuchi, T., G. Leser, et al. (1996). "The Ion Channel Activity of the Influenza Virus M2 Protein Affects Transport through the Golgi Apparatus." J Cell Biol **133**(4): 733-747.

Sakaguchi, T., Q. Tu, et al. (1997). "The active oligomeric state of the minimalistic influenza virus M2 ion channel is a tetramer." Proc Natl Acad Sci U S A **94**: 5000-5005.

Salom, D., B. Hill, et al. (2000). "pH-Dependent Tetramerization and Amantadine Binding of the Transmembrane Helix of M2 from the Influenza A Virus." Biochemistry **39**: 14160-14170.

Sansom, M., I. Kerr, et al. (1997). "The Influenza A Virus M2 Channel: A Molecular Modeling and Simulation Study." Virology **233**: 163-173.

Schnell, J. and J. Chou (2008). "Structure and mechanism of the M2 proton channel of influenza A virus." Nature **451**(7178): 591-595.

Schroeder, C., C. Ford, et al. (1994). "Functional reconstitution in lipid vesicles of influenza virus M2 protein expressed by baculovirus: evidence for proton transfer activity." J Gen Virol **75**: 3477-3484.

Seddon, A., P. Curnow, et al. (2004). "Membrane protiens, lipids, and detergents: not just a soap opera." Biochim Biophys Acta **1666**(1-2): 105-117.

Shimbo, K., D. Brassard, et al. (1995). "Viral and Cellular Small Integral Membrane Proteins Can Modify Ion Channels Endogenous to Xenopus Oocytes." Biophys J **69**: 1819-1829.

Simonsen, L., M. Clarke, et al. (1998). "Pandemic versus epidemic influenza mortality: a pattern of changing age distribution." J Infect Dis **178**: 53-60.

Smith, W., C. Andrewes, et al. (1933). "A virus obtained from influenza patients." Lancet **2**: 66-68.
Smondyrev, A. and G. Voth (2002). "Molecular Dynamics Simulation of Proton Transport through the Influenza A Virus M2 Channel." Biophys J **83**: 1987-1996.
Stoeva, S., P. Dolashka, et al. (1995). "Spectroscopic properties of Callinectes sapidus hemocyanin subunits." Spectrochimica Acta **A51**: 1965-1974.
Stouffer, A., R. Acharya, et al. (2008). "Structural basis for the function and inhibition of an influenza virus proton channel." Nature **451**(7178): 596-599.
Stouffer, A., C. Ma, et al. (2008). "The interplay of functional tuning, drug resistance, and thermodynamic stability in the evolution of the M2 proton channel from the influenza A virus." Structure **16**(7): 1067-1076.
Stouffer, A., V. Nanda, et al. (2005). "Sequence determinants of a transmembrane proton channel: an inverse relationship between stability and function." J Mol Biol **347**: 169-179.
Sugrue, R., G. Bahadur, et al. (1990). "Specific structural alteration of the influenza haemagglutinin by amantadine." EMBO J **9**(11): 3469-3476.
Sugrue, R., R. Belshe, et al. (1990). "Palmitoylation of the influenza A virus M2 protein." Virology **179**(1): 51-56.
Suzuki, H. and S. Takeuchi (2008). "Microtechnologies for membrane protein studies." Anal Bioanal Chem **391**: 2695-2702.
Szoka Jr, F. and D. Papahadjopoulos (1980). "Comparative properties and methods of preparation of lipid vesicles (liposomes)." Ann Rev Biophys Bioeng **9**: 467-508.
Szucs, T. (1999). "The socio-economic burden of influenza." J Antimicrob Chemother. **44**(Suppl B): 11-15.
Tajkhorshid, E., P. Nollert, et al. (2002). "Control of the selectivity of the aquaporin water channel family by global orientational tuning." Science **296**(5567): 525-530.
Tammaro, P., K. Shimomura, et al. (2008). "Xenopus oocytes as a heterologous expression system for studying ion channels with the patch-clamp technique." Methods Mol Biol **491**: 127-139.
Tang, Y., F. Zaitseva, et al. (2002). "The Gate of the Influenza Virus M2 Proton Channel Is Formed by a Single Tryptophan Residue." J Biol Chem **277**(42): 39880-39886.
Taylor, R. (1951). "A further note on 1233 ("influenza C") virus." Arch Gesamte Virusforsch **4**: 485-495.
Thompson, W., D. Shay, et al. (2003). "Mortality Associated With Influenza and Respiratory Syncytial Virus in the United States " JAMA **289**(2): 179-186.
Tian, C., P. Gao, et al. (2003). "Initial structural and dynamic characterization of the M2 protein transmembrane and amphipathic helices in lipid bilayers." Protein Sci **12**: 2597-2605.
Tobler, K., M. Kelly, et al. (1999). "Effect of Cytoplasmic Tail Truncations on the Activity of the M2 Ion Channel of Influenza A Virus." J Virol **73**(12): 9695-9701.
Torres, J. and I. Arkin (2002). "C-Deuterated Alanine: A New Label to Study Membrane Protein Structure Using Site-Specific Infrared Dichroism." Biophys J **82**: 1068-1075.

Torres, J., A. Kukol, et al. (2000). "Use of a Single Glycine Residue to Determine the Tilt and Orientation of a Transmembrane Helix. A New Structural Label for Infrared Spectroscopy." Biophys J **79**: 3139-3143.

Tosteson, M., L. Pinto, et al. (1994). "Reconstitution of the influenza virus M2 ion channel in lipid bilayers." J Membr Biol **142**(1): 117-126.

Treanor, J., F. Hayden, et al. (2000). "Efficacy and safety of the oral neuraminidase inhibitor oseltamivir in treating acute influenza: a randomized controlled trial. US Oral Neuraminidase Study Group." JAMA **283**(8): 1016-1024.

Tripp, R. and S. Tompkins (2008). "Recombinant vaccines for influenza virus." Curr Opin Investig Drugs **9**(8): 836-845.

Varghese, J., W. Laver, et al. (1983). "Structure of the influenza virus glycoprotein antigen neuraminidase at 2.9 A resolution." Nature **303**: 35-40.

Venkataraman, P., R. Lamb, et al. (2005). "Chemical Rescue of Histidine Selectivity Filter Mutants of the M2 Ion Channel of Influenza A Virus." J Biol Chem **280**(22): 21463-21472.

von Itzstein, M. and R. Thomson (2009). "Anti-influenza drugs: the development of sialidase inhibitors." Handb Exp Pharmacol **189**: 111-154.

von Itzstein, M., W. Wu, et al. (1993). "Rational design of potent sialidase-based inhibitors of influenza virus replication." Nature **363**: 418-423.

Wang, C., R. Lamb, et al. (1994). "Direct measurement of the influenza A virus M2 protein ion channel activity in mammalian cells." Virology **205**(1): 133-140.

Wang, C., R. Lamb, et al. (1995). "Activation of the M2 Ion Channel of Influenza Virus: A Role for the Transmembrane Domain Histidine Residue." Biophys J **69**: 1363-1371.

Wang, C., K. Takeuchi, et al. (1993). "The ion channel activity of the influenza A virus M2 protein: chacterization of the amantadine block." J Virol **67**: 5585-5594.

Wang, J., S. Cady, et al. (2009). "Discovery of spiro-piperidine inhibitors and their modulation of the dynamics of the M2 proton channel from influenza A virus." J Am Chem Soc **131**(23): 8066-8076.

Wang, J., S. Kim, et al. (2001). Protein Sci **10**: 2241-2250.

Webster, R., W. Laver, et al. (1980). "The mechanism of antigenic drift in influenza viruses: analysis of Hong Kong (H3N2) variants with monoclonal antibodies to the hemagglutinin molecule." Ann N Y Acad Sci **354**: 142-161.

White, S. (2004). "The progress of membrane protein structure determination." Protein Sci **13**(7): 1948-1949.

Wilson, I. and N. Cox (1990). "Structural basis of immune recognition of influenza virus hemagglutinin." Ann Rev Immunol **8**: 737-771.

Wilson, I., J. Skehel, et al. (1981). "Structure of the hemagglutinin membrane glycoprotein of influenza A virus at 3A resolution." Nature **289**: 366-373.

Wilton, P. (1993). "Spanish flu outdid WW I in number of lives claimed." Can Med Assoc J **148**(11): 2036-2037.

Witchel, H., J. Milnes, et al. (2002). "Troubleshooting problems with in vitro screening of drugs for QT interval prolongation using HERG K+ channels expressed in

mammalian cell lines and Xenopus oocytes." J Pharmacol Toxicol Methods **48**(2): 65-80.
Yi, M., T. Cross, et al. (2008). "A secondary gate as a mechanism for inhibition of the M2 proton channel by amantadine." J Phys Chem B **112**(27): 7977-7979.
Zhang, M., D. Zharikova, et al. (2006). "Fine specificity and sequence of antibodies directed against the ectodomain of matrix protein 2 of influenza A virus." Mol Immunol **43**(14): 2195-2206.
Zhirnov, O. (1990). "Solubilization of matrix protein M/M1 from virions occurs at different pH for orthomyxo- and paramyxoviruses." Virology **176**: 274-279.
Zhirnov, O. (1992). "Isolation of matrix protein M1 from influenza viruses by acid-dependent extraction with nonionic detergent." Virology **186**: 324-330.
Ziegler, T., M. Hemphill, et al. (1999). "Low incidence of rimantadine resistance in field isolates of influenza A viruses." J Infect Dis **180**(4): 935-939.

Unpublished Data:

Polishchuk, A. Unpublished data.

World Wide Web Sites:

Gang, X. (1997, 2005). "Linear Solver." Retrieved October, 2008, from http://wims.unice.fr/wims/en_tool~linear~linsolver.en.html.
NIST (National Institute of Standards and Technology) (2008). "3-(C2H5)-Pyridine." Chemistry WebBook, Retrieved September, 2008, from http://webbook.nist.gov/cgi/inchi/InChI%3D1S/C7H9N/c1-2-7-4-3-5-8-6-7/h3-6H%2C2H2%2C1H3.
White, S. "Membrane Proteins of Known Structure." Retrieved 26 Aug 2009, from http://blanco.biomol.uci.edu/Membrane_Proteins_xtal.html.